MANY-BODY GREEN'S FUNCTIONS AND THE BETHE-SALPETER EQUATION IN CHEMISTRY: FROM SINGLE MOLECULES TO COMPLEX SYSTEMS

EDITED BY: Bjoern Baumeier, Patrick Rinke, Linn Leppert, Marc Dvorak and Dorothea Golze

PUBLISHED IN: Frontiers in Chemistry

frontiers Research Topics

ISSN 1664-8714
ISBN 978-2-83250-228-0
DOI 10.3389/978-2-83250-228-0

About Frontiers

Frontiers is more than just an open-access publisher of scholarly articles: it is a pioneering approach to the world of academia, radically improving the way scholarly research is managed. The grand vision of Frontiers is a world where all people have an equal opportunity to seek, share and generate knowledge. Frontiers provides immediate and permanent online open access to all its publications, but this alone is not enough to realize our grand goals.

Frontiers Journal Series

The Frontiers Journal Series is a multi-tier and interdisciplinary set of open-access, online journals, promising a paradigm shift from the current review, selection and dissemination processes in academic publishing. All Frontiers journals are driven by researchers for researchers; therefore, they constitute a service to the scholarly community. At the same time, the Frontiers Journal Series operates on a revolutionary invention, the tiered publishing system, initially addressing specific communities of scholars, and gradually climbing up to broader public understanding, thus serving the interests of the lay society, too.

Dedication to Quality

Each Frontiers article is a landmark of the highest quality, thanks to genuinely collaborative interactions between authors and review editors, who include some of the world's best academicians. Research must be certified by peers before entering a stream of knowledge that may eventually reach the public - and shape society; therefore, Frontiers only applies the most rigorous and unbiased reviews.
Frontiers revolutionizes research publishing by freely delivering the most outstanding research, evaluated with no bias from both the academic and social point of view. By applying the most advanced information technologies, Frontiers is catapulting scholarly publishing into a new generation.

What are Frontiers Research Topics?

Frontiers Research Topics are very popular trademarks of the Frontiers Journals Series: they are collections of at least ten articles, all centered on a particular subject. With their unique mix of varied contributions from Original Research to Review Articles, Frontiers Research Topics unify the most influential researchers, the latest key findings and historical advances in a hot research area! Find out more on how to host your own Frontiers Research Topic or contribute to one as an author by contacting the Frontiers Editorial Office: frontiersin.org/about/contact

MANY-BODY GREEN'S FUNCTIONS AND THE BETHE-SALPETER EQUATION IN CHEMISTRY: FROM SINGLE MOLECULES TO COMPLEX SYSTEMS

Topic Editors:
Bjoern Baumeier, Eindhoven University of Technology, Netherlands
Patrick Rinke, Aalto University, Finland
Linn Leppert, University of Twente, Netherlands
Marc Dvorak, Aalto University, Finland
Dorothea Golze, Aalto University, Finland

Citation: Baumeier, B., Rinke, P., Leppert, L., Dvorak, M., Golze, D., eds. (2022). Many-Body Green's Functions and the Bethe-Salpeter Equation in Chemistry: From Single Molecules to Complex Systems. Lausanne: Frontiers Media SA. doi: 10.3389/978-2-83250-228-0

Table of Contents

frontiers in Chemistry

EDITORIAL
published: 21 February 2022
doi: 10.3389/fchem.2022.866492

Editorial: Many-Body Green's Functions and the Bethe-Salpeter Equation in Chemistry: From Single Molecules to Complex Systems

Marc Dvorak[1], Björn Baumeier[2]*, Dorothea Golze[1,3]*, Linn Leppert[4]* and Patrick Rinke[1]**

[1]Department of Applied Physics, Aalto University, Espoo, Finland, [2]Department of Mathematics and Computer Science and Institute for Complex Molecular Systems, Eindhoven University of Technology, Eindhoven, Netherlands, [3]Faculty of Chemistry and Food Chemistry, Technische Universität Dresden, Dresden, Germany, [4]MESA+ Institute for Nanotechnology, University of Twente, Enschede, Netherlands

Keywords: many-body Green's function, GW approximation, Bethe-Salpeter equation, computational chemistry, theoretical spectroscopy

Edited and reviewed by:
Sam P. De Visser,
The University of Manchester,
United Kingdom

****Correspondence:***
Marc Dvorak
marc.dvorak@aalto.fi
Björn Baumeier
B.Baumeier@tue.nl
Dorothea Golze
dorothea.golze@aalto.fi
Linn Leppert
l.leppert@utwente.nl
Patrick Rinke
patrick.rinke@aalto.fi

Specialty section:
This article was submitted to Theoretical and Computational Chemistry, a section of the journal Frontiers in Chemistry

Received: *31 January 2022*
Accepted: *31 January 2022*
Published: *21 February 2022*

Citation:
Dvorak M, Baumeier B, Golze D, Leppert L and Rinke P (2022) Editorial: Many-Body Green's Functions and the Bethe-Salpeter Equation in Chemistry: From Single Molecules to Complex Systems. Front. Chem. 10:866492. doi: 10.3389/fchem.2022.866492

Editorial on the Research Topic

Many-Body Green's Functions and the Bethe-Salpeter Equation in Chemistry: From Single Molecules to Complex Systems

The utility of many-body Green's function methods for computing excitation energies and spectra of correlated systems continues to impress. While applications and implementations of the *GW* approach were initially developed in the solid-state physics community, the method and its combination with the Bethe-Salpeter Equation (BSE) has more recently taken a foothold among quantum chemists. Across disciplines, the field continues to grow and it currently carries great momentum: it is therefore timely to collect articles showcasing the latest triumphs and outstanding shortcomings of this family of methods.

The contributions to this Research Topic range from theory and method development to applications of Green's function-based methods. Applications of *GW* to organic crystals and FeS_2 are motivated by the importance of an atomistic understanding of excited states for technological applications such as photovoltaics. Contributions that highlight the predictive power of the *GW* approach and present low-scaling implementations showcase the potential of the theory for applications to complex heterogeneous materials. Additionally, method and theory development for *GW*, BSE, and non-*GW* calculations of the single-particle Green's function form important parts of this collection of articles.

In *The GW/BSE Method in Magnetic Fields*, Holzer et al. benchmark their new *GW*/BSE implementation in external magnetic fields. External fields pose a challenge to electronic structure theory because they require complex orbitals to ensure gauge-invariant results, raising the computational expense. Furthermore, kernels of time-dependent density functional theory can be unstable in the presence of the perturbing field. *GW*/BSE presents a solution to the latter problem, and the authors implement the theory with complex London orbitals to circumvent gauge dependence.

The fundamental band gaps of two phases of FeS_2 remain somewhat undetermined: theoretical calculations are scattered and experiments only reliably measure the optical band gap. In *Accurate Prediction of Band Structure of* FeS_2*: A Hard Quest of Advanced First-Principles Approaches*, Zhang and Jiang set out to resolve the theoretical discrepancy by performing *GW* calculations on both phases with the most complete basis to date: a linearized augmented plane wave basis (LAPW) supplemented with high-energy local orbitals (HLOs). The authors find that very high momentum

HLOs are necessary to converge the sum over unoccupied states in *GW* and attribute inconsistencies in previous theoretical work to underconvergence.

Molecular crystals are a modern success of *GW*. Their high tunability through packing and choice of substrate render them an interesting playing field for computational exploration. The *GW* approach affords an excellent description of the important effect of substrate screening. In *Exciton Modulation in Perylene-Based Molecular Crystals Upon Formation of a Metal-Organic Interface From Many-Body Perturbation Theory*, Shunak et al. explore the change in quasiparticle and excitonic properties of octyl perylene diimide (C8-PDI) adsorbed on gold. They find that exciton binding energies are unchanged due to the local character of screening between electron and hole but that fundamental band gaps are dependent on layer number, stacking, and substrate.

Most low-scaling *GW* algorithms are restricted to diagonal G_0W_0. In *Low-Order Scaling Quasiparticle Self-Consistent GW for Molecules*, Förster and Visscher present their low-scaling implementation of quasiparticle self-consistent *GW* (qsGW) based on the space-time method. They validate their implementation against other results and then include a polarizable continuum model to study DNA oligomers.

The cumulant approximation makes an exponential ansatz to the Green's function $G_c(t) = G_c^0(t)e^{C(t)}$, and is known to produce satellite and shake-up features of the spectral function better than Dyson-equation-based calculations. *Equation-of-Motion Coupled-Cluster Cumulant Green's Function for Excited States and X-Ray Spectra* by Vila et al. presents a real-time formulation for computing X-ray spectra that draws on connections between coupled-cluster and cumulant approaches. Core ionization energies from the improved EOM-CC method are presented for CH_4, NH_3, H_2O, HF, and Ne, and a full X-ray absorption spectrum is presented for NH_3.

The Hubbard model remains a valuable test bed for theoretical physics since it permits both analytic and numerically exact solutions in certain cases. *Scrutinizing GW-Based Methods Using the Hubbard Dimer* by Di Sabatino et al. finds that different starting points for constructing G_0 and W_0 lead to the existence of multiple quasiparticle solutions, loss of particle number, or discontinuities in physical quantitites as a function of interaction strength. Fully self-consistent *GW* removes these artifacts but does not necessarily improve the accuracy of the results.

The GW Miracle in Many-Body Perturbation Theory for the Ionization Potential of Molecules systematically tests ionization potentials for the *GW*100 test set computed with G_0W_0 against a series of alternative many-body theories. Bruneval et al. find that, while more accurate theories may exist, they come at much greater expense; the cost-accuracy balance of G_0W_0 is unbeatable. They also note that the most substantial improvement to G_0W_0 comes not by incorporating additional diagrams but from an improved mean-field starting point.

Calculations of optical spectra in solids with the Bethe-Salpeter equation require an enormously dense **k**-point grid due to the extended character of excitons in real space. This remains a bottleneck in applying the method to solids. *Double k-Grid Method for Solving the Bethe-Salpeter Equation via Lanczos Approaches* by Alliati et al. presents an efficient interpolation scheme to ameliorate this problem. It computes the optical absorption on a fine **k**-grid, on which each diagonal block of the Hamiltonian is taken from the calculation of the kernel on a coarse **k**-grid. The scheme reproduces optical spectra of Si, GaAs, and MoS_2 with good accuracy.

In *Photoemission Spectra from the Extended Koopman's Theorem, Revisited*, Di Sabatino et al. show that their recent work developing many-body effective energy theory (MEET) is more closely related to the well-known Extended Koopman's Theorem (EKT) than previously appreciated. The lowest level of approximation to MEET is equivalent to the diagonal approximation of the EKT. The authors explore the asymmetric Hubbard dimer and find that the MEET energies depend on the choice of basis, corroborating previous work.

The continued development of theory and algorithms, progression of computational power, and importance of excited state spectra ensure that many-body Green's functions will play a role in fundamental science for the forseeable future.

AUTHOR CONTRIBUTIONS

All authors listed have made a substantial, direct, and intellectual contribution to the work and approved it for publication.

Conflict of Interest: The authors declare that the research was conducted in the absence of any commercial or financial relationships that could be construed as a potential conflict of interest.

Publisher's Note: All claims expressed in this article are solely those of the authors and do not necessarily represent those of their affiliated organizations, or those of the publisher, the editors and the reviewers. Any product that may be evaluated in this article, or claim that may be made by its manufacturer, is not guaranteed or endorsed by the publisher.

frontiers in Chemistry

ORIGINAL RESEARCH
published: 03 September 2021
doi: 10.3389/fchem.2021.736591

Low-Order Scaling Quasiparticle Self-Consistent GW for Molecules

Arno Förster and Lucas Visscher*

Theoretical Chemistry, Vrije Universiteit, Amsterdam, Netherlands

Low-order scaling GW implementations for molecules are usually restricted to approximations with diagonal self-energy. Here, we present an all-electron implementation of quasiparticle self-consistent GW for molecular systems. We use an efficient algorithm for the evaluation of the self-energy in imaginary time, from which a static non-local exchange-correlation potential is calculated via analytical continuation. By using a direct inversion of iterative subspace method, fast and stable convergence is achieved for almost all molecules in the GW100 database. Exceptions are systems which are associated with a breakdown of the single quasiparticle picture in the valence region. The implementation is proven to be starting point independent and good agreement of QP energies with other codes is observed. We demonstrate the computational efficiency of the new implementation by calculating the quasiparticle spectrum of a DNA oligomer with 1,220 electrons using a basis of 6,300 atomic orbitals in less than 4 days on a single compute node with 16 cores. We use then our implementation to study the dependence of quasiparticle energies of DNA oligomers consisting of adenine-thymine pairs on the oligomer size. The first ionization potential in vacuum decreases by nearly 1 electron volt and the electron affinity increases by 0.4 eV going from the smallest to the largest considered oligomer. This shows that the DNA environment stabilizes the hole/electron resulting from photoexcitation/photoattachment. Upon inclusion of the aqueous environment *via* a polarizable continuum model, the differences between the ionization potentials reduce to 130 meV, demonstrating that the solvent effectively compensates for the stabilizing effect of the DNA environment. The electron affinities of the different oligomers are almost identical in the aqueous environment.

Keywords: GW approximation, convergence acceleration, analytical continuation, quasiparticle, quasiparticle self-consistent *GW*, DNA photodamage, theoretical spectroscopy

OPEN ACCESS

Edited by:
Dorothea Golze,
Aalto University, Finland

Reviewed by:
Jan Wilhelm,
University of Regensburg, Germany
Ivan Duchemin,
Commissariat à l'Energie Atomique et aux Energies Alternatives (CEA), France

****Correspondence:***
Arno Förster
a.t.l.foerster@vu.nl

Specialty section:
This article was submitted to Theoretical and Computational Chemistry, a section of the journal Frontiers in Chemistry

Received: *05 July 2021*
Accepted: *13 August 2021*
Published: *03 September 2021*

Citation:
Förster A and Visscher L (2021) Low-Order Scaling Quasiparticle Self-Consistent GW for Molecules. Front. Chem. 9:736591. doi: 10.3389/fchem.2021.736591

1 INTRODUCTION

The *GW* approximation (GWA) to Hedin's equations (Hedin, 1965) is a popular approach to calculate charged excitations in molecular systems. Recent applications include the calculation of band gaps and elucidation of charge-transfer in organic donor-acceptor compounds (Blase and Attaccalite, 2011; Blase et al., 2011; Caruso et al., 2014), applications to dye-sensitized solar cells (Marom et al., 2011; Faber et al., 2012; Umari et al., 2013; Marom et al., 2014; Mowbray and Migani, 2015), electronic level alignment in photocatalytic interfaces (Migani et al., 2013, 2014), core-ionization spectra of medium sized molecules (Van Setten et al., 2018; Golze et al., 2018, 2020) or photo-electron spectra of transition metal oxides (Berardo et al., 2017; Hung et al., 2017; Shi et al., 2018; Rezaei and Ögüt, 2021). Combined with the Bethe-Salpeter equation (BSE) formalism (Salpeter

and Bethe, 1951; Strinati, 1988) the GWA has been used to calculate optical spectra of Cyanins (Boulanger et al., 2014), the Bacteriochlorin molecule (Duchemin et al., 2012) or Bacteriochlorophylls and Chlorophylls (Hashemi and Leppert, 2021). At the same time, the GWA has been implemented into an increasing number of molecular electronic structure codes (Ke, 2011; Caruso et al., 2012; Caruso et al., 2013; Ren et al., 2012; Van Setten et al., 2013; Kaplan et al., 2015, 2016; Bruneval et al., 2016; Wilhelm et al., 2016; Tirimbò et al., 2020b). Traditionally, these implementations use localized basis functions and the resolution-of the identity or density fitting approximation (Baerends et al., 1973; Whitten, 1973; Dunlap et al., 1979) within the global Coulomb metric (RI-V) (Vahtras et al., 1993), leading to a scaling of N^4 with system size. Systems of around 100 atoms are within reach on standard hardware (Knight et al., 2016), while highly parallel implementations enable applications to systems with more than 300 atoms on modern supercomputers (Wilhelm et al., 2016; Wilhelm et al., 2018; Wilhelm et al., 2021).

Over the last years, many algorithms with reduced asymptotic scaling with system size have been proposed. These are usually based on the space-time approach by Godby and coworkers (H. N. Rojas et al., 1995; Rieger et al., 1999). The original space-time method is based on the observation that it is much simpler to solve the Dyson equations in the GWA in reciprocal space and imaginary frequency while the kernels of these Dyson equations are most easily evaluated in real space and imaginary time, reducing the asymptotic scaling of the GWA to N^3. Building on earlier work by Almlöf (Almlöf et al., 1982), Kresse, Kaltak and coworkers could significantly reduce the prefactor of these calculations by using non-uniform spaced grids in imaginary time and imaginary frequency and an efficient way to switch between both domains (Kaltak et al., 2014a; Kaltak et al., 2014b; Kaltak and Kresse, 2020). Over the last years, there has been a surge of new *GW* implementations based on the space-time method for periodic (Kutepov et al., 2012; Chu et al., 2016; Liu et al., 2016; Kutepov et al., 2017; Grumet et al., 2018; Kutepov, 2020; Singh and Wang, 2020; Foerster and Gueddida, 2021) and finite (Wilhelm et al., 2018; Koval et al., 2019; Förster and Visscher, 2020; Duchemin and Blase, 2021; Wilhelm et al., 2021) systems. Other recent examples of low-order scaling implementations include the spectral function based approach by Foerster et al. (2011), the time-shredded propagator formalism by Ismail-Beigi and coworkers (Kim et al., 2020), stochastic *GW* developed by Neuhauser et al. (2014), Vlček et al. (2017), Vlček et al. (2018), Weng and Vlcek (2021), and also a fragment molecular orbital based implementation (Fujita et al., 2019).

For molecular systems, diagonal approximations to the self-energy are commonly made. They rely on the assumption that the wave function of generalized Kohn-Sham (KS) density functional theory (DFT) is similar to the GW wave function. One then evaluates corrections to the DFT single orbital energies by calculating the diagonal elements of the self-energy matrix Σ. The most economical way to calculate these corrections is the one-shot G_0W_0 approach which heavily depends on the mean-field starting point. Extensive benchmarks (Marom et al., 2012; Bruneval and Marques, 2013; Caruso et al., 2016; Knight et al., 2016) have provided substantial evidence that hybrid functionals with a rather large amount of exact exchange or long-range corrected hybrids are usually a suitable starting point. In addition, non-empirical procedures to select an optimal starting point for a given system have been proposed (Gallandi and Körzdörfer, 2015; Dauth et al., 2016; Bois and Körzdörfer, 2017). Finally, in eigenvalue-only self-consistent *GW* (evGW) the QP energies are updated until they are stationary, removing the starting point dependence to a large extent.

QP energies calculated following these strategies are almost always more accurate than fully self-consistent *GW* (scGW) calculations for molecules. As discussed by Kotani, van Schilfgaarde and Valeev, QP approximations, i.e. approximations in which satellites are neglected, emphasize the importance of the Ward identity (Ward, 1950) in the long-range and low-frequency limit. The Ward identity demands '*Z*-factor cancellation' (Kotani et al., 2007) between the three-point Vertex and the renormalized electron propagator. Z is the QP renormalization factor. In QP approximations, neither the vertex is included nor is the propagator renormalized, and the effect of both approximations cancel in the above-mentioned limit. This limit can be expected to be of particular importance for weakly correlated molecules to which the GWA is frequently applied.

As opposed to diagonal approximations, scGW is strictly starting point independent and also allows to calculate 1-particle reduced density matrices (1RDM) including electron correlation effects from first principles. Most importantly, it does not contain any adjustable parameters. Another method which also offers these advantages is the QP self-consistent *GW* (qs*GW*) method by Kotani, van Schilfgaarde and Faleev. (Van Schilfgaarde et al., 2006; Kotani et al., 2007). qs*GW* can be seen as a non-empirical procedure to find an optimal starting point for a G_0W_0 calculation. This is accomplished by mapping the *GW* self-energy self-consistently to a non-local, Hermitian, and static exchange-correlation potential. This potential has been shown to be optimal in a variational sense (Ismail-Beigi, 2017). Diagonalization of the resulting mean-field Hamiltonian yields eigenvectors and eigenvalues from which a new non-interacting Green's function is obtained. This self consistent field (SCF) procedure is reminiscent of generalized KS theory, with the notable difference that the exchange-correlation potential is not a functional of the 1RDM but rather of the non-interacting single-particle Green's function. qs*GW* is starting point independent and fulfills the Ward identity in the low frequency and long range limit.

In canonical implementations (Ke, 2011; Bruneval, 2012; Koval et al., 2014; Kaplan et al., 2015; Kaplan et al., 2016), the need to calculate the off-diagonal elements of the self-energy matrix and the fact that it is typically more difficult to converge make qs*GW* typically an order of magnitude more expensive than ev*GW* (Gui et al., 2018) which in turn is typically 5–10 times more expensive than G_0W_0 due to the requirement of self-consistency. Moreover, low-order scaling implementations for molecules are typically restricted to diagonal approximations only (Wilhelm et al., 2018; Förster and Visscher, 2020; Duchemin and Blase, 2021; Wilhelm et al., 2021) To fill this gap, we extend the recently

developed low-order scaling diagonal *GW* implementation in ADF (Baerends et al., 2020; Förster and Visscher, 2020, Förster and Visscher, 2021) to qs*GW*. We evaluate the qs*GW* self-energy as a direct product in imaginary time, in the same way as in the diagonal approximation. Even though the qs*GW* self-energy is static, for larger systems evaluation of the self-energy at an array of imaginary time points is more efficient than its evaluation at a single real frequency point. The procedure is similar to the linearized qs*GW* method by Kutepov and coworkers (Kutepov et al., 2017) which is also based on the imaginary time formalism and in which the self-energy is averaged over all frequencies. However, in our implementation, we only average over frequencies for the off-diagonal elements but retain the optimum exchange-correlation potential on the diagonal. We achieve stable and rapid convergence of the SCF procedure by a suitable implementation of the direct inversion in the iterative subspace (DIIS) Pulay (1980) approach. Most importantly, the proposed algorithm is easy to implement and only requires to combine the qs*GW* approach with the space-time implementation for the self-energy and an efficient method to evaluate the exact exchange-contribution to the Fock matrix.

This work is organized as follows: In **section 2** we first recapitulate the qs*GW* procedure and describe some aspects of our implementation. We focus on the implementation of the DIIS and on the analytical continuation (AC) of the self-energy. In **section 3**, we confirm the correctness of our implementation by comparison to ionization potentials (IP) (Kaplan et al., 2016) from TURBOMOLE (Balasubramani et al., 2020) and investigate the convergence of the SCF equations. We also illustrate the computational performance of our implementation with a proof-of principle application to large DNA oligomers. In **section 4** we summarize and conclude this work.

2 METHODS

In this section, we review the qs*GW* method and comment on our implementation, focusing on the AC of the self-energy as well as our approach to accelerate convergence of the SCF procedure. Greek lowercase letters $\mu, \nu \ldots$ label atomic orbitals (AO) and run from 1 to n_{AO}. Latin lowercase letters $p, q, r, \ldots$ label general MOs and run from 1 to n_{MO}. i, j, k (a, b, c) label occupied (virtual) MOs and run from 1 to N_{occ} (N_{virt}). Latin symbols without labels denote tensors in some basis which will always be clear from the context.

2.1 QP Self-Consistent GW

The GWA is an approximation to the self-energy appearing in Dyson's equation (Dyson, 1949),

$$\sum_r \Sigma_{pr}(\omega_p) U_{rq}(\omega_p) = \left[\omega_p - \epsilon_p\right] U_{pq}(\omega_p). \tag{1}$$

We mostly work in a basis of molecular orbitals (MO),

$$\phi_p^{(n)}(\boldsymbol{r}) = \sum_\mu \chi_\mu(\boldsymbol{r}) b_{\mu p}^{(n)}, \tag{2}$$

where the χ_μ are AOs. Dysons's equation is non-linear and will be solved *via* a fixed point iteration. The superscript (n) means that we are in the nth iteration of a SCF procedure. The self-energy Σ is non-Hermitian and energy dependent. Thus, U is complex and energy dependent as well. We will neglect spin in the following.

The ε_p are obtained from solving the generalized KS problem,

$$\sum_\nu H_{\mu\nu}^{(0)} b_{\nu p}^{(0)} = \sum_\nu S_{\mu\nu} b_{\nu p}^{(0)} \epsilon_p^{(0)}, \quad H_{KS} = T + V_{ext} + V_{Hxc}[P], \tag{3}$$

where V_{Hxc} is the sum of exchange-correlation potential V_{xc} and Hartree potential V_H, being functionals of the 1RDM P and the electron density, respectively. T and V_{ext} are kinetic energy and external potential, respectively. S is the overlap matrix of AOs and b defines a transformation from AO to MO basis,

$$M_{pq} = b_{p\mu} M_{\mu\nu} \left[b^\dagger\right]_{\nu q}. \tag{4}$$

In the AO basis, P is given as

$$P_{\mu\nu} = 2 \sum_i^{N_{occ}} b_{\mu i} \left[b^\dagger\right]_{i\nu}. \tag{5}$$

We also define the Hamiltonian of the Hartree approximation,

$$H_H = H_{KS} - V_{xc}. \tag{6}$$

The Green's function G_0 corresponding to the non-interacting Hamiltonian is diagonal in the MO basis with

$$[G_0]_{pp}(\omega) = \left[i\omega - \epsilon_p\right]^{-1}. \tag{7}$$

We can then expand Σ in terms of G_0 as follows (Hedin, 1965; Martin et al., 2016),

$$\Sigma(\omega) = (G_0 * W_0)(\omega) + \ldots, \tag{8}$$

and in the GWA the expansion is truncated after first order. W_0 is the screened Coulomb interaction, calculated in the bubble approximation (Onida et al., 2002) from G_0 (Hedin, 1965). Without further approximations to Σ, one typically avoids solving (**Eq. 1**) but instead calculates the interacting Green's function G by inversion of

$$[G(\omega)]^{-1} = [G_0(\omega)]^{-1} - \Sigma(\omega). \tag{9}$$

From there one proceeds by building the self-energy (**Eq. 8**) but replaces G_0 by G, and W_0 by W and repeats this procedure until self-consistency is reached. In more approximate GW schemes, one avoids solving (**Eq. 9**). In diagonal approximations to Dysons's equation, one assumes Σ to be diagonal. In that case, U in (**Eq. 1**) is unity for all ω and (**Eq. 1**) reduces to a set of independent non-linear equations for ω. In qsGW on the other hand, one does not make the diagonal approximation but Σ is mapped to a Hermitian and frequency-independent exchange-correlation potential V_{xc}^{qsGW}. For this mapping, it is convenient to define

$$W_0(\omega) = V_c + \tilde{W}_0(\omega), \tag{10}$$

with V_c being the bare Coulomb potential. The self-energy can then be decomposed into a static and dynamic part

$$\Sigma(\omega) = \Sigma_x + (G_0 * \tilde{W}_0)(\omega) = \Sigma_x + \Sigma_c(\omega). \quad (11)$$

Σ_x is the Fock exchange potential, $V_x^{qsGW} = \Sigma_x$, and following Kotani et al. (2007), the correlation part of V_{xc} is obtained from Σ by taking one of the real symmetric definitions

$$\left[V_c^{qsGW}\right]_{pq} = \frac{1}{2}\left[\mathrm{Re}\ [\Sigma_c]_{pq}(\epsilon_p) + \mathrm{Re}\ [\Sigma_c]_{pq}(\epsilon_q)\right], \quad (12)$$

or

$$\left[V_c^{qsGW}\right]_{pq} = \delta_{pq}\mathrm{Re}\ [\Sigma_c]_{pq}(\epsilon_p) + (1-\delta_{pq})\mathrm{Re}\ [\Sigma_c]_{pq}(\omega = 0). \quad (13)$$

There are formal reasons why (**Eq. 12**) should be preferred over (**Eq. 13**). Constructing the qs*GW* Hamiltonian *via* (**Eq. 12**) minimizes the length of the gradient of the Klein functional (Klein, 1961) with respect to G_0 (Ismail-Beigi, 2017) and can be seen as an optimized effective non-local potential. The approach bears strong resemblance to what is usually referred to as the optimized effective potential (OEP) method (Talman and Shadwick, 1976). Another possibility is to linearize the self-energy around the chemical potential. This has been implemented by Kutepov et al. (2017). Physically, it is equivalent to taking the static limit of the self-energy, or averaging over frequencies. We will discuss in more detail below that such an approach has advantages with regards to numerical stability. However, we think that one should use the optimum potential at least for the diagonal elements. (**Eq. 13**) is a hybrid between (**Eq. 12**) and $\Sigma(\omega = 0)$ which retains the optimum potential on the diagonal. Employing (**Eq. 13**) can be justified if one assumes that the effect of using the optimum potential as opposed to $\Sigma(\omega = 0)$ will cancel out to a large extent for the off-diagonal elements. We provide numerical evidence later on that this is indeed true. Also an approach using Löwdin's orthogonalization has been proposed to construct the QP Hamiltonian (Sakuma et al., 2009) but that construction is not considered here.

With these simplifications, we can now solve (**Eq. 1**) self-consistently. In each iteration, we solve

$$\sum_r H_{pr}^{qsGW^{(n+1)}} U_{rq}^{(n+1)} = \omega_p^{(n+1)} U_{pq}^{(n+1)}, \quad (14)$$

with

$$H^{qsGW^{(n+1)}} = H_H + \Delta V_H^{(n+1)} + V_{xc}^{qsGW^{(n+1)}} \quad (15)$$

and

$$V_{xc}^{qsGW^{(n+1)}} = V_x[P^{(n)}] + V_c^{qsGW}[G_0^{(n)}]. \quad (16)$$

In each iteration, H^{qsGW} is expressed in the basis in which $G_0^{(n)}$ is diagonal. That is, at the $n+1$st iteration, H^{qsGW} is expressed in terms of the $\left\{\phi_i^{(n)}\right\}$ and unless self-consistency has been reached, $U^{(n)}$ will not be unity and defines a rotation of the molecular orbitals. We now set

$$\begin{aligned} b_{\mu p}^{(n+1)} &= \sum_q b_{\mu q}^{(n)} U_{qp}^{(n+1)} \\ \epsilon_p^{(n+1)} &= \omega_p^{(n+1)} \ \forall p \end{aligned} \quad (17)$$

and evaluate $G_0^{(n+1)}$ *via* (**Eq. 7**) which in turn is used to evaluate (**Eq. 11**) and finally (**Eq. 12**) or (**Eq. 13**). $P^{(n+1)}$ is then evaluated from (**Eq. 5**) and the change in the Hartree-potential is calculated as

$$\Delta V_H^{(n+1)} = V_H[\Delta P^{(n+1)}], \quad (18)$$

with

$$\Delta P^{(n+1)} = P^{(n+1)} - P^{(n)}. \quad (19)$$

The cycle is repeated until self-consistency is reached.

2.2 Implementation

As already stressed in the introduction, for the qsGW implementation no modifications of the code described in Förster and Visscher (2020) for the calculation of the self-energy are needed. A description of the algorithm can be found in Förster and Visscher (2020) and in Förster and Visscher (2021) we reported important modification of our original implementation, increasing accuracy and robustness. The only points we discuss hered are related to the convergence and stability of the self-consistent field (SCF) procedure.

2.2.1 Analytical Continuation

In space-time implementations of the GWA, the self-energy is evaluated in imaginary time and then Fourier transformed to the imaginary frequency axis. In ADF, the self-energy is calculated in the AO basis on a non-uniform grid of imaginary time points. After transformation to the reference basis [the MO basis from the generalized KS calculation in the first iteration and the basis defined by (**Eq. 17**) later], the self-energy matrix is Fourier transformed to a non-uniform grid in imaginary frequency space. For the implementation of this transformation, we refer to Kaltak et al. (2014b) and to the appendix of Förster and Visscher (2021). Since the non-uniform grids depend on the QP energies used to build G_0 we also need to recalculate these grids at the beginning of each qs*GW* iteration to ensure independence of the results from the initial guess.

After this transformation, Σ is known on a discrete set of points $\mathcal{W} = \left\{i\omega_\beta\right\}_{\beta=1,N_\omega}$ on the imaginary frequency axis. However, to evaluate **Eq. 13**, we need to know the self-energy on the real frequency axis at the positions of the QP energies $\epsilon_p^{(n)}$. To this end, we seek to find a function f which is analytic in the largest possible domain $\mathcal{A} \subset \mathbb{C}$ and coincides with Σ in $\mathcal{W}$. For a meromorphic function (as the self-energy) which is known on the whole imaginary axis, it is always possible to find such a function so that $\mathcal{A} = \mathbb{C}$, but since we only know the self-energy on a small subset of points, only an approximate solution can be found. The problem here is, that the AC is exceptionally ill-conditioned, i.e. numerical noise in the input data might significantly affect the output (Shinaoka et al., 2017).

Among the many developed algorithms [see for instance Levy et al. (2017) for an overview], the construction of a continued fraction (Vidberg and Serene, 1977; Beach et al., 2000) via a Padé approximant is most common in implementations of the GWA. While in many codes Thiele's reciprocal difference method is implemented, (Liu et al., 2016; Grumet et al., 2018; Foerster and Gueddida, 2021), ADF, implements the variant by Vidberg

and Serene (Vidberg and Serene, 1977), which for example has also been implemented by Kutepov (Kutepov, 2020). In the latter variant, the coefficients of the continued fraction are calculated while the former method returns the value of the continued fraction (Beach et al., 2000). While it has been claimed that the former variant is numerically more stable (Liu et al., 2016), we did not experience any numerical issues with our implementation for diagonal self-energies. This procedure typically yields good results for states close to the HOMO-LUMO gap while it becomes unreliable for core states (Golze et al., 2018, 2020). Exceptions are cases for which the self-energy has a pole close to the position of the QP energy (Govoni and Galli, 2018). Partial self-consistency in G pushes the poles away from the QP peak (Golze et al., 2019), and consequently, these issues should not be present in qsGW as well. This is different from situations in which the independent QP picture breaks down and the spectral weight of a single excited electrons is distributed between multiple peaks. The former is a purely numerical issue while the latter is caused by strong correlation and can not be overcome by partial self-consistency. It has also been shown in Wilhelm et al., 2021 that AC yields accurate results for semi-core and inner valence states in case the real part of the self-energy does not have poles in the vicinity of the QP solutions.

If one is only interested in accurate valence states, AC *via* Padé approximants is not problematic for G_0W_0 where (**Eq. 1**) reduces to a set of N independent non-linear equations where N is the number of MOs. In evGW, the situation is only slightly different. The N equations are still independent, but information from all QP energies enters the polarizability so that there is an implicit dependence of the QP energies on each other. In practice, this is also not an issue since the numerical errors are typically orders of magnitude smaller than the absolute values of the QP energies.

The situation is different for qsGW. The Off-diagonal elements of Σ_c are often equal to or very close to zero (Kaplan et al., 2015) and generally small compared to the diagonal elements. For these off-diagonal elements, numerical errors from AC can be orders of magnitudes larger than the values of the off-diagonal elements. Since there are many of them, this might significantly alter the solutions of **Eq. 14**. Due to the non-linear nature of the QP equations, this can complicate convergence of the SCF procedure or even lead to erroneous results. The development of more reliable methods for AC is a very active field of research (Bergeron and Tremblay, 2016; Levy et al., 2017; Otsuki et al., 2017; Gull et al., 2018; Fournier et al., 2020; Fei et al., 2021) and it would certainly be interesting to investigate whether other techniques are more suitable for qsGW. For now, we restrict ourselves to the techniques of Padé-approximants. To ensure numerical stability, two aspects need to be considered:

First, it seems reasonable to assume that AC close to the Fermi energy is also more reliable for the off-diagonal elements of Σ. To this end, using (**Eq. 13**) to construct the exchange-correlation potential seems to be more suitable for our implementation than (**Eq. 12**). As we will see later on, both constructions of the exchange-correlation potential lead to similar results, but using (**Eq. 13**), the SCF procedure is significantly easier to converge. In fact, applying the same reasoning one could justify to use Σ ($\omega = 0$) (Kutepov et al., 2017) instead. However, as we will show below, using (**Eq. 13**) is sufficiently numerically stable.

Second, after evaluating **Eq. 13** or (**Eq. 12**), numerical noise needs to be removed rigorously from V_c^{qsGW}. At self-consistency, the off-diagonal elements of V_c^{qsGW} need to be zero: In the $n+1$ the iteration, V_c^{qsGW} is expressed in the basis which diagonalizes the operator defined in (**Eq. 15**) in the nth iteration. At self-consistency $b^{(n+1)} = b^{(n)}$, which will not be the case when the off-diagonal elements of V_c^{qsGW} will be different from zero. In our present implementation, we set all values with magnitude smaller than $1e^{-6}$ to zero. This cut-off is of the order of the numerical noise introduced by the AC. As we will show later on, despite this drastic cut-off the HOMO and LUMO energies can be converged to a degree that the QP energies are converged within a few meV.

2.2.2 Convergence Acceleration

As outlined so far, in each iteration of the self-consistency cycle the previous qsGW Hamiltonian is replaced by the new one, similar to the Roothaan algorithm for the Hartree-Fock (HF) equations. For Hartree-Fock, it is well known, that such a procedure can be numerically unstable (Cances and Le Bris, 2000) and convergence difficulties are encountered already for the simplest molecules (Koutecký and Bonačić, 1971; Bonačić-Koutecký and Koutecký, 1975). Also in many GW implementations, convergence has been shown to be much slower than with a simple linear mixing scheme (Caruso et al., 2013; Kaplan et al., 2016). While the latter seems to work reasonably well for evGW (Gui et al., 2018), it seems that there is room for improvement for qsGW (Gui et al., 2018). An iterative fixed point procedure of the general form

$$\left\{G_0^{(m)}\right\}_{0\leq m\leq n+1} \rightarrow \tilde{H}^{qsGW^{n+1}} \rightarrow \epsilon^{(n+1)}, b^{(n+1)} \tag{20}$$

is clearly a better option. A practical way to implement this is to replace (**Eq. 14**) by

$$\sum_r \tilde{H}_{pr}^{qsGW^{(n+1)}} U_{rq}^{(n+1)} = \omega_p^{(n+1)} U_{pq}^{(n+1)}, \tag{21}$$

with

$$\tilde{H}^{qsGW^{(n+1)}} = \sum_{m=n-n_0}^{n+1} \alpha_m H^{qsGW^{(m)}}, \tag{22}$$

where

$$\sum_{m=n-n_0}^{n} \alpha_m = 1, \tag{23}$$

needs to be fulfilled and n_0 is the maximum number of previous iterations taken into account. We determine the expansion coefficients α_m using Pulay's DIIS method (Pulay, 1980). In the DIIS method, we seek to minimise the residual error

$$r^{(n+1)} = \sum_{m=n-n_0}^{n} \alpha_m r^{(m)}, \tag{24}$$

subject to the constraint **Eq. 23**. One might additionally require the α_m to be positive (what is usually called EDIIS) (Kudin et al., 2002) but we did not find any improvement over the simple DIIS. Different implementations of DIIS differ in the definition of the

residual error. Since G_0 uniquely determines H^{qsGW}, we would ideally define

$$r^{(n+1)} = G_0^{(n+1)} - G_0^{(n)}, \tag{25}$$

however, storage (or recalculation) of this quantity for n_0 iterations is inefficient. Therefore, one can use

$$r^{(n+1)} = P^{(n+1)} - P^{(n)}, \tag{26}$$

which is related to the time-ordered Green's function by taking the limit $\tau \to 0^-$ (τ is the difference between both time arguments). In this work, we have used a different definition for the residual which is, however, identical to (**Eq. 26**).[1]

Technically, in the nth iteration we solve (**Eq. 14**) and evaluate the corresponding $b^{(n)}$ from which we calculate $P^{(n)}$ and $Q^{(n)}$. We check for convergence by evaluating the Frobenius norm of the residual (**Eq. 26**),

$$N_F = \frac{1}{N_{MO}^2}\sqrt{\sum_{\mu\nu}\left[r_{\mu\nu}^{(n+1)}\right]^2}, \tag{27}$$

and terminate the SCF as soon as $N_F < \varepsilon_{SCF}$ for two subsequent iterations. As we will show later on, $\varepsilon_{SCF} = 1e^{-7}$ leads to QP energies which are converged within a few meV for all systems in the GW100 database (Van Setten et al., 2015). Subsequently, we store $r^{(n+1)}$ and $H^{qsGW^{(n+1)}}$ and determine the expansion coefficients α_m using the DIIS method, setting $n_0 = 10$. Finally, we solve (**Eq. 21**) and use the resulting U to evaluate (**Eq. 17**).

2.3 Computational Details

All calculations have been performed with a locally modified development version of ADF2020 using the implementation as described Förster and Visscher (2020) and using the updated imaginary frequency grids as described in Förster and Visscher (2021).

2.3.1 GW100

We use the same structures as in for our previous benchmarks (Förster and Visscher, 2020; Förster and Visscher, 2021). We use the non-augmented TZ3P and QZ6P basis sets described in Förster and Visscher (2021). Complete basis set (CBS) limit extrapolated results are obtained as described in Förster and Visscher (2021). In all calculations, we set the `numericalQuality` key to `Good`. Exceptions are a few systems for which we observed inconsistencies with the `Good` fit set: For Pentasilane, Na_2, Na_4, and Na_6, we used the `Excellent` fit set, and for the nucleobases we used the `VeryGood` fitset. We used 32 imaginary time and 32 imaginary frequency points each [We refer to the explanations in the appendix of Förster and Visscher (2021)]. For all TZ3P calculations, we set `Dependency Bas = 1e-3` and for QZ6P we set `Dependency Bas = 5e-3` in the AMS input as described in Förster and Visscher (2020). All calculations using augmented basis sets (aug-TZ3P and aug-QZ6P) have been performed in the same way, but using the `Excellent` auxiliary fit set and `numericalQuality VeryGood`. No relativistic effects have been taken into account.

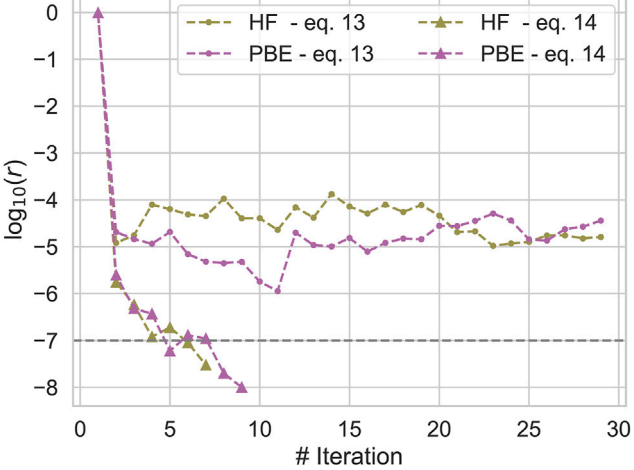

FIGURE 1 | Convergence of the qs*GW* SCF for Methane for different initial guesses and constructions of the correlation potential. $\log_{10}r$, r defined in **Eq. 26**, is plotted against the number of iterations.

2.3.2 DNA Fragments

The structures of the DNA fragments have been taken from Doser et al. (2009). We performed *qsGW* calculations using the TZ2P (Van Lenthe and Baerends, 2003), TZ3P and QZ6P basis sets, starting from a PBE0 (Adamo and Barone, 1999; Ernzerhof and Scuseria, 1999) initial guess. We set the numerical quality to `VeryGood`, but used the `Good` fitset, with the exception of the QZ6P calculations were we also used the `VeryGood` fitset. We also set `MBPT. ThresholdQuality = Normal`. In Förster and Visscher (2020) we have shown that these thresholds are sufficient to converge quasi-particle energies within a few 10 meV. 16 grid points in imaginary time and imaginary frequency have been used. Solvent effects have been accounted for exclusively on the KS level using the conductor like screening model (COSMO) (Klamt and Schüürmann, 1993; Klamt, 1995; Klamt and Jonas, 1996) as implemented in ADF (Pye and Ziegler, 1999) using the BLYP (Becke, 1988; Lee et al., 1988;

[1]We experimented with different residuals: In the implementation used in this work, we have used

$$r^{(n+1)} = \left[P^{(n+1)} + Q^{(n+1)}\right] - \left[P^{(n)} + Q^{(n)}\right].$$

Here, Q is defined like P, but with the summation spanning the virtual orbital space,

$$Q_{\mu\nu} = \sum_a^{N_{virt}} b_{\mu a}\left[b^\dagger\right]_{a\nu}.$$

This was based on the intuitive assumption that convergence could be improved by including information about the virtual orbitals in the residual. However, note that $S^{-1} = \frac{1}{2}P + Q$, so that we obtain $P + Q = \frac{1}{2}P + S^{-1}$. Apart from the factor of 1/2 (**Eq. 26**) is therefore completely equivalent to this expression. We thank one of the reviewers for pointing this out

Miehlich et al., 1989) functional with D3 dispersion correction (Grimme et al., 2010) with Becke-Johnson damping (Grimme et al., 2011) and the TZ2P basis set. `Numericalquality Good` has been used. The solvent correction ΔE_s is then obtained as $\Delta E_s = E_s^{(+)} - E_s^{(0)}$, i.e. as the difference between the solvent contributions to the bonding energies of the oxidized species and the neutral species both at the equilibrium geometry of the neutral species.

3 RESULTS

3.1 Benchmarks

3.1.1 Comparison of Exchange-Correlation Potentials in qs*GW*

We already noticed in **section 2** that the correlated part of the exchange-correlation potential of qs*GW* can be defined in different ways. Here we compare the two most common ways to construct this quantity (Kotani et al., 2007; Shishkin et al., 2007; Shishkin and Kresse, 2007; Kaplan et al., 2016) (**Eq. 12** and **Eq. 13**) for a subset of molecules from the GW100 database. The data is shown in the supporting information and shows that the exchange-correlation potential obtained from (**Eq. 12**) is significantly harder to converge than the one from (**Eq. 13**). An example of the convergence behaviour of both variants is shown in **Figure 1**. **Figure 1** plots $\log_{10} r$ with r defined in **Eq. 26** against the number of iterations with two different initial guesses for Methane. We see, that using (**Eq. 13**), the SCF rapidly converges towards a fixed point, while $\log_{10} r$ always remains much larger than −6 for (**Eq. 12**). On the other hand, for the 10 converged calculations differences in the final QP energies are small; for both, IPs and EAs, both variants differ by only 20 meV on average, i. e the error introduced by averaging over the off-diagonal elements of the self-energy are small. For this reason, we decided to use the correlation potential as defined in (**Eq. 13**) in all subsequent calculations.

3.1.2 Self Consistent Field Convergence

Next, we comment on the convergence of the qs*GW* SCF procedure. To this end, we compare IPs and electron affinities (EA) for the molecules in the GW100 database for 3 different starting points, PBE (Perdew et al., 1996a; Perdew et al., 1996b), PBE0, and HF. At self-consistency, the QP energies should be independent from the initial guess and their differences will thus provide information about the obtained convergence of the QP energies for a given ε_{SCF}. In all calculations we set $\varepsilon_{SCF} = 1e^{-7}$ and restrict all calculations to a maximum of 30 iterations.

Independent of the starting point, we could not reach convergence for Mgo, BeO, BN, Cu_2, and CuCN with our DIIS implementation. Employing a linear mixing procedure as implemented in Wilhelm et al. (2021) with $\alpha = 0.35$ we could reach convergence for these systems, albeit with a large number of iterations. These systems are problematic for GW approaches since the single the spectral weight of the single excited electron is distributed between multiple peaks (Govoni and Galli, 2018). qs*GW* relies on the validity of the single QP picture. In situations, in which the quasi-particle equations might have multiple solutions (Govoni and Galli, 2018; Golze et al., 2019) corresponding to the same non-interacting state, different solutions may be found in different iterations of the qs*GW* SCF procedure. qs*GW* should select the solution with largest QP weight (Ismail-Beigi, 2017) but in situations where there are at least two solutions with (almost) equal QP weight, the "physical" solution might change in each iteration. In such cases, the DIIS algorithm tries to minimize the residual SCF error by interpolating between different solutions and no fixed point of the map (**Eq. 20**) is found. On the other hand, linear mixing results in a smooth but slow convergence pattern, if only α is chosen small enough to make sure that in all iterations the same solution is found. We do not know, how to best solve this issue but we do not consider it to be a major concern as such convergence problems are only encountered for systems in which the single QP picture is not valid. This then merely signals that qs*GW* is not an appropriate level of theory.

Figure 2 shows mean absolute deviations (MAD) as well as maximum absolute deviations of the IPs and EAa obtained from different starting points. With MAD of 6 and 2 meV, respectively, EAs are better converged than IPs. Also the maximum error is about twice as small for EAs than for IPs. These differences are related to the AC procedure which gives smaller errors for unoccupied states with usually featureless self-energy matrix elements. The maximum error never exceeds 50 meV and is of the same order of magnitude than the experimental resolution of photoionization experiments (Knight et al., 2016) of the typical basis set errors of *GW* calculations after extrapolation. (Knight et al., 2016; Maggio et al., 2017; Govoni and Galli, 2018; Bruneval et al., 2020; Förster and Visscher, 2021). The distribution of iterations required for convergence is displayed in **Figure 3**. This includes the 5 problematic cases discussed above. The calculations on average converge in around 10 iteration, with little dependence on the initial guess.

3.1.3 Comparison of Ionization Potentials for the GW100 Database

We now compare the IPs from our algorithm to the ones obtained with the TURBOMOLE code for GW100. The TURBOMOLE results have been obtained with the GTO-type def2-TZVPP basis sets. For some systems, TURBOMOLE results are not available and we exclude these from our discussion. We use the TZ3P basis sets which we have shown to give comparable results to def2-TZVP for GW100 (Förster and Visscher, 2021). However, quantitative accuracy can not be expected.

The deviations to TURBOMOLE are shown in **Figure 4**. The average deviation between both codes is close to zero, and with one exception, for all IPs deviations are considerably smaller than 300 meV, with the deviations for the majority of systems being smaller than 100 meV. Thus, our results are qualitatively similar and deviations can be attributed to different basis set errors and different constructions of the qs*GW* exchange-correlation potential. The IP of Cyclooctatetrane is the only exception. Here, TURBOMOLE gives an IP of 9.30 eV, while the ADF IP is with 8.38 eV nearly 1 eV smaller. For different starting points, we obtained the same result within an accuracy of only a

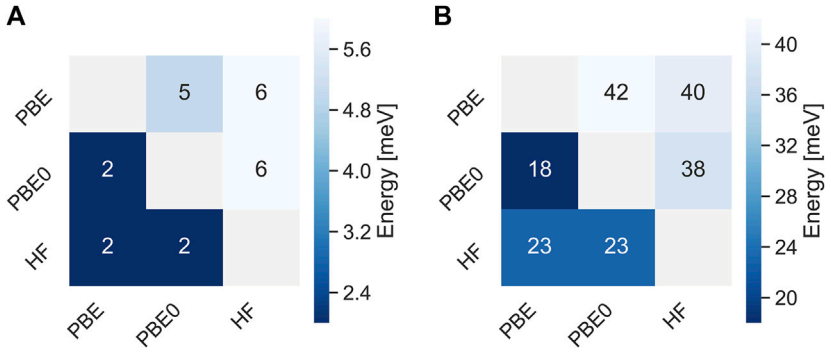

FIGURE 2 | Mean absolute deviations **(A)** and maximum absolute deviations **(B)** of qsGW IPs (upper triangle) and EAs (lower triangle) obtained with different initial guesses for the GW100 database. All values are in meV.

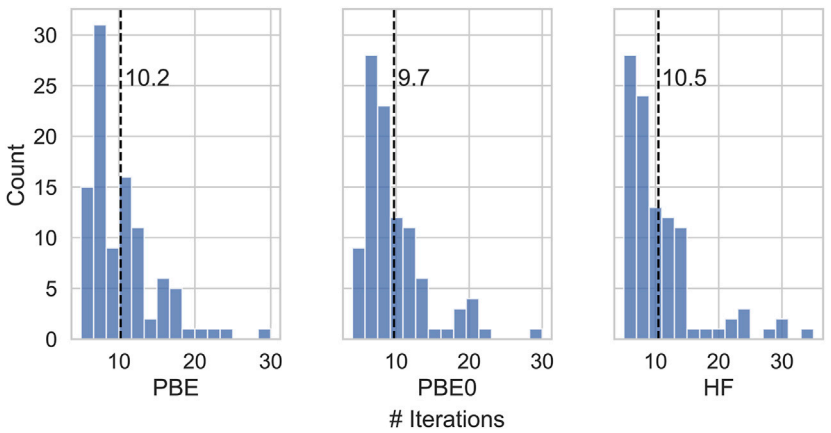

FIGURE 3 | Number of iterations needed to attain convergence of the SCF for different initial guesses.

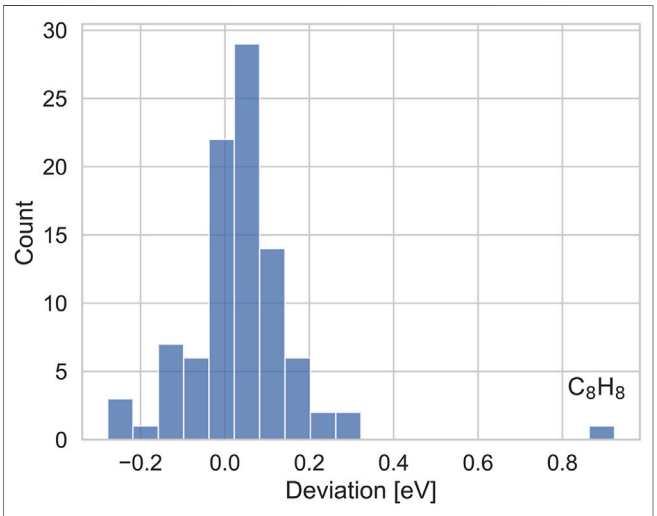

FIGURE 4 | Distribution of deviations (in eV) of the IPs from TURBOMOLE and with our implementation.

few meV, indicating that our IP is well converged. The TURBOMOLE qsGW IPs on average overestimate the CCSD(T) reference values for GW100 by Klopper and coworkers (Krause and Klopper, 2017) in the same basis set by only a little more than 100 meV, while the deviation for Cycloocatetrane is nearly 1 eV. The CCSD (T) IP for this system, is 8.35 eV, which is in very good agreement with our value. These numbers indicate that our IP is reasonable, despite the large deviation to TURBOMOLE.

Ideally, we would also like to compare our EAs against literature data, however, with only one exception (were optimized structures do not seem to be available) (Ke, 2011), we are not aware of any published EAs for molecular systems.

3.1.4 Basis Set Limit Extrapolated Ionization Potentials and Electron Affinities for the GW100 Database

In the supporting information, we report CBS limit extrapolated EAs and IPs for the GW100 database. The qs*GW* QP energies seem to converge faster to the CBS limit than their G_0 W_0 counterparts. Going from TZ3P to QZ6P, the basis set

TABLE 1 | Comparison of electron affinities for linear alkanes from Methane to Butane using augmented, and non-augmented basis sets.

	Non-augmented			Augmented		
Name	**TZ3P**	**QZ6P**	**Extrap**	**Aug-TZ3P**	**Aug-QZ6P**	**Extrap**
Methane	−2.30	−−1.62	−0.78	−0.79	−0.58	−0.26
Ethane	−2.27	−1.56	−0.65	−0.72	−0.57	−0.35
Propane	−2.23	−1.51	−0.56	−0.72	−0.55	−0.30
Butane	−2.24	−1.50	−0.52	−0.71	−0.55	−0.30

incompleteness error reduces by 80 meV on average, while for G_0W_0@PBE, we found an average reduction of 130 meV (Förster and Visscher, 2021). Self-consistent approaches might converge faster than G_0W_0 - Caruso et al. have already observed that scGW converges faster to the CBS limit than G_0W_0 (Caruso et al., 2013). For the EAs, the average differences are much larger which is also due to the many systems with negative EA in the GW100 database. For these systems CBS limit extrapolation is not reliable without adding diffuse functions. Repeating these calculations with augmented basis sets (Förster and Visscher, 2021) yields smaller differences between the aug-TZ3P and aug-QZ6P basis sets. (Förster and Visscher, 2021). In **Table 1**, these differences are shown for the series of linear alkanes from Methane to Butane (for more numbers we refer to the supporting information). On both the TZ and QZ level the augmented basis sets give a much higher EA. Also, the differences between aug-TZ3P and aug-QZ6P are with in between 150 and 200 meV modest, while they are huge for the non-augmented basis sets. Also the extrapolated values are much smaller using the augmented basis sets. The effect of augmentation is also profound for other systems. For example, using the non-augmented basis sets, the EA of carbontetrachloride is negative (−0.27 eV). Using the augmented basis sets, it becomes positive (0.17 eV) which is in much better agreement with experiment (0.80 ± 0.34 eV) (Staneke et al., 1995).

3.2 Application to DNA Fragments

Oxidation of DNA is related to genetic damage and to investigate the mechanisms behind these processes quantum chemically, electron addition and removal energies need to be computed with high accuracy. A necessary first step for such studies is the selection of appropriate model system which should represent DNA under physiological conditions as accurately as possible while still being computationally feasible. As an illustrative example how the new qsGW implementation can be used effectively in practice, we investigate the dependence of IP and EA of oligomers of Adenine-Thymine (AT) base pairs on the oligomer size.

The calculated charged excitations are shown in **Table 2** for different basis sets and fragment sizes between 1 and 4 AT pairs (We refer to these systems as ATx, were x denotes the number of AT base pairs). These systems are shown in **Figure 5**. For all fragments, we calculated the IPs with the TZ2P and TZ3P basis set with 1d1f, and 2d1f shells of polarization functions for second and third row atoms (and analogously for other atoms). We see, that going from TZ2P to TZ3P only has a small effect on the IPs and EAs, reducing the basis set incompleteness error by only a few 10 meV. These calculations with two rather similar basis sets are necessary to rule out the possibility that a result is simply an artefact of a chosen basis set. Going from TZ3P to QZ6P, the IP of the AT1+B increases by modest 60 meV, while the EA reduces by 180 meV. Based on the TZ3P and QZ6P calculations, we can estimate the QP energies at the CBS limit by extrapolation. Comparing the TZ3P results to the extrapolated ones, we find a basis set limit incompleteness error of 140 meV for the IP and of 420 meV for the EA of AT1. For AT1, we find a similar basis set limit incompleteness error of 80 meV for the IP and of 340 meV for the EA.

On standard hardware, calculations on the QZ level are not feasible for AT4 and already for AT2, the QZ calculation is cumbersome. This is not only due to the large number of diffuse AOs which make makes it difficult to exploit distance-based cut-offs (Förster and Visscher, 2020) but also due to the large auxiliary basis sets which are required to make the calculations numerically stable. However, we can estimate the CBS limit based on the differences between the QP energies at the CBS limit and the largest affordable basis set for the larger systems for the smaller fragments. This is justified with the observations made in Förster and Visscher (2020) for G_0W_0 were we found the basis set incompleteness error on average to decrease with increasing system size but only to a certain extent since basis functions are localised. Based on this assumption, we correct the IPs and

TABLE 2 | Ionization potentials (IPs) and electron affinities (EAS) of DNA fragments consisting of different numbers of adenine-thymine base pairs calculated with different basis sets and contributions of solvent from ΔBLYP calculations. Extra denotes extrapolation to the CBS limit based on TZ3P and QZ6P calculations and numbers in parentheses are obtained by adding the difference between $\epsilon_i^{CBS} - \epsilon_i^{TZ3P}$ to the result obtained at the TZ3P level. Δsol. has been calculated using COSMO. All values are in eV.

	IP				EA			
Calculation	**AT1**	**AT1+B**	**AT2**	**AT4**	**AT1**	**AT1+B**	**AT2**	**AT4**
TZ2P	—	7.84	7.34	6.94	—	−0.84	−0.65	−0.45
TZ3P	8.47	7.90	7.35	6.97	−0.41	−0.80	−0.63	−0.40
QZ6P	8.50	7.96	—	—	−0.26	−0.62	—	—
Extra	8.55	8.04	(7.49)	(7.11)	0.07	-0.38	(−0.21)	(0.02)
Δsol	−1.82	-0.99	−0.52	−0.01	1.55	—	1.87	1.62
ϵ + Δsol	6.73	7.05	6.97	7.10	1.62	—	1.66	1.64

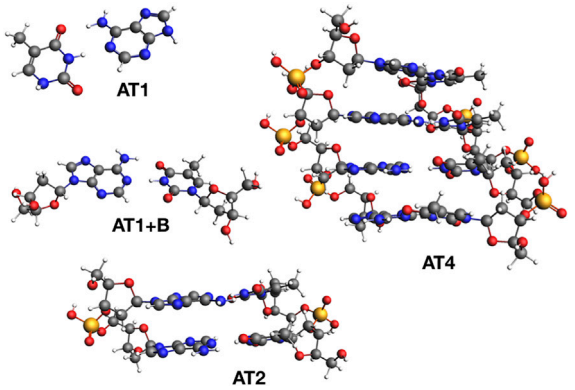

FIGURE 5 | DNA model systems used in this work.

EAs of AT2 and AT4 on the TZ3P level by the basis set limit incompleteness error found for AT1+B. (140 and 420 meV, respectively). There is of course a small uncertainty due to the different basis set errors for AT1 and AT1+B. For the extrapolation itself, we assume the error to be rather small for the IP, since the difference between TZ3P and QZ6P are rather small. For the EAs, the error might be larger. Still, we can safely assume, that the basis set errors for AT2 and AT4 are below 100 meV.

The energy required to remove or add an electron from a DNA oligomer in vacuum is strongly size dependent: The vertical IP in vacuum decreases rapidly with increasing oligomer size, with a difference of almost 1 eV between AT1 and AT4. For the EA, a difference of 0.4 eV is found. The IPs of the solvated DNA oligomers, on the other hand, are almost independent of the number of base pairs. When an electron is removed from the oligomer, the surrounding cloud of electrons stabilizes the resulting hole. Increasing the oligomer size thus reduces the IP potential since the hole becomes more and more stabilized. In the aqueous environment, the solvent plays the same role and consequently, the inclusion of water via the COSMO effectively compensates for the effect of the DNA environment. Of course, the comparison is slightly skewed since the DNA environment and the solvent are not treated at the same level of theory. However, there is some evidence that COSMO and other polarizable continuum models are fairly accurate in describing the dielectric screening properties of water (Deglmann and Schenk, 2012).

The IP of AT1+B, AT2, and AT4, all agree within 130 meV. In light of possible basis set errors and errors of the qsGW method itself, the difference is well within the error margin of our method. Only for AT1 we obtain a significantly lower IP, which indicates that the DNA backbone apparently plays an important role in stabilizing ionized DNA oligomers. For the EAs, we arrive at the same conclusion. The differences between the considered systems are even smaller, the aqueous EAs of AT1, AT2 and AT4 being with 1.62, 1.66, and 1.64 eV in excellent agreement. Recently, Pluhařová et al. (2011), Pluhařová et al. (2013), Pluhařová et al. (2015) also concluded that the effect of the DNA environment on the IPs of individual aqueous nucleobases seems to be modest. On the BMK (Boese and Martin, 2004)/6–31G* level of theory, they obtained an IP of 7.24 eV for a fragment of 2 solvated AT base pairs including backbone from the Dickerson dodecamer, but for the isoltaed AT base pair, they obtained and IP of 7.58 eV. The first number is in good agreement with ours, while the second one differs from our result for AT1 by almost 1 eV. However, the difference of only 340 meV between both fragments is of the same order as our difference between the IPs of AT1 and AT2 of 260 meV. Thus, our conclusions regarding the role of the explicit inclusion of the DNA environment on the calculated IPs are very similar.

Finally, we shortly discuss the compute times of the qsGW calculations for the DNA fragments. A detailed timing analysis for the evaluation of the self-energy in ADF has already been performed in Förster and Visscher (2020). The asymptotic scaling of qsGW will be the same as for G_0W_0: The only additional cubic step is the diagonalization of the Hamiltonian in each iteration. The LU factorization of each of the N_ω $N_{fit} \times N_{fit}$ matrices in each iteration to calculate the screened interaction (Förster and Visscher, 2020) requires roughly $\frac{2}{3}N_{fit}^3$ FLOPS, while the dominant step in the single diagonalization of the $N_{bas} \times N_{bas}$ matrix in each iteration requires $\frac{4}{3}N_{bas}^3$ FLOPS. Since we have $N_{bas} \approx 5 \times N_{fit}$ in a typical calculation, the compute time for diagonalization is negligible. Of course, a qsGW calculation requires multiple iterations and is consequently slower than a G_0W_0 calculation. For the DNA fragments, all calculations required between 6 and 8 iterations to converge. This is considerably faster than the average number of iterations found for GW100, where we have already observed that convergence is typically faster for organic systems. We have set the converge threshold for all calculations in this section to $log_{10}(\varepsilon_{SCF}) = -8$, as opposed to −7 for GW100. However, the increasing sparsity of G_0 ($\tau \to 0^+$) and G_0 ($\tau \to 0^-$) with increasing system size is also responsible for this fast convergence.

The largest calculation here is the one for AT4 using the TZ3P basis set. The system has 260 atoms and 1,220 electrons. We used 6,374 MOs and 33,678 auxiliary fit functions. The calculation took 6 iterations to converge and has been performed on 16 cores of a single Dual AMD EPYC 7302@ 3.0GHz, 2x RTX2070 machine with 256 GB of memory. On average, a single iteration took a little more than 15 h, or 243 core hours.

4 CONCLUSION

As opposed to GW calculations with diagonal self-energy, qsGW is a general, parameter-free, and starting point independent method for the calculation of QP energies. While qsGW is known to severely overestimate band gaps and IPs in three-dimensional (3D) materials (Shishkin et al., 2007; Tal et al., 2021) there is evidence that qsGW is more accurate for molecules (Caruso et al., 2016; Kaplan et al., 2016). In canonical implementations, qsGW is usually a magnitude slower than evGW (Gui et al., 2018) and so far, low-order scaling implementations for molecular systems have focused on

diagonal approximations to *GW* (Wilhelm et al., 2018, Wilhelm et al., 2021; Förster and Visscher, 2020; Duchemin and Blase, 2021). To fill this gap, we have presented a low-order scaling implementation of qs*GW* for molecular systems and demonstrated its accuracy and robustness. In a proof-of-principle application to DNA fragments we have showcased the capabilities of the new implementation for systems of practical interest (Pluhařová et al., 2015; Balanikas et al., 2020). We have shown, that IPs and EAs of the considered DNA fragments in vacuum are strongly size-dependent. Upon taking into account the effect of the aqueous environment, the QP energies become almost independent of the system size. This confirms the results of previous DFT studies. (Pluhařová et al., 2015, Pluhařová et al., 2013). For the largest of the considered fragments with 1,220 electrons, the respective qsGW calculation with more than 6,300 spherical AOs converged within 6 iterations in less than 4 days on a single compute node with 16 cores.

All in all, the herein presented implementation is a necessary stepping stone towards accurate *ab initio* studies of the spectroscopic properties of large molecules in realistic environments, relevant to organic optoelectronics or biochemistry. To be able to also study optical properties of large systems, it needs to be combined with an implementation of the BSE formalism. Our implementation does not allow to take into account solvent effects directly. In the present work, we have done that *via* a ΔDFT calculation and obtained consistent results. However, it would be desirable to take into account environmental effects more directly by combining qsGW with COSMO (or a PCM) (Duchemin et al., 2016; Li et al., 2018) and/or molecular mechanics calculations (Tirimbò et al., 2020a; Tirimbò et al., 2020b).

Another issue in practice is the slow convergence of the QP energies to the CBS limit. This is especially true for algorithms like the present one which exploit sparsity in the AO basis. It is encouraging that this convergence is seemingly faster than for qsGW than G_0W_0. This doesn't eliminate the need for basis set limit extrapolation, but the extrapolation schemes become more reliable with decreasing basis set error. Basis set errors for large systems can also be accurately estimated based on results for smaller, chemically similar systems, as exemplified in this work.

DATA AVAILABILITY STATEMENT

The original contributions presented in the study are included in the article/**Supplementary Material**, further inquiries can be directed to the corresponding author.

AUTHOR CONTRIBUTIONS

All authors listed have made a substantial, direct, and intellectual contribution to the work and approved it for publication.

FUNDING

This research received funding from Netherlands Organisation for Scientific Research (NWO) in the framework of the Innovation Fund for Chemistry and from the Ministry of Economic Affairs in the framework of the *TKI/PPS-Toeslagregeling* (award number 731.017.417).

SUPPLEMENTARY MATERIAL

The Supplementary Material for this article can be found online at: https://www.frontiersin.org/articles/10.3389/fchem.2021.736591/full#supplementary-material

REFERENCES

Adamo, C., and Barone, V. (1999). Toward Reliable Density Functional Methods without Adjustable Parameters: The PBE0 Model. *J. Chem. Phys.* 110, 6158–6170. doi:10.1063/1.478522

Almlöf, J., Faegri, K., and Korsell, K. (1982). Principles for a DirectSCFapproach toLICAO-MOab-Initiocalculations. *J. Comput. Chem.* 3, 385–399. doi:10.1002/jcc.540030314

Baerends, E. J., Ellis, D. E., and Ros, P. (1973). Self-Consistent Molecular Hartree-Fock-Slater Calculations I. The Computational Procedure. *Chem. Phys.* 2, 41–51. doi:10.1016/0301-0104(73)80059-x

Baerends, E., Ziegler, T., Atkins, A., Autschbach, J., Baseggio, O., Bashford, D., et al. (2020). [Dataset]. *ADF2020, Locally Modified Development Version*.

Balanikas, E., Banyasz, A., Douki, T., Baldacchino, G., and Markovitsi, D. (2020). Guanine Radicals Induced in DNA by Low-Energy Photoionization. *Acc. Chem. Res.* 53, 1511–1519. doi:10.1021/acs.accounts.0c00245

Balasubramani, S. G., Chen, G. P., Coriani, S., Diedenhofen, M., Frank, M. S., Franzke, Y. J., et al. (2020). TURBOMOLE : Modular Program Suite for Ab Initio Quantum-Chemical and Condensed-Matter Simulations. *J. Chem. Phys.* 152, 184107. doi:10.1063/5.0004635

Beach, K. S. D., Gooding, R. J., and Marsiglio, F. (2000). Reliable Pade Analytical Continuation Method Based on a High-Accuracy Symbolic Computation Algorithm. *Phys. Rev. B* 61, 5147–5157. doi:10.1103/physrevb.61.5147

Becke, A. D. (1988). Density-fUnctional Exchange-Energy Approximation with Correct Asymptotic Behavior. *Phys. Rev. A.* 38, 3098–3100. doi:10.1063/1.174983510.1103/physreva.38.3098

Berardo, E., Kaplan, F., Bhaskaran-Nair, K., Shelton, W. A., Van Setten, M. J., Kowalski, K., et al. (2017). Benchmarking the Fundamental Electronic Properties of Small TiO2 Nanoclusters by GW and Coupled Cluster Theory Calculations. *J. Chem. Theor. Comput.* 13, 3814–3828. doi:10.1021/acs.jctc.7b00538

Bergeron, D., and Tremblay, A. M. (2016). Algorithms for Optimized Maximum Entropy and Diagnostic Tools for Analytic Continuation. *Phys. Rev. E* 94, 1–25. doi:10.1103/PhysRevE.94.023303

Blase, X., and Attaccalite, C. (2011). Charge-transfer Excitations in Molecular Donor-Acceptor Complexes within the many-body Bethe-Salpeter Approach. *Appl. Phys. Lett.* 99, 12–14. doi:10.1063/1.3655352

Blase, X., Attaccalite, C., and Olevano, V. (2011). First-principles GW Calculations for Fullerenes, Porphyrins, Phtalocyanine, and Other Molecules of Interest for Organic Photovoltaic Applications. *Phys. Rev. B* 83, 1–9. doi:10.1103/PhysRevB.83.115103

Boese, A. D., and Martin, J. M. (2004). Development of Density Functional for Thermochemical Kinetics. *J. Chem. Phys.* 121, 3405–3416. doi:10.1063/1.1774975

Bois, J., and Körzdörfer, T. (2017). Size-Dependence of Nonempirically Tuned DFT Starting Points for G0W0 Applied to π-Conjugated Molecular Chains. *J. Chem. Theor. Comput.* 13, 4962–4971. doi:10.1021/acs.jctc.7b00557

Bonačić-Koutecký, V., and Koutecký, J. (1975). General Properties of the Hartree-Fock Problem Demonstrated on the Frontier Orbital Model - I. Relation

Among Various Types of Extrema. *Theor. Chim. Acta* 36, 149–161. doi:10.1007/BF00572556

Boulanger, P., Jacquemin, D., Duchemin, I., and Blase, X. (2014). Fast and Accurate Electronic Excitations in Cyanines with the many-body Bethe-Salpeter Approach. *J. Chem. Theor. Comput.* 10, 1212–1218. doi:10.1021/ct401101u

Bruneval, F., and Marques, M. A. (2013). Benchmarking the Starting Points of the GW Approximation for Molecules. *J. Chem. Theor. Comput.* 9, 324–329. doi:10.1021/ct300835h

Bruneval, F., Rangel, T., Hamed, S. M., Shao, M., Yang, C., and Neaton, J. B. (2016). MOLGW 1: Many-body Perturbation Theory Software for Atoms, Molecules, and Clusters. *Comput. Phys. Commun.* 208, 149–161. doi:10.1016/j.cpc.2016.06.019

Bruneval, F., Maliyov, I., Lapointe, C., and Marinica, M.-C. (2020). Extrapolating Unconverged GW Energies up to the Complete Basis Set Limit with Linear Regression. *J. Chem. Theor. Comput.* 16, 4399–4407. doi:10.1021/acs.jctc.0c00433

Bruneval, F. (2012). Ionization Energy of Atoms Obtained from GW Self-Energy or from Random Phase Approximation Total Energies. *J. Chem. Phys.* 136, 194107. doi:10.1063/1.4718428

Cances, E., and Le Bris, C. (2000). On the Convergence of SCF Algorithms for the Hartree-Fock Equations. *ESAIM Math. Model. Numer. Anal.* 34, 749–774. doi:10.1051/m2an:2000102

Caruso, F., Rinke, P., Ren, X., Scheffler, M., and Rubio, A. (2012). Unified Description of Ground and Excited States of Finite Systems: The Self-Consistent GW Approach. *Phys. Rev. B* 86, 1–5. doi:10.1103/PhysRevB.86.081102

Caruso, F., Rinke, P., Ren, X., Rubio, A., and Scheffler, M. (2013). Self-consistent GW: All-Electron Implementation with Localized Basis Functions. *Phys. Rev. B* 88, 1–18. doi:10.1103/PhysRevB.88.075105

Caruso, F., Atalla, V., Ren, X., Rubio, A., Scheffler, M., and Rinke, P. (2014). First-Principles Description of Charge Transfer in Donor-Acceptor Compounds from Self-Consistent Many-Body Perturbation Theory. *Phys. Rev. B - Condens. Matter Mater. Phys.* 90, 085141. doi:10.1103/PhysRevB.90.085141

Caruso, F., Dauth, M., Van Setten, M. J., and Rinke, P. (2016). Benchmark of GW Approaches for the GW100 Test Set. *J. Chem. Theor. Comput.* 12, 5076–5087. doi:10.1021/acs.jctc.6b00774

Chu, I. H., Trinastic, J. P., Wang, Y. P., Eguiluz, A. G., Kozhevnikov, A., Schulthess, T. C., et al. (2016). All-electron Self-Consistent GW in the Matsubara-Time Domain: Implementation and Benchmarks of Semiconductors and Insulators. *Phys. Rev. B* 93, 1–12. doi:10.1103/PhysRevB.93.125210

Dauth, M., Caruso, F., Kümmel, S., and Rinke, P. (2016). Piecewise Linearity in the GW Approximation for Accurate Quasiparticle Energy Predictions. *Phys. Rev. B* 93, 121115(R). doi:10.1103/PhysRevB.93.121115

Deglmann, P., and Schenk, S. (2012). Thermodynamics of Chemical Reactions with COSMO-RS: The Extreme Case of Charge Separation or Recombination. *J. Comput. Chem.* 33, 1304–1320. doi:10.1002/jcc.22961

Doser, B., Lambrecht, D. S., Kussmann, J., and Ochsenfeld, C. (2009). Linear-scaling Atomic Orbital-Based Second-Order Møller-Plesset Perturbation Theory by Rigorous Integral Screening Criteria. *J. Chem. Phys.* 130, 064107. doi:10.1063/1.3072903

Duchemin, I., and Blase, X. (2021). Cubic-Scaling All-Electron GW Calculations with a Separable Density-Fitting Space-Time Approach. *J. Chem. Theor. Comput.* 17, 2383–2393. doi:10.1021/acs.jctc.1c00101

Duchemin, I., Deutsch, T., and Blase, X. (2012). Short-range to Long-Range Charge-Transfer Excitations in the Zincbacteriochlorin-Bacteriochlorin Complex: A Bethe-Salpeter Study. *Phys. Rev. Lett.* 109, 1–6. doi:10.1103/PhysRevLett.109.167801

Duchemin, I., Jacquemin, D., and Blase, X. (2016). Combining the GW Formalism with the Polarizable Continuum Model: A State-specific Non-equilibrium Approach. *J. Chem. Phys.* 144, 164106. doi:10.1063/1.4946778

Dunlap, B. I., Connolly, J. W., and Sabin, J. R. (1979). On Some Approximations in Applications of Xα Theory. *J. Chem. Phys.* 71, 3396–3402. doi:10.1063/1.438728

Dyson, F. J. (1949). The S Matrix in Quantum Electrodynamics. *Phys. Rev.* 75, 1736–1755. doi:10.1103/PhysRev.75.1736

Ernzerhof, M., and Scuseria, G. E. (1999). Assessment of the Perdew–Burke–Ernzerhof Exchange-Correlation Functional. *J. Chem. Phys.* 110, 5029. doi:10.1063/1.478401

Faber, C., Duchemin, I., Deutsch, T., and Blase, X. (2012). Many-body Green's Function Study of Coumarins for Dye-Sensitized Solar Cells. *Phys. Rev. B - Condens. Matter Mater. Phys.* 86, 1–7. doi:10.1103/PhysRevB.86.155315

Fei, J., Yeh, C. N., and Gull, E. (2021). Nevanlinna Analytical Continuation. *Phys. Rev. Lett.* 126, 56402. doi:10.1103/PhysRevLett.126.056402

Förster, A., and Visscher, L. (2020). Low-Order Scaling G0W0 by Pair Atomic Density Fitting. *J. Chem. Theor. Comput.* 16, 7381–7399. doi:10.1021/acs.jctc.0c00693

Förster, A., and Visscher, L. (2021). GW100: A Slater-Type Orbital Perspective. *J. Chem. Theory Comput.* 17 (8), 5080–5097. doi:10.1021/acs.jctc.1c00308

Foerster, D., and Gueddida, S. (2021). A Low Resources Space Time Approach to the GW Approximation. *Comput. Mater. Sci.* 187, 110078. doi:10.1016/j.commatsci.2020.110078

Foerster, D., Koval, P., and Snchez-Portal, D. (2011). An O(N3) Implementation of Hedins GW Approximation for Molecules. *J. Chem. Phys.* 135, 074105. doi:10.1063/1.3624731

Fournier, R., Wang, L., Yazyev, O. V., and Wu, Q. S. (2020). Artificial Neural Network Approach to the Analytic Continuation Problem. *Phys. Rev. Lett.* 124, 56401. doi:10.1103/PhysRevLett.124.056401

Fujita, T., Noguchi, Y., and Hoshi, T. (2019). Charge-transfer Excited States in the Donor/acceptor Interface from Large-Scale GW Calculations. *J. Chem. Phys.* 151, 114109. doi:10.1063/1.5113944

Gallandi, L., and Körzdörfer, T. (2015). Long-range Corrected DFT Meets GW: Vibrationally Resolved Photoelectron Spectra from First Principles. *J. Chem. Theor. Comput.* 11, 5391–5400. doi:10.1021/acs.jctc.5b00820

Golze, D., Wilhelm, J., Van Setten, M. J., and Rinke, P. (2018). Core-Level Binding Energies from GW: An Efficient Full-Frequency Approach within a Localized Basis. *J. Chem. Theor. Comput.* 14, 4856–4869. doi:10.1021/acs.jctc.8b00458

Golze, D., Dvorak, M., and Rinke, P. (2019). The GW Compendium: A Practical Guide to Theoretical Photoemission Spectroscopy. *Front. Chem.* 7, 377. doi:10.3389/fchem.2019.00377

Golze, D., Keller, L., and Rinke, P. (2020). Accurate Absolute and Relative Core-Level Binding Energies from GW. *J. Phys. Chem. Lett.* 11, 1840–1847. doi:10.1021/acs.jpclett.9b03423

Govoni, M., and Galli, G. (2018). GW100: Comparison of Methods and Accuracy of Results Obtained with the WEST Code. *J. Chem. Theor. Comput.* 14, 1895–1909. doi:10.1021/acs.jctc.7b00952

Grimme, S., Antony, J., Ehrlich, S., and Krieg, H. (2010). A Consistent and Accurate Ab Initio Parametrization of Density Functional Dispersion Correction (DFT-D) for the 94 Elements H-Pu. *J. Chem. Phys.* 132, 154104. doi:10.1063/1.3382344

Grimme, S., Ehrlich, S., and Goerigk, L. (2011). Effect of the Damping Function in Dispersion Corrected Density Functional Theory. *J. Comput. Chem.* 32, 1456–1465. doi:10.1002/jcc.21759

Grumet, M., Liu, P., Kaltak, M., Klimeš, J., and Kresse, G. (2018). Beyond the Quasiparticle Approximation: Fully Self-Consistent GW Calculations. *Phys. Rev. B* 98, 1–9. doi:10.1103/PhysRevB.98.155143

Gui, X., Holzer, C., and Klopper, W. (2018). Accuracy Assessment of GW Starting Points for Calculating Molecular Excitation Energies Using the Bethe-Salpeter Formalism. *J. Chem. Theor. Comput.* 14, 2127–2136. doi:10.1021/acs.jctc.8b00014

Gull, E., Iskakov, S., Krivenko, I., Rusakov, A. A., and Zgid, D. (2018). Chebyshev Polynomial Representation of Imaginary-Time Response Functions. *Phys. Rev. B* 98, 1–10. doi:10.1103/PhysRevB.98.075127

Hashemi, Z., and Leppert, L. (2021). Assessment of the Ab Initio Bethe - Salpeter Equation Approach for the Low-Lying Excitation Energies of Bacteriochlorophylls and Chlorophylls. *J. Phys. Chem. A.* 125, 2163–2172. doi:10.1021/acs.jpca.1c01240

Hedin, L. (1965). New Method for Calculating the One-Particle Green's Function with Application to the Electron-Gas Problem. *Phys. Rev.* 139, A796. doi:10.1103/physrev.139.a796

Hung, L., Bruneval, F., Baishya, K., and Öğüt, S. (2017). Benchmarking the GW Approximation and Bethe-Salpeter Equation for Groups IB and IIB Atoms and Monoxides. *J. Chem. Theor. Comput.* 13, 2135–2146. doi:10.1021/acs.jctc.7b00123

Ismail-Beigi, S. (2017). Justifying Quasiparticle Self-Consistent Schemes via Gradient Optimization in Baym-Kadanoff Theory. *J. Phys. Condens. Matter* 29, 385501. doi:10.1088/1361-648x/aa7803

Kaltak, M., and Kresse, G. (2020). Minimax Isometry Method: A Compressive Sensing Approach for Matsubara Summation in many-body Perturbation Theory. *Phys. Rev. B* 101, 205145. doi:10.1103/PhysRevB.101.205145

Kaltak, M., Klimeš, J., and Kresse, G. (2014a). Cubic Scaling Algorithm for the Random Phase Approximation: Self-Interstitials and Vacancies in Si. *Phys. Rev. B* 90, 1–11. doi:10.1103/PhysRevB.90.054115

Kaltak, M., Klimeš, J., and Kresse, G. (2014b). Low Scaling Algorithms for the Random Phase Approximation: Imaginary Time and Laplace Transformations. *J. Chem. Theor. Comput.* 10, 2498–2507. doi:10.1021/ct5001268

Kaplan, F., Weigend, F., Evers, F., and Van Setten, M. J. (2015). Off-diagonal Self-Energy Terms and Partially Self-Consistency in GW Calculations for Single Molecules: Efficient Implementation and Quantitative Effects on Ionization Potentials. *J. Chem. Theor. Comput.* 11, 5152–5160. doi:10.1021/acs.jctc.5b00394

Kaplan, F., Harding, M. E., Seiler, C., Weigend, F., Evers, F., and Van Setten, M. J. (2016). Quasi-Particle Self-Consistent GW for Molecules. *J. Chem. Theor. Comput.* 12, 2528–2541. doi:10.1021/acs.jctc.5b01238

Ke, S. H. (2011). All-electron GW Methods Implemented in Molecular Orbital Space: Ionization Energy and Electron Affinity of Conjugated Molecules. *Phys. Rev. B* 84, 4–7. doi:10.1103/PhysRevB.84.205415

Kim, M., Martyna, G. J., and Ismail-Beigi, S. (2020). Complex-time Shredded Propagator Method for Large-Scale GW Calculations. *Phys. Rev. B* 101, 1–24. doi:10.1103/physrevb.101.035139

Klamt, A., and Jonas, V. (1996). Treatment of the Outlying Charge in Continuum Solvation Models. *J. Chem. Phys.* 105, 9972–9981. doi:10.1063/1.472829

Klamt, A., and Schüürmann, G. (1993). COSMO: A New Approach to Dielectric Screening in Solvents with Explicit Expressions for the Screening Energy and its Gradient. *J. Chem. Soc. Perkin Trans.* 2, 799–805. doi:10.1039/P29930000799

Klamt, A. (1995). Conductor-like Screening Model for Real Solvents: A New Approach to the Quantitative Calculation of Solvation Phenomena. *J. Phys. Chem.* 99, 2224–2235. doi:10.1021/j100007a062

Klein, A. (1961). Perturbation Theory for an Infinite Medium of Fermions. *Phys. Rev.* 121, 950–956. doi:10.1103/PhysRev.112.99410.1103/physrev.121.950

Knight, J. W., Wang, X., Gallandi, L., Dolgounitcheva, O., Ren, X., Ortiz, J. V., et al. (2016). Accurate Ionization Potentials and Electron Affinities of Acceptor Molecules III: A Benchmark of GW Methods. *J. Chem. Theor. Comput.* 12, 615–626. doi:10.1021/acs.jctc.5b00871

Kotani, T., Van Schilfgaarde, M., and Faleev, S. V. (2007). Quasiparticle Self-Consistent GW Method: A Basis for the Independent-Particle Approximation. *Phys. Rev. B* 76, 1–24. doi:10.1103/PhysRevB.76.165106

Koutecký, J., and Bonačić, V. (1971). On Convergence Difficulties in the Iterative Hartree-Fock Procedure. *J. Chem. Phys.* 55, 2408–2413. doi:10.1063/1.1676424

Koval, P., Foerster, D., and Sánchez-Portal, D. (2014). Fully Self-Consistent GW and Quasiparticle Self-Consistent GW for Molecules. *Phys. Rev. B - Condens. Matter Mater. Phys.* 89, 1–19. doi:10.1103/PhysRevB.89.155417

Koval, P., Ljungberg, M. P., Müller, M., and Sánchez-Portal, D. (2019). Toward Efficient GW Calculations Using Numerical Atomic Orbitals: Benchmarking and Application to Molecular Dynamics Simulations. *J. Chem. Theor. Comput.* 15, 4564–4580. doi:10.1021/acs.jctc.9b00436

Krause, K., and Klopper, W. (2017). Implementation of the Bethe-Salpeter Equation in the TURBOMOLE Program. *J. Comput. Chem.* 38, 383–388. doi:10.1002/jcc.24688

Kudin, K. N., Scuseria, G. E., and Cancès, E. (2002). A Black-Box Self-Consistent Field Convergence Algorithm: One Step Closer. *J. Chem. Phys.* 116, 8255–8261. doi:10.1063/1.1470195

Kutepov, A., Haule, K., Savrasov, S. Y., and Kotliar, G. (2012). Electronic Structure of Pu and Am Metals by Self-Consistent Relativistic GW Method. *Phys. Rev. B - Condens. Matter Mater. Phys.* 85. doi:10.1103/PhysRevB.85.155129

Kutepov, A. L., Oudovenko, V. S., and Kotliar, G. (2017). Linearized Self-Consistent Quasiparticle GW Method: Application to Semiconductors and Simple Metals. *Comput. Phys. Commun.* 219, 407–414. doi:10.1016/j.cpc.2017.06.012

Kutepov, A. L. (2020). Self-consistent GW Method: O(N) Algorithm for Polarizability and Self Energy. *Comput. Phys. Commun.* 257, 107502. doi:10.1016/j.cpc.2020.107502

Lee, C., Yang, W., and Parr, R. G. (1988). Development of the Colle-Salvetti Correlation-Energy Formula into a Functional of the Electron Density. *Phys. Rev. B* 37, 785–789. doi:10.1103/PhysRevB.37.785

Levy, R., LeBlanc, J. P., and Gull, E. (2017). Implementation of the Maximum Entropy Method for Analytic Continuation. *Comput. Phys. Commun.* 215, 149–155. doi:10.1016/j.cpc.2017.01.018

Li, J., D'Avino, G., Duchemin, I., Beljonne, D., and Blase, X. (2018). Accurate Description of Charged Excitations in Molecular Solids from Embedded many-body Perturbation Theory. *Phys. Rev. B* 97, 1–13. doi:10.1103/PhysRevB.97.035108

Liu, P., Kaltak, M., Klimeš, J., and Kresse, G. (2016). Cubic Scaling GW: Towards Fast Quasiparticle Calculations. *Phys. Rev. B* 94, 1–13. doi:10.1103/physrevb.94.165109

Maggio, E., Liu, P., Van Setten, M. J., and Kresse, G. (2017). GW100: A Plane Wave Perspective for Small Molecules. *J. Chem. Theor. Comput.* 13, 635–648. doi:10.1021/acs.jctc.6b01150

Marom, N., Moussa, J. E., Ren, X., Tkatchenko, A., and Chelikowsky, J. R. (2011). Electronic Structure of Dye-Sensitized TiO 2 Clusters from many-body Perturbation Theory. *Phys. Rev. B - Condens. Matter Mater. Phys.* 84, 1–15. doi:10.1103/physrevb.84.245115

Marom, N., Caruso, F., Ren, X., Hofmann, O. T., Körzdörfer, T., Chelikowsky, J. R., et al. (2012). Benchmark of GW Methods for Azabenzenes. *Phys. Rev. B* 86, 1–16. doi:10.1103/PhysRevB.86.245127

Marom, N., Körzdörfer, T., Ren, X., Tkatchenko, A., and Chelikowsky, J. R. (2014). Size Effects in the Interface Level Alignment of Dye-Sensitized TiO2 Clusters. *J. Phys. Chem. Lett.* 5, 2395–2401. doi:10.1021/jz5008356

Martin, R., Reining, L., and Ceperley, D. (2016). Interacting Electrons: Theory and Computational Approaches. Cambridge: Cambridge University Press. doi:10.1017/CBO9781139050807

Miehlich, B., Savi, A., Stoll, H., and Preuss, H. (1989). Results Obtained with the Correlation Energy Density Functionals of Becke and Lee, Yang and Parr. *J. Pediatr. Urol.* 157, 200–206. doi:10.1016/0009-2614(89)87234-3

Migani, A., Mowbray, D. J., Iacomino, A., Zhao, J., Petek, H., and Rubio, A. (2013). Level Alignment of a Prototypical Photocatalytic System: Methanol on TiO2(110). *J. Am. Chem. Soc.* 135, 11429–11432. doi:10.1021/ja4036994

Migani, A., Mowbray, D. J., Zhao, J., Petek, H., and Rubio, A. (2014). Quasiparticle Level Alignment for Photocatalytic Interfaces. *J. Chem. Theor. Comput.* 10, 2103–2113. doi:10.1021/ct500087v

Mowbray, D. J., and Migani, A. (2015). Using G0W0 Level Alignment to Identify Catechol's Structure on TiO2(110). *J. Phys. Chem. C* 119, 19634–19641. doi:10.1021/acs.jpcc.5b05392

Neuhauser, D., Gao, Y., Arntsen, C., Karshenas, C., Rabani, E., and Baer, R. (2014). Breaking the Theoretical Scaling Limit for Predicting Quasiparticle Energies: The Stochastic GW Approach. *Phys. Rev. Lett.* 113, 1–5. doi:10.1103/PhysRevLett.113.076402

Onida, G., Reining, L., and Rubio, A. (2002). Electronic Excitations: Density-Functional versus many-body Green's-function Approaches. *Rev. Mod. Phys.* 74, 601. doi:10.1103/RevModPhys.74.601

Otsuki, J., Ohzeki, M., Shinaoka, H., and Yoshimi, K. (2017). Sparse Modeling Approach to Analytical Continuation of Imaginary-Time Quantum Monte Carlo Data. *Phys. Rev. E* 95, 4–9. doi:10.1103/PhysRevE.95.061302

Perdew, J. P., Burke, K., and Ernzerhof, M. (1996a). Generalized Gradient Approximation Made Simple. *Phys. Rev. Lett.* 77, 3865–3868. doi:10.1103/physrevlett.77.3865

Perdew, J. P., Ernzerhof, M., and Burke, K. (1996b). [ERRATA] Generalized Gradient Approximation Made Simple. *Phys. Rev. Lett.* 77, 3865–3868. doi:10.1103/physrevlett.77.3865

Pluhařová, E., Jungwirth, P., Bradforth, S. E., and Slavíček, P. (2011). Ionization of Purine Tautomers in Nucleobases, Nucleosides, and Nucleotides: From the Gas Phase to the Aqueous Environment. *J. Phys. Chem. B* 115, 1294–1305. doi:10.1021/jp110388v

Pluhařová, E., Schroeder, C., Seidel, R., Bradforth, S. E., Winter, B., Faubel, M., et al. (2013). Unexpectedly Small Effect of the DNA Environment on Vertical Ionization Energies of Aqueous Nucleobases. *J. Phys. Chem. Lett.* 4, 3766–3769. doi:10.1021/jz402106h

Pluhařová, E., Slavíček, P., and Jungwirth, P. (2015). Modeling Photoionization of Aqueous DNA and its Components. *Acc. Chem. Res.* 48, 1209–1217. doi:10.1021/ar500366z

Pulay, P. (1980). Convergence Acceleration of Iterative Sequences. The Case of Scf Iteration. *Chem. Phys. Lett.* 73, 393–398. doi:10.1016/0009-2614(80)80396-4

Pye, C. C., and Ziegler, T. (1999). An Implementation of the Conductor-like Screening Model of Solvation within the Amsterdam Density Functional Package. *Theor. Chem. Acc.* 101, 396–408. doi:10.1007/s002140050457

Ren, X., Rinke, P., Blum, V., Wieferink, J., Tkatchenko, A., Sanfilippo, A., et al. (2012). Resolution-of-identity Approach to Hartree-Fock, Hybrid Density Functionals, RPA, MP2 and GW with Numeric Atom-Centered Orbital Basis Functions. *New J. Phys.* 14, 053020. doi:10.1088/1367-2630/14/5/053020

Rezaei, M., and Ögüt, S. (2021). Photoelectron Spectra of Early 3d-Transition Metal Dioxide Molecular Anions from GW Calculations. *J. Chem. Phys.* 154, 094307. doi:10.1063/5.0042106

Rieger, M. M., Steinbeck, L., White, I. D., Rojas, H. N., and Godby, R. W. (1999). GW Space-Time Method for the Self-Energy of Large Systems. *Comput. Phys. Commun.* 117, 211–228. doi:10.1016/S0010-4655(98)00174-X

Rojas, H. N., Godby, R. W., and Needs, R. J. (1995). Space-Time Method for Ab Initio Calculations ofSelf-Energies and Dielectric Response Functions of Solids. *Phys. Rev. Lett.* 74, 1827–1831. doi:10.1103/physrevlett.74.1827

Sakuma, R., Miyake, T., and Aryasetiawan, F. (2009). Effective Quasiparticle Hamiltonian Based on Löwdin's Orthogonalization. *Phys. Rev. B - Condens. Matter Mater. Phys.* 80, 1–8. doi:10.1103/PhysRevB.80.235128

Salpeter, E. E., and Bethe, H. A. (1951). A Relativistic Equation for Bound-State Problems. *Phys. Rev.* 84, 1232–1242. doi:10.1103/PhysRev.84.1232

Shi, B., Weissman, S., Bruneval, F., Kronik, L., and Öğüt, S. (2018). Photoelectron Spectra of Copper Oxide Cluster Anions from First Principles Methods. *J. Chem. Phys.* 149, 064306. doi:10.1063/1.5038744

Shinaoka, H., Otsuki, J., Ohzeki, M., and Yoshimi, K. (2017). Compressing Green's Function Using Intermediate Representation between Imaginary-Time and Real-Frequency Domains. *Phys. Rev. B* 96, 1–8. doi:10.1103/PhysRevB.96.035147

Shishkin, M., and Kresse, G. (2007). Self-consistent GW Calculations for Semiconductors and Insulators. *Phys. Rev. B - Condens. Matter Mater. Phys.* 75, 1–9. doi:10.1103/PhysRevB.75.235102

Shishkin, M., Marsman, M., and Kresse, G. (2007). Accurate Quasiparticle Spectra from Self-Consistent GW Calculations with Vertex Corrections. *Phys. Rev. Lett.* 99, 14–17. doi:10.1103/PhysRevLett.99.246403

Singh, Y., and Wang, L. W. (2020). Analysis of diagonal G and Subspace W Approximations within Fully Self-Consistent GW Calculations for Bulk Semiconducting Systems. *Phys. Rev. B* 101, 1–14. doi:10.1103/PhysRevB.101.235157

Staneke, P. O., Groothuis, G., Ingemann, S., and Nibbering, N. M. (1995). Formation, Stability and Structure of Radical Anions of Chloroform, Tetrachloromethane and Fluorotrichloromethane in the Gas Phase. *Int. J. Mass. Spectrom. Ion Process.* 142, 83–93. doi:10.1016/0168-1176(94)04127-S

Strinati, G. (1988). Application of the Green's Functions Method to the Study of the Optical Properties of Semiconductors. *La. Riv. Del. Nuovo Cim. Ser.* 11, 1–86. doi:10.1007/BF02725962

Tal, A., Chen, W., and Pasquarello, A. (2021). Vertex Function Compliant with the Ward Identity for Quasiparticle Self-Consistent Calculations beyond GW. *Phys. Rev. B* 103, 161104. doi:10.1103/PhysRevB.103.L161104

Talman, J. D., and Shadwick, W. F. (1976). Optimized Effective Atomic central Potential. *Phys. Rev. A.* 14, 36–40. doi:10.1103/physreva.14.36

Tirimbò, G., De Vries, X., Weijtens, C. H., Bobbert, P. A., Neumann, T., Coehoorn, R., et al. (2020a). Quantitative Predictions of Photoelectron Spectra in Amorphous Molecular Solids from Multiscale Quasiparticle Embedding. *Phys. Rev. B* 101, 035402. doi:10.1103/PhysRevB.101.035402

Tirimbò, G., Sundaram, V., Çaylak, O., Scharpach, W., Sijen, J., Junghans, C., et al. (2020b). Excited-state Electronic Structure of Molecules Using many-body Green's Functions: Quasiparticles and Electron-Hole Excitations with VOTCA-XTP. *J. Chem. Phys.* 152, 114103. doi:10.1063/1.5144277

Umari, P., Giacomazzi, L., De Angelis, F., Pastore, M., and Baroni, S. (2013). Energy-level Alignment in Organic Dye-Sensitized TiO2 from GW Calculations. *J. Chem. Phys.* 139, 014709. doi:10.1063/1.4809994

Vahtras, O., Almlöf, J., and Feyereisen, M. W. (1993). Integral Approximations for LCAO-SCF Calculations. *Chem. Phys. Lett.* 213, 514–518. doi:10.1016/0009-2614(93)89151-7

Van Lenthe, E., and Baerends, J. E. (2003). Optimized Slater-type Basis Sets for the Elements 1–118. *J. Comput. Chem.* 24, 1142–1156. doi:10.1002/jcc.10255

Van Schilfgaarde, M., Kotani, T., and Faleev, S. (2006). Quasiparticle Self-Consistent GW Theory. *Phys. Rev. Lett.* 96, 1–4. doi:10.1103/PhysRevLett.96.226402

Van Setten, M. J., Weigend, F., and Evers, F. (2013). The GW-Method for Quantum Chemistry Applications: Theory and Implementation. *J. Chem. Theor. Comput.* 9, 232–246. doi:10.1021/ct300648t

Van Setten, M. J., Caruso, F., Sharifzadeh, S., Ren, X., Scheffler, M., Liu, F., et al. (2015). GW100: Benchmarking G0W0 for Molecular Systems. *J. Chem. Theor. Comput.* 11, 5665–5687. doi:10.1021/acs.jctc.5b00453

Van Setten, M. J., Costa, R., Viñes, F., and Illas, F. (2018). Assessing GW Approaches for Predicting Core Level Binding Energies. *J. Chem. Theor. Comput.* 14, 877–883. doi:10.1021/acs.jctc.7b01192

Vidberg, H. J., and Serene, J. W. (1977). Solving the Eliashberg Equations by Means of N-point Padé Approximants. *J. Low Temp. Phys.* 29, 179–192. doi:10.1007/bf00655090

Vlček, V., Rabani, E., Neuhauser, D., and Baer, R. (2017). Stochastic GW Calculations for Molecules. *J. Chem. Theor. Comput.* 13, 4997–5003. doi:10.1021/acs.jctc.7b00770

Vlček, V., Li, W., Baer, R., Rabani, E., and Neuhauser, D. (2018). Swift GW beyond 10,000 Electrons Using Sparse Stochastic Compression. *Phys. Rev. B* 98, 0–10. doi:10.1103/PhysRevB.98.075107

Ward, J. C. (1950). An Identity in Quantum Electrodynamics. *Phys. Rev.* 78, 182. doi:10.1103/physrev.78.182

Weng, G., and Vlcek, V. (2021). *Efficient Treatment of Molecular Excitations in the Liquid Phase Environment via Stochastic many-body Theory*, 1–9. arXiv: 2105.14374.

Whitten, J. L. (1973). Coulombic Potential Energy Integrals and Approximations. *J. Chem. Phys.* 58, 4496–4501. doi:10.1063/1.1679012

Wilhelm, J., Del Ben, M., and Hutter, J. (2016). GW in the Gaussian and Plane Waves Scheme with Application to Linear Acenes. *J. Chem. Theor. Comput.* 12, 3623–3635. doi:10.1021/acs.jctc.6b00380

Wilhelm, J., Golze, D., Talirz, L., Hutter, J., and Pignedoli, C. A. (2018). Toward GW Calculations on Thousands of Atoms. *J. Phys. Chem. Lett.* 9, 306–312. doi:10.1021/acs.jpclett.7b02740

Wilhelm, J., Seewald, P., and Golze, D. (2021). Low-scaling GW with Benchmark Accuracy and Application to Phosphorene Nanosheets. *J. Chem. Theor. Comput.* 17, 1662–1677. doi:10.1021/acs.jctc.0c01282

Conflict of Interest: The authors declare that the research was conducted in the absence of any commercial or financial relationships that could be construed as a potential conflict of interest.

Publisher's Note: All claims expressed in this article are solely those of the authors and do not necessarily represent those of their affiliated organizations, or those of the publisher, the editors and the reviewers. Any product that may be evaluated in this article, or claim that may be made by its manufacturer, is not guaranteed or endorsed by the publisher.

frontiers in Chemistry

ORIGINAL RESEARCH
published: 20 September 2021
doi: 10.3389/fchem.2021.743391

Exciton Modulation in Perylene-Based Molecular Crystals Upon Formation of a Metal-Organic Interface From Many-Body Perturbation Theory

Liran Shunak[1], *Olugbenga Adeniran*[2], *Guy Voscoboynik*[1], *Zhen-Fei Liu*[2] *and Sivan Refaely-Abramson*[1]*

[1]*Department of Molecular Chemistry and Materials Science, Weizmann Institute of Science, Rehovot, Israel,* [2]*Department of Chemistry, Wayne State University, Detroit, MI, United States*

Excited-state processes at organic-inorganic interfaces consisting of molecular crystals are essential in energy conversion applications. While advances in experimental methods allow direct observation and detection of exciton transfer across such junctions, a detailed understanding of the underlying excitonic properties due to crystal packing and interface structure is still largely lacking. In this work, we use many-body perturbation theory to study structure-property relations of excitons in molecular crystals upon adsorption on a gold surface. We explore the case of the experimentally-studied octyl perylene diimide (C8-PDI) as a prototypical system, and use the GW and Bethe-Salpeter equation (BSE) approach to quantify the change in quasiparticle and exciton properties due to intermolecular and substrate screening. Our findings provide a close inspection of both local and environmental structural effects dominating the excitation energies and the exciton binding and nature, as well as their modulation upon the metal-organic interface composition.

Keywords: GW-BSE, Bethe–Salpeter equation, many-body perturbation theory (MBPT), exciton properties, metal-organic interface, molecular crystals, perylene diimide (PDI)

OPEN ACCESS

Edited by:
Linn Leppert,
University of Twente, Netherlands

Reviewed by:
Michele Ceotto,
University of Milan, Italy
Terry. J Frankcombe,
University of New South Wales, Australia

***Correspondence:**
Sivan Refaely-Abramson
sivan.refaely-abramson@weizmann.ac.il

Specialty section:
This article was submitted to Theoretical and Computational Chemistry, a section of the journal Frontiers in Chemistry

Received: *18 July 2021*
Accepted: *07 September 2021*
Published: *20 September 2021*

Citation:
Shunak L, Adeniran O, Voscoboynik G, Liu Z-F and Refaely-Abramson S (2021) Exciton Modulation in Perylene-Based Molecular Crystals Upon Formation of a Metal-Organic Interface From Many-Body Perturbation Theory. Front. Chem. 9:743391. doi: 10.3389/fchem.2021.743391

Organic-inorganic interfaces play a key role in energy conversion and transfer processes (Wasielewski, 1992; Grätzel, 2001). Photoexcitations in the organic component typically generate bound electron and hole pairs, i.e., excitons, which serve as the main energy carriers and can effectively transfer energy across the interface (Ginley and Cahen, 2011). In particular, organic molecular crystals, composed of aromatic organic molecules bound together by van der Waals interactions (Klauk, 2006; Kronik and Neaton, 2016), are widely studied due to their easily adjustable characteristics and tunable excitonic properties (Sato et al., 1981; Smith and Michl, 2013; Luo et al., 2020), with relatively long diffusion lengths (Wan et al., 2015; Penwell et al., 2017; Schnedermann et al., 2019; Delor et al., 2020) stemming from their crystal structure, for example through singlet fission processes and the formation of long-lived triplet states (Wilson et al., 2013; Rao and Friend, 2017; Gish et al., 2019). The coupling between excitonic properties in molecular crystals and their underlying crystal packing and symmetry offers desirable tunability of their exciton relaxation processes and can lead to extended energy-transfer efficiency through material and interface design (Refaely-Abramson et al., 2017; Troisi and Orlandi, 2005; Cocchi et al., 2018; Arias et al., 2016; Cudazzo et al., 2012; Rangel et al., 2016). Of particular interest are the family of perylene diimide (PDI) molecular crystals, composed of a perylene body and an imide group and

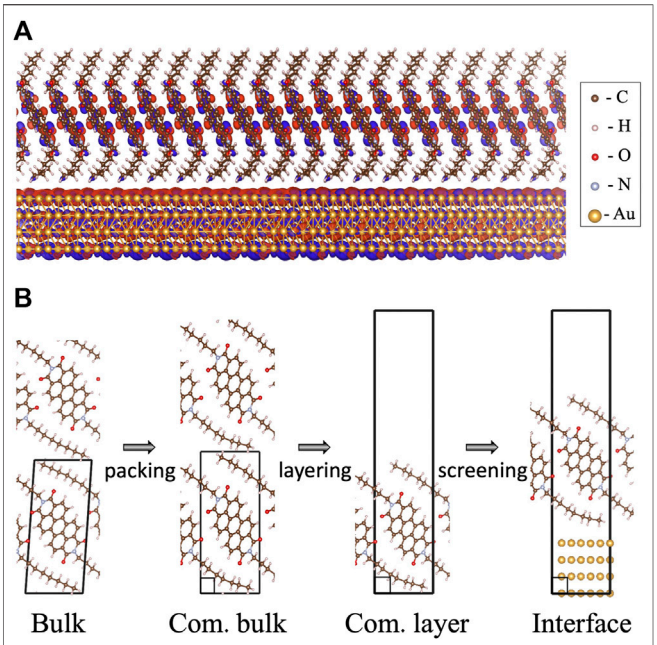

FIGURE 1 | (A) The examined C8-PDI@Au metal-organic interface composed of an organic monolayer, commensurate with a four-layer Au (111) surface. The charge distribution computed for the lowest bound singlet exciton is also shown. **(B)** The different structural modifications of the interface compositions as examined in this work: C8-PDI intermolecular packing, layering, and adsorption on Au surface. The four main structures discussed in the text are termed as "bulk", for the experimental triclinic crystal structure (Briseno et al., 2007); "com. bulk", for an artificial construction of a commensurate phase; "com. layer", for a monolayer structure of the commensurate phase; and "interface", for an interface formed between the commensurate monolayer and four layers of Au (111).

assembled by π-π interaction (Würthner et al., 2016; Schierl et al., 2018; Krieg et al., 2019; Santosh et al., 2010). Crystal packing and symmetry in PDI crystals vary strongly depending on their residues, allowing structural control of the exciton nature and diffusion length (Würthner et al., 2016; Schierl et al., 2018; Eaton et al., 2013; Zhang et al., 2018; Piland and Bardeen, 2015; Hestand and Spano, 2018; Oleson et al., 2019; Carter and Grossman, 2020; Wei et al., 2020), for example via a change in the imide substitution (Le et al., 2018; Felter et al., 2019). A commonly studied PDI crystal in organic optoelectronics is octyl-PDI (C8-PDI) (Felter et al., 2019; O'Brien et al., 2011; Krauss et al., 2009), shown in **Figure 1A**. The intermolecular interaction nature in this crystal gives rise to strongly bound excitons on one hand, and significant exciton dispersion on the other, making it a natural candidate for efficient exciton transfer upon formation of an organic-inorganic interface (Le et al., 2018; Cotton et al., 2020). In particular, C8-PDI single crystals and monolayers serve as a gate dielectric interface in working metal-organic devices, and the subtle details of interface design and structural inhomogeneity on charge and energy transfer efficiency within such junctions have been widely explored (Youn et al., 2012; Liscio et al., 2013; Ciccullo et al., 2015).

These control capabilities at the atomistic level call for a computational examination of the change in excitonic properties stemming from the underlying structure, and in particular upon experimentally-accessible structural modifications. Such excitonic properties can be reliably computed using many-body perturbation theory (MBPT) within the GW and Bethe-Salpeter equation framework (GW-BSE) (Hybertsen and Louie, 1986; Rohlfing and Louie, 2000; Deslippe et al., 2012), a Green's function based *ab initio* approach. GW-BSE computations have the predictive power required to relate the change in crystal packing to electronic and excitonic interaction nature. As such, this method has been applied in recent years to study quasiparticle and excitonic properties in bulk organic molecular crystals (Cudazzo et al., 2012; Sharifzadeh et al., 2012; Cudazzo et al., 2013; Sharifzadeh et al., 2013; Refaely-Abramson et al., 2015; Cudazzo et al., 2015; Kronik and Neaton, 2016; Rangel et al., 2016; Refaely-Abramson et al., 2017; Cocchi et al., 2018; Rangel et al., 2018). However, its explicit application on a metal-organic PDI interface is far from trivial, as it is highly computationally demanding. Nevertheless, such investigation can supply a comprehensive *ab initio* understanding of the relation between the structural changes at the various steps of interface construction - from the freestanding phase to an adsorbate on a metal surface - and the changes in quasiparticle and excitation properties dominating the energy transfer mechanisms.

In this study, we explore the change in excitonic properties in the C8-PDI organic molecular crystal upon structural modifications associated with metal-organic interface formation. For this, we investigate a series of systems, from the bulk molecular crystal with modified unit cells, through a monolayer structure, and finally an organic-inorganic interface formed by the adsorption of the C8-PDI monolayer on Au (111) surface. We use GW-BSE to study the quasiparticle and optical excitation energies in each system, and analyze the involved electron-hole binding as a function of intermolecular packing and layering. We demonstrate a close relationship between exciton localization and molecular arrangement in the crystal, manifesting the importance of intermolecular interactions beyond the Frenkel excitonic picture. We further investigate the effect of interlayer screening on the fundamental and optical gaps, and the resulting exciton binding energy. We show that while the quasiparticle energies are strongly affected by intermolecular and interlayer interactions, the optical excitation energies are far less sensitive to these structural modifications, demonstrating that the long-range nature of the interaction dominates the former and the short-range nature of the interaction dominates the latter. As a result, the computed exciton binding energy strongly depends on the crystal modifications. Our study presents an *ab initio* structure-sensitive understanding of excitonic properties in the C8-PDI@Au organic-inorganic interface, as a prototypical example which sheds light on the excited-state phenomena associated with the exciton transfer processes across such interfaces.

The paper is organized as follows: We first present the GW-BSE computational approaches used. Then we discuss the bulk C8-PDI quasiparticle and excitonic properties, emphasizing the exciton dispersion and the singlet and triplet state localization,

and explore the effect of intermolecular packing upon unit cell modification to a commensurate structure. Finally, we examine variations in the excitonic picture in a freestanding layer, as opposed to the bulk structure, and upon adsorption on an Au substrate. The main steps in the structural modification explored are demonstrated in **Figure 1B**.

1 COMPUTATIONAL METHODS

We perform structural relaxation and compute initial electronic wavefunctions and energies, using density functional theory (DFT) (Kohn and Sham, 1965) and the Perdew-Burke-Ernzerhof (PBE) (Perdew et al., 1996) exchange-correlation functional, as implemented in the Quantum Espresso package (Giannozzi et al., 2017) (see full computational details in the SI). The DFT Kohn-Sham eigenvalues and eigenfunctions are then taken as the first guess for the MBPT calculations. We use the GW approximation to compute the quasiparticle energies and bandstructure (Hybertsen and Louie, 1986; Deslippe et al., 2012; Hedin, 1965), where we calculate self-energy corrections via $\Sigma = iGW$, for G the single-particle Green's function and W the screened Coulomb interaction, $W_{\mathbf{GG'}}(\mathbf{q};0) = \varepsilon^{-1}_{\mathbf{GG'}}(\mathbf{q};0)v(\mathbf{q}+\mathbf{G'})$, where $\mathbf{G}$, $\mathbf{G'}$ are reciprocal lattice vectors, v is the bare Coulomb interaction, and $\varepsilon_{\mathbf{GG'}}(\mathbf{q};0)$ is the dielectric function of the system for interaction wavevector $\mathbf{q}$ and zero frequency, evaluated via (Hybertsen and Louie, 1986; Deslippe et al., 2012):

$$\varepsilon_{\mathbf{GG'}}(\mathbf{q};0) = \delta_{\mathbf{GG'}} - v(\mathbf{q}+\mathbf{G})\chi^0_{\mathbf{GG'}}(\mathbf{q};0), \tag{1}$$

with $\chi^0_{\mathbf{GG'}}(\mathbf{q};0)$ the non-interacting electronic polarizability calculated using the random-phase approximation.

Optical excitations and excitonic properties are computed through the BSE formalism (Rohlfing and Louie, 1998; Rohlfing and Louie, 2000)

$$\left(E_{c\mathbf{k}+\mathbf{Q}} - E_{v\mathbf{k}}\right)A^S_{vc\mathbf{kQ}} + \sum_{v'c'\mathbf{k}'} \langle v\mathbf{k}; c\mathbf{k}+\mathbf{Q}|K^{eh}|v'\mathbf{k}'; c'\mathbf{k}'+\mathbf{Q}\rangle A^S_{v'c'\mathbf{k}'\mathbf{Q}} = \Omega^S_{\mathbf{Q}} A^S_{vc\mathbf{kQ}} \tag{2}$$

for a hole state $|v\mathbf{k}\rangle$ and an electron state $|c\mathbf{k}+\mathbf{Q}\rangle$, where $\mathbf{k}$ is the crystal momentum and $\mathbf{Q}$ is the exciton center-of-mass momentum. S indexes the exciton state at momentum $\mathbf{Q}$. $A^S_{vc\mathbf{kQ}}$ is the amplitude of the free electron-hole pair. $E_{c\mathbf{k}+\mathbf{Q}}$ and $E_{v\mathbf{k}}$ are the quasiparticle energies calculated within the GW approximation; $\Omega^S_{\mathbf{Q}}$ is the excitation energy; and K^{eh} is the electron-hole interaction kernel. Exciton dispersion is obtained by solving the BSE at different exciton momenta $\mathbf{Q}$ following the methodology developed in Refs. (Gatti and Sottile, 2013; Qiu et al., 2015). The GW-BSE exciton wavefunction can be represented as $|\Psi_{S,\mathbf{Q}}\rangle = \sum_{vc\mathbf{k}} A^S_{vc\mathbf{kQ}}|c\mathbf{k}+\mathbf{Q}\rangle|v\mathbf{k}\rangle$.

We compute the dielectric screening at the C8-PDI@Au interface using two approaches. The first is a direct calculation using G_0W_0 for the interface, which is highly computationally challenging and is made possible due to recent advances both in large-scale computing capabilities and associated code development (Del Ben et al., 2019). As a comparison, we also compute the dielectric function of the interface using a recently developed substrate screening GW approach (Liu et al., 2019). In this approach, the non-interacting polarizability of the interface is approximated by the summation of the separately calculated polarizabilies of the substrate (Au) and adsorbate (C8-PDI), i.e.,

$$\chi^0_{\mathrm{tot},\mathbf{GG'}}(\mathbf{q};0) \approx \chi^0_{\mathrm{mol},\mathbf{GG'}}(\mathbf{q};0) + \chi^0_{\mathrm{sub},\mathbf{GG'}}(\mathbf{q};0), \tag{3}$$

where χ^0_{mol} and χ^0_{sub} are the polarizabilities associated with the standalone molecular layer and metal substrates, respectively. This approximation holds for systems with weak hybridization between the adsorbate and the substrate (Liu et al., 2019; Xuan et al., 2019; Adeniran et al., 2020). The goal is to assess the validity of **Eq. 3** against a direct GW calculation of the interface, to determine the nature of the surface effect on quasiparticle and exciton properties of the C8-PDI.

As shown in **Figure 1B**, we mainly study four different structures: (i) "bulk", a bulk crystal in its experimentally resolved triclinic unit cell and relaxed atomic coordinates; (ii) "com. bulk", a modified bulk structure in an orthorhombic lattice, so that it is commensurate with the lattice of the Au substrate; (iii) "com. layer", a layered orthorhombic structure with large vacuum, taken as one molecular layer along the c axis from (ii); and (iv) "interface", the C8-PDI monolayer from (iii) adsorbed on four layers of Au (111) surface, with each layer consisting of 2×3 Au atoms and an adsorption height of 3.18 Å. Such thickness of the simulated Au surface was previously found to sufficiently capture wavefunction hybridization and dielectric screening effects (Liu et al., 2017; Refaely-Abramson et al., 2019). We apply periodic boundary conditions to all structures, and fully relax the internal coordinates for each one of the structures. For (i) and (ii), the calculations were carried out using the converged parameters of a $(8 \times 4 \times 4)$ k-point grid and 600 bands in the summation to compute the dielectric matrix, as well as a kinetic energy cutoff of 80 Ry and a dielectric cutoff of 10 Ry. The calculation of the absorption spectrum was carried out via an interpolation to a finer $(12 \times 6 \times 6)$ k-point grid. For (iii) and (iv), the calculations used a k-point grid of $(8 \times 4 \times 1)$ and 1,000 bands in the summation to compute the dielectric matrix, as well as the same cutoffs as (i) and (ii). (i)-(iii) used a semiconductor screening treatment of the $\mathbf{q} \to 0$ limit and (iv) used a metallic screening, as implemented in the BerkeleyGW package (Deslippe et al., 2012). Furthermore, (iii) and (iv) used a slab truncation for the Coulomb interaction.

2 CRYSTAL PACKING EFFECT ON EXCITON NATURE

We begin with investigating the electronic and excitonic properties of the bulk C8-PDI system, using the experimentally-resolved crystal structure (Briseno et al., 2007), shown in **Figure 2A** (see full structural details in the SI). **Figure 2B** shows the computed GW quasiparticle bandstructure for this system (solid, red line). The three frontier electronic bands shown, valence (v_1), conduction (c_1), and second conduction (c_2), dominate the low-lying excitonic

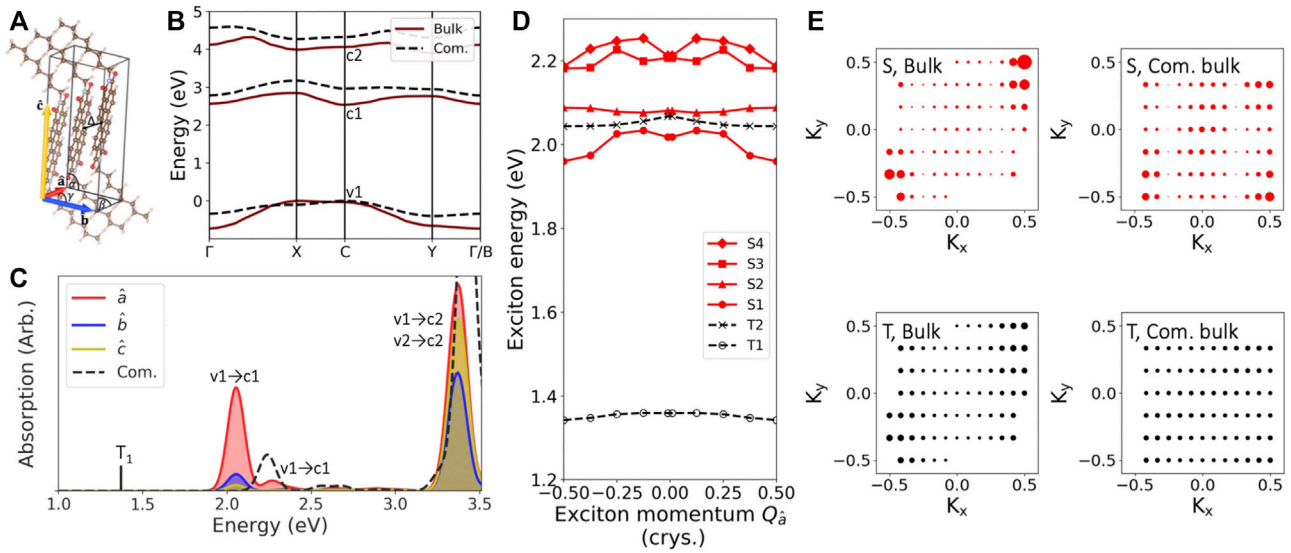

FIGURE 2 | Structural and excitation properties of the bulk C8-PDI molecular crystal: **(A)** The unit cell showing the crystallographic parameters, which are modified among the various bulk structures examined. Δ denotes the intermolecular distance. **(B)** Computed GW quasiparticle bandstrcuture for the bulk (solid red) and the commensurate bulk (dashed black) structures. **(C)** Computed GW-BSE absorption spectra with the polarization of the light aligned along different cell directions. The low-lying triplet state is also shown (black line). Solid lines are for the bulk structure, and dashed black line is for the commensurate bulk structure. **(D)** Exciton bandstructure of the four lowest singlet states (solid red) and the two lowest triplet states (dashed black) of the bulk structure. **(E)** Exciton coefficients as a function of electron momentum in the (K_x, K_y) crystal plane for the lowest singlet and triplet states, of both the bulk and the commensurate bulk structures.

spectra we discuss in this work. The computed GW quasiparticle gap is 2.6 eV, with an expected large self-energy correction on top of the DFT (PBE) gap of 1.1 eV. The quasiparticle bands are well isolated, as typical in molecular crystals due to the molecular-like nature of the material (Refaely-Abramson et al., 2013; Kronik and Neaton, 2016); still, we note a significant band dispersion of ~0.7 eV for the valence band between k-points *X* and Γ and 0.3 eV for the conduction bands between *C* and *X*, reflecting non-negligible intermolecular electronic coupling.

To explore the effect of intermolecular orientation, we computed different bulk structures through variation of relative intermolecular distance and the crystallographic parameters of the unit cell (see SI for full details). Our motivation to vary these parameters is twofold: first, to explore the effect of molecular packing on the quasiparticles and excitons; second, to look into the effect of changes in unit cell vectors, which are needed to achieve proper commensurateness between the unit cell of the C8-PDI crystal and that of the Au surface. In order to maintain minimal strain within the Au surface, we only vary the PDI cell parameters. For the case of a single C8-PDI molecule per cell, this results in a modified cell ("com. bulk" in **Figure 1B**), in which the intermolecular distance grows compared to the original structure. Here we explore the limiting case of an orthorhombic molecular crystal unit cell, although a monoclinic cell leads to very similar results (see SI). By allowing more molecules per cell, commensurate layers can be achieved with smaller atomic modifications, however, performing GW-BSE calculations on these large supercells in an accurate manner is highly computationally challenging. The associated structures and the computed GW bandstructures for each of these cells in its bulk form are given in **Supplementary Table S1**; **Supplementary Figure S1**.

Since the electronic and excitonic states stem from the molecular building blocks, the effect of such unit-cell modification is not trivial and depends on the level of the electronic and excitonic wavefunction localization. Upon structural reorganization from the "bulk" structure to the "com. bulk" cell that is commensurate with the Au surface, the intermolecular distance increases from 3.4 Å to 3.6 Å, and the cell angle γ (**Figure 2A**) changes from 82° to 90°. As a result, the computed GW quasiparticle gap increases by 0.4 eV and the band dispersion decreases by 0.35 eV, as shown in **Figure 2B**. Two other bulk structures with intermediate variations reveal a gradual modification between these values (see SI).

The strong structural dependence of the quasiparticle band dispersion reveals a somewhat surprisingly large effect of the molecular packing and orientation on the quasiparticle and exciton picture. It stems from intermolecular interactions and screening, which vary significantly with intermolecular distances and relative orientation. **Figure 2C** shows the computed BSE absorption spectra of the "bulk" structure, with a low-energy singlet peak at 2.05 eV, in good agreement with the experimental value of ~2.2 eV (Le et al., 2018; Felter et al., 2019). The absorption spectra along the three main polarization directions are shown in different colors, with the main optically-active dipole transitions along the $\hat{a}$ axis, namely through the $\pi - \pi$ stacking direction, and the least active direction along the *c* axis. The low-lying triplet exciton is found at 1.4 eV, shown with a black line. As a comparison, the absorption computed for the commensurate bulk structure is shown as well (dashed black

TABLE 1 | Quasiparticle and optical excitation energies from GW-BSE for the various structures examined. All energies are in eV.

System	Crystal	Com. bulk	Com. layer	Interface
Quasiparticle gap	2.57	2.97	3.40	2.94
Lowest singlet excitation	2.05	2.24	2.13	2.24
Lowest triplet excitation	1.37	1.43	1.33	1.52
Singlet binding energy	0.52	0.73	1.27	0.70

line). As shown in **Table 1**, comparing the "com. bulk" structure with the "bulk" structure, the lowest singlet excitation energy increases by 0.19 eV; however, the lowest triplet excitation energy increases by only 0.06 eV.

We further examine the effect of intermolecular coupling on the exciton nature by investigating the exciton dispersion, where the center-of-mass momentum **Q** represents the momentum difference between the hole and the excited electron, which is taken into account in the BSE, **Eq. 2**; (Qiu et al., 2015). **Figure 2D** shows the computed exciton bandstructure along the optically-active $\hat{a}$ direction (other crystal directions are shown in the SI). The exciton band shape varies along the reciprocal space due to indirect transitions occurring between the Γ and X points. At small exciton momentum **Q**, the lowest singlet exciton, S_1, shows a parabolic behavior, with effective mass of $0.35m_e$ (for m_e the electron mass). Higher singlet excitons are also shown, revealing varying levels of localization. As expected, the low-lying triplet state has a larger effective mass of $2.7m_e$, supporting its higher degree of real-space localization, as typical in organic molecular crystals (Rangel et al., 2016; Refaely-Abramson et al., 2017).

Figure 2E shows the exciton coefficients ($A^S_{vc\mathbf{k}}$ in **Eq. 2**) for the **Q** = 0 transition as a function of quasiparticle momentum in the (K_x, K_y) crystal plane. The lowest singlet state shows high localization in momentum space at the C point ([0.5,0.5,0] in reciprocal space), suggesting spatial delocalization. On the contrary, for the lowest triplet state, the exciton coefficients are nearly uniform within the Brillouin zone, pointing to spatial localization. In the commensurate bulk structure, the same singlet excitons are more spread in reciprocal space, reflecting increased real-space localization. The triplet state is localized in both structures and experiences a smaller change due to the structural modification, compared to the singlet state. The sizable differences between singlet and triplet localization is coupled to the short-range exchange in C8-PDI, dominating intermolecular electron-hole coupling (Rohlfing and Louie, 2000; Rangel et al., 2016). Upon changes in intermolecular packing, induced exciton localization leads to enhanced exchange interactions. Our results thus reveal strong state- and structure-dependence of the exciton nature in bulk C8-PDI, as an outcome of the intermolecular interactions dominating the electron-hole coupling.

3 DIMENSIONALITY AND INTERFACE EFFECTS ON EXCITON BINDING

Next, we study the effect of crystal layering and surface adsorption on the excitation energies. As shown in **Table 1**, for the commensurate structure, the quasiparticle gap of a freestanding C8-PDI layer increases by ~0.4 eV, while both the singlet and triplet exciton energies decrease by ~0.1 eV, compared to the commensurate bulk structure. This results in a significant increase of the exciton binding energy, an expected result due to the strong dimensionality effect on the dielectric screening, as we further elaborate in the discussion section below. From a computational point of view, constructing a monolayer is motivated by its subsequent adsorption on Au substrate within a computationally tractable periodic cell. In the following we directly compare the charged and neutral excitations of the freestanding layer with the adsorbed one, to gain direct insight into the Au screening effect on exciton binding.

To capture the dielectric screening at the C8-PDI@Au interface, we compare two approaches: an explicit GW calculation of the entire interface, with the simulation cell presented in **Figure 1**; and a substrate screening GW approach (Liu et al., 2019), in which the polarizabilities of the two parts of the interface are computed separately and then combined in the interface cell, as we discuss in the methods section. Our motivation is to verify the validity of the substrate screening approximation for the C8-PDI@Au interface. If this is true, we can conclude that the effect of the Au substrate merely provides a dielectric media that renormalizes the quasiparticle and excitation energies within the C8-PDI molecular layer, rather than altering the nature of the quasiparticle orbitals and excitons of the C8-PDI via orbital hybridization.

Figure 3A shows the computed GW quasiparticle projected density of states (pDOS) of the full interface at high symmetry k-points onto C8-PDI (purple) and Au (orange) atomic orbitals. Dashed black lines represent the pDOS associated with the freestanding C8-PDI layer, which we align with the pDOS onto C8-PDI at the resonance corresponding to the highest occupied molecular orbital (at about −0.8 eV in **Figure 3A**). The quasiparticle gap associated with the molecular levels is reduced by 0.46 eV compared to the monolayer, due to the Au surface. The associated valence and conduction electronic charge distributions for the PDI-localized interface wavefunctions are well separated from the Au states, demonstrating the negligible interface hybridization in this system. The change in quasiparticle energies is a direct outcome of interface screening. **Figure 3B** compares the computed dielectric function $\varepsilon_{\mathbf{00}}$ (**Eq. 1**) of the commensurate bulk, layered, and interface systems for the head elements, namely $\mathbf{G} = \mathbf{G}' = 0$. At large interaction distance **q**, corresponding to short-range interactions in real space, the dielectric function reaches the expected limit of $\varepsilon = 1$. At small **q**, however, the dielectric function increases significantly due to the Au screening, while remaining close to unity for the freestanding layer due to its reduced dimensionality.

The computed GW quasiparticle gap resulting from the substrate screening approach is 2.95 eV, which is in very good agreement with the direct calculation (2.94 eV). Additionally, in **Supplementary Figure S5**, we compare the diagonal elements of the non-interacting polarizability of the interface (χ^0_{tot}) computed using the two approaches, and find that they agree very well. We can infer from these results that there is negligible orbital

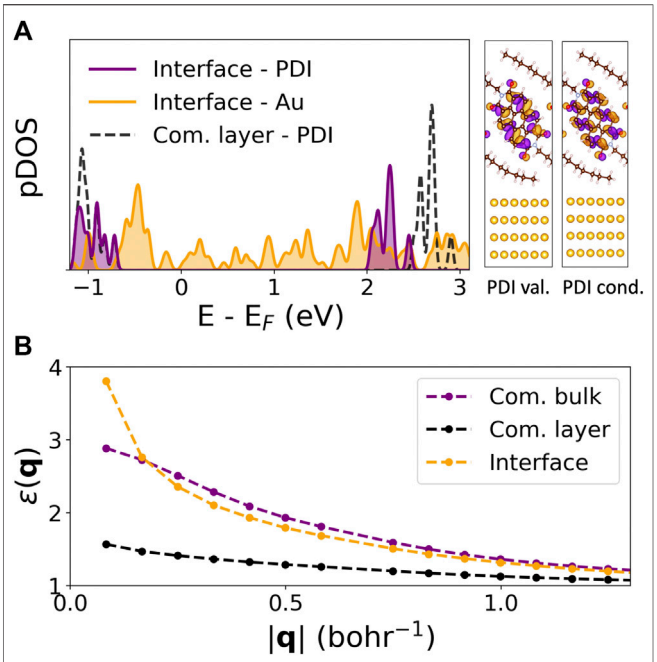

FIGURE 3 | Quasiparticle and dielectric properties of the C8-PDI@Au interface: **(A)** GW pDOS on C8-PDI (purple) and Au (orange) atomic orbitals, compared to the freestanding molecular layer (dashed black). The right panel shows the electronic distributions of the PDI-localized valence and conduction states. **(B)** Computed GW dielectric function, $\varepsilon(\mathbf{q})$, for the commensurate bulk (purple), commensurate layer (black), and the interface structure (orange).

hybridization at the C8-PDI@Au interface, and that the Au substrate simply provides a dielectric environment that effectively screens the molecular crystal. We expect that the substrate screening approach, based on the additivity of the non-interacting polarizability of the interface (Liu et al., 2019; Xuan et al., 2019), is applicable to other systems without significant orbital hybridization or covalent bonding.

We believe this conclusion could help us understand the *physical* interface where a C8-PDI monolayer in its pristine bulk lattice (rather than the artificial commensurate lattice as we did in this work) is adsorbed on Au (111). From a computational perspective, such a physical interface is incommensurate and is prohibitively expensive to calculate. However, based on the conclusion achieved in this section, we can infer what would happen if we were modelling the incommensurate physical interface: all the properties associated to the exciton wavefunctions of the C8-PDI bulk crystal as reported in **Figure 2** will be qualitatively unchanged in the interface, thanks to the negligible orbital hybridization. The exciton binding energies will be renormalized due to the dielectric screening of the Au substrate.

4 DISCUSSION AND CONCLUSION

Our results demonstrate the effect of intermolecular and surface screening on both quasiparticle and exciton properties via a step-by-step structural variation. Specifically, we look closely at the exciton nature as a function of molecular crystal packing and dielectric environment, as summarized in **Figure 4**. For the case of Frenkel-like molecular excitons, the exciton nature should stay roughly unchanged upon changes in crystal packing, as the environmental effect will be mainly manifested through an effective dielectric constant (Sharifzadeh et al., 2012; Cudazzo et al., 2013). Nonetheless, we find that the bulk C8-PDI excitons do have dispersion and are crystal-momentum dependent, reflecting non-negligible excitonic coupling beyond the Frenkel picture. The dispersion is more enhanced in singlet states compared to triplet states due to the exchange interaction, as observed before in related organic molecular crystals (Rangel et al., 2016; Refaely-Abramson et al., 2017; Rangel et al., 2018). On top of this effect, the dielectric screening induces further variations: upon crystal layering, the quasiparticle gap increases, and upon surface adsorption it renormalizes, while the exciton energies remain largely unchanged. This is a direct outcome of the non-local screening that dominates the quasiparticle energies, compared to local screening that dominates the electron-hole binding in the low-lying excitons. These dielectric effects are captured in the GW calculation through an explicit evaluation of the dielectric function (Hybertsen and Louie, 1986; Deslippe et al., 2012). As shown in **Figure 3B**, the dielectric functions of the various structures are similar at the short-range interaction regime and differ greatly at the long-range interaction regime.

Table 1 indicate the strong sensitivity of the charged quasiparticle excitation energies (as reflected in gaps) to the dielectric environment and the weak sensitivity of the neutral excitation energy (as reflected in optical transitions in the case of strong electron-hole coupling) to the environment (Kronik et al., 2012; Refaely-Abramson et al., 2015). The change in the optical gaps and the exciton binding energies between the C8-PDI monolayer and the C8-PDI@Au interface points to a significant decrease in the exciton binding energy upon formation of the interface with Au. This effect is expected, as the enhanced screening has a significant influence on the quasiparticle gap (Neaton et al., 2006; Egger et al., 2015; Liu et al., 2017). On the other hand, simple metal surfaces tend to have a much weaker influence on the optical excitations localized within the adsorbate (Spataru, 2013; Deilmann and Thygesen, 2019).

Importantly, the computational approach we employed here is not limited to cases of weak hybridization at the interface, and can be hence further used to investigate other types of PDI interfaces where the exciton separation mechanisms are expected to involve significant charge-transfer components. For example, triplet exciton transfer across C8-PDI and SiO_2 interfaces was recently suggested to be strongly coupled to changes in intermolecular interactions due to surface hybridization (Cotton et al., 2020). In addition, few recent studies explored the role of surface passivation in modifying and controlling the efficiency of exciton transfer from acene molecular crystals adsorbed on silicon substrates (Einzinger et al., 2019; Daiber et al., 2020). The relation between interface

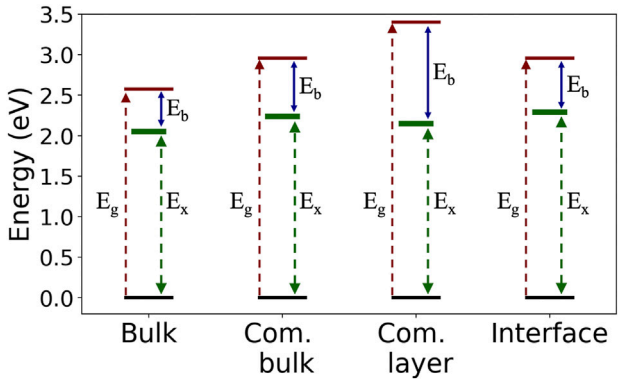

FIGURE 4 | Summary of the computed GW quasiparticle gap, E_g; optical gap, E_x; and the exciton binding energy, E_b, in the four examined structures.

bonding, charge and exciton localization far from and at the junction, and the resulting energy-transfer efficiency at PDI-based junctions is intriguing, and the results we present here for the case of weak metal-organic coupling can be thought of as a computational test case at the weakly interacting regime. Our results thus demonstrate that the GW-BSE approach offers a reliable tool to explore interface effects on excitonic properties at organic-inorganic interfaces with various levels of interface hybridization.

To conclude, we studied the effect of structural modifications on quasiparticle and exciton nature in the C8-PDI molecular crystal and its interface with Au. We explored the excitonic properties of the bulk system in detail, and investigated the effect of crystal packing and interface dielectric screening, building a structural modification route from the bulk structure to a heterogeneous interface. Our results demonstrate that while the quasiparticle band gap undergoes significant variations upon the structural modification and surface adsorption, the optical gap is much less affected by them, leading to strong structural sensitivity of the exciton binding energies. Our methods allow us to quantify this effect, and relate it to the specifics of local and non-local structural modifications.

DATA AVAILABILITY STATEMENT

The datasets presented in this study can be found in online repositories. The names of the repository/repositories and accession number(s) can be found in the article/ **Supplementary Material**.

AUTHOR CONTRIBUTIONS

LS performed most of the DFT, GW, and GW-BSE computations presented in this work. OA performed the interface calculations using the substrate screening GW approach. GV performed DFT and GW examination to explore additional packing effects. Z-FL constructed and led the substrate screening GW calculations. SR-A is the corresponding author in this work and instructed the DFT, GW, and GW-BSE computations. All authors contributed to the manuscript writing.

FUNDING

This research was supported by a grant from the United States-Israel Binational Science Foundation (BSF), Jerusalem, Israel, awarded to Z-FL and SR-A (Grant Number 2018113). OA acknowledges A. Paul and Carole C. Schaap Endowed Distinguished Graduate Award and Rumble Fellowship from Wayne State University. Z-FL acknowledges start-up funds and an Ebbing faculty development award from Wayne State University. SR-A is an incumbent of the Leah Omenn Career Development Chair, and acknowledges research grants from the Peter and Patricia Gruber Awards and an Alon Fellowship. This research used computational resources within a PRACE Allocation Grant, Project No. 2019204916, at the Barcelona Supercomputing Center (BSC-CNS), as well as at the Chemfarm cluster at the Weizmann Institute of Science and at the Center for Functional Nanomaterials, which is a U.S. Department of Energy Office of Science Facility, at Brookhaven National Laboratory under Contract No. DE-SC0012704. Additional computational resources were provided by the National Energy Research Scientific Computing Center (NERSC), a U.S. Department of Energy Office of Science User Facility operated under Contract No. DE-AC02-05CH11231.

ACKNOWLEDGMENTS

We thank Boris Rybtchinski and Angelica Elkan for valuable discussions, Mark Vilensky for administrative support, and Diana Qiu and Felipe da Jornada for helpful discussions.

SUPPLEMENTARY MATERIAL

The Supplementary Material for this article can be found online at: https://www.frontiersin.org/articles/10.3389/fchem.2021.743391/full#supplementary-material

REFERENCES

Adeniran, O., Refaely-Abramson, S., and Liu, Z. F. (2020). Layer-Dependent Quasiparticle Electronic Structure of the P3HT: PCBM Interface From a First-Principles Substrate Screening GW Approach. *J. Phys. Chem. C* 124 (25), 13592–13601. doi:10.1021/acs.jpcc.0c03543

Arias, D. H., Ryerson, J. L., Cook, J. D., Damrauer, N. H., and Johnson, J. C. (2016). Polymorphism Influences Singlet Fission Rates in Tetracene Thin Films. *Chem. Sci.* 7, 1185–1191. doi:10.1039/c5sc03535j

Briseno, A. L., Mannsfeld, S. C. B., Reese, C., Hancock, J. M., Xiong, Y., Jenekhe, S. A., et al. (2007). Perylenediimide Nanowires and Their Use in Fabricating Field-Effect Transistors and Complementary Inverters. *Nano Lett.* 7, 2847–2853. doi:10.1021/nl071495u

Carter, K.-J. B., and Grossman, J. C. (2020). Design Rules for Transparent Push-Pull Electron Acceptors: A Case Study on Perylenediimide Derivatives. *J. Phys. Chem. Lett.* 11, 9265–9271. doi:10.1021/acs.jpclett.0c02485

Ciccullo, F., Savu, S.-A., Gerbi, A., Bauer, M., Ovsyannikov, R., Cassinese, A., et al. (2015). Chemisorption, Morphology, and Structure of a N-type Perylene Diimide Derivative at the Interface with Gold: Influence on Devices from Thin Films to Single Molecules. *Chem. Eur. J.* 21, 3766–3771. doi:10.1002/chem.201404901

Cocchi, C., Breuer, T., Witte, G., and Draxl, C. (2018). Polarized Absorbance and Davydov Splitting in Bulk and Thin-Film Pentacene Polymorphs. *Phys. Chem. Chem. Phys.* 20, 29724–29736. doi:10.1039/c8cp06384b

Cotton, D. E., Moon, A. P., and Roberts, S. T. (2020). Using Electronic Sum-Frequency Generation to Analyze the Interfacial Structure of Singlet Fission-Capable Perylenediimide Thin Films. *J. Phys. Chem. C* 124, 11401–11413. doi:10.1021/acs.jpcc.0c01025

Cudazzo, P., Gatti, M., and Rubio, A. (2012). Excitons in Molecular Crystals from First-Principles many-body Perturbation Theory: Picene versus Pentacene. *Phys. Rev. B* 86, 195307. doi:10.1103/physrevb.86.195307

Cudazzo, P., Gatti, M., Rubio, A., and Sottile, F. (2013). Frenkel versus Charge-Transfer Exciton Dispersion in Molecular Crystals. *Phys. Rev. B* 88, 195152. doi:10.1103/physrevb.88.195152

Cudazzo, P., Sottile, F., Rubio, A., and Gatti, M. (2015). Exciton Dispersion in Molecular Solids. *J. Phys. Condens. Matter* 27, 113204. doi:10.1088/0953-8984/27/11/113204

Daiber, B., Maiti, S., Ferro, S. M., Bodin, J., van den Boom, A. F. J., Luxembourg, S. L., et al. (2020). Change in Tetracene Polymorphism Facilitates Triplet Transfer in Singlet Fission-Sensitized Silicon Solar Cells. *J. Phys. Chem. Lett.* 11, 8703–8709. doi:10.1021/acs.jpclett.0c02163

Deilmann, T., and Thygesen, K. S. (2019). Important Role of Screening the Electron-Hole Exchange Interaction for the Optical Properties of Molecules Near Metal Surfaces. *Phys. Rev. B* 99, 045133. doi:10.1103/physrevb.99.045133

Del Ben, M., da Jornada, F. H., Canning, A., Wichmann, N., Raman, K., Sasanka, R., et al. (2019). Large-scale GW Calculations on Pre-exascale HPC Systems. *Comp. Phys. Commun.* 235, 187–195. doi:10.1016/j.cpc.2018.09.003

Delor, M., Weaver, H. L., Yu, Q., and Ginsberg, N. S. (2020). Imaging Material Functionality through Three-Dimensional Nanoscale Tracking of Energy Flow. *Nat. Mater.* 19, 56–62. doi:10.1038/s41563-019-0498-x

Deslippe, J., Samsonidze, G., Strubbe, D. A., Jain, M., Cohen, M. L., and Louie, S. G. (2012). BerkeleyGW: A Massively Parallel Computer Package for the Calculation of the Quasiparticle and Optical Properties of Materials and Nanostructures. *Comp. Phys. Commun.* 183, 1269–1289. doi:10.1016/j.cpc.2011.12.006

D. S. Ginley and D. Cahen (Editors) (2011). *Fundamentals of Materials for Energy and Environmental Sustainability* (Cambridge University Press).

Eaton, S. W., Shoer, L. E., Karlen, S. D., Dyar, S. M., Margulies, E. A., Veldkamp, B. S., et al. (2013). Singlet Exciton Fission in Polycrystalline Thin Films of a Slip-Stacked Perylenediimide. *J. Am. Chem. Soc.* 135, 14701–14712. doi:10.1021/ja4053174

Egger, D. A., Liu, Z.-F., Neaton, J. B., and Kronik, L. (2015). Reliable Energy Level Alignment at Physisorbed Molecule-Metal Interfaces from Density Functional Theory. *Nano Lett.* 15, 2448–2455. doi:10.1021/nl504863r

Einzinger, M., Wu, T., Kompalla, J. F., Smith, H. L., Perkinson, C. F., Nienhaus, L., et al. (2019). Sensitization of Silicon by Singlet Exciton Fission in Tetracene. *Nature* 571, 90–94. doi:10.1038/s41586-019-1339-4

Felter, K. M., Caselli, V. M., Günbaş, D. D., Savenije, T. J., and Grozema, F. C. (2019). Interplay between Charge Carrier Mobility, Exciton Diffusion, Crystal Packing, and Charge Separation in Perylene Diimide-Based Heterojunctions. *ACS Appl. Energ. Mater.* 2, 8010–8021. doi:10.1021/acsaem.9b01490

Gatti, M., and Sottile, F. (2013). Exciton Dispersion from First Principles. *Phys. Rev. B* 88, 155113. doi:10.1103/physrevb.88.155113

Giannozzi, P., Andreussi, O., Brumme, T., Bunau, O., Buongiorno Nardelli, M., Calandra, M., et al. (2017). Advanced Capabilities for Materials Modelling with Quantum ESPRESSO. *J. Phys. Condens. Matter* 29, 465901. doi:10.1088/1361-648x/aa8f79

Gish, M. K., Pace, N. A., Rumbles, G., and Johnson, J. C. (2019). Emerging Design Principles for Enhanced Solar Energy Utilization with Singlet Fission. *J. Phys. Chem. C* 123, 3923–3934. doi:10.1021/acs.jpcc.8b10876

Grätzel, M. (2001). Photoelectrochemical Cells. *Nature* 414, 338–344. doi:10.1038/35104607

Hedin, L. (1965). New Method for Calculating the One-Particle Green's Function With Application to the Electron-Gas Problem. *Phys. Rev.* 139, A796. doi:10.1103/PhysRev.139.A796

Hestand, N. J., and Spano, F. C. (2018). Expanded Theory of H- and J-Molecular Aggregates: The Effects of Vibronic Coupling and Intermolecular Charge Transfer. *Chem. Rev.* 118, 7069–7163. doi:10.1021/acs.chemrev.7b00581

Hybertsen, M. S., and Louie, S. G. (1986). Electron Correlation in Semiconductors and Insulators: Band Gaps and Quasiparticle Energies. *Phys. Rev. B* 34 (8), 5390. doi:10.1103/PhysRevB.34.5390

Klauk, H. (2006). *Organic Electronics: Materials, Manufacturing, and Applications*. John Wiley & Sons.

Kohn, W., and Sham, L. J. (1965). Self-Consistent Equations Including Exchange and Correlation Effects. *Phys. Rev.* 140, A1133–A1138. doi:10.1103/physrev.140.a1133

Krauss, T. N., Barrena, E., de Oteyza, D. G., Zhang, X. N., Major, J., Dehm, V., et al. (2009). X-ray/Atomic Force Microscopy Study of the Temperature-dependent Multilayer Structure of PTCDI-C8 Films on SiO2. *J. Phys. Chem. C* 113, 4502–4506. doi:10.1021/jp808037w

Krieg, E., Niazov-Elkan, A., Cohen, E., Tsarfati, Y., and Rybtchinski, B. (2019). Noncovalent Aqua Materials Based on Perylene Diimides. *Acc. Chem. Res.* 52, 2634–2646. doi:10.1021/acs.accounts.9b00188

Kronik, L., and Neaton, J. B. (2016). Excited-State Properties of Molecular Solids from First Principles. *Annu. Rev. Phys. Chem.* 67, 587–616. doi:10.1146/annurev-physchem-040214-121351

Kronik, L., Stein, T., Refaely-Abramson, S., and Baer, R. (2012). Excitation Gaps of Finite-Sized Systems from Optimally Tuned Range-Separated Hybrid Functionals. *J. Chem. Theor. Comput.* 8, 1515–1531. doi:10.1021/ct2009363

Le, A. K., Bender, J. A., Arias, D. H., Cotton, D. E., Johnson, J. C., and Roberts, S. T. (2018). Singlet Fission Involves an Interplay between Energetic Driving Force and Electronic Coupling in Perylenediimide Films. *J. Am. Chem. Soc.* 140, 814–826. doi:10.1021/jacs.7b11888

Liscio, F., Albonetti, C., Broch, K., Shehu, A., Quiroga, S. D., Ferlauto, L., et al. (2013). Molecular Reorganization in Organic Field-Effect Transistors and its Effect on Two-Dimensional Charge Transport Pathways. *ACS nano* 7, 1257–1264. doi:10.1021/nn304733w

Liu, Z.-F., da Jornada, F. H., Louie, S. G., and Neaton, J. B. (2019). Accelerating GW-Based Energy Level Alignment Calculations for Molecule-Metal Interfaces Using a Substrate Screening Approach. *J. Chem. Theor. Comput.* 15, 4218–4227. doi:10.1021/acs.jctc.9b00326

Liu, Z.-F., Egger, D. A., Refaely-Abramson, S., Kronik, L., and Neaton, J. B. (2017). Energy Level Alignment at Molecule-Metal Interfaces from an Optimally Tuned Range-Separated Hybrid Functional. *J. Chem. Phys.* 146, 092326. doi:10.1063/1.4975321

Luo, X., Han, Y., Chen, Z., Li, Y., Liang, G., Liu, X., et al. (2020). Mechanisms of Triplet Energy Transfer Across the Inorganic Nanocrystal/Organic Molecule Interface. *Nat. Commun.* 11, 1. doi:10.1038/s41467-019-13951-3

Neaton, J. B., Hybertsen, M. S., and Louie, S. G. (2006). Renormalization of Molecular Electronic Levels at Metal-Molecule Interfaces. *Phys. Rev. Lett.* 97, 216405. doi:10.1103/physrevlett.97.216405

O'Brien, D. B., Anglin, T. C., and Massari, A. M. (2011). Surface Chemistry and Annealing-Driven Interfacial Changes in Organic Semiconducting Thin Films on Silica Surfaces. *Langmuir* 27, 13940. doi:10.1021/la202443u

Oleson, A., Zhu, T., Dunn, I. S., Bialas, D., Bai, Y., Zhang, W., et al. (2019). Perylene Diimide-Based Hj- and hJ-Aggregates: The Prospect of Exciton Band Shape Engineering in Organic Materials. *J. Phys. Chem. C* 123, 20567–20578. doi:10.1021/acs.jpcc.9b04429

Penwell, S. B., Ginsberg, L. D. S., Noriega, R., and Ginsberg, N. S. (2017). Resolving Ultrafast Exciton Migration in Organic Solids at the Nanoscale. *Nat. Mater* 16, 1136–1141. doi:10.1038/nmat4975

Perdew, J. P., Ernzerhof, M., and Burke, K. (1996). Rationale for Mixing Exact Exchange with Density Functional Approximations. *J. Chem. Phys.* 105, 9982–9985. doi:10.1063/1.472933

Piland, G. B., and Bardeen, C. J. (2015). How Morphology Affects Singlet Fission in Crystalline Tetracene. *J. Phys. Chem. Lett.* 6, 1841–1846. doi:10.1021/acs.jpclett.5b00569

Qiu, D. Y., Cao, T., and Louie, S. G. (2015). Nonanalyticity, Valley Quantum Phases, and Lightlike Exciton Dispersion in Monolayer Transition Metal Dichalcogenides: Theory and First-Principles Calculations. *Phys. Rev. Lett.* 115, 176801. doi:10.1103/physrevlett.115.176801

Rangel, T., Berland, K., Sharifzadeh, S., Brown-Altvater, F., Lee, K., Hyldgaard, P., et al. (2016). Structural and Excited-State Properties of Oligoacene Crystals from First Principles. *Phys. Rev. B* 93, 115206. doi:10.1103/physrevb.93.115206

Rangel, T., Rinn, A., Sharifzadeh, S., da Jornada, F. H., Pick, A., Louie, S. G., et al. (2018). Low-lying Excited States in Crystalline Perylene. *Proc. Natl. Acad. Sci. U.S.A.* 115, 284–289. doi:10.1073/pnas.1711126115

Rao, A., and Friend, R. H. (2017). Harnessing Singlet Exciton Fission to Break the Shockley-Queisser Limit. *Nat. Rev. Mater.* 2, 17063. doi:10.1038/natrevmats.2017.63

Refaely-Abramson, S., da Jornada, F. H., Louie, S. G., and Neaton, J. B. (2017). Origins of Singlet Fission in Solid Pentacene from an Ab Initio Green's Function Approach. *Phys. Rev. Lett.* 119, 267401. doi:10.1103/physrevlett.119.267401

Refaely-Abramson, S., Jain, M., Sharifzadeh, S., Neaton, J. B., and Kronik, L. (2015). Solid-State Optical Absorption From Optimally Tuned Time-Dependent Range-Separated Hybrid Density Functional Theory. *Phys. Rev. B* 92 (8), 081204. doi:10.1103/PhysRevB.92.081204

Refaely-Abramson, S., Liu, Z.-F., Bruneval, F., and Neaton, J. B. (2019). First-Principles Approach to the Conductance of Covalently Bound Molecular Junctions. *J. Phys. Chem. C* 123, 6379–6387. doi:10.1021/acs.jpcc.8b12124

Refaely-Abramson, S., Sharifzadeh, S., Jain, M., Baer, R., Neaton, J. B., and Kronik, L. (2013). Gap Renormalization of Molecular Crystals From Density-Functional Theory. *Phys. Rev. B* 88, 081204. doi:10.1103/physrevb.88.081204

Rohlfing, M., and Louie, S. G. (2000). Electron-hole Excitations and Optical Spectra from First Principles. *Phys. Rev. B* 62, 4927–4944. doi:10.1103/physrevb.62.4927

Rohlfing, M., and Louie, S. G. (1998). Electron-Hole Excitations in Semiconductors and Insulators. *Phys. Rev. Lett.* 81, 2312–2315. doi:10.1103/physrevlett.81.2312

Santosh, G., Shirman, E., Weissman, H., Shimoni, E., Pinkas, I., Rudich, Y., et al. (2010). Photofunctional Self-Assembled Nanostructures Formed by Perylene Diimide–Gold Nanoparticle Hybrids. *J. Phys. Chem. B* 114, 14389–14396. doi:10.1021/jp100662b

Sato, N., Seki, K., and Inokuchi, H. (1981). Polarization Energies of Organic Solids Determined by Ultraviolet Photoelectron Spectroscopy. *J. Chem. Soc. Faraday Trans. 2* 77, 1621. doi:10.1039/f29817701621

Schierl, C., Niazov-Elkan, A., Shimon, L. J., Feldman, Y., Rybtchinski, B., and Guldi, D. M. (2018). Singlet Fission in Self-Assembled PDI Nanocrystals. *Nanoscale* 10, 20147–20154. doi:10.1039/C8NR04155E

Schnedermann, C., Sung, J., Pandya, R., Verma, S. D., Chen, R. Y. S., Gauriot, N., et al. (2019). Ultrafast Tracking of Exciton and Charge Carrier Transport in Optoelectronic Materials on the Nanometer Scale. *J. Phys. Chem. Lett.* 10, 6727–6733. doi:10.1021/acs.jpclett.9b02437

Sharifzadeh, S., Biller, A., Kronik, L., and Neaton, J. B. (2012). Quasiparticle and Optical Spectroscopy of the Organic Semiconductors Pentacene and PTCDA from First Principles. *Phys. Rev. B* 85, 125307. doi:10.1103/physrevb.85.125307

Sharifzadeh, S., Darancet, P., Kronik, L., and Neaton, J. B. (2013). Low-Energy Charge-Transfer Excitons in Organic Solids from First-Principles: The Case of Pentacene. *J. Phys. Chem. Lett.* 4, 2197–2201. doi:10.1021/jz401069f

Smith, M. B., and Michl, J. (2013). Recent Advances in Singlet Fission. *Annu. Rev. Phys. Chem.* 64, 361–386. doi:10.1146/annurev-physchem-040412-110130

Spataru, C. D. (2013). Electronic and Optical gap Renormalization in Carbon Nanotubes Near a Metallic Surface. *Phys. Rev. B* 88, 125412. doi:10.1103/physrevb.88.125412

Troisi, A., and Orlandi, G. (2005). Band Structure of the Four Pentacene Polymorphs and Effect on the Hole Mobility at Low Temperature. *J. Phys. Chem. B* 109, 1849–1856. doi:10.1021/jp0457489

Wan, Y., Guo, Z., Zhu, T., Yan, S., Johnson, J., and Huang, L. (2015). Cooperative Singlet and Triplet Exciton Transport in Tetracene Crystals Visualized by Ultrafast Microscopy. *Nat. Chem* 7, 785–792. doi:10.1038/nchem.2348

Wasielewski, M. R. (1992). Photoinduced Electron Transfer in Supramolecular Systems for Artificial Photosynthesis. *Chem. Rev.* 92, 435–461. doi:10.1021/cr00011a005

Wei, W., Ouyang, S., and Zhang, T. (2020). Perylene Diimide Self-Assembly: From Electronic Structural Modulation to Photocatalytic Applications. *J. Semicond.* 41, 091708. doi:10.1088/1674-4926/41/9/091708

Wilson, M. W. B., Rao, A., Ehrler, B., and Friend, R. H. (2013). Singlet Exciton Fission in Polycrystalline Pentacene: From Photophysics toward Devices. *Acc. Chem. Res.* 46, 1330–1338. doi:10.1021/ar300345h

Würthner, F., Saha-Möller, C. R., Fimmel, B., Ogi, S., Leowanawat, P., and Schmidt, D. (2016). Perylene Bisimide Dye Assemblies as Archetype Functional Supramolecular Materials. *Chem. Rev.* 116, 962–1052. doi:10.1021/acs.chemrev.5b00188

Xuan, F., Chen, Y., and Quek, S. Y. (2019). Quasiparticle Levels at Large Interface Systems from Many-Body Perturbation Theory: The XAF-GW Method. *J. Chem. Theor. Comput.* 15, 3824–3835. doi:10.1021/acs.jctc.9b00229

Youn, J., Dholakia, G. R., Huang, H., Hennek, J. W., Facchetti, A., and Marks, T. J. (2012). Influence of Thiol Self-Assembled Monolayer Processing on Bottom-Contact Thin-Film Transistors Based on N-type Organic Semiconductors. *Adv. Funct. Mater.* 22, 1856–1869. doi:10.1002/adfm.201102312

Zhang, G., Zhao, J., Chow, P. C. Y., Jiang, K., Zhang, J., Zhu, Z., et al. (2018). Nonfullerene Acceptor Molecules for Bulk Heterojunction Organic Solar Cells. *Chem. Rev.* 118, 3447–3507. doi:10.1021/acs.chemrev.7b00535

Conflict of Interest: The authors declare that the research was conducted in the absence of any commercial or financial relationships that could be construed as a potential conflict of interest.

Publisher's Note: All claims expressed in this article are solely those of the authors and do not necessarily represent those of their affiliated organizations, or those of the publisher, the editors and the reviewers. Any product that may be evaluated in this article, or claim that may be made by its manufacturer, is not guaranteed or endorsed by the publisher.

frontiers in Chemistry

REVIEW
published: 22 September 2021
doi: 10.3389/fchem.2021.734945

Equation-of-Motion Coupled-Cluster Cumulant Green's Function for Excited States and X-Ray Spectra

F. D. Vila[1], J. J. Kas[1], J. J. Rehr[1], K. Kowalski[2] and B. Peng[2]*

[1]Department of Physics, University of Washington, Seattle, WA, United States, [2]Physical and Computational Science Directorate, Pacific Northwest National Laboratory, Richland, WA, United States

Green's function methods provide a robust, general framework within many-body theory for treating electron correlation in both excited states and x-ray spectra. Conventional methods using the Dyson equation or the cumulant expansion are typically based on the *GW* self-energy approximation. In order to extend this approximation in molecular systems, a non-perturbative real-time coupled-cluster cumulant Green's function approach has been introduced, where the cumulant is obtained as the solution to a system of coupled first order, non-linear differential equations. This approach naturally includes non-linear corrections to conventional cumulant Green's function techniques where the cumulant is linear in the *GW* self-energy. The method yields the spectral function for the core Green's function, which is directly related to the x-ray photoemission spectra (XPS) of molecular systems. The approach also yields very good results for binding energies and satellite excitations. The x-ray absorption spectrum (XAS) is then calculated using a convolution of the core spectral function and an effective, one-body XAS. Here this approach is extended to include the full coupled-cluster-singles (CCS) core Green's function by including the complete form of the non-linear contributions to the cumulant as well as all single, double, and triple cluster excitations in the CC amplitude equations. This approach naturally builds in orthogonality and shake-up effects analogous to those in the Mahan-Noizeres-de Dominicis edge singularity corrections that enhance the XAS near the edge. The method is illustrated for the XPS and XAS of NH_3.

Keywords: coupled cluster, cumulant, green's function, excited states, x-ray

OPEN ACCESS

Edited by:
Bjoern Baumeier, Eindhoven University of Technology, Netherlands

Reviewed by:
Juhan Matthias Kahk, University of Tartu, Estonia
Jinasena Wathogala Hewage, University of Ruhuna, Sri Lanka

****Correspondence:***
J. J. Rehr
jjr@uw.edu

Specialty section:
This article was submitted to Theoretical and Computational Chemistry, a section of the journal Frontiers in Chemistry

Received: *01 July 2021*
Accepted: *06 September 2021*
Published: *22 September 2021*

Citation:
Vila FD, Kas JJ, Rehr JJ, Kowalski K and Peng B (2021) Equation-of-Motion Coupled-Cluster Cumulant Green's Function for Excited States and X-Ray Spectra. Front. Chem. 9:734945. doi: 10.3389/fchem.2021.734945

1 INTRODUCTION

The core-level x-ray absorption spectra (XAS) $\mu(\omega)$ is typically described formally by Fermi's golden rule. However, this formulation requires calculations of and summations over eigenstates of the many-body Hamiltonian H and is computationally intractable. Simplifications such as the determinantal ΔSCF approach, in terms of Slater determinants (Liang et al., 2017; Liang and Prendergast, 2019; Nozieres and Combescot, 1971) have similar limitations. Although still computationally demanding, Green's function methods provide an attractive alternative since summation over final states is implicit (Lee et al., 2012; Bertsch and Lee, 2014; Rehr et al., 2009). Real-time approaches can also be advantageous as they avoid explicit calculations of eigenstates. Our treatment here exploits real-time approaches, following several recent developments: 1) Equation of motion coupled-cluster (EOM-CC) approaches for molecular systems have been formulated for the Green's function in energy-space (Peng and Kowalski,

2016; Peng and Kowalski, 2018a), 2) An approach has also been developed (Rehr et al., 2020) for calculations of many-body XAS $\mu(\omega)$ in terms of the convolution of a one-body XAS $\mu_1(\omega)$ and the spectral function of the core-hole $A_c(\omega)$

$$\mu(\omega) = \int dt e^{-i\omega t}\mu(t) = \int d\omega' \mu_1(\omega') A_c(\omega - \omega'). \quad (1)$$

This result originates from the time-correlation approach (Nozieres and de Dominicis, 1969) that was used to solve the x-ray edge-singularity problem. In this approach the time-domain XAS transition amplitude $\mu(t)$ is given by the factorization

$$\mu(t) = \langle \Psi | D(0) D(t) | \Psi \rangle = L(t) G_c(t). \quad (2)$$

Here $L(t)$ is an effective one-body transition amplitude and $A_c(\omega) = -(1/\pi)\mathrm{Im}\ G_c(t)$. 3) A real-time EOM-CC approach for the cumulant core Green's function G_c has been developed including excitations up to CC-singles (CCS). Intrinsic losses induced by the sudden creation of the core hole lead to shake-up effects, characterized by satellites in $A_c(\omega)$, as observed in x-ray photoemission spectra (XPS). The effective one-body XAS $\mu_1(\omega)$ also builds in orthogonality corrections leading to edge enhancements, as predicted by Mahan, Nozieres and de Dominicis (Mahan, 1967). Our goal here is to review these developments and to combine the one-particle absorption spectrum with a more accurate treatment of the core Green's function, including the complete form of the CCS cumulant, as well as the full single, doubles and triple cluster excitations in the cluster amplitude equations.

In the rest of this review, **Section 2** describes the theoretical approaches used, in particular a brief introduction to the cumulant approach (**Section 2.1**), the real-time equation of motion, coupled cluster (RT-EOM-CC) approach (**Section 2.2**), the frequency space implementation of the Green's Function coupled clusters (GFCC) approach (**Section 2.3**), and the application to XAS (**Section 2.4**). **Section 3** presents results for the core binding energies of small molecules, and a comparison of the theory to XPS and XAS experimental results for NH_3. Finally, **Section 4** presents a summary and discusses future developments.

2 THEORY

2.1 Cumulant Approach

Within the cumulant approximation, the core-level Green's function is defined by an exponential expression

$$G_c(t) = G_c^0(t) e^{C(t)}, \quad (3)$$

where $G_c^0(t) = -i\theta(t)e^{-i\epsilon_c t}$ is the independent particle Green's function (Hartree-Fock in this paper), with single particle energy ε_c, and denotes the core-level in question. $C(t)$ is the cumulant function, which builds the correlation into the Green's function. This cumulant can be expressed in Landau form (Landau, 1944), in terms of an excitation spectrum $\beta(\omega)$,

$$C(t) = \int d\omega\ \frac{\beta(\omega)}{\omega^2}\left[e^{-i\omega t} + i\omega t - 1\right]. \quad (4)$$

As a consequence, the cumulant Green's function is naturally normalized, with an occupation $G_c(t = 0) = 1$. One can also analyze $A(\omega) = -(1/\pi)\mathrm{Im}\ G_c(\omega)$, which is the natural quantity to compare to experimental x-ray photoemission spectra, and to assess the quality of many-body correlation approximations since satellites appearing in spectral quantities such as XPS are directly related to those seen in the spectral function. The above form of the cumulant also permits a natural separation into quasiparticle and satellite contributions. Separating the terms in the expression for the cumulant above, we have

$$C(t) = -a + i\Delta t + \tilde{C}(t), \quad (5)$$

where $a = \int d\omega \beta(\omega)/\omega^2$ is the net satellite strength, $\Delta = \int d\omega \beta(\omega)/\omega$ is the quasiparticle shift, or core-level "relaxation energy", and $\tilde{C}(t)$ is the remainder of the cumulant, which contains the information about the satellites. By expanding about small $\tilde{C}$, the spectral function can be obtained analytically in terms of $\beta(\omega)$, i.e.,

$$A_c(\omega) = Z_c \delta(\omega - E_c) * \left[1 + A_{\mathrm{sat}}(\omega) + \frac{1}{2} A_{\mathrm{sat}}(\omega) * A_{\mathrm{sat}}(\omega) + \cdots\right], \quad (6)$$

where $Z_c = e^{-a}$ is the quasiparticle renormalization, $E_c = \epsilon_c - \Delta$ is the quasiparticle energy, and $A_{\mathrm{sat}}(\omega) = \beta(\omega)/\omega^2$ is the satellite spectral function (Aryasetiawan et al., 1996).

The cumulant kernel or excitation spectrum $\beta(\omega)$ can be approximated in a variety of ways. The most common approximation is to expand the Green's function to low order either in the bare Coulomb interaction, giving $\beta(\omega)$ in terms of the second order self-energy (Vila et al., 2020), or by expanding in terms of the screened Coulomb interaction, which produces an approximation in terms of the GW self-energy (Hedin, 1999; Guzzo et al., 2011; Zhou et al., 2015). Approximate non-linear corrections can be included using real-time TDDFT (Tzavala et al., 2020). Here, as described in the next section, we calculate the cumulant including non-linear corrections within a non-perturbative approach, by expressing the Green's function in terms of the time-dependent EOM-CC states.

2.2 RT-EOM-CC Theory

Our treatment of the core-hole Green's function $G_c(t)$ is based on the CC-ansatz for the time-evolved initial state of the system with a core-hole created at $t = 0^+$: $|\Psi_c(0)\rangle \equiv |\Psi_c\rangle = c_c|\Psi\rangle$ where c_c is the core annihilation operator and $|\Psi\rangle$ is the ground state Hartree-Fock Slater determinant:

$$|\Psi_c(t)\rangle \equiv N_c(t) e^{T(t)} |\Psi_c\rangle. \quad (7)$$

Then $G_c(t) = -i\langle \Psi_c | e^{i(H-E_0)t} | \Psi_c \rangle \theta(t)$ simply becomes

$$G_c(t) = -iN_c(t) e^{-iE_0 t}\theta(t). \quad (8)$$

Calculations of $G_c(t)$ are based on the real-time equation of motion coupled cluster (RT-EOM-CC) ansatz of Schönhammer and Gunnarsson (SG) (Schönhammer and

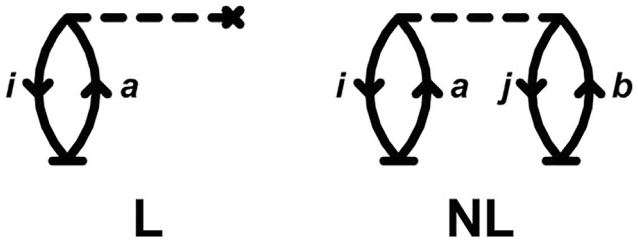

FIGURE 1 | Linear (L) and non-linear (NL) CC diagrams (Crawford and Schaefer, 2000; Brandow, 1967) for the time-derivative of the cumulant in **Eq. 14**. Unlike in traditional EOM-CC diagrams, the base vertices (*t*) are time-dependent.

Gunnarsson, 1978), in which the time-evolution of $|\Psi_c(t)\rangle$ is carried out using an initial value problem and propagation via the Schrödinger equation of motion $i\,\partial|\Psi_c(t)\rangle/\partial t = H|\Psi_c(t)\rangle$. The time-evolved wave-function $|\Psi_c(t)\rangle$ can then be expressed using the CC ansatz in **Eq. 7**. The use of a single-excitations CC ansatz is justified for a single-determinant reference state approximation due to Thouless' theorem (Thouless, 1961). In **Eq. 7** $N_c(t)$ is a normalization factor, while the CC operator $T(t)$ is defined in terms of single, double, etc., excitation creation operators $a_n^\dagger$, i.e.,

$$T(t) = \sum_n t_n(t) a_n^\dagger. \tag{9}$$

For example, for single excitations $n = (i, a)$ and $a_n^\dagger = c_a^\dagger c_i$; for double excitations $n = i, j, a, b$ and $a_n^\dagger = c_a^\dagger c_b^\dagger c_j c_i$; etc. As is conventional in CC, the indices $i, j\ldots$ refer to occupied single-particle states, $a, b, \ldots$ to unoccupied, and $p, q, \ldots$ to either occupied or unoccupied ones. Projecting the EOM with either the ground state, or with singly-excited versions of it, the equations decouple naturally, i.e.,

$$i\,\partial \ln N_c(t)/\partial t = \langle\Psi_c|\bar{H}(t)|\Psi_c\rangle, \tag{10}$$

$$i\,\partial\, t_n(t)/\partial t = \langle n|\bar{H}(t)|\Psi_c\rangle, \tag{11}$$

where $|n\rangle = a_n^\dagger|\Psi_c\rangle$ and $\bar{H} = e^{-T}He^T$ is the similarity-transformed Hamiltonian. The first of these results shows that the normalization factor $N_c(t)$ is a pure exponential, so that the core Green's function $G_c(t)$ has a natural cumulant representation $G_c(t) = G_c^0(t)e^{C(t)}$ with a cumulant defined as

$$C(t) = -i\int_0^t dt'\,\langle\Psi_c|(\bar{H}(t') - E_0')|\Psi_c\rangle, \tag{12}$$

where $E_0' = E_0 - \epsilon_c$, and E_0 is the ground state energy. As noted above, the EOM-CC cumulant can have a Landau form (**Eq. 4**) (Landau, 1944) that simplifies analysis of its spectrum. The cumulant kernel or excitation spectrum $\beta(\omega)$ from the EOM-CC approach is given by

$$\beta(\omega) = \frac{1}{\pi}\mathrm{Re}\int_0^\infty dt\, e^{-i\omega t}\frac{d}{dt}\langle\Psi_c|\bar{H}(t)|\Psi_c\rangle \tag{13}$$

This amplitude accounts for the transfer of oscillator strength from the main peak in XPS to the satellite excitations at frequencies ω. The cumulant initial conditions $C(0) = C'(0) = 0$ guarantee the normalization of the spectral function. In addition, they ensure that its centroid remains invariant at the Koopmans' energy $-\epsilon_c$. After some straightforward diagrammatic analysis to compute the matrix elements in **Eqs. 10**, **12**, we obtain a compact expression for the time-derivative of the cumulant

$$-i\frac{dC(t)}{dt} = \sum_{ia} f_{ia}t_i^a + \frac{1}{2}\sum_{ijab} v_{ij}^{ab}t_j^b t_i^a, \tag{14}$$

where $t_i^a = t_n(t)$ when $n = (i, a)$, and the f_{ia} and v_{ij}^{ab} coefficients correspond, respectively, to the one- and two-particle elements that define the second-quantized Hamiltonian in a core-hole reference (Vila et al., 2020). The terms on the rhs of **Eq. 14** correspond to the linear- (L) and non-linear (NL) CC diagrams (Crawford and Schaefer, 2000; Brandow, 1967) shown in **Figure 1**. The linear term arises from the coupling of the core-hole to the $i \rightarrow a$ excitation, while the second term [which is quadratic in the amplitudes t (NL)] represents valence polarization effects that screen the core-hole.

Remarkably, these diagrams are completely analogous to the time-independent diagrams for the CCSD energy if only single excitations (T_1) are included. It is interesting to note that only one more diagram is needed to obtain the complete CC cumulant for the core-hole Green's function, namely that from double excitations similar to the NL diagram in **Figure 1**, but with a cluster line joining the base vertices representing the T_2 operator.

The EOM for the matrix elements of the CC amplitudes in **Eq. 11** can be calculated using similar diagrammatic analysis which yield a set of coupled first-order differential equations.

$$-it_i^a = -v_{ac}^{ic} + (\epsilon_a - \epsilon_i)t_i^a \tag{15a}$$

$$+\sum_j v_{jc}^{ic}t_j^a - \sum_b v_{ac}^{bc}t_i^b + \sum_{jb} v_{ja}^{bi}t_j^b + \sum_{jb} v_{jc}^{bc}t_i^b t_j^a \tag{15b}$$

$$+\sum_{jbd} v_{aj}^{bd}t_i^b t_j^d - \sum_{jkb} v_{jk}^{ib}t_j^a t_k^b \tag{15c}$$

$$-\sum_{jkbd} v_{jk}^{bd}t_i^b t_j^a t_k^d, \tag{15d}$$

where ϵ_p are the bare single-particle energies. The low order terms are identical to those in our original paper (Rehr et al., 2020). However, now the complete CCS T_1 approximation is used, including terms up to third order in t_i^a. The similarity in the form of **Eq. 14** and **Eq. 15** to the time-independent matrix elements used in standard CC theory implies that the overall scaling of the RT-EOM-CC approach per time step is equivalent to that of the standard CC equations of the same order per solution iteration (i.e. N^4 for CCS, N^6 for CCSD, etc.). The main difference arises in that while for the latter only a few tens of iterations are needed for convergences, RT-EOM-CC requires hundreds to thousands of steps to described the core dynamics. One final difference arises from the complex nature of the time-dependent CC amplitudes, which doubles the computational demands. Thus, approximations are highly desirable and here we review four possible levels of approximation:

1) Lowest order approximation, with only the leading terms, i.e., **Eq. 15a**: At this level the EOM is exactly solvable giving

$t_i^a(t) = -v_{ac}^{ic}[\exp(i\omega_{ia}t) - 1]$, with $\omega_{ia} = \epsilon_a - \epsilon_i$. Moreover, the second-order self-energy cumulant (Vila et al., 2020) is obtained if only the linear part in **Eq. 14** is kept. However this low level of approximation produced mean absolute errors for the core binding energies an order of magnitude larger than those with the next higher levels of approximation to **Eq. 15** (2–4, as summarized below) which we have used for the results presented in **Section 3**.

2) Core-valence approximation: **Eq. 15a** together with the dominant, first four sums in **Eq. 15b**. This approximation includes the linear core- and valence-valence contributions and a non-linear term corresponding to excitations linked to the core-hole.
3) Full second order approximation: Keeping all terms of level 2, and the non-linear valence-valence excitations from the two sums in **Eq. 15c**. This gives corrections that close the gap between the QP peak and the satellites.
4) Full third order T_1 level: This approximation retains all the terms in the T_1 EOM in **Eq. 15**, including the cubic term in **Eq. 15d**.

Each of the approximation levels to **Eq. 15** can be combined with either the linear (L), or both the linear and non-linear (NL) components of $C(t)$ defined in **Eq. 14**. As we have demonstrated previously (Vila et al., 2020), the NL component is key for obtaining accurate core binding energies. Consequently it is useful to focus on the 2_{NL}, 3_{NL} and 4_{NL} results only. For comparison results are also shown for the solution of the Dyson equation (DSE2) (Linderberg and Öhrn, 2004; Szabo and Ostlund, 1996)

$$G_c(\omega) = [1 - G_c^0(\omega)\Sigma^{(2)}(\omega)]^{-1} G_c^0(\omega) \tag{16}$$

where $\Sigma^{(2)}(\omega)$ is the second order self-energy (Szabo and Ostlund, 1996); and for the frequency space Green's function GFCCSD and GFCC-i (2, 3) methods (Peng and Kowalski, 2018a; Peng and Kowalski, 2018b).

2.3 GFCC Theory

In this section we briefly review the GFCC formalism introduced by Nooijen et al. (Nooijen and Snijders, 1992; Nooijen and Snijders, 1993; Nooijen and Snijders, 1995, see also Meissner and Bartlett, 1993; Kowalski et al., 2014; Bhaskaran-Nair et al., 2016; Peng and Kowalski, 2016; Peng and Kowalski, 2018a), which draws heavily on the bi-variational CC formalism (Arponen, 1983; Stanton and Bartlett, 1993) where the ground-state bra- ket ($\langle\Psi_g|$) and ($|\Psi_g\rangle$) states are parametrized in a different way.

$$\langle\Psi_g| = \langle\Phi|(1 + \Lambda)e^{-T} \tag{17}$$

$$|\Psi_g\rangle = e^T|\Phi\rangle, \tag{18}$$

where the reference function $|\Phi\rangle$ is typically chosen as a Hartree-Fock Slater determinant (for the original papers on the CC ansatz see Coester, 1958; Coester and Kümmel, 1960; Čížek, 1966; Paldus et al., 1972; Purvis and Bartlett, 1982; Paldus and Li, 1999; Bartlett and Musiał, 2007). In the above equations the T and Λ operators refer to the so-called cluster and de-excitation operators, respectively, which can be obtained by solving canonical CC equations for the N-electron system. For simplicity, in this review we will discuss the algebraic form of the retarded part of the frequency dependent CC Green's function defined by matrix elements $G_{pq}^R(\omega)$:

$$G_{pq}^R(\omega) = \langle\Psi_g|c_q^\dagger(\omega + (H - E_0) - i\eta)^{-1}c_p|\Psi_g\rangle. \tag{19}$$

Here H is the electronic Hamiltonian for the N-electron system, E_0 the corresponding ground-state energy, η is a broadening factor, and c_p ($c_q^\dagger$) operator is an annihilation (creation) operator for an electron in the q-th spin-orbital. The bi-variational CC formalism then leads to a formula for the general matrix element $G_{pq}^R(\omega)$ given by:

$$G_{pq}^R(\omega) = \langle\Phi|(1 + \Lambda)\overline{c_q^\dagger}(\omega + \bar{H}_N - i\eta)^{-1}\bar{c}_p|\Phi\rangle, \tag{20}$$

The similarity transformed operators here $\bar{A}$ ($A = H, c_p, c_q^\dagger$) are defined as $\bar{A} = e^{-T}A\,e^T$. By defining ω-dependent auxiliary operators $X_p(\omega)$

$$\begin{aligned} X_p(\omega) &= X_{p,1}(\omega) + X_{p,2}(\omega) + \ldots \\ &= \sum_i x^i(\omega)_p c_i + \sum_{i<j,a} x_a^{ij}(\omega)_p c_a^\dagger c_j c_i + \ldots, \quad \forall_p \end{aligned} \tag{21}$$

that satisfy equations

$$(\omega + \bar{H}_N - i\eta)X_p(\omega)|\Phi\rangle = \bar{c}_p|\Phi\rangle, \tag{22}$$

Equation 20 can then be re-expressed compactly as

$$G_{pq}^R(\omega) = \langle\Phi|(1 + \Lambda)\overline{c_q^\dagger}X_p(\omega)|\Phi\rangle. \tag{23}$$

The $X_p(\omega)$ operators can be effectively solved using a parallel implementation of the GFCC formalism based on the approximate forms of T, Λ, and $X_p(\omega)$ (Peng et al., 2021).

The RT-EOM-CC Green's function differs from the frequency-space GFCC approaches (Peng and Kowalski, 2016; Peng and Kowalski, 2018b) in several respects. In particular RT-EOM-CC is based on a transformation to an initial value problem with the propagation of the $N-1$ particle system carried out after the creation of the core-hole; in contrast the GFCC methods are implemented in frequency-space. In addition, RT-EOM-CC assumes an uncorrelated N-particle single-determinant ground state, while the GFCC approaches calculate this ground state using the CC ansatz (**Eq. 17** and **Eq. 18**). Finally, the RT-EOM-CC cumulant treats the $N-1$ particle excited states at the CCS level, while the GFCCSD approximation solves for the excitations of the $N-1$ particle system at the approximate CCSD level, keeping only single and double excitations, as discussed near **Eq. 14** of Peng and Kowalski, 2018a. Thus high order diagrams are implicitly built in the RT-EOM-CC GF from the exponential form of the cumulant (Gunnarsson et al., 1994; Lange and Berkelbach, 2018). While the RT-EOM-CC utilizes a unique approximation for the time-dependent $T(t)$ operator, the GFCC formalisms permit the use of several levels of approximation for the T, Λ and $X_p(\omega)$ operators (for assuring size-extensivity of diagrams defining the $G_{pq}^R(\omega)$ matrix elements, the "n+1" rule of Peng and Kowalski, 2018b has to be followed). The numerical complexities of the RT-EOM-CC and GFCC methods, aside from complicated tensor contractions, originate

in the time propagation algorithms, and the need for solving a large number of linear equations for frequency domain, respectively. Efficient algorithms have already been tested to alleviate possible numerical problems and instabilities (Peng et al., 2019; Peng et al., 2021).

2.4 X-Ray Spectra

Our treatment here is adapted from that in our original EOM-CC paper (Rehr et al., 2020), but updated here with a more detailed treatment of the EOM discussed above. As outlined in the introduction, the contribution from a deep core level $|c\rangle$ to the XAS is given by the time-correlation function $\mu(t) = L(t)$ $G_c(t)$ in **Eq. 2**, as in Nozieres and de Dominicis, 1969 and Rehr et al., 2020. The core-hole Green's function G_c can be obtained from the RT-EOM-CC **Eq. 8**. Calculations of $L(t)$, the one-body time-dependent transition amplitude, can be carried out using coupled equation of motion or equivalent integral equations (Langreth, 1969; Grebennikov et al., 1977; Privalov et al., 2001). Alternatively, propagation based on the overlap integrals $u_{ij}(t)$ can also be used, as done by Nozieres and Combescot (NC) (Nozieres and Combescot, 1971). However, it is more convenient to replace the sums over k with the complete set of eigenstates κ of the final state one-particle Hamiltonian $h' = \sum_\kappa \epsilon_\kappa c_\kappa^\dagger c_\kappa$. Then, defining the core transition operator D in terms of the transition matrix elements $M_{c\kappa} = \langle c|d|\kappa\rangle$, $D = \Sigma_\kappa M_{c\kappa} c_\kappa^\dagger c_c$, the single-particle XAS amplitude $L(t)$ becomes.

$$L(t) = \sum_{\kappa,\kappa'} M_{c\kappa}^* M_{c\kappa'} L_{\kappa,\kappa'}(t), \tag{24}$$

$$L_{\kappa,\kappa'}(t) = e^{i\epsilon_\kappa t}\left[u_{\kappa,\kappa'}(t) - \sum_{ij}^{occ} u_{\kappa i}(t) u_{ij}^{-1}(t) u_{j\kappa'}(t)\right]. \tag{25}$$

The leading term on the rhs of **Eq. 25** can be interpreted as a contribution to $L_{\kappa,\kappa'}(t)$ from the independent particle transition amplitude for the final state when the core-hole is present $L_0(t) = \Sigma_\kappa |M_{c\kappa}|^2 \exp(i\epsilon_\kappa t)$, consistent with the final-state rule of von Barth and Grossman (von Barth and Grossmann, 1982). The diagonal terms $\kappa = \kappa'$ in **Eq. 25** suppress transitions to the occupied states $\kappa < k_F$ by yielding the theta function $\theta(k_F - k)$. The off-diagonal terms in $L_{\kappa,\kappa'}(t)$ are controlled by states with either κ (or κ') $> k_F$ or κ' (or κ) $< k_F$. Interestingly the net result can be approximated accurately by the expression

$$L(t) \approx \sum_\kappa |\tilde{M}_{c\kappa}|^2 e^{i\epsilon_\kappa t}, \tag{26}$$

equivalent to the one derived by Friedel (Friedel, 1969), where $\tilde{M}_{c\kappa} = \langle c|d\bar{P}|\kappa\rangle$, and $\bar{P} = 1 - \Sigma_{i=1}^N |i\rangle\langle i|$ projects out the occupied valence states in the ground state. Note that the sum-rule $\int d\omega$ $\mu(\omega) = \pi L(0)$ for the XAS is also preserved by this formula. The additional terms $-\Sigma_i \langle c|d|i\rangle\langle i|\kappa\rangle$ from $\bar{P}$ are termed *replacement transitions* (Friedel, 1969). Physically, these terms are necessary to remove transitions into the initial occupied levels. First order perturbation theory shows that, for an attractive core-hole potential and $\kappa > i$, the integral for the overlap $\langle i|\kappa\rangle \approx -v_{ik}/\omega_{ik}$ < 0. Thus these terms imply an intrinsic edge enhancement factor $L/L_0 = (1 + \chi_\kappa)$ for each photoelectron level κ in the XAS where $\chi_\kappa \approx -2\Sigma_{i=1}^N (M_{ci}/M_{c\kappa})\langle i|\kappa\rangle$. Though this edge-enhancement effect is non-singular in molecular systems, it is consistent with the power-law singularity $\mu_1 \sim |(\epsilon - \epsilon_F)/\epsilon_F|^{-2\delta_l/\pi}$ predicted by Mahan for metallic systems (Mahan, 1967). The XAS in **Eq. 1** is finally given by a convolution of $\mu_1(\omega)$ with the spectral function $A_c(\omega)$. It is convenient to shift $\mu_1(\omega)$ and $A_c(\omega)$ by ϵ_c, the energy of the core level, with $\omega = \epsilon - \epsilon_c$, so that for the non-interacting system, $\mu_1(\omega)$ reduces to the independent particle XAS. The shifted $A_c(\omega)$ then accounts for the shake-up excitation spectrum

$$A_c(\omega) = \sum_n |S_n|^2 \delta(\omega - \epsilon_n). \tag{27}$$

Here $S_n = \langle \Psi_c | \Psi_n' \rangle$ is the $N - 1$, many-body overlap integral, and $\epsilon_n = E_n' - E_0$ is the shake-up energy. The net effect of the spectral function $A_c(\omega)$ is to broaden the XAS and significantly reduce its magnitude near the edge, transferring the weight to the satellite peaks. For metallic systems this yields an Anderson power-law singularity $[(\epsilon - \epsilon_F)/\epsilon_F]^\alpha$ (Nozieres and de Dominicis, 1969). This reduction effect has opposite sign to and competes with the Mahan enhancement L/L_0 in $\mu_1(\omega)$. However, the above formulation neglects extrinsic losses and interference effects, which will likely lessen these effects. The net result, however, is a many-body amplitude correction to the independent particle XAS visible in experimental XPS. This spectrum is proportional to the spectral function $J_k(\omega) \sim A_c(\omega - \epsilon_k)$, and usually measured vs photoelectron energy ϵ_k at fixed photon energy ω. Thus the peaks in the XPS correspond to a quasiparticle peak as well as satellite excitations at higher binding energies, as discussed in more detail below.

3 RESULTS AND DISCUSSION

As an example of the accuracy of the RT-EOM-CCS method for core ionization energies we show results for CH_4, NH_3, H_2O, HF and Ne, i.e. the ten-electron series, using the experimental geometries (NIST, 2019) for all systems (r_{CH} = 1.087 Å, r_{NH} = 1.012 Å, a_{HNH} = 106.67 degree, r_{OH} = 0.958 Å, a_{HOH} = 104.48 degree, r_{FH} = 0.917 Å), and the aug-cc-pVDZ basis set (Kendall et al., 1992). We also show spectral function and XAS results for NH_3 for which experimental values are available in the literature. The ground state single-particle states and molecular orbitals integrals for the RT-EOM-CCS approach and the ΔSCF method were calculated from a Hartree-Fock (HF) reference, while those for the core-excited ΔSCF were derived from a spin-symmetric and occupation-constrained HF reference. The final spectra were broadened to compare with experiment as in Rehr et al., 2020 and Vila et al., 2020 with varying (1–6 eV) broadening to account for the limited basis set for the continuum; similarly XAS used constant broadening consistent with experimental broadening below and 3.5 eV above the binding energy.

Figure 2 shows a comparison of errors vs experiment for the core binding energies of the ten-electron series molecules. The RT-EOM-CCS method shows small errors even at the simplest non-linear level of approximation (2_{NL}), with a mean-absolute error (MAE) across systems of only 0.5 eV, significantly smaller

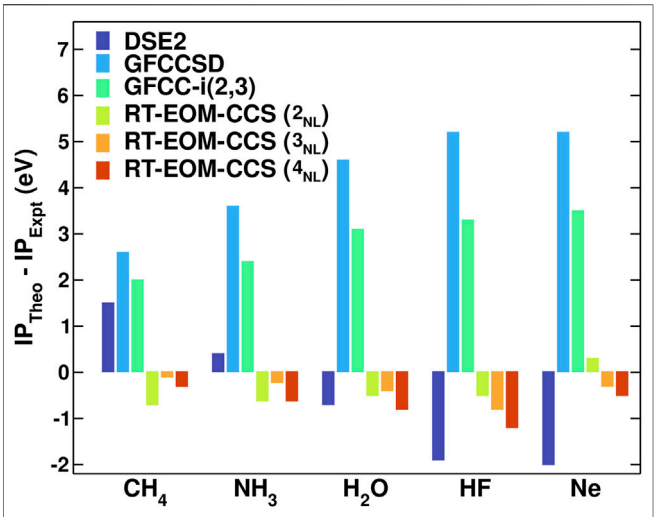

FIGURE 2 | Comparison of the theory errors *vs* experiment (Karlsen et al., 2002; Buttersack et al., 2019; Viñes et al., 2018; Jolly et al., 1984; Williams, 2009) for the core binding energies. The theoretical calculations were performed with the 2-4$_{NL}$ RT-EOM-CCS approximations with the aug-cc-pVDZ basis set. Also shown are results from the second order Dyson equation (DSE2) and the standard GFCCSD and GFCC-i (2, 3) coupled-cluster Green's function methods (Peng and Kowalski, 2016; Peng and Kowalski, 2018a).

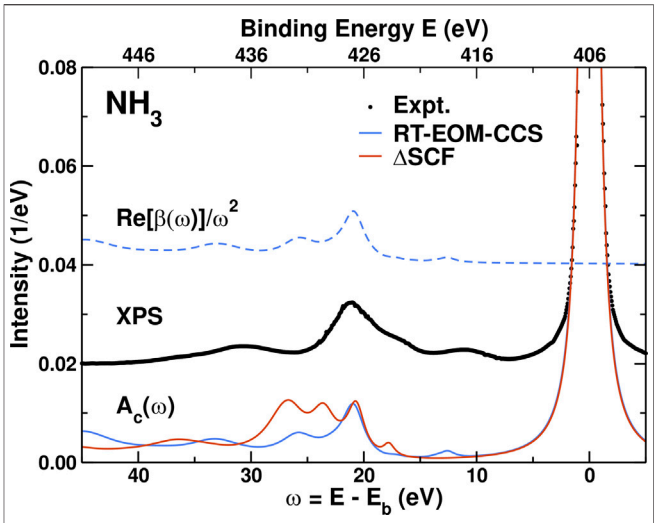

FIGURE 3 | Comparison of the 4$_{NL}$ RT-EOM-CCS and ΔSCF core spectral functions $A_c(\omega)$ (full lines) and cumulant kernel $\beta(\omega)$ (dashed lines, shown only for the RT-EOM-CC method) for the NH_3 molecule, to the experimental XPS (dots) (Sankari et al., 2006). Energies are shows in either absolute binding energy E or versus excitation energy $\omega = E–E_b$ with respect to the experimental core binding energy E_b = 405.52 eV (Sankari et al., 2006). All the theoretical results were obtained with the aug-cc-pVDZ basis set. The theoretical $A_c(\omega)$ were broadened and include a scissors shift of 3.9 eV.

than for the other methods tested. Although better core-optimized basis sets need to be tested to ensure full convergence with basis set size, we find (Vila et al., 2020) similar errors even for smaller basis sets (e.g. DZVP and cc-pVDZ). We emphasize that these accurate results arise from the non-linear terms in v_{ij}^{ab} in the expression of the cumulant (**Eq. 14**), which reduce the error typically by an order of magnitude. Of the ten-electron systems, the Ne atom has the smallest MAE across the methods (0.3 eV), while for the molecules the MAE increases systematically from CH_4 (0.4 eV) to HF (0.8 eV). It should be noted that these results do not include contributions from changes in the vibrational zero point energy (which are expected to be an order of magnitude smaller) or from relativistic effects. The latter can be significant even for these light elements (Keller et al., 2020). For instance, the inclusion of relativistic effects in the calculation of the C, N, O and F atoms increases the 1s core binding energies by 0.1, 0.3, 0.5 and 0.8 eV, respectively (Pueyo Bellafont et al., 2016). If these corrections are applied to our results the MAE are reduced by 50%.

Figure 3 shows results for the spectral function $A_c(\omega)$ and the cumulant kernel $\beta(\omega)$. These are shown vs. binding energy to compare more readily to the experimental XPS. $\beta(\omega)$ is dominated by shake-up excitation peaks about 20–30 eV above the quasiparticle peak that correspond precisely with the inelastic losses in $A_c(\omega)$. The satellites structure is in reasonable agreement with that observed in XPS (Sankari et al., 2006) once scissors corrections are included, despite the fact that our HF-based Hamiltonian overestimates the excitation energies. From the Landau form in **Eq. 4**, the strength of the quasi-particle peak is defined by the renormalization constant Z, where for the 4$_{NL}$ approximation to the EOM-CC cumulant $Z = \exp(-a) = 0.70$. The satellite strength is $a = \int d\omega\, \beta(\omega)/\omega^2 = 0.35$. This matches the numerical integration over the QP peak that yields $Z = 0.70$, in good agreement with the ΔSCF value $Z = 0.76$. The renormalization constant Z is also partly responsible for the amplitude reduction factor S_0^2 for the XAS fine structure (Rehr et al., 1978). We also find that the RT-EOM-CCS values for Z agree with those obtained using the frequency-space CC Green's function methods (Peng and Kowalski, 2016; Peng and Kowalski, 2018a). Moreover, the energy shift Δ from the middle term in **Eq. 5** is the "relaxation energy," that introduces electron-electron correlations corrections to the Koopmans' theorem approximation of the core binding energy. Here we find that $\Delta = \int d\omega\, \beta(\omega)/\omega = 17.1$ eV, with a core binding energy $E_b = |\epsilon_c| - \Delta = 406.1$ eV, in good agreement with the experimental value of 405.52 eV, and the position of the quasiparticle peak in $A_c(\omega)$ at 404.9 eV.

Results for the XAS, including experiment (Wight and Brion, 1974), are shown in **Figure 4**. The overall agreement between theory and experiment is quite good for the positions and relative intensities of the first two peaks. The third peak, at 403.5 eV, is almost in the continuum and is more difficult to describe with our limited basis set. For this molecule, the corrections to the independent particle XAS ($L_0(\epsilon)$) are clearly visible: First, the edge enhancement factor $1 + \chi$ increases the intensity to $L(\epsilon)$. Second, the amplitude reduction factor from the spectral function $A_c(\epsilon)$, which has opposite sign and is approximately twice as strong, reduces the intensity to the final $\mu(\epsilon)$. Since the leading satellites peaks in $A_c(\epsilon)$ are 20–30 eV above the QP peak, the

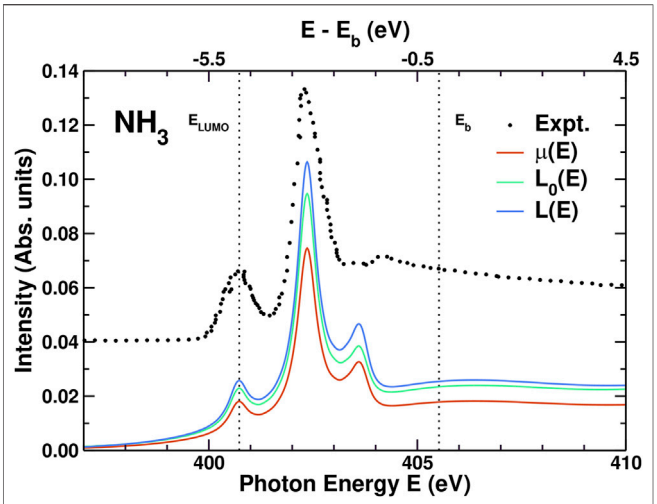

FIGURE 4 | Comparison of the experimental XAS $\mu(E)$ for NH_3 (Wight and Brion, 1974) vs photon energy E to those calculated from the convolution in **Eq. 2**, the effective one-body XAS $L(E) = \mu_1(E)$ and the independent particle XAS $L_0(E) = \mu_0(E)$ from **Eq. 25**. The N x-ray K edge lies just under E_{LUMO} while E_b is the ionization threshold. In order to account for the sparsity of the Gaussian-type orbital basis set in the continuum region above E_b, the comparison to experiment includes variable broadening (see text) that increases to a maximum of 3.5 eV above E_b.

corresponding XAS satellite features fall in the continuum and are thus not visible.

4 CONCLUSIONS

This review describes a combined equation of motion coupled cluster approach in real-time to calculate excitations corresponding to intrinsic losses in XAS and XPS. The approach is based on the cumulant form of the Green's function representation for the core-hole spectral function that arises naturally from the coupled cluster ansatz. This theoretical connection between the cumulant approach, a powerful tool for computing satellites in solid state physics, to the coupled cluster approach which is the gold standard for accuracy in quantum chemistry brings together two previously mostly unrelated fields, thus opening new areas of research. Unlike our previous treatment of the XAS, where an approximate, effective single-particle Hamiltonian was used, here we use the full two-particle one, yet for simplicity we still limit the representation of the reference wavefunctions functions to single-determinants. We show that the cumulant form aids in both the physical interpretation of many-body effects observed in the spectra as well as the numerical simulations. We find that, for the XAS, a convolution form in terms of an effective single-particle spectrum and the core-hole spectral function is key to accounting for two types of many-body effects: First, inelastic losses caused by shake up excitations, accounted for the spectral function. Second the edge enhancement due to orthogonality. Both effects modulate the XAS amplitude in opposite direction near threshold, despite being non-singular for molecular systems. Interference terms and extrinsic losses from the coupling between the core-hole and the photoelectron are ignored. Nevertheless, these effects tend to cancel due to their opposite signs. The formal behavior of the RT-EOM-CC cumulant Green's function is similar to that in other approaches, e.g., field-theoretic methods such as the linked-cluster theorem, or the quasi-boson approximation (Nozieres and de Dominicis, 1969; Langreth, 1970; Hedin, 1999). For condensed matter systems, the cumulant kernel function $\beta(\omega)$ is directly connected to the loss function or the screened Coulomb interaction, and represents collective excitations such as density fluctuations arising from the sudden creation of the core-hole (Langreth, 1970; Kas and Rehr, 2017). Other extensions to the approach reviewed here are feasible. For instance, an analogous treatment is possible to study x-ray emission spectra instead of XAS (Nozieres and Combescot, 1971) by changing the unoccupied single-particle states for the occupied ones. Finally, bigger systems computed with a more user-friendly and efficient implementation, including higher excitations, will be presented elsewhere.

DATA AVAILABILITY STATEMENT

The data that support the findings of this study are available from the corresponding author upon reasonable request.

AUTHOR CONTRIBUTIONS

All authors contributed to the derivation of the theory described in this work and to the writing of the manuscript. FV developed the EOM-CC code and performed all the calculations behind the results presented except for the GFCCSD and GFCC-i(2,3) which were performed by BP.

FUNDING

This work was supported by the Computational Chemical Sciences Program of the U.S. Department of Energy, Office of Science, BES, Chemical Sciences, Geosciences and Biosciences Division in the Center for Scalable and Predictive methods for Excitations and Correlated phenomena (SPEC) at the Pacific Northwest National Laboratory. This research used resources of the National Energy Research Scientific Computing Center (NERSC), a U.S. Department of Energy Office of Science User Facility located at Lawrence Berkeley National Laboratory, operated under Contract No. DE-AC02-05CH11231.

ACKNOWLEDGMENTS

We thank N. Hirshberg, X. Li, J. Lisschner, D. Prendergast, K. Schönhammer, and M. Tzavala, for comments. BP also acknowledges the support of Laboratory Directed Research and Development (LDRD) program from PNNL.

REFERENCES

Arponen, J. (1983). Variational Principles and Linked-Cluster Exp S Expansions for Static and Dynamic many-body Problems. *Ann. Phys.* 151, 311–382. doi:10.1016/0003-4916(83)90284-1

Aryasetiawan, F., Hedin, L., and Karlsson, K. (1996). Multiple Plasmon Satellites in Na and Al Spectral Functions from Ab Initio Cumulant Expansion. *Phys. Rev. Lett.* 77, 2268–2271. doi:10.1103/physrevlett.77.2268

Bartlett, R. J., and Musiał, M. (2007). Coupled-cluster Theory in Quantum Chemistry. *Rev. Mod. Phys.* 79, 291–352. doi:10.1103/revmodphys.79.291

Bertsch, G. F., and Lee, A. J. (2014). Time-dependent Mean-Field Theory for X-ray Near-Edge Spectroscopy. *Phys. Rev. B* 89, 075135. doi:10.1103/physrevb.89.075135

Bhaskaran-Nair, K., Kowalski, K., and Shelton, W. A. (2016). Coupled Cluster Green Function: Model Involving Single and Double Excitations. *J. Chem. Phys.* 144, 144101. doi:10.1063/1.4944960

Brandow, B. H. (1967). Linked-cluster Expansions for the Nuclear many-body Problem. *Rev. Mod. Phys.* 39, 771–828. doi:10.1103/revmodphys.39.771

Buttersack, T., Mason, P. E., McMullen, R. S., Martinek, T., Brezina, K., Hein, D., et al. (2019). Valence and Core-Level X-ray Photoelectron Spectroscopy of a Liquid Ammonia Microjet. *J. Am. Chem. Soc.* 141, 1838–1841. doi:10.1021/jacs.8b10942

Čížek, J. (1966). On the Correlation Problem in Atomic and Molecular Systems. Calculation of Wavefunction Components in Ursell-type Expansion Using Quantum-Field Theoretical Methods. *J. Chem. Phys.* 45, 4256–4266.

Coester, F. (1958). Bound States of a many-particle System. *Nucl. Phys.* 7, 421–424. doi:10.1016/0029-5582(58)90280-3

Coester, F., and Kümmel, H. (1960). Short-range Correlations in Nuclear Wave Functions. *Nucl. Phys.* 17, 477–485. doi:10.1016/0029-5582(60)90140-1

Crawford, T. D., and Schaefer, H. F. (2000). An Introduction to Coupled Cluster Theory for Computational Chemists. *Rev. Comp. Ch.* 14, 33–136.

Friedel, J. (1969). X-ray Absorption and Emission Edges in Metals. *Comments Solid State. Phys.* 2, 21.

Grebennikov, V., Babanov, Y., and Sokolov, O. (1977). Extra-atomic Relaxation and X-ray Spectra of Narrow-Band Metals. I. Formalism. *Phys. Stat. Sol. (B)* 79, 423. doi:10.1002/pssb.2220790204

Gunnarsson, O., Meden, V., and Schönhammer, K. (1994). Corrections to Migdal's Theorem for Spectral Functions: A Cumulant Treatment of the Time-dependent Green's Function. *Phys. Rev. B* 50, 10462–10473. doi:10.1103/physrevb.50.10462

Guzzo, M., Lani, G., Sottile, F., Romaniello, P., Gatti, M., Kas, J. J., et al. (2011). Valence Electron Photoemission Spectrum of Semiconductors: Ab Initio Description of Multiple Satellites. *Phys. Rev. Lett.* 107, 166401. doi:10.1103/physrevlett.107.166401

Hedin, L. (1999). On Correlation Effects in Electron Spectroscopies and the GW Approximation. *J. Phys. Condens. Matter* 11, R489. doi:10.1088/0953-8984/11/42/201

Jolly, W., Bomben, K., and Eyermann, C. (1984). Core-electron Binding Energies for Gaseous Atoms and Molecules. *Atom. Data Nucl. Data* 31, 433–493. doi:10.1016/0092-640x(84)90011-1

Karlsen, T., Børve, K. J., Sæthre, L. J., Wiesner, K., Bässler, M., and Svensson, S. (2002). Toward the Spectrum of Free Polyethylene: Linear Alkanes Studied by Carbon 1s Photoelectron Spectroscopy and Theory. *J. Am. Chem. Soc.* 124, 7866–7873. doi:10.1021/ja010649j

Kas, J. J., and Rehr, J. J. (2017). Finite Temperature Green's Function Approach for Excited State and Thermodynamic Properties of Cool to Warm Dense Matter. *Phys. Rev. Lett.* 119, 176403. doi:10.1103/physrevlett.119.176403

Keller, L., Blum, V., Rinke, P., and Golze, D. (2020). Relativistic Correction Scheme for Core-Level Binding Energies from GW. *J. Chem. Phys.* 153, 114110. doi:10.1063/5.0018231

Kendall, R. A., Dunning, T. H., and Harrison, R. J. (1992). Electron Affinities of the First-Row Atoms Revisited. Systematic Basis Sets and Wave Functions. *J. Chem. Phys.* 96, 6796–6806. doi:10.1063/1.462569

Kowalski, K., Bhaskaran-Nair, K., and Shelton, W. A. (2014). Coupled-cluster Representation of Green Function Employing Modified Spectral Resolutions of Similarity Transformed Hamiltonians. *J. Chem. Phys.* 141, 094102. doi:10.1063/1.4893527

Landau, L. (1944). On the Energy Loss of Fast Particles by Ionization. *J. Phys. USSR* 8, 201–205.

Lange, M. F., and Berkelbach, T. C. (2018). On the Relation between Equation-Of-Motion Coupled-Cluster Theory and the GW Approximation. *J. Chem. Theor. Comput.* 14, 4224–4236. doi:10.1021/acs.jctc.8b00455

Langreth, D. C. (1969). Singularities in the X-ray Absorption and Emission of Metals. *Phys. Rev.* 182, 973–974. doi:10.1103/physrev.182.973

Langreth, D. C. (1970). Singularities in the X-ray Spectra of Metals. *Phys. Rev. B* 1, 471–477. doi:10.1103/physrevb.1.471

Lee, A. J., Vila, F. D., and Rehr, J. J. (2012). Local Time-Correlation Approach for Calculations of X-ray Spectra. *Phys. Rev. B* 86, 115107. doi:10.1103/physrevb.86.115107

Liang, Y., and Prendergast, D. (2019). *Taming Convergence in the Determinant Approach for X-ray Excitation Spectra*. ArXiv:1905.00542v1.

Liang, Y., Vinson, J., Pemmaraju, S., Drisdell, W. S., Shirley, E. L., and Prendergast, D. (2017). Accurate X-ray Spectral Predictions: An Advanced Self-Consistent-Field Approach Inspired by many-body Perturbation Theory. *Phys. Rev. Lett.* 118, 096402. doi:10.1103/PhysRevLett.118.096402

Linderberg, J., and Öhrn, Y. (2004). *Propagators in Quantum Chemistry*. Wiley. Theoretical chemistry.

Mahan, G. D. (1967). Excitons in Metals: Infinite Hole Mass. *Phys. Rev.* 163, 612. doi:10.1103/physrev.163.612

Meissner, L., and Bartlett, R. J. (1993). Electron Propagator Theory with the Ground State Correlated by the Coupled-Cluster Method. *Int. J. Quan. Chem.* 48, 67–80. doi:10.1002/qua.560480810

Nist (2019). in *NIST Computational Chemistry Comparison and Benchmark Database*. Editor R. D. Johnson III (NIST). vol. Release 20 of NIST Standard Reference Database Number 101. doi:10.18434/T47C7Z

Nooijen, M., and Snijders, J. G. (1992). Coupled Cluster Approach to the Single-Particle Green's Function. *Int. J. Quan. Chem.* 44, 55–83. doi:10.1002/qua.560440808

Nooijen, M., and Snijders, J. G. (1993). Coupled Cluster Green's Function Method: Working Equations and Applications. *Int. J. Quan. Chem.* 48, 15–48. doi:10.1002/qua.560480103

Nooijen, M., and Snijders, J. G. (1995). Second Order many-body Perturbation Approximations to the Coupled Cluster Green's Function. *J. Chem. Phys.* 102, 1681–1688. doi:10.1063/1.468900

Nozieres, P., and Combescot, M. (1971). Infrared Catastrophy and Excitons in the X-ray Spectra of Metals. *J. de Physique* 32, 11.

Nozieres, P., and de Dominicis, C. (1969). Singularities in the X-ray Absorption and Emission of Metals. III. One-Body Theory Exact Solution. *Phys. Rev.* 178, 1097. doi:10.1103/physrev.178.1097

Paldus, J., Čížek, J., and Shavitt, I. (1972). Correlation Problems in Atomic and Molecular Systems. IV. Extended Coupled-Pair many-electron Theory and its Application to the BH_3 Molecule. *Phys. Rev. A.* 5, 50–67. doi:10.1103/physreva.5.50

Paldus, J., and Li, X. (1999). A Critical Assessment of Coupled Cluster Method in Quantum Chemistry. *Adv. Chem. Phys.* 110, 1–175.

Peng, B., and Kowalski, K. (2016). Coupled-cluster Green's Function: Analysis of Properties Originating in the Exponential Parametrization of the Ground-State Wave Function. *Phys. Rev. A.* 94, 062512. doi:10.1103/physreva.94.062512

Peng, B., and Kowalski, K. (2018b). Green's Function Coupled Cluster Formulations Utilizing Extended Inner Excitations. *J. Chem. Phys.* 149, 214102. doi:10.1063/1.5046529

Peng, B., and Kowalski, K. (2018a). Green's Function Coupled-Cluster Approach: Simulating Photoelectron Spectra for Realistic Molecular Systems. *J. Chem. Theor. Comput.* 14, 4335–4352. doi:10.1021/acs.jctc.8b00313

Peng, B., Panyala, A., Kowalski, K., and Krishnamoorthy, S. (2021). GFCCLib: Scalable and Efficient Coupled-Cluster Green's Function Library for Accurately Tackling many-body Electronic Structure Problems. *Computphys. Commun.* 265, 108000. doi:10.1016/j.cpc.2021.108000

Peng, B., Van Beeumen, R., Williams-Young, D. B., Kowalski, K., and Yang, C. (2019). Approximate Green's Function Coupled Cluster Method Employing Effective Dimension Reduction. *J. Chem. Theor. Comput.* 15, 3185–3196. doi:10.1021/acs.jctc.9b00172

Privalov, T., Gel'mukhanov, F., and Ågren, H. (2001). Role of Relaxation and Time-dependent Formation of X-ray Spectra. *Phys. Rev. B* 64, 165115. doi:10.1103/physrevb.64.165115

Pueyo Bellafont, N., Viñes, F., and Illas, F. (2016). Performance of the Tpss Functional on Predicting Core Level Binding Energies of Main Group Elements Containing Molecules: A Good Choice for Molecules Adsorbed on Metal Surfaces. *J. Chem. Theor. Comput.* 12, 324–331. doi:10.1021/acs.jctc.5b00998

Purvis, G., and Bartlett, R. (1982). A Full Coupled-Cluster Singles and Doubles Model: The Inclusion of Disconnected Triples. *J. Chem. Phys.* 76, 1910–1918. doi:10.1063/1.443164

Rehr, J. J., Kas, J. J., Prange, M. P., Sorini, A. P., Takimoto, Y., and Vila, F. (2009). Ab Initio theory and Calculations of X-ray Spectra. *CR Phys.* 10, 548–559. doi:10.1016/j.crhy.2008.08.004

Rehr, J. J., Stern, E. A., Martin, R. L., and Davidson, E. R. (1978). Extended x-ray-absorption fine-structure Amplitudes—Wave-Function Relaxation and Chemical Effects. *Phys. Rev. B* 17, 560–565. doi:10.1103/physrevb.17.560

Rehr, J. J., Vila, F. D., Kas, J. J., Hirshberg, N., Kowalski, K., and Peng, B. (2020). Equation of Motion Coupled-Cluster Cumulant Approach for Intrinsic Losses in X-ray Spectra. *J. Chem. Phys.* 152, 174113. doi:10.1063/5.0004865

Sankari, R., Ehara, M., Nakatsuji, H., Fanis, A. D., Aksela, H., Sorensen, S., et al. (2006). High Resolution O 1s Photoelectron Shake-Up Satellite Spectrum of H_2O. *Chem. Phys. Lett.* 422, 51–57. doi:10.1016/j.cplett.2006.02.018

Schönhammer, K., and Gunnarsson, O. (1978). Time-dependent Approach to the Calculation of Spectral Functions. *Phys. Rev. B* 18, 6606–6614. doi:10.1103/physrevb.18.6606

Stanton, J. F., and Bartlett, R. J. (1993). The Equation of Motion Coupled-Cluster Method. A Systematic Biorthogonal Approach to Molecular Excitation Energies, Transition Probabilities, and Excited State Properties. *J. Chem. Phys.* 98, 7029–7039. doi:10.1063/1.464746

Szabo, A., and Ostlund, N. (1996). *Modern Quantum Chemistry: Introduction to Advanced Electronic Structure Theory*. Dover Publications). Dover Books on Chemistry.

Thouless, D. (1961). *The Quantum Mechanics of Many-Body Systems*. (New York: Academic).

Tzavala, M., Kas, J. J., Reining, L., and Rehr, J. J. (2020). Nonlinear Response in the Cumulant Expansion for Core-Level Photoemission. *Phys. Rev. Res.* 2, 033147. doi:10.1103/PhysRevResearch.2.033147

Vila, F. D., Rehr, J. J., Kas, J. J., Kowalski, K., and Peng, B. (2020). Real-time Coupled-Cluster Approach for the Cumulant Green's Function. *J. Chem. Theor. Comput.* 16, 6983–6992. doi:10.1021/acs.jctc.0c00639

Viñes, F., Sousa, C., and Illas, F. (2018). On the Prediction of Core Level Binding Energies in Molecules, Surfaces and Solids. *Phys. Chem. Chem. Phys.* 20, 8403–8410. doi:10.1039/c7cp08503f

von Barth, U., and Grossmann, G. (1982). Dynamical Effects in X-ray Spectra and the Final-State Rule. *Phys. Rev. B* 25, 5150–5179. doi:10.1103/physrevb.25.5150

Wight, G., and Brion, C. (1974). K-shell Excitation of CH_4, NH_3, H_2O, CH_3OH, CH_3OCH_3 and CH_3NH_2 by 2.5 keV Electron Impact. *J. Electron. Spectrosc. Relat. Phenom.* 4, 25–42. doi:10.1016/0368-2048(74)80040-x

Williams, G. P. (2009). *X-Ray Data Booklet: Section 1.1 ELECTRON BINDING ENERGIES*. Berkeley): Lawrence Berkeley National Laboratory.

Zhou, J., Kas, J., Sponza, L., Reshetnyak, I., Guzzo, M., Giorgetti, C., et al. (2015). Dynamical Effects in Electron Spectroscopy. *J. Chem. Phys.* 143, 184109. doi:10.1063/1.4934965

Conflict of Interest: The authors declare that the research was conducted in the absence of any commercial or financial relationships that could be construed as a potential conflict of interest.

Publisher's Note: All claims expressed in this article are solely those of the authors and do not necessarily represent those of their affiliated organizations, or those of the publisher, the editors and the reviewers. Any product that may be evaluated in this article, or claim that may be made by its manufacturer, is not guaranteed or endorsed by the publisher.

frontiers in Chemistry

ORIGINAL RESEARCH
published: 28 September 2021
doi: 10.3389/fchem.2021.747972

Accurate Prediction of Band Structure of FeS_2: A Hard Quest of Advanced First-Principles Approaches

*Min-Ye Zhang and Hong Jiang**

Beijing National Laboratory for Molecular Sciences, College of Chemistry and Molecular Engineering, Peking University, Beijing, China

The pyrite and marcasite polymorphs of FeS_2 have attracted considerable interests for their potential applications in optoelectronic devices because of their appropriate electronic and optical properties. Controversies regarding their fundamental band gaps remain in both experimental and theoretical materials research of FeS_2. In this work, we present a systematic theoretical investigation into the electronic band structures of the two polymorphs by using many-body perturbation theory with the *GW* approximation implemented in the full-potential linearized augmented plane waves (FP-LAPW) framework. By comparing the quasi-particle (QP) band structures computed with the conventional LAPW basis and the one extended by high-energy local orbitals (HLOs), denoted as LAPW + HLOs, we find that one-shot or partially self-consistent *GW* (G_0W_0 and GW_0, respectively) on top of the Perdew-Burke-Ernzerhof (PBE) generalized gradient approximation with a converged LAPW + HLOs basis is able to remedy the artifact reported in the previous *GW* calculations, and leads to overall good agreement with experiment for the fundamental band gaps of the two polymorphs. Density of states calculated from G_0W_0@PBE with the converged LAPW + HLOs basis agrees well with the energy distribution curves from photo-electron spectroscopy for pyrite. We have also investigated the performances of several hybrid functionals, which were previously shown to be able to predict band gaps of many insulating systems with accuracy close or comparable to *GW*. It is shown that the hybrid functionals considered in general fail badly to describe the band structures of FeS_2 polymorphs. This work indicates that accurate prediction of electronic band structure of FeS_2 poses a stringent test on state-of-the-art first-principles approaches, and the G_0W_0 method based on semi-local approximation performs well for this difficult system if it is practiced with well-converged numerical accuracy.

Keywords: iron disulfide, band structure, GW approximation, self-energy, linearized augmented plane waves, hybrid functionals

OPEN ACCESS

Edited by:
Patrick Rinke,
Aalto University, Finland

Reviewed by:
Walter Lambrecht,
Case Western Reserve University, United States
Takao Kotani,
Tottori University, Japan

****Correspondence:***
Hong Jiang
jianghchem@pku.edu.cn

Specialty section:
This article was submitted to Theoretical and Computational Chemistry, a section of the journal Frontiers in Chemistry

Received: *27 July 2021*
Accepted: *14 September 2021*
Published: *28 September 2021*

Citation:
Zhang M-Y and Jiang H (2021) Accurate Prediction of Band Structure of FeS_2: A Hard Quest of Advanced First-Principles Approaches. Front. Chem. 9:747972. doi: 10.3389/fchem.2021.747972

1 INTRODUCTION

Iron disulfide FeS_2 was studied extensively in the last century in the desire of understanding the structural and electronic properties of transition metal dichalcogenides (TMDC) featuring localized or band-like *d* electrons (Hulliger and Mooser, 1965a; Hulliger and Mooser, 1965b; Goodenough, 1972; Wilson, 1972; Li et al., 1974; Schlegel and Wachter, 1976; Folkerts et al., 1987). Since 1980s

(Chatzitheodorou et al., 1986; Ennaoui et al., 1986), increasing practical interest has been drawn to pyrite FeS_2 for its potential as a cheap and competitive candidate material for efficient solar energy conversion (Wadia et al., 2009) because of its natural abundance, non-toxicity, suitable optical gap and extraordinarily large absorption coefficient (Ferrer et al., 1990; Ennaoui et al., 1993). This has led to new solutions under various optoelectronic scenarios, including photovoltaics (Khalid et al., 2018), photo-catalysis (Tian et al., 2015; Barawi et al., 2016), solid-state photo-capacitors (Gong et al., 2013a) and photo-detectors (Wang et al., 2012; Gong et al., 2013b). However, practical application of FeS_2-based optoelectronic devices is seriously hampered by its unexpected low efficiency due to a loss of open-circuit voltage V_{OC} (Cabán-Acevedo et al., 2014). A number of factors possibly responsible for the low V_{OC} have been suggested and examined, including the intrinsic and defect surface states (Bronold et al., 1994; Sun et al., 2011; Herbert et al., 2013; Lazić et al., 2013; Cabán-Acevedo et al., 2014; Limpinsel et al., 2014; Walter et al., 2017), bulk sulfur deficiency (Birkholz et al., 1991; Cabán-Acevedo et al., 2014; Shukla et al., 2016) and presence of the metastable marcasite phase as a small-gap impurity (Spagnoli et al., 2010; Sun et al., 2011; Schena et al., 2013).

Despite progress towards understanding the origin of the low V_{OC} in pyrite FeS_2 (Rahman et al., 2020), consensus is still not reached on the fundamental band gaps of the two FeS_2 phases. Experimentally, values varying from 0.6 to 2.6 eV have been reported for pyrite, primarily due to differences in sample preparation, measuring technique, and analytical model of spectra used in experimental studies (Ferrer et al., 1990; Ennaoui et al., 1993). Measurements of the pyrite band gap are generally carried out through optical absorption spectroscopy (Schlegel and Wachter, 1976; Kou and Seehra, 1978; Ennaoui et al., 1993), which features the neutral excitation (exciton) instead of the charged one as in the photo-electron spectroscopy (PES). Therefore, the measured excitation energies are in fact coupled to the electron-hole binding. Careful investigation by absorption spectroscopy for the marcasite phase is done only recently and gives an optical gap similar to pyrite, which essentially precludes the possibility of marcasite being the culprit for the low V_{OC} of FeS_2 photovoltaics (Sánchez et al., 2016; Wu et al., 2016). Furthermore, even though PES measurements of pyrite FeS_2 have been conducted (Ohsawa et al., 1974; van der Heide et al., 1980; Folkerts et al., 1987; Mamiya et al., 1997; Ollonqvist et al., 1997; Nesbitt et al., 2003), combined studies of direct and inverse PES (IPS) for regions near the Fermi level are rare. Reported relevant works (Folkerts et al., 1987; Mamiya et al., 1997) were done more than 20 years ago and the spectra were not resolved enough to identify a well-defined fundamental band gap.

Difficulties in characterizing band structures of FeS_2 polymorphs are also encountered from the perspective of first-principles calculations. Within the framework of density functional theory (DFT) (Hohenberg and Kohn, 1964), calculations with Perdew-Burke-Ernzerhof (PBE) generalized gradient approximation (GGA) (Perdew et al., 1996a) predict pyrite to have a band gap of about 0.3 eV smaller than the experimental value of 0.95 eV as generally accepted (Ennaoui et al., 1993; Schena et al., 2013; Kolb and Kolpak, 2013; Li et al., 2015). Considering the well-known band gap problem of local density approximation (LDA) or GGA (Perdew et al., 1982), orbital-dependent functionals in spirit of generalized Kohn-Sham (GKS) DFT (Seidl et al., 1996; Perdew et al., 2017; Zhang et al., 2020) are also employed to tackle the problem, e.g. PBE plus the Hubbard-U correction (DFT + U) and hybrid functionals (Becke, 1993a; Becke, 1993b; Perdew et al., 1996b). Using an *ad hoc* U of 2 eV, the PBE + U method is able to reproduce the experimental band gap (Sun et al., 2011; Hu et al., 2012; Li et al., 2018) but meanwhile deteriorates the simulated optical spectra compared to PBE (Choi et al., 2012; Schena et al., 2013). Furthermore, despite the good performance in predicting band gaps for typical semiconducting materials (Heyd et al., 2005; Paier et al., 2006b,a; Marsman et al., 2008), hybrid functionals such as Heyd-Scuseria-Ernzerhof (HSE) method (Heyd et al., 2003, 2006) have been shown to give large band gaps for pyrite of over 2 eV (Muscat et al., 2002; Sun et al., 2011; Choi et al., 2012; Hu et al., 2012; Schena et al., 2013; Liu et al., 2019). There are also works using beyond-DFT methods, particularly, the *GW* method based on many-body perturbation theory (MBPT) (Hedin, 1965). However, the *GW* results for the pyrite phase are rather scattered, ranging from 0.3 to 1.1 eV (Choi et al., 2012; Lehner et al., 2012; Kolb and Kolpak, 2013; Schena et al., 2013). It is worth noting that Schena and coworkers conducted the state-of-the-art all-electron G_0W_0 calculations with the linearized augmented plane-wave (LAPW) basis for both pyrite and marcasite, and report a pyrite band gap only about 0.3 eV (Schena et al., 2013). The *GW* gap value is smaller than that from PBE, which is rarely observed in *GW* practices and hence deserves closer investigation.

For *GW* implementations involving explicit summation of states, it is established recently by a number of works (Friedrich et al., 2006; Friedrich et al., 2011a; Friedrich et al., 2011b; Klimes et al., 2014; Jiang and Blaha, 2016; Nabok et al., 2016; Jiang, 2018; Zhang and Jiang, 2019; Ren et al., 2021) that an accurate description of high-lying empty states is essential to give accurate correlation self-energy operator and consequent QP band structure. In the pseudo-potential framework, one can improve the accuracy by using a norm-conserving potential with specifically tailored projectors at high energies (Klimes et al., 2014; van Setten et al., 2018). In all-electron calculations with the LAPW basis set, local orbitals with large energy parameters (usually $10^{1\sim2}$ Ry higher than the Fermi level) are introduced as additional basis functions to remove the linearization error in unoccupied states up high in the conduction band regime (Friedrich et al., 2006, 2011a,b; Jiang and Blaha, 2016; Nabok et al., 2016). The LAPW basis extended by these high-energy local orbitals (HLOs), termed as LAPW + HLOs, has succeeded in helping produce accurate QP band structures in good agreement with experiment for a variety of semiconductors (Jiang and Blaha, 2016) including the conventionally challenging systems such as ZnO (Friedrich et al., 2011a; Friedrich et al., 2011b; Stankovski et al., 2011; Jiang and Blaha, 2016; Nabok et al., 2016), *d*/*f*-electron oxides (Jiang, 2018) and cuprous and silver halides (Zhang and Jiang, 2019). Particularly, the effects of including HLOs on the QP correction have been demonstrated quantitatively to be larger for

states with stronger metal-*d* characters (Zhang and Jiang, 2019). For the FeS_2 polymorphs with states of significant Fe-3*d* characters in both valence and low-energy conduction band regimes, *GW* with LAPW + HLOs is likely to give better description of the QP energies and dispersion relation than that with the standard LAPW basis.

A competitive alternative in the DFT framework to *GW* for band structure prediction is the doubly screened hybrid (DSH) functional method (Cui et al., 2018) in the category of hybrid functionals with system-dependent parameters (Zhang et al., 2020). Derived from a model dielectric function (Cappellini et al., 1993; Shimazaki and Yoshihiro, 2008), the exchange-correlation potential in DSH can be regarded as a further approximation to the Coulomb hole and screened exchange (COHSEX) approximation to the *GW* self-energy, and is able to capture both dielectric and metallic screening in the exchange interaction (Cui et al., 2018). It is shown that the DSH can evaluate band gaps of typical *sp* semiconductors with accuracy comparable to *GW* with the LAPW + HLOs basis while only at modest computational cost (Cui et al., 2018). Furthermore, the one-shot variant DSH0 can outperform fixed-parameter hybrid functionals for band gap predictions in a wide range of materials including narrow-gap semiconductors and transition metal mono-oxides (Cui et al., 2018; Liu et al., 2020). Hence we consider DSH as a hopeful approach to solve the FeS_2 band gap puzzle within the GKS framework of DFT.

In the present work, we investigate the electronic band structures of the pyrite and marcasite polymorphs of FeS_2 by applying the state-of-the-art all-electron *GW* method with the LAPW + HLOs basis. For comparison, we examine the results from *GW* with the standard LAPW basis as well. We also investigate the performances of several hybrid functionals, including PBE0 (Perdew et al., 1996b), HSE06 (Heyd et al., 2003, Heyd et al., 2006), screened-exchange-PBE hybrid functional (SX-PBE) (Bylander and Kleinman, 1990; Seidl et al., 1996) and DSH (Cui et al., 2018), in attempt to obtain insights into the failure of the conventional fixed-parameter functionals in predicting the band gap of FeS_2.

2 THEORY AND METHODS

2.1 The *GW* Method

The central task of the *GW* method is to solve the quasi-particle (QP) equation with the self-energy operator Σ in the frequency domain expressed as (Hedin, 1965)

$$\Sigma(\mathbf{r},\mathbf{r}';\omega)=\frac{\mathrm{i}}{2\pi}\int_{-\infty}^{\infty}d\omega'\mathrm{e}^{\mathrm{i}\omega'\delta}G(\mathbf{r},\mathbf{r}';\omega+\omega')W(\mathbf{r}',\mathbf{r};\omega') \tag{1}$$

where *G* is the time-ordered Green's function

$$G(\mathbf{r},\mathbf{r}';\omega)=\sum_{n\mathbf{k}}\frac{\psi_{n\mathbf{k}}(\mathbf{r})\psi^{*}_{n\mathbf{k}}(\mathbf{r}')}{\omega-\varepsilon_{n\mathbf{k}}+\mathrm{i}\eta\mathrm{sgn}(\varepsilon_{n\mathbf{k}}-\mu)} \tag{2}$$

With $\psi_{n\mathbf{k}}$ and $\varepsilon_{n\mathbf{k}}$ being the wave function and energy of the single-particle state $|n\mathbf{k}\rangle$ respectively, μ the chemical potential, and δ and η positive infinitesimals. Atomic units are used throughout the paper. The screened Coulomb interaction *W* writes

$$W(\mathbf{r},\mathbf{r}';\omega)=\int d\mathbf{r}''\varepsilon^{-1}(\mathbf{r},\mathbf{r}'';\omega)v(\mathbf{r}'',\mathbf{r}') \tag{3}$$

where $v(\mathbf{r},\mathbf{r}')=1/|\mathbf{r}-\mathbf{r}'|$ is the bare Coulomb interaction and $\varepsilon(\mathbf{r},\mathbf{r}';\omega)$ is the microscopic dielectric function calculated at the level of random phase approximation (RPA). In principle, **Eqs 1–3** have to be solved self-consistently along with the Dyson equation for the Green's function (Hedin, 1965). However, due to the computational cost and generally unsatisfactory results of the fully self-consistent *GW* for solids [e.g. Grumet et al. (2018)], one usually turns to the non-self-consistent variant G_0W_0. Considering the resemblance of KS and QP wave functions in weakly correlated systems (Hybertsen and Louie, 1986), the self-energy or QP energy $\varepsilon^{\mathrm{QP}}_{n\mathbf{k}}$ can be computed perturbatively upon the acquisition of Σ from the KS states as

$$\varepsilon^{\mathrm{QP}}_{n\mathbf{k}}=\varepsilon^{\mathrm{KS}}_{n\mathbf{k}}+Z_{n\mathbf{k}}\langle n\mathbf{k}|\hat{\Sigma}(\varepsilon^{\mathrm{KS}}_{n\mathbf{k}})-\hat{V}_{\mathrm{xc}}\big|n\mathbf{k}\rangle \tag{4}$$

where V_{xc} is the KS exchange-correlation potential and $Z_{n\mathbf{k}}$ a renormalization factor. One can further perform the so-called energy-only self-consistent GW_0 calculations, where QP energies $\varepsilon^{\mathrm{QP}}_{n\mathbf{k}}$ in place of $\varepsilon^{\mathrm{KS}}_{n\mathbf{k}}$ in **Eq. 2** are updated iteratively while *W* is kept the same as in G_0W_0 (Shishkin and Kresse, 2007). The *GW* method has been implemented in various numerical frameworks (Jiang, 2011; Golze et al., 2019). For a detailed explanation of the basic theory and computational techniques used in the present *GW* implementation, the readers can refer to Jiang et al. (2013).

2.2 All-Electron Calculations With HLOs-Extended LAPW Basis

In the all-electron framework with LAPW, KS wave functions are expanded by the LAPW basis (Andersen, 1975; Singh and Nordström, 2006; Blaha et al., 2020)

$$\varphi^{\mathrm{LAPW}}_{\mathbf{k}+\mathbf{G}}(\mathbf{r})=\begin{cases}\dfrac{1}{\sqrt{V}}\mathrm{e}^{\mathrm{i}(\mathbf{k}+\mathbf{G})\cdot\mathbf{r}} & \mathbf{r}\notin V_\alpha\\ \sum\limits_{lm}\left[A^{\mathbf{k}+\mathbf{G}}_{\alpha lm}u_{\alpha l}(r^\alpha;E_{\alpha l})+B^{\mathbf{k}+\mathbf{G}}_{\alpha lm}\dot{u}_{\alpha l}(r^\alpha;E_{\alpha l})\right]Y^m_l(\hat{\mathbf{r}}^\alpha) & \mathbf{r}\in V_\alpha\end{cases} \tag{5}$$

where V_α is the region enclosed by the muffin-tin (MT) sphere of atom α centered at $\mathbf{r}_\alpha$ with radius R^α_{MT}, $\mathbf{r}^\alpha=\mathbf{r}-\mathbf{r}_\alpha$, $u_{\alpha l}(E_{\alpha l})$ is the solution of radial KS equation inside V_α at chosen energy $E_{\alpha l}$, $\dot{u}_{\alpha l}(E_{\alpha l})\equiv\partial u_{\alpha l}(E)/\partial E|_{E=E_{\alpha l}}$, and Y^m_l is the spherical harmonic function. The coefficients $A^{\mathbf{k}+\mathbf{G}}_{\alpha lm}$ and $B^{\mathbf{k}+\mathbf{G}}_{\alpha lm}$ are determined by enforcing that $\varphi^{\mathrm{LAPW}}_{\mathbf{k}+\mathbf{G}}(\mathbf{r})$ be smooth at the boundary of V_α. Local orbitals (LOs) which vanish outside the atomic spheres are proposed to supplement the LAPW basis to better describe the semi-core states (Singh, 1991). Inside the atomic sphere V_α, LOs take the following form

$$\varphi^{\mathrm{LO},i}_{alm}(\mathbf{r})=\left[A^{\mathrm{LO},i}_{alm}u_{al}(r^\alpha;E_{al})+B^{\mathrm{LO},i}_{alm}\dot{u}_{al}(r^\alpha;E_{al})+C^{\mathrm{LO},i}_{alm}u_{al}(r^\alpha;E^{\mathrm{LO},i}_{al})\right]Y^m_l(\hat{\mathbf{r}}^\alpha) \tag{6}$$

where $E_{\alpha l}^{\mathrm{LO},i}$ is the energy parameter for the ith LO centered on atom α with angular and azimuthal quantum numbers l and m, respectively.

HLOs fall into the category of LOs with $E_{\alpha l}^{\mathrm{LO}}$ typically 10 ~ 100 Ry above the Fermi level. Such extra LOs have been found to facilitate accurate description of unoccupied states by remedying the linearization error therein when using the LAPW basis (Krasovskii et al., 1994; Krasovskii, 1997; Friedrich et al., 2006; Michalicek et al., 2013). In ground state calculations with LDA/GGA or hybrid functionals, the error causes no essential difficulties, since only occupied and low-lying unoccupied states are involved which are usually handled in sufficient accuracy with the usual or standard LAPW basis generated as default in popular DFT implementations with LAPW basis (Blaha et al., 2020). However, the error can be detrimental to the numerical accuracy of methods where the summation over unoccupied states is required, e.g. *GW* and DFT methods with density approximations belonging to the fifth rung of Jacobi ladder (Perdew and Schmidt, 2001) such as the adiabatic-connection dissipation-fluctuation (ACFD) calculation under RPA for ground-state energy (Ren et al., 2012; Cui et al., 2016; Zhang et al., 2018). In these methods, the completeness of summation and quality of unoccupied states play a crucial role. Previous *GW* studies (Jiang and Blaha, 2016; Jiang, 2018; Zhang and Jiang, 2019; Shen et al., 2020) have suggested that both can be taken into account by including localized orbitals energetically higher than the Fermi level in addition to the standard LAPW basis. HLOs have been shown to effectively improve the optical properties (Krasovskii et al., 1994; Krasovskii, 1997), NMR chemical shifts (Laskowski and Blaha, 2012; Laskowski and Blaha, 2014), *GW* QP energies (Friedrich et al., 2006; Friedrich et al., 2011a; Jiang and Blaha, 2016; Nabok et al., 2016; Jiang, 2018; Zhang and Jiang, 2019), optimized effective potential (Betzinger et al., 2011, 2012) and RPA correlation energy (Betzinger et al., 2015).

In the current implementation, HLOs are generated systematically by following the way described by Laskowski and Blaha (2012). The quality of LAPW + HLOs is controlled by two parameters besides those for the LAPW basis, namely, the additional number of nodes in the radial function of highest energy local orbital with respect to that of the LAPW function with the same angular quantum number and the maximum angular quantum number of used HLOs, denoted as n_{LO} and $l_{\mathrm{max}}^{(\mathrm{LO})}$, respectively. Generally speaking, the larger n_{LO} and $l_{\mathrm{max}}^{(\mathrm{LO})}$ are, the higher the HLOs can reach in the energy space. We use $n_{\mathrm{LO}} = 0$ to denote the usual or standard LAPW basis. Since the convergence rate of the QP energy with respect to the two parameters can be different for states featuring distinct atomic characters, careful convergence check is required to obtain numerically accurate *GW* results.

2.3 Hybrid Functionals

Hybrid functionals have been widely used in first-principles simulations of condensed matter for their good balance between performance and computational cost, and have been actively developed to further exploit the potential of its particular functional form. Readers interested in detailed description on the current status of hybrid functional development are directed to several recent reviews (Kümmel and Kronik, 2008; Baer et al., 2010; Maier et al., 2019; Zhang et al., 2020). Here we briefly introduce the general formalism of the range-separated hybrid functionals and the variants relevant to the current study.

The essential ingredient in hybrid functional methods is the exchange-correlation energy E_{xc} or potential V_{xc} composed of non-local orbital-dependent (screened) Hartree-Fock (HF) exchange terms. In the present work, we focus on hybrid functionals with V_{xc} in the range-separated form as (Zhang et al., 2020)

$$\begin{aligned} V_{\mathrm{xc}}(\mathbf{x},\mathbf{x}') = {} & \alpha_{\mathrm{sr}}\left[V_{\mathrm{x}}^{\mathrm{HF,sr}}(\mathbf{x},\mathbf{x}';\mu) - V_{\mathrm{x}}^{\mathrm{SL,sr}}(\mathbf{x};\mu)\delta(\mathbf{x}-\mathbf{x}')\right] \\ & +\alpha_{\mathrm{lr}}\left[V_{\mathrm{x}}^{\mathrm{HF,lr}}(\mathbf{x},\mathbf{x}';\mu) - V_{\mathrm{x}}^{\mathrm{SL,lr}}(\mathbf{x};\mu)\delta(\mathbf{x}-\mathbf{x}')\right] \\ & +V_{\mathrm{xc}}^{\mathrm{SL}}(\mathbf{x})\delta(\mathbf{x}-\mathbf{x}') \end{aligned} \quad (7)$$

where $V_{\mathrm{x}}^{\mathrm{HF,sr}}$ and $V_{\mathrm{x}}^{\mathrm{HF,lr}}$ are the short- and long-ranged Fock exchange potentials, respectively, which, using the reduced density-matrix defined as $\rho(\mathbf{x},\mathbf{x}') \equiv \sum_{i\in\mathrm{occ}}\psi_i(\mathbf{x})\psi_i^*(\mathbf{x}')$, can be written as

$$\begin{aligned} V_{\mathrm{x}}^{\mathrm{HF,sr}}(\mathbf{x},\mathbf{x}';\mu) &= -\rho(\mathbf{x},\mathbf{x}')v^{\mathrm{sr}}(\mathbf{r},\mathbf{r}';\mu) \\ V_{\mathrm{x}}^{\mathrm{HF,lr}}(\mathbf{x},\mathbf{x}';\mu) &= -\rho(\mathbf{x},\mathbf{x}')\left[v(\mathbf{r},\mathbf{r}') - v^{\mathrm{sr}}(\mathbf{r},\mathbf{r}';\mu)\right]. \end{aligned} \quad (8)$$

In **Eq. 8** $v^{\mathrm{sr}}(\mathbf{r},\mathbf{r}';\mu)$ denotes the short-ranged Coulomb interaction of a certain form characterized by screening parameter μ (Zhang et al., 2020). $\mathbf{x}$ denotes collectively the spatial and spin coordinates of an electron, $\mathbf{x} \equiv (\mathbf{r},\sigma)$. $V_{\mathrm{x}}^{\mathrm{SL,sr}}$ and $V_{\mathrm{x}}^{\mathrm{SL,lr}}$ are the semi-local (SL) counterparts of the exchange potentials in LDA, GGA or meta-GGA. μ and the mixing ratios α_{sr} and α_{lr} are the adjustable parameters of the hybrid functional form.

Conventionally, the parameters are determined by either theoretical analysis or fitting against some dataset of particular properties, and then applied to other systems as fixed. Famous examples of the fixed-parameter hybrid functionals include PBE0 $\alpha_{\mathrm{sr}} = \alpha_{\mathrm{lr}} = 1/4$ (Perdew et al., 1996b) and the HSE series $\alpha_{\mathrm{sr}} = 1/4$, $\alpha_{\mathrm{lr}} = 0$, $\mu = 0.2$–0.3 Å^{-1} (Heyd et al., 2003; Heyd et al., 2006). Recently, hybrid functionals with system-dependent parameters are developed by several groups (Shimazaki and Yoshihiro, 2008; Marques et al., 2011; Kronik et al., 2012; Koller et al., 2013; Skone et al., 2014; Chen et al., 2018; Cui et al., 2018). Among different methods, the doubly screened hybrid (DSH) functional has been demonstrated as a competitive candidate for accurate description of band structures of both wide- and narrow-gap semiconductors (Cui et al., 2018). The underlying idea of DSH is to approximate the screening effect in solids by employing the Bechstedt model dielectric function (Bechstedt et al., 1992)

$$\varepsilon(q) = 1 + \left[(\varepsilon_{\mathrm{M}} - 1)^{-1} + \alpha\left(\frac{q}{q_{\mathrm{TF}}}\right)^2\right] \quad (9)$$

where ε_{M} is the macroscopic dielectric constant, q_{TF} the Thomas-Fermi wave vector and α an empirical parameter chosen for semiconductors (Cappellini et al., 1993). A screened Coulomb interaction can be derived from this model to take both dielectric and metallic screening into account, leading to parameters in **Eq. 7** as

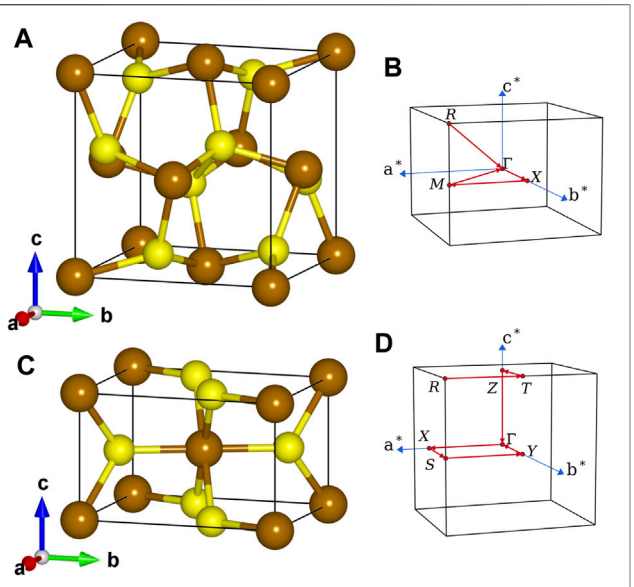

FIGURE 1 | Lattice structures **(A,C)** and first Brillouin zones **(B,D)** of pyrite **(upper)** and marcasite **(lower)** phases of FeS_2. Brown and yellow spheres represent Fe and S atoms, respectively.

$$\alpha_{\rm sr} = 1, \qquad \alpha_{\rm lr} = \frac{1}{\varepsilon_{\rm M}}, \qquad \mu = \frac{2q_{\rm TF}}{3\sqrt{\alpha}}\left(\frac{1}{\varepsilon_{\rm M}-1}+1\right)^{1/2}. \tag{10}$$

The corresponding short-ranged Coulomb interaction in **Eq. 8** is

$$v^{\rm sr}(\mathbf{r},\mathbf{r}';\mu) = \frac{\mathrm{erfc}(\mu|\mathbf{r}-\mathbf{r}'|)}{|\mathbf{r}-\mathbf{r}'|} \tag{11}$$

where erfc is the complementary error function. In practice, an initial $\varepsilon_{\rm M}$ is required, which can be obtained from the PBE calculation or experimental measurements, to construct the DSH potential and solve the GKS equation. The resulting single-particle states act as the inputs to compute a new $\varepsilon_{\rm M}$, which is in turn used to update the DSH potential. The self-consistent loop stops when $\varepsilon_{\rm M}$ is converged. Alternatively, one can break after solving the GKS equation with the initial $\varepsilon_{\rm M}$, leading to the one-shot scheme denoted as DSH0.

2.4 Computational Details

The unit cells of pyrite and marcasite FeS_2 used in our calculations are shown in the left panel of **Figure 1**. The crystal structure of pyrite FeS_2 (**Figure 1A**) can be viewed as a faced-centered cubic cell of Fe atoms with S_2 dumbbells occupying the octahedral interstitials and pointing to different <111> crystallographic axes. The anion coordination octahedra (FeS6) are connected only through sharing vertices. In the orthorhombic marcasite phase (**Figure 1C**), (FeS6) are connected by sharing edges with the two neighbors along *c*-axis and linked together through sharing vertices on the *aOb* plane. In terms of lattice parameters, we use a = 5.418 Å, u = 0.3850 for pyrite (space group $Pa\bar{3}$) and a = 4.443 Å, b = 5.425 Å, c = 3.387 Å, u = 0.2005, v = 0.3783 for marcasite (space group *Pnnm*). These values follow the results from X-ray diffraction experiments at ambient conditions (Brostigen and Kjekshus, 1969; Brostigen et al., 1973; Chattopadhyay and Von Schnering, 1985; Zuñiga-Puelles et al., 2019). The corresponding S-S bond lengths in the two polymorphs are 2.16 and 2.21 Å, respectively.

The present all-electron *GW* calculations are performed by the *GW* facilities in the GAP2 program (Jiang et al., 2013; Jiang and Blaha, 2016) interfaced to WIEN2K (Blaha et al., 2001, 2020). Results in both G_0W_0 and GW_0 schemes are presented, where KS orbital energies and wave functions calculated with the PBE (Perdew et al., 1996a) GGA are used as the input to construct one-body Green's function and screened Coulomb interaction. The KS states are obtained by using charge density pre-converged under self-consistent field (SCF) calculation with PBE and the standard LAPW basis. The energy criterion for convergence of SCF iterations is set to 10^{-8} Rydberg (Ry). 64 (4 × 4 × 4) and 120 (5 × 4 × 6) **k** points are sampled in the first Brillouin zones of pyrite and marcasite FeS_2, respectively. All available unoccupied states are considered in the summation of states for screened Coulomb interaction W and self-energy Σ. Mixed product basis is used to describe the wave function products in the two-point functions, e.g. W and Σ (Aryasetiawan and Gunnarsson, 1994; Kotani and van Schilfgaarde, 2002). We choose Q = 0.75 and $l_{\rm max}^{\rm MB}$ = 3for the interstitial plane wave and MT product basis, respectively [Jiang et al. (2013) for the meanings of these parameters]. LAPW and LOs with $E_{\alpha l}$ < 20 Ry are used to build the MT product basis. Frequency dependence of W is treated explicitly on a 16-point double Gauss-Legendre grids along the positive imaginary axis. Σ on the same grid is calculated and analytically continued to the real axis (Rojas et al., 1995). A rather coarse **k**/**q**-point mesh, 2 × 2 × 2 for pyrite and 4 × 2 × 4 for marcasite, is sufficient to converge the direct band gap at the Γ point $E_{\rm g}^{\Gamma}$ within 0.01 eV. The QP band structure diagrams along particular **k**-point paths (see the right panel of **Figure 1**) are calculated by interpolating the QP energies obtained with the above mesh using the Fourier interpolation technique (Pickett et al., 1988).

In terms of the LAPW basis, the usual or standard LAPW basis set is created automatically in the recent version of WIEN2K (Blaha et al., 2001), which is actually a mixture of the APW + lo basis for the valence states (Madsen et al., 2001), the ordinary LAPW basis for higher l channels up to $l_{\rm max}$ = 10 and additional local orbitals (LOs) for semi-core Fe-3*s* and Fe-3*p* states (Blaha et al., 2001). The convergence with respect to the two HLOs parameters $n_{\rm LO}$ and $l_{\rm max}^{\rm (LO)}$ is investigated, the latter being represented by $\Delta l_{\rm LO} = l_{\rm max}^{\rm (LO)} - l_{\rm max}^{\rm (v)}$ where $l_{\rm max}^{\rm (v)}$ is the largest l of valence orbitals for each element. In the present study, $l_{\rm max}^{\rm (v)} = 2$ and $l_{\rm max}^{\rm (v)} = 1$ for Fe and S, respectively. Since the convergence with respect to HLOs parameters are decoupled from the choice of **k**-point mesh, we choose marcasite with a coarse 2 × 1 × 2 mesh for HLOs convergence test. $RKmax \equiv R_{\rm MT,min}K_{\rm max} = 7.0$ is chosen for the plane-wave cut-off in the interstitial region, where $R_{\rm MT,min}$ is the minimal muffin-tin radius $R_{\rm MT}$ used in the lattice. In the present

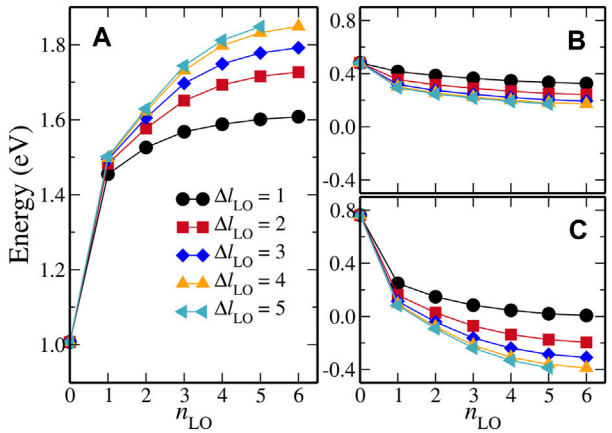

FIGURE 2 | Dependence on HLOs parameters of G_0W_0@PBE calculated **(A)** the indirect band gap between *X* and Γ, $E_g^{X-\Gamma}$, and self-energy corrections to **(B)** bottommost conduction state at the Γ point, $\Delta\epsilon_c^{\Gamma}$, and **(C)** topmost valence state at the *X* point, $\Delta\epsilon_v^{X}$, for marcasite FeS_2.

FeS_2 case, R_{MT} is set to 2.1 Bohr for Fe and 1.9 Bohr for S. Using $RKmax = 9.0$ will reduce the band gap from *GW* (LAPW + HLOs) by less than 0.03 eV, indicating that adequate accuracy can be delivered with the current $RKmax = 7.0$ setup. Due to limited computational resources, $RKmax = 6.0$ is used for HLOs convergence test. Following Laskowski and Blaha (2012), the linear independence of HLO basis functions is assured by choosing the energy parameters such that the overlap between the HLO radial functions is smaller than a threshold, which is 0.6 in the present work.

For hybrid functional calculations, we consider PBE0 (Perdew et al., 1996b), HSE06 (Heyd et al., 2003, 2006) and screened exchange SX-PBE (Bylander and Kleinman, 1990) methods as well as DSH. All hybrid functional calculations are performed with the projector augmented waves (PAW) method (Blöchl, 1994) implemented in the Vienna *ab-initio* Simulation Package (VASP) (Kresse and Furthmüller, 1996). The static dielectric function is calculated from the average of diagonal elements of macroscopic dielectric tensor computed by using density functional perturbation theory (DFPT) with local field effect included (Baroni et al., 2001). Apart from 3*d* and 4*s*, the 3*s* and 3*p* electrons of Fe are also treated explicitly in the valence region. The Thomas-Fermi wave vectors are 2.57 and 2.56 $Å^{-1}$ for pyrite and marcasite FeS_2, respectively. The cut-off energy of plane-wave basis for wave function expansion is chosen as 400 eV, which is sufficient to converge E_g^{Γ} of both FeS_2 polymorphs within 2 meV. In terms of **k**-point mesh, 64 (4 × 4 × 4) and 120 (5 × 4 × 6) **k** points are sampled in the first Brillouin zones of pyrite and marcasite for the self-consistent calculations, respectively. Using a finer 6 × 6 × 6 sampling for pyrite will change the band gap by less than 0.01 eV, and hence we consider the results well converged with respect to the **k**-point mesh. The energy convergence criterion is chosen to be 10^{-6} eV for the SCF iterations.

TABLE 1 | Energy parameters (unit: Rydberg) of high-energy local orbitals (HLOs) used in pyrite FeS_2 corresponding to HLOs parameters $n_{LO} = 4$, $\Delta l_{LO} = 4$ for Fe and S. Those for marcasite are essentially the same with difference by 0.02 Ry at most in each element and *l* channel.

l =	0	1	2	3	4	5	6
S	5.30	15.72	14.46	24.02	33.08	42.40	—
—	35.76	34.72	30.82	43.64	55.88	68.30	—
—	62.42	59.66	53.00	69.00	84.30	99.70	—
—	95.04	90.32	80.96	99.94	118.24	136.60	—
—	133.50	—	—	—	—	—	—
Fe	18.72	19.68	8.15	18.22	26.44	34.42	42.66
—	38.14	38.46	20.29	33.16	44.28	55.00	65.86
—	62.80	62.28	37.37	52.92	66.72	80.06	93.46
—	92.48	90.90	59.25	77.40	93.78	109.62	125.50

3 RESULTS AND DISCUSSION

3.1The *GW* Results

In this part, we present the electronic band structures of pyrite and marcasite FeS_2 computed by the all-electron *GW* method. In particular, we analyse the effect of high-energy local-orbitals (HLOs) by comparing the results from *GW* with the standard LAPW and LAPW + HLOs basis.

3.1.1 Convergence of QP Energies with Respect to HLOs Parameters

To achieve a balance between the computational cost and numerical accuracy of the LAPW + HLOs based *GW* method, we have to decide an optimized HLOs setup for the FeS_2 polymorphs of interest. That is to say, certain convergence with respect to the two HLOs parameters, namely n_{LO} and Δl_{LO}, must be achieved for the QP band structures of both polymorphs, while the number of basis functions should be kept as few as possible. To simplify the notation, we denote the setup of HLOs by (n_{LO}, Δl_{LO}) so that (1, 1) indicates a set of HLOs with $n_{LO} = 1$ and $\Delta l_{LO} = 1$, for example. Since we are most interested in the band gaps (direct and indirect) of the systems, we choose the indirect band gap from the *X* point to the Γ point, $E_g^{X-\Gamma}$, as the descriptor for the band structure, and investigate its dependence on the two HLOs parameters for marcasite.

Before discussing the results, we briefly illustrate the appropriateness of this choice. First of all, $E_g^{X-\Gamma}$ is a representative band gap energy for pyrite and marcasite FeS_2. This is because in both phases, the topmost valence state at the *X* point, X_v, is close to the valence band maximum (VBM) and the bottommost conduction state at the Γ point, Γ_c, is the conduction band minimum (CBM) (that is the case for marcasite given the coarse 2 × 1 × 2 **k** mesh in the convergence study). Second, either X_v or Γ_c has similar atomic contributions in the two polymorphs, and the effects of HLOs on such states are also similar, as shown in the results for other polymorphs like zinc-blende and wurtzite ZnO (Jiang and Blaha, 2016). Therefore the parameters optimized for marcasite are considered transferable and can be applied to the pyrite polymorph. Last but not least, as we will discuss later, the effects of HLOs on X_v and Γ_c differ significantly, avoiding considerable error cancellation in change of the QP correction to the band gap upon including HLOs.

TABLE 2 | Fundamental band gap (indicated by "fund.") and other direct and indirect band gaps (unit: eV) for pyrite and marcasite FeS_2 calculated by PBE and *GW* methods. Results from previous *GW* studies and experimental measurements are presented for comparison. To simplify the notation, we use "L" and "L + H" to denote the standard LAPW and LAPW + HLOs basis sets, respectively. PBE is used as the starting point for G_0W_0 and GW_0 calculations unless stated otherwise.

Methods	Pyrite					Marcasite				
	Fund.	**Γ → Γ**	***X* → Γ**	***X* → *X***	***M* → Γ**	**Fund.**	**Γ → Γ**	**Γ → *T***	***X* → Γ**	***X* → *T***
PBE	0.70	0.82	0.72	1.68	0.85	0.83	1.74	1.37	1.32	0.95
G_0W_0 (L)	0.06	0.11	0.08	1.96	0.32	0.57	0.88	1.62	0.80	1.53
GW_0 (L)	metal	—	—	—	—	0.29	0.60	1.62	0.59	1.61
G_0W_0 (L + H)	1.04	1.16	1.06	2.14	1.18	1.15	1.80	1.55	1.54	1.28
GW_0 (L + H)	1.14	1.28	1.16	2.21	1.28	1.16	1.87	1.56	1.59	1.28
Previous *GW*	—	—	—	—	—	—	—	—	—	—
G_0W_0[a]	—	0.28	0.31	1.67	—	1.06	1.40	—	1.19	1.40
G_0W_0[b]	—	0.61	0.63	1.72	—	—	1.88	—	1.57	1.25
GW_0[c]	0.97	—	—	—	—	—	—	—	—	—
sc*GW*[d]	1.01	—	—	—	—	—	—	—	—	—
QS*GW*[e]	0.81	—	—	—	—	—	—	—	—	—
Expt	0.95[f], 0.82[g]	—	—	—	—	0.83[g]	—	—	—	—

[a]*From Schena et al. (2013), using LAPW extended by HLOs up to 800 eV and with Fe 3s, 3p LOs included.*
[b]*From Schena et al. (2013), using LAPW extended by HLOs up to 800 eV but without Fe 3s, 3p LOs.*
[c]*From Ouarab and Boumaour (2017).*
[d]*From Kolb and Kolpak (2013), using PAW method and experimental lattice constants.*
[e]*From Lehner et al. (2012), using LMTO method.*
[f]*From Ennaoui et al. (1993).*
[g]*From Sánchez et al. (2016), optical gap at room temperature using diffuse reflectance spectroscopy.*

Figure 2 summarizes the results of convergence study for the G_0W_0@PBE method. $E_g^{X-\Gamma}$ (**Figure 2A**) is about 1.0 eV with the standard LAPW basis ($n_{LO} = 0$) and is significantly increased by extending LAPW with HLOs. One can see that the convergence rate of $E_g^{X-\Gamma}$ with respect to n_{LO} differs with different Δl_{LO}, and is faster for lower Δl_{LO}. The reverse is also true, i.e. the convergence with respect to Δl_{LO} is faster when n_{LO} is smaller. It clearly indicates that the convergence with respect to n_{LO} and Δl_{LO} is coupled. Increasing HLOs parameters from (4, 4) to (5, 5) changes $E_g^{X-\Gamma}$ by less than 0.05 eV, indicating that HLOs (4,4) is able to deliver an adequate accuracy. Therefore, unless stated otherwise, HLOs (4, 4), amounting to 196 and 145 HLOs for Fe and S atoms, respectively, is considered optimized and will be used in the subsequent *GW* calculations denoted by LAPW + HLOs. The energy parameters for HLOs (4, 4) can be found in **Table 1**.

It is worth noting that the effect of including HLOs on the QP correction to $E_g^{X-\Gamma}$ is different from those on the valence and conduction states. To illustrate this, we show the dependence on n_{LO} and Δl_{LO} of the self-energy corrections to Γ_c ($\Delta\varepsilon_c^{\Gamma}$) and X_v ($\Delta\varepsilon_v^{X}$) states in **Figures 2B,C**, respectively. Both $\Delta\varepsilon_c^{\Gamma}$ and $\Delta\varepsilon_v^{X}$ decrease with increasing n_{LO} or Δl_{LO}, but the former converges much faster than the latter, which agrees with the general trend observed previously (Jiang and Blaha, 2016; Zhang and Jiang, 2019). With the standard LAPW basis, G_0W_0@PBE gives $\Delta\varepsilon_c^{\Gamma}$ = 0.48 eV and $\Delta\varepsilon_v^{X}$ = 0.76 eV, indicating a negative QP correction to the band gap, which is rarely observed in LDA/GGA-based *GW* calculations of semiconductors (Jiang and Blaha, 2016). When HLOs (5, 5) are included, $\Delta\varepsilon_c^{\Gamma}$ decreases by 0.3 eV, much smaller compared to the decreasing of 1.2 eV in $\Delta\varepsilon_v^{X}$. Such biased effects of including HLOs on valence and conduction band states can be attributed to the difference in atomic characteristics between the states, and will be further discussed in the following sections.

3.1.2 Quasi-Particle Band Gaps

After having obtained the optimized HLOs, we perform the PBE-based *GW* calculations for pyrite and marcasite FeS_2 with the LAPW + HLOs basis set, and compare with the PBE method and *GW* with the standard LAPW basis.

The band gaps of pyrite and marcasite FeS_2 calculated by PBE and *GW* methods are presented in **Table 2**. The fundamental band gaps are obtained by computing the band energies along the **k**-point paths indicated in the right panel of **Figure 1**. In the PBE reference, pyrite and marcasite are predicted to have indirect fundamental band gaps of 0.70 and 0.83 eV, respectively. Our PBE results are consistent with those from previous all-electron LAPW study (Schena et al., 2013) and close to the recently reported optical band gaps obtained from diffuse reflectance spectroscopy (Sánchez et al., 2016). However, our PBE band gap for pyrite is slightly larger than several reported PBE results (Sun et al., 2011; Kolb and Kolpak, 2013; Lazić et al., 2013; Li et al., 2015; Zhang et al., 2018). This can be attributed to the use of different lattice structures in those studies (Eyert et al., 1998; Lazić et al., 2013; Schena et al., 2013) from the current work. Particularly, geometry optimization by PBE (Eyert et al., 1998; Schena et al., 2013) generally gives a longer S-S dimer, which leads to smaller splitting between bonding and anti-bonding S-3$p\sigma$ orbitals and a consequent shrink in the band gap.

For *GW* calculations with the standard LAPW basis, the QP fundamental band gaps by G_0W_0@PBE are smaller than the PBE counterparts in both FeS_2 polymorphs. Pyrite FeS_2 is predicted to have a band gap of only 0.06 eV, which is 0.64 eV smaller than that by PBE. The negative QP correction for pyrite band gap has been reported by Schena et al. (2013). The QP fundamental band gap for marcasite predicted by G_0W_0@PBE (LAPW) is also smaller than PBE, while the change (0.26 eV) is less dramatic

than that for pyrite. Such negative QP corrections to LDA/GGA band gaps are uncommon in *GW* studies for closed-shell systems (Klimes et al., 2014; Jiang and Blaha, 2016; van Setten et al., 2017; Zhang and Jiang, 2019) as well as open-shell *d*/*f*-electron semiconductors (Jiang, 2018). Switching on self-consistency of the Green's function by GW_0@PBE further reduces the fundamental band gaps of FeS_2. In particular, pyrite is predicted to be metallic by GW_0@PBE, which disagrees qualitatively with its semiconducting nature in experiment (Ennaoui et al., 1993). For other direct and indirect band gaps, those for $\Gamma \rightarrow \Gamma$ and $X \rightarrow \Gamma$ in pyrite and marcasite and $M \rightarrow \Gamma$ in marcasite are decreased from PBE to G_0W_0@PBE (LAPW). The decrease is largest for the $\Gamma \rightarrow \Gamma$ gap in the two phases, 0.71 and 0.86 eV for pyrite and marcasite, respectively. On the other hand, the gaps for $X \rightarrow X$ in pyrite, $\Gamma \rightarrow T$ and $X \rightarrow T$ in marcasite are increased by 0.28, 0.25, and 0.58 eV, respectively. However, it should be noted that the distinction in signs of corrections to the QP gaps in different channels should not be considered as intrinsic for FeS_2. Instead, it is an artifact as a result of the incomplete basis, which we will discuss in details below.

Now we turn to the LAPW + HLOs-based *GW* calculations. With the G_0W_0@PBE method, including HLOs increases the QP fundamental gap by 0.98 eV for pyrite and 0.58 eV for marcasite. The resulting G_0W_0@PBE band gaps are 1.04 and 1.15 eV for pyrite and marcasite, respectively. In contrast, all band gaps investigated are increased by G_0W_0 with LAPW + HLOs compared to their PBE counterparts. We note that HLOs have distinct effects among band gaps for different channels. Once the HLOs are included, band gaps for channels with the conduction state at the Γ point are increased by about 1 eV. On the other hand, the QP correction to the $X \rightarrow X$ band gap in pyrite increases by only 0.18 eV. Moreover, the gaps for $\Gamma \rightarrow T$ and $X \rightarrow T$ in marcasite even decrease. With the LAPW + HLOs basis, using GW_0 to switch on partial self-consistency further increases the band gaps, but the change is moderate and no more than 0.1 eV.

As explained at the beginning, the fundamental band gap of FeS_2 has been controversial in the recent decades, partly due to the widely varying experimental values (Ennaoui et al., 1993). In the present study, the GW_0@PBE method with the LAPW + HLOs predicts that pyrite and marcasite have indirect fundamental band gaps of 1.14 and 1.16 eV, respectively. The GW_0 gap of pyrite is slightly larger than the generally accepted experimental value of 0.95 eV (Ennaoui et al., 1993). Furthermore, the fact that the two polymorphs have almost identical band gaps is consistent with the optical measurements by Sánchez et al. (2016), although our predicted band gaps are about 0.3 eV larger. However, it should be noted that one must take exciton binding energy E_B into account for a meaningful comparison between the QP fundamental band gap and experimentally measured optical gap. The difference between the fundamental and optical gaps can be significant when the exciton is localized, i.e. of Frenkel type (Fox, 2010). On the other hand, while it is more straightforward to compare the QP gap with spectral data from direct and inverse PES (Folkerts et al., 1987; Mamiya et al., 1997), the resolutions of available measurements for pyrite FeS_2 are too low to extract a meaningful gap value for comparison. Moreover, to the best knowledge of the authors, no data of combined PES/IPS measurements are available for marcasite. Therefore, further experimental studies are required to determine and verify the band gaps of the FeS_2 polymorphs.

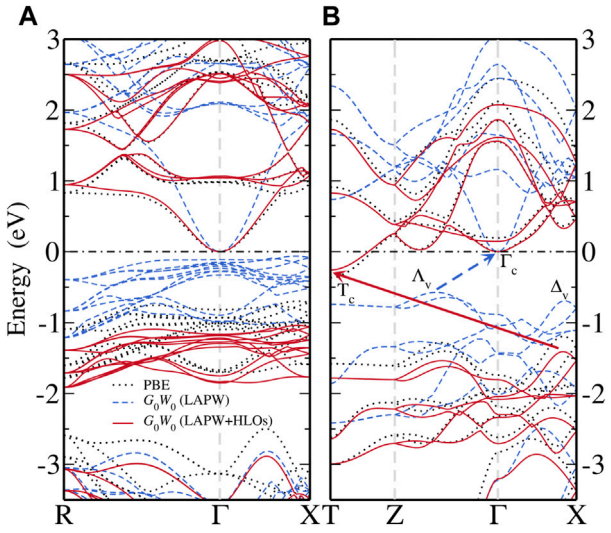

FIGURE 3 | Comparison of band structures computed from PBE (black dotted), G_0W_0@PBE with the standard LAPW basis (blue dashed) and G_0W_0@PBE with the LAPW basis extended by optimized HLOs (LAPW + HLOs, red solid) for **(A)** pyrite and **(B)** marcasite FeS_2. The conduction band minimum is aligned as the energy zero and marked by the black dash-dotted line.

To close this part, we highlight that the present work resolve two issues reported in previous *GW* studies in terms of QP band structures of FeS_2. First, Schena et al. (2013) performed a G_0W_0@PBE study on pyrite and marcasite FeS_2 with similar HLOs-extended LAPW basis. The fundamental band gap of pyrite was estimated as about 0.3 eV, by which the authors claimed to explain the low V_{OC} encountered in the pyrite solar cell. However, according to our convergence study, such a small band gap is likely to result from inadequate convergence with respect to HLOs. More specifically, the largest angular momentum of HLOs $l_{max}^{(LO)}$ used in Schena et al. (2013) is 3, i.e. *f* orbital, while $l_{max}^{(LO)} = 2 + 4 = 6$ (*i* orbital) is used in the optimized HLOs of the present work. As a result, the highest energy covered by HLOs in Schena et al. (2013) (800 eV) is much smaller than that used in the present work (about 1800 eV). Second, fully self-consistent *GW* (sc*GW*) and quasi-particle self-consistent *GW* (QPsc*GW* or QS*GW*) calculations have also been carried out to study the band structure of pyrite, and give apparently satisfactory results (Lehner et al., 2012; Kolb and Kolpak, 2013). However, variants of self-consistent *GW* without taking the vertex function into account tend to overestimate the band gaps of typical semiconductors, as indicated by several works (Shishkin and Kresse, 2007; Deguchi et al., 2016; Cao et al., 2017; Grumet et al., 2018). Thus the error cancellation between the general tendency of overestimating band gaps of semiconductors and the

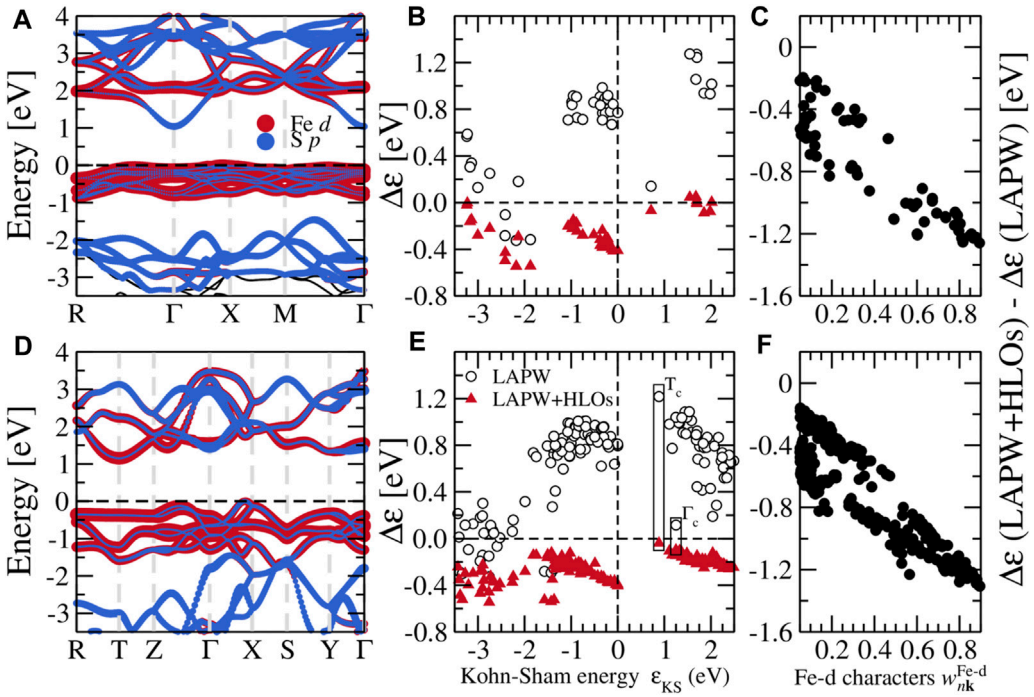

FIGURE 4 | (A) Projected band structure from *GW* with the LAPW + HLOs basis, **(B)** self-energy corrections $\Delta\varepsilon$ to Kohn-Sham states, and **(C)** the difference between $\Delta\varepsilon$ with LAPW + HLOs and LAPW basis against the weight of Fe-*d* characters $w_{n\mathbf{k}}^{\text{Fe}-d}$ defined by **Eq. 12** for pyrite FeS_2. *GW* are performed at the G_0W_0 level. The quasi-particle **(A)** and Kohn-Sham **(B)** energies are aligned to the corresponding valence band maximum. In **(A)**, projections of states on Fe-*d* and S-*p* orbitals are proportional to the diameters of red and blue circles, respectively. **(D–F)** are the counterparts for the marcasite phase.

numerical inaccuracy in the LAPW basis or the use of conventional pseudo-potentials could contribute to the apparent agreement between the generally accepted band gap and the self-consistent *GW* results. Of course, without looking into computational details of previous self-consistent *GW* calculations, this is just our speculation. Further investigations are needed to fully clarify this issue. We also note that similar LAPW + HLOs calculation has been conducted for the pyrite phase by Ouarab and Boumaour (2017) and gives a band gap (0.97 eV) close to ours.

3.1.3 Quasi-Particle Band Structure

To further illustrate the significance of HLOs in applying the *GW* methods to FeS_2, we present the QP band structures of pyrite and marcasite FeS_2 calculated from the G_0W_0@PBE method with the LAPW + HLOs basis set, and compare the results to those with the standard LAPW basis.

Figure 3 shows the electronic band structures of the two FeS_2 phases from different methods. Note that the bands are aligned to the CBM at the Γ point for a better view of QP correction to the valence states. With PBE, pyrite (**Figure 3A**) is found to be an indirect band gap material with the CBM located at the Γ point and the VBM near the *X* point along Γ–*X*. The top valence bands within 1 eV below the VBM are dominated by the localized Fe-3*d* states, also manifested by their flat dispersion. The dispersive bands about 2 eV below the VBM are mainly composed of S-3*p* states and well separated from the Fe-3*d* (t_{2g}) valence bands. In the conduction band region, the lowermost conduction bands are also largely composed of Fe-3*d* (e_g), except for the states close to the Γ point with predominant S-3*p* characters. Particularly, the CBM Γ_c state is exclusively formed by the σ anti-bonding overlapping of S-3*p* orbitals in the S-S dimer (see projected bands in **Figure 4A**). Valence and conduction bands with strong Fe-3*d* characters are separated by about 2 eV. For marcasite, an indirect band gap is also observed, with the CBM located at the *T* point (T_c) and the VBM along Γ–*X* (Δ_v). Both states at the VBM and CBM of marcasite are of dominant Fe-3*d* characters (**Figure 4D**), in contrast to pyrite where CBM is of pure S-3*p* characters. The wider Fe-3*d* valence bands overlap with the S-3*p* bands near about 1.5 eV below the VBM, which indicates stronger covalent bonding between Fe and S in marcasite than in pyrite.

Then we compare the QP band structures obtained from G_0W_0@PBE with the LAPW and LAPW + HLOs basis (**Figure 3**). With the standard LAPW basis, G_0W_0@PBE predicts pyrite almost as a semimetal with a nearly vanishing band gap (**Figure 3A**). Dispersion of the conduction band around the Γ point and the separation between the Fe-3*d* and S-3*p* valence bands are enhanced compared to the PBE reference. For marcasite (**Figure 3B**), although a noticeable gap (0.57 eV) is predicted by G_0W_0@PBE, the band edges are different from those in PBE: the CBM is located at the Γ point (Γ_c) and the VBM in the middle of the *Z*–Γ path (Λ_v). The change in the nature of band edges from semi-local functional to *GW* method is also observed by Schena et al.

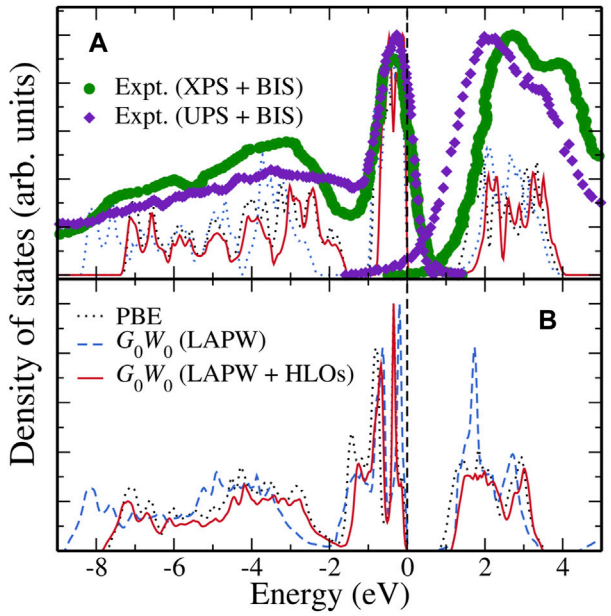

FIGURE 5 | Density of states (DOS) computed from PBE (black dotted), G_0W_0@PBE with the standard LAPW basis (blue dashed) and G_0W_0@PBE with the LAPW + HLOs basis (red solid) for **(A)** pyrite and **(B)** marcasite FeS_2. Energy distribution curves (EDCs) of pyrite extracted from photo-electron spectroscopy (PES) are presented for comparison. Each dataset is normalized with respect to its highest peak. Theoretical data are aligned to its valence band maximum as energy zero. The XPS + BIS and UPS + BIS data for pyrite are obtained from Folkerts et al. (1987) and Mamiya et al. (1997), respectively. To take into account the different definitions of the Fermi level in theory and experiment, a rigid shift of 0.60 and 0.40 eV are employed for the EDCs from XPS + BIS and UPS + BIS, respectively, to match the highest valence peaks below the Fermi level.

(2013). Once HLOs are included in the basis set, QP band gaps of both phases are dramatically enlarged. The fundamental gaps of pyrite and marcasite are 1.04 and 1.15 eV, respectively, which are 0.2 ~ 0.3 eV larger than the optical gaps from absorption spectra (Sánchez et al., 2016). Band edges of marcasite by *GW* are also recovered to those by PBE. The comparison indicates that both negative QP corrections to band gaps and change of band edges in *GW* (LAPW) are indeed artifacts due to the inadequate numerical accuracy of the basis set.

To better understand how the HLOs basis functions influence the QP band structures of FeS_2, we scrutinize the QP correction to Kohn-Sham state $\Delta\varepsilon$, defined by the difference between the QP energy ε_{QP} and the KS energy ε_{KS}, i.e. $\Delta\varepsilon \equiv \varepsilon_{QP} - \varepsilon_{KS}$. For pyrite, with the standard LAPW basis, $\Delta\varepsilon$ to the CBM is smaller than those to the valence Fe-3*d* t_{2g} and conduction Fe-3*d* e_g states as shown in **Figure 4B**. Particularly, $\Delta\varepsilon$ for the VBM is about 0.7 eV greater than that for the CBM. This leads to a up-shift of Fe-3*d* states with respect to the CBM on a whole. Extending LAPW with HLOs reduces $\Delta\varepsilon$ for all states, but the reduction in $\Delta\varepsilon$ to the VBM is more than that to the CBM by about 1.0 eV, resulting in the sign change of the QP correction to the band gap. Similar conclusion can be drawn from $\Delta\varepsilon$ in the marcasite phase (**Figure 4E**). With the standard LAPW method, $\Delta\varepsilon$ to T_c exceeds that to Γ_c by more than 1.1 eV. Consequently, Γ_c drops down below T_c and becomes the CBM, as we have seen in **Figure 3B**. Upon including HLOs, $\Delta\varepsilon$ to T_c is reduced more significantly than $\Delta\varepsilon$ to Γ_c such that T_c recovers the conduction band edge as in PBE.

Such biased effects of HLOs are clearly associated with the atomic characteristics of Kohn-Sham states, as we have demonstrated in the *GW* calculations of cuprous and silver halides (Zhang and Jiang, 2019). In **Figures 4C,F**, we plot the difference between $\Delta\varepsilon$ computed by G_0W_0 with LAPW + HLOs and LAPW against the weight of Fe-*d* characters of the Kohn-Sham orbitals $|\psi_{n\mathbf{k}}\rangle$, $w_{n\mathbf{k}}^{\mathrm{Fe}-d}$, defined by

$$w_{n\mathbf{k}}^{\mathrm{Fe}-d} = \sum_i \sum_{m=-2}^{2} \left|\langle \phi_{l=2,m}^{\mathrm{Fe}_i} | \psi_{n\mathbf{k}} \rangle\right|^2 \tag{12}$$

where $\phi_{l=2,m}^{\mathrm{Fe}_i}$ represents the pre-defined atomic function centered on the *i*th Fe atom featuring spherical harmonic function Y_2^m. The negative difference implies that including HLOs generally brings down $\Delta\varepsilon$. Moreover, the difference is more dramatic for states with larger $w_{n\mathbf{k}}^{\mathrm{Fe}-d}$, indicating that numerical error is more significant for states with stronger Fe-*d* characters in *GW* calculations with the incomplete LAPW basis.

3.1.4 *GW* Density of States

To end this section, we present the *GW* calculated density of states (DOS) of FeS_2 polymorphs in **Figure 5**. The results for pyrite FeS_2 are shown in **Figure 5A**. Due to different definitions of the Fermi level in theoretical results and experimental spectral data, we have shifted the experimental data to match up the highest valence peak near the Fermi level. With this alignment, the overall DOS from G_0W_0 (LAPW + HLOs) agrees well with the energy distribution curves (EDCs) from the PES experiments. The width of the valence Fe-3*d* band and separation between the Fe-3*d* and S-3*p* valence bands are consistent with the UPS experiment by Mamiya et al. (1997) and the XPS experiment by Folkerts et al. (1987). The location of the first peak in the conduction band region is also in good agreement with the BIS data (Folkerts et al., 1987). Interestingly, although G_0W_0 (LAPW) underestimates the band gap severely, the location of the first peak in the conduction region is almost identical to that by G_0W_0 (LAPW + HLOs), probably due to the error cancellation between QP corrections to the valence and conduction Fe-3*d* bands. However, such fortuitous cancellation does not hold in the valence region as inferred by the too deep S-3*p* band in the G_0W_0 (LAPW) results.

Figure 5B shows the calculated DOS for marcasite. Regardless of the theoretical method used, the valence Fe-3*d* band of marcasite has larger width than that of pyrite, indicating a stronger Fe-S interaction in the marcasite phase. In the conduction region, a sharp peak is observed with the G_0W_0 (LAPW) method, while only a plateau is found with G_0W_0 (LAPW + HLOs). However, the sharp peak is actually an artifact of wrongly pushed up Fe-3*d* conduction bands due to the inaccuracy of the standard LAPW basis as explained above.

TABLE 3 | Fundamental band gap (indicated by "fund.") and other direct and indirect band gaps (unit: eV) for pyrite and marcasite FeS_2 calculated by different hybrid functionals. Results from other theoretical studies and experimental measurements are presented as comparison.

Methods	Pyrite					Marcasite				
	Fund.	Γ → Γ	*X* → Γ	*X* → *X*	*M* → Γ	Fund.	Γ → Γ	Γ → *T*	*X* → Γ	*X* → *T*
PBE0	2.94	2.94	3.04	4.34	3.03	2.95	3.63	4.01	3.22	3.60
HSE06	2.22	2.22	2.32	3.58	2.31	2.26	2.91	3.26	2.53	2.88
MHSE	1.16	1.29	1.18	2.32	1.27	1.47	2.09	1.96	1.72	1.59
DSH0[a]	2.43	2.87	2.70	4.06	2.55	2.16	3.49	4.25	2.59	3.35
DSH0[b]	2.72	3.19	3.02	4.39	2.85	—	—	—	—	—
DSH[c]	2.96	3.46	3.28	4.67	3.10	2.57	3.90	4.69	3.00	3.79
SX-PBE	1.69	1.74	1.82	3.20	1.73	1.64	3.08	3.00	2.30	2.21
HSE06[d]	2.76	—	—	—	—	2.72	—	—	—	—
HSE06[e]	2.69	—	—	—	—	—	—	—	—	—
HSE06[f]	2.70	—	—	—	—	—	—	—	—	—
HSE06[g]	2.2	—	—	—	—	—	—	—	—	—
HSE06[h]	2.40	—	—	—	—	2.16	—	—	—	—
MHSE[h]	1.14	—	—	—	—	1.26	—	—	—	—
PBE0[h]	2.76	—	—	—	—	2.94	—	—	—	—
Expt.	0.95[i], 0.82[j]	—	—	—	—	0.83[j]	—	—	—	—

[a]*Using* ε_M^{PBE} *calculated by finite field method.*
[b]*Using* ε_M *= 10.9 obtained from Husk and Seehra (1978).*
[c]*Converged* ε_M*: pyrite 7.8 and marcasite 9.2.*
[d]*From Sun et al. (2011), using PAW with experimental lattice constants.*
[e]*From Hu et al. (2012), using PAW with optimized lattice parameters (*a *= 5.422 Å,* u *= 0.385).*
[f]*From Choi et al. (2012), using PAW with experimental lattice constants.*
[g]*From Schena et al. (2013), using LAPW with optimized lattice parameters (*a *= 5.403 Å,* u *= 0.383).*
[h]*From Liu et al. (2019), using PAW.*
[i]*From Ennaoui et al. (1993).*
[j]*From Sánchez et al. (2016), optical gap at room temperature using diffuse reflectance spectroscopy.*

3.2 Results From Hybrid Functionals

As mentioned in the introduction, previous theoretical studies found that various hybrid functionals, which are typically able to describe the band gaps of semiconductors quite accurately, performed badly for FeS_2. In this section, we look into this issue and present results by several hybrid schemes including the DSH functional with system-dependent parameters.

3.2.1 Band Gaps by Hybrid Functionals

Band gaps computed by different hybrid functionals are collected in **Table 3**. The widely used PBE0 and HSE06 functionals have been reported to predict fundamental gaps of pyrite and marcasite FeS_2 larger than 2 eV in the literature (Sun et al., 2011; Choi et al., 2012; Hu et al., 2012; Schena et al., 2013; Liu et al., 2019), which is confirmed by our results. DSH, the hybrid functional with system-tuned parameters, does not improve the prediction over PBE0 and HSE06. This is surprising, given that DSH has been previously shown to outperform several other hybrids in evaluating band structures for wide- and narrow-gap systems (Cui et al., 2018; Liu et al., 2020), including PBE0, HSE06 and the dielectric-dependent hybrid (DDH) functionals (Marques et al., 2011; Skone et al., 2014). SX-PBE screened exchange functional gives band gaps of FeS_2 significantly smaller than the hybrids mentioned above, but the gaps are still larger than those from *GW* with the LAPW + HLOs basis (**Table 2**) by about 0.5 eV.

Considering that the one-shot DSH, i.e. DSH0, may outperform the self-consistent scheme in some transition metal compounds (Cui et al., 2018; Liu et al., 2020), we also employ DSH0 to calculate the two FeS_2 polymorphs. The macroscopic dielectric constant calculated with PBE ε_M^{PBE} is 20.6 for pyrite, which agrees well with ε_M^{PBE} = 21 from a previous study (Choi et al., 2012). DSH0 with ε_M^{PBE} predicts smaller band gaps than DSH, but the values are still above 2 eV. Meanwhile, DSH0 with experimentally obtained ε_M = 10.9 (Husk and Seehra, 1978) gives the pyrite band gap of 2.72 eV. In contrast, a modified HSE functional (MHSE) with HSE06 screening parameter and 10% hybrid ratio, which is roughly equal to the inverse of the experimental dielectric constant, as suggested by Liu et al. (2019), gives band gaps close to the GW_0 (LAPW + HLOs) result. The MHSE results agree with those by Liu et al. (2019) and seem to verify the suggestion by Schena et al. (2013) of using $1/\varepsilon_M$ as the hybrid ratio in the HSE-type screened hybrid functional.

3.2.2 Band Structures by Hybrid Functionals

As summarized above, the investigated hybrid functionals except for MHSE fail to give reasonable predictions for the band gaps of pyrite and marcasite FeS_2. In this section, we take a close look at the band structures computed from these methods to understand the failure.

The band structures for pyrite calculated from selected hybrid functionals are shown in the upper panel of **Figure 6**. With PBE0 and HSE06 (**Figures 6A,B**), the fundamental band gap is a direct one with both VBM and CBM located at the Γ point. An indirect

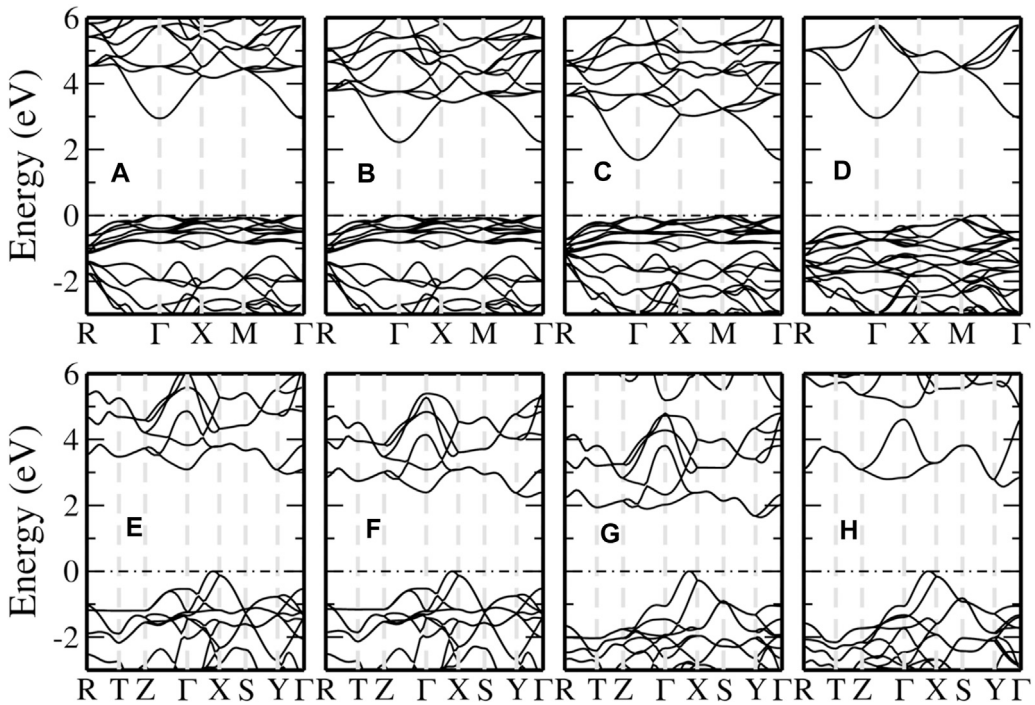

FIGURE 6 | Band structures of pyrite **(upper panel)** and marcasite **(lower panel)** FeS_2 computed from different hybrid functional methods. From left to right, the methods used are PBE0 **(A,E)**, HSE06 **(B,F)**, SX-PBE **(C,G)** and DSH **(D,H)**, respectively. The valence band maximum is aligned as the energy zero and indicated by the black dash-dotted line.

fundamental gap is obtained by SX-PBE and DSH (**Figures 6C,D**), but the VBM is different from that in PBE or the *GW* method (**Figure 3A**). In addition, compared to the *GW* (LAPW + HLOs) results, the separation between valence Fe-3*d* and S-3*p* bands is reduced and the splitting between the valence and conduction Fe-3*d* bands is significantly increased by the hybrid functionals. We note that both features can be understood tentatively as a result of increased ligand field strength from the perspective of ligand field theory. This indicates an overestimated interaction between the ligand S-3*pσ* and Fe-3*d* orbitals in the selected hybrid functionals than that in PBE. The overestimation is most significant in the DSH method (**Figure 6D**), where the state of predominant S-3*pπ* characters along the *M*–Γ path becomes the VBM and conduction Fe-3*d* bands are raised beyond 6 eV above the Fermi level.

We can observe similar features in marcasite band structures from hybrid functionals, as shown in the lower panel of **Figure 6**. In the valence band region, the S-3*p* bands are pushed up relatively to Fe-3*d* bands compared with PBE and *GW*. The increase is so significant that the VBM along Γ–*X*, which is mainly of Fe-3*d* in PBE and *GW*, is now of predominant S-3*p* characters. This also leads to a considerable overlap between the two sets of bands in the energy window 1 ~ 3 eV below the Fermi level. The conduction bands are also shifted to higher energies. However, the shifts are larger for the conduction Fe-3*d* bands than for S-3*p*. For the DSH method as an extreme case, the Fe-3*d* bands are raised up too high and even separated from the S-3*p* bands.

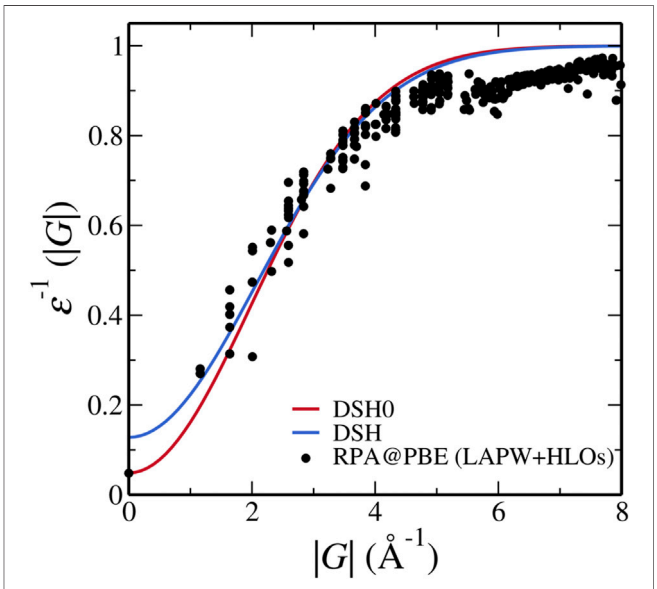

FIGURE 7 | Inverse dielectric functions of pyrite used in the DSH model and calculated from RPA@PBE with the LAPW + HLOs basis set. Dielectric constant computed by PBE is used in the one-shot DSH0 method.

The radical failure of DSH invites a close inspection of feasibility of DSH for FeS_2. As a preliminary exploration to the possible cause, we make a direct comparison between the

inverse static dielectric function used in the DSH with ε_M^{PBE} and that from the RPA calculation with the LAPW + HLOs basis in pyrite FeS_2 as a function of the length of wave vector in the long-range limit, i.e. $q \rightarrow 0$. The inverse dielectric function corresponding to DSH reads (Liu et al., 2020)

$$\varepsilon_{DSH}^{-1}(\mathbf{G}) = 1 - \left(1 - \frac{1}{\varepsilon_M}\right)\left(\mathbf{e}^{-|\mathbf{G}|^2/4\mu^2}\right). \quad (13)$$

We note that **Eq. 13** differs from the inverse of **Eq. 9** because in the derivation of DSH, the exponential function is replaced by erfc [Cui et al. (2018) for more details]. As shown in **Figure 7**, while DSH overestimates ε^{-1} and underestimates the screening in the short-wavelength region, i.e. near $|\mathbf{G}| = 0$, DSH0 model dielectric function with ε_M^{PBE} closely resembles that from RPA calculation, which is similar to the observation by Liu et al. (2020) in transition metal oxides. Hence we consider that the screening effect is reasonably captured in DSH0. Further investigation is needed to understand the cause for the failure of DSH for FeS_2.

4 CONCLUSION

In the present study, we have investigated the electronic band structures of two FeS_2 polymorphs, namely pyrite and marcasite, by using methods in different frameworks. With the all-electron many-body *GW* method implemented in the LAPW framework, we find that by using GW_0@PBE with the LAPW + HLOs basis, pyrite and marcasite are predicted to have indirect fundamental band gaps of 1.14 and 1.16 eV, respectively. The closeness of band gaps for the two polymorphs agrees with the experimental observation (Sánchez et al., 2016). The pyrite band gap from GW_0@PBE with LAPW + HLOs is very close to the generally accepted experimental value (Ennaoui et al., 1993) and the corresponding density of states also agrees well with energy distribution curves obtained from the photoelectron spectroscopy measurements (Folkerts et al., 1987; Mamiya et al., 1997). In contrast, with the standard LAPW basis, PBE-based G_0W_0 and GW_0 both lead to negative QP correction to the PBE fundamental gap, which is rarely observed in LDA/GGA-based G_0W_0 and GW_0 treatments of semiconductors. The splitting between Fe-3*d* and S-3*p* valence bands of pyrite is also significantly overestimated compared to experiment. These artifacts exist not only in calculations with the standard LAPW basis, but also in those with LAPW basis extended by an inadequately converged HLOs (Schena et al., 2013). Therefore in order to eliminate such artifacts, it is instrumental to carefully converge the fundamental band gap with respect to the two controlling parameters, namely n_{LO} and Δl_{LO}. We have further studied electronic band structures of FeS_2 polymorphs with different hybrid functionals, including PBE0, HSE06, the screened exchange SX-PBE and the recently developed DSH functional with system-tuned hybridization parameters. We find that all those methods overestimate the band gaps of the two polymorphs by 0.5 ~ 1.9 eV compared to the results obtained from G_0W_0 (LAPW + HLOs). The overestimation by PBE0 and HSE06 as reported in the literature is reproduced in this work. Furthermore, either self-consistent or one-shot DSH method fails to improve over the conventional fixed-parameter hybrid functionals. By comparing the model dielectric function used in DSH with that from RPA calculation with LAPW + HLOs in pyrite, we point out that the failure of DSH may not be caused by the insufficiency of the dielectric model used and therefore requires further investigation. Our investigations clearly show that accurate prediction of electronic band structures of FeS_2 polymorphs poses a stringent test on the state-of-the-art first-principles approaches, and the *GW* method based on semi-local density approximation performs well for this difficult system if it is practiced with well-converged numerical accuracy.

Finally, we note that further work in the following aspects can be done to shed more light onto the band gap problem of FeS_2 in terms of *GW* and hybrid functional calculations. For one thing, it is possible to build the screened Coulomb interaction *W* using the KS states from the LAPW calculations and calculate the self-energy Σ with *G* from LAPW + HLOs. One can compare it with *GW* using LAPW to see whether it is the inaccurate band summation in *W* or *G* to blame. For another, replacing the PBE with the hybrid functional as starting point will be worthwhile to evaluate the dependence of G_0W_0/GW_0 results on initial input for FeS_2. Particularly, considering the severe overestimation of FeS_2 band gaps by the hybrid functionals, it is of great interest to see whether G_0W_0/GW_0 can produce a negative QP correction to the gap from hybrid functional calculations such that the experimental gap is approached from above.

DATA AVAILABILITY STATEMENT

The original contributions presented in the study are included in the article/Supplementary Material, further inquiries can be directed to the corresponding author.

AUTHOR CONTRIBUTIONS

M-YZ performed the calculations, conducted the analysis and wrote the manuscript. HJ revised the manuscript and supervised all the work. All authors listed contributed to the article and approved it for publication.

FUNDING

National Natural Science Foundation of China (grant numbers: 21873005 and 21911530231).

ACKNOWLEDGMENTS

The authors acknowledge the support by High-performance Computing Platform of Peking University for the computational resources.

REFERENCES

Andersen, O. K. (1975). Linear Methods in Band Theory. *Phys. Rev. B* 12, 3060–3083. doi:10.1103/physrevb.12.3060

Aryasetiawan, F., and Gunnarsson, O. (1994). Product-basis Method for Calculating Dielectric Matrices. *Phys. Rev. B* 49, 16214–16222. doi:10.1103/physrevb.49.16214

Baer, R., Livshits, E., and Salzner, U. (2010). Tuned Range-Separated Hybrids in Density Functional Theory. *Annu. Rev. Phys. Chem.* 61, 85–109. doi:10.1146/annurev.physchem.012809.103321

Barawi, M., Ferrer, I. J., Flores, E., Yoda, S., Ares, J. R., and Sánchez, C. (2016). Hydrogen Photoassisted Generation by Visible Light and an Earth Abundant Photocatalyst: Pyrite (FeS2). *J. Phys. Chem. C* 120, 9547–9552. doi:10.1021/acs.jpcc.5b11482

Baroni, S., de Gironcoli, S., Dal Corso, A., and Giannozzi, P. (2001). Phonons and Related crystal Properties from Density-Functional Perturbation Theory. *Rev. Mod. Phys.* 73, 515–562. doi:10.1103/revmodphys.73.515

Bechstedt, F., Del Sole, R., Cappellini, G., and Reining, L. (1992). An Efficient Method for Calculating Quasiparticle Energies in Semiconductors. *Solid State. Commun.* 84, 765–770. doi:10.1016/0038-1098(92)90476-p

Becke, A. D. (1993a). A New Mixing of Hartree-Fock and Local Density-functional Theories. *J. Chem. Phys.* 98, 1372–1377. doi:10.1063/1.464304

Becke, A. D. (1993b). Density-functional Thermochemistry. III. The Role of Exact Exchange. *J. Chem. Phys.* 98, 5648–5652. doi:10.1063/1.464913

Betzinger, M., Friedrich, C., Blügel, S., and Görling, A. (2011). Local Exact Exchange Potentials within the All-Electron Flapw Method with Pseudopotential Results and a Comparison. *Phys. Rev. B* 83, 045105. doi:10.1103/physrevb.83.045105

Betzinger, M., Friedrich, C., Görling, A., and Blügel, S. (2015). Precise All-Electron Dynamical Response Functions: Application to Cohsex and the Rpa Correlation Energy. *Phys. Rev. B* 92, 245101. doi:10.1103/physrevb.92.245101

Betzinger, M., Friedrich, C., Görling, A., and Blügel, S. (2012). Precise Response Functions in All-Electron Methods: Application to the Optimized-Effective-Potential Approach. *Phys. Rev. B* 85, 245124. doi:10.1103/physrevb.85.245124

Birkholz, M., Fiechter, S., Hartmann, A., and Tributsch, H. (1991). Sulfur Deficiency in Iron Pyrite (FeS2−x) and its Consequences for Band-Structure Models. *Phys. Rev. B* 43, 11926–11936. doi:10.1103/physrevb.43.11926

Blaha, P., Schwarz, K., Madsen, G. K. H., Kvasnicka, D., and Luitz, J. (2001). *WIEN2K, an Augmented Plane Wave + Local Orbitals Program For Calculating Crystal Properties (Karlheinz Schwarz, Techn*. Universität Wien, Austria).

Blaha, P., Schwarz, K., Tran, F., Laskowski, R., Madsen, G. K. H., and Marks, L. D. (2020). WIEN2k: An APW+lo Program for Calculating the Properties of Solids. *J. Chem. Phys.* 152, 074101. doi:10.1063/1.5143061

Blöchl, P. E. (1994). Projector Augmented-Wave Method. *Phys. Rev. B* 50, 17953–17979. doi:10.1103/physrevb.50.17953

Bronold, M., Pettenkofer, C., and Jaegermann, W. (1994). Surface Photovoltage Measurements on Pyrite (100) Cleavage Planes: Evidence for Electronic Bulk Defects. *J. Appl. Phys.* 76, 5800–5808. doi:10.1063/1.358393

Brostigen, G., Kjekshus, A., Astrup, E. E., Nordal, V., Lindberg, A. A., and Craig, J. C. (1969). Redetermined crystal Structure of FeS2 (Pyrite). *Acta Chem. Scand.* 23, 2186–2188. doi:10.3891/acta.chem.scand.23-2186

Brostigen, G., Kjekshus, A., Rømming, C., Gronowitz, S., Koskikallio, J., and Swahn, C.-G. (1973). Compounds with the Marcasite Type crystal Structure. VIII. Redetermination of the Prototype. *Acta Chem. Scand.* 27, 2791–2796. doi:10.3891/acta.chem.scand.27-2791

Bylander, D. M., and Kleinman, L. (1990). Good Semiconductor Band Gaps with a Modified Local-Density Approximation. *Phys. Rev. B* 41, 7868–7871. doi:10.1103/physrevb.41.7868

Cabán-Acevedo, M., Kaiser, N. S., English, C. R., Liang, D., Thompson, B. J., Chen, H.-E., et al. (2014). Ionization of High-Density Deep Donor Defect States Explains the Low Photovoltage of Iron Pyrite Single Crystals. *J. Am. Chem. Soc.* 136, 17163–17179. doi:10.1021/ja509142w

Cao, H., Yu, Z., Lu, P., and Wang, L.-W. (2017). Fully Converged Plane-Wave-Based Self-Consistent *GW* Calculations of Periodic Solids. *Phys. Rev. B* 95, 035139. doi:10.1103/physrevb.95.035139

Cappellini, G., Del Sole, R., Reining, L., and Bechstedt, F. (1993). Model Dielectric Function for Semiconductors. *Phys. Rev. B* 47, 9892–9895. doi:10.1103/physrevb.47.9892

Chattopadhyay, T., and Von Schnering, H. G. (1985). High Pressure X-ray Diffraction Study on P-FeS2, M-FeS2 and MnS2 to 340 Kbar: A Possible High Spin-Low Spin Transition in MnS2. *J. Phys. Chem. Sol.* 46, 113–116. doi:10.1016/0022-3697(85)90204-5

Chatzitheodorou, G., Fiechter, S., Könenkamp, R., Kunst, M., Jaegermann, W., and Tributsch, H. (1986). Thin Photoactive FeS2 (Pyrite) Films. *Mater. Res. Bull.* 21, 1481–1487. doi:10.1016/0025-5408(86)90088-7

Chen, W., Miceli, G., Rignanese, G.-M., and Pasquarello, A. (2018). Nonempirical Dielectric-dependent Hybrid Functional with Range Separation for Semiconductors and Insulators. *Phys. Rev. Mater.* 2, 073803. doi:10.1103/physrevmaterials.2.073803

Choi, S. G., Hu, J., Abdallah, L. S., Limpinsel, M., Zhang, Y. N., Zollner, S., et al. (2012). Pseudodielectric Function and Critical-point Energies of Iron Pyrite. *Phys. Rev. B* 86, 115207. doi:10.1103/physrevb.86.115207

Cui, Z.-H., Wang, Y.-C., Zhang, M.-Y., Xu, X., and Jiang, H. (2018). Doubly Screened Hybrid Functional: An Accurate First-Principles Approach for Both Narrow- and Wide-gap Semiconductors. *J. Phys. Chem. Lett.* 9, 2338–2345. doi:10.1021/acs.jpclett.8b00919

Cui, Z.-H., Wu, F., and Jiang, H. (2016). First-principles Study of Relative Stability of Rutile and Anatase Tio_2 Using the Random Phase Approximation. *Phys. Chem. Chem. Phys.* 18, 29914–29922. doi:10.1039/c6cp04973g

Deguchi, D., Sato, K., Kino, H., and Kotani, T. (2016). Accurate Energy Bands Calculated by the Hybrid Quasiparticle Self-consistentGWmethod Implemented in the Ecalj Package. *Jpn. J. Appl. Phys.* 55, 051201. doi:10.7567/jjap.55.051201

Ennaoui, A., Fiechter, S., Jaegermann, W., and Tributsch, H. (1986). Photoelectrochemistry of Highly Quantum Efficient Single-Crystalline N -FeS2 (Pyrite). *J. Electrochem. Soc.* 133, 97–106. doi:10.1149/1.2108553

Ennaoui, A., Fiechter, S., Pettenkofer, C., Alonso-Vante, N., Büker, K., Bronold, M., et al. (1993). Iron Disulfide for Solar Energy Conversion. *Solar Energ. Mater. Solar Cell* 29, 289–370. doi:10.1016/0927-0248(93)90095-k

Eyert, V., Höck, K.-H., Fiechter, S., and Tributsch, H. (1998). Electronic Structure ofFeS2: The Crucial Role of Electron-Lattice Interaction. *Phys. Rev. B* 57, 6350–6359. doi:10.1103/physrevb.57.6350

Ferrer, I. J., Nevskaia, D. M., de las Heras, C., and Sánchez, C. (1990). About the Band gap Nature of FeS2 as Determined from Optical and Photoelectrochemical Measurements. *Solid State. Commun.* 74, 913–916. doi:10.1016/0038-1098(90)90455-k

Folkerts, W., Sawatzky, G. A., Haas, C., Groot, R. A. d., and Hillebrecht, F. U. (1987). Electronic Structure of Some 3d Transition-Metal Pyrites. *J. Phys. C: Solid State. Phys.* 20, 4135–4144. doi:10.1088/0022-3719/20/26/015

Fox, M. (2010). *Optical Properties of Solids*. second edn. Oxford: OUP.

Friedrich, C., Müller, M. C., and Blügel, S. (2011a). Band Convergence and Linearization Error Correction of All-Electron *GW* Calculations: The Extreme Case of Zinc Oxide. *Phys. Rev. B* 83, 081101(R). doi:10.1103/physrevb.83.081101

Friedrich, C., Müller, M. C., and Blügel, S. (2011b). Erratum: Band Convergence and Linearization Error Correction of All-Electron GW Calculations: The Extreme Case of Zinc Oxide. *Phys. Rev. B* 83, 081101(r), 2011b . 2011*Phys. Rev. B* 84, 039906. doi:10.1103/physrevb.83.081101

Friedrich, C., Schindlmayr, A., Blügel, S., and Kotani, T. (2006). Elimination of the Linearization Error in GW Calculations Based on the Linearized Augmented-Plane-Wave Method. *Phys. Rev. B* 74, 045104. doi:10.1103/physrevb.74.045104

Golze, D., Dvorak, M., and Rinke, P. (2019). The GW Compendium: A Practical Guide to Theoretical Photoemission Spectroscopy. *Front. Chem.* 7, 377. doi:10.3389/fchem.2019.00377

Gong, M., Kirkeminde, A., Kumar, N., Zhao, H., and Ren, S. (2013a). Ionic-passivated FeS2 Photocapacitors for Energy Conversion and Storage. *Chem. Commun.* 49, 9260–9262. doi:10.1039/c3cc45088k

Gong, M., Kirkeminde, A., Xie, Y., Lu, R., Liu, J., Wu, J. Z., et al. (2013b). Iron Pyrite (FeS2) Broad Spectral and Magnetically Responsive Photodetectors. *Adv. Opt. Mater.* 1, 78–83. doi:10.1002/adom.201200003

Goodenough, J. B. (1972). Energy Bands in TX2 Compounds with Pyrite, Marcasite, and Arsenopyrite Structures. *J. Solid State. Chem.* 5, 144–152. doi:10.1016/0022-4596(72)90022-9

Grumet, M., Liu, P., Kaltak, M., Klimeš, J., and Kresse, G. (2018). Beyond the Quasiparticle Approximation: Fully Self-Consistent GW Calculations. *Phys. Rev. B* 98, 155143. doi:10.1103/physrevb.98.155143

Hedin, L. (1965). New Method for Calculating the One-Particle Green's Function with Application to the Electron-Gas Problem. *Phys. Rev.* 139, A796–A823. doi:10.1103/physrev.139.a796

Herbert, F. W., Krishnamoorthy, A., Van Vliet, K. J., and Yildiz, B. (2013). Quantification of Electronic Band gap and Surface States on FeS2(100). *Surf. Sci.* 618, 53–61. doi:10.1016/j.susc.2013.08.014

Heyd, J., Peralta, J. E., Scuseria, G. E., and Martin, R. L. (2005). Energy Band Gaps and Lattice Parameters Evaluated with the Heyd-Scuseria-Ernzerhof Screened Hybrid Functional. *J. Chem. Phys.* 123, 174101. doi:10.1063/1.2085170

Heyd, J., Scuseria, G. E., and Ernzerhof, M. (2003). Hybrid Functionals Based on a Screened Coulomb Potential. *J. Chem. Phys.* 118, 8207–8215. doi:10.1063/1.1564060

Heyd, J., Scuseria, G. E., and Ernzerhof, M. (2006). Erratum: "Hybrid Functionals Based on a ScreenedCoulomb Potential" [j. chem. phys.118, 8207 (2003)]. *J. Chem. Phys.* 124, 219906.

Hohenberg, P., and Kohn, W. (1964). Inhomogeneous Electron Gas. *Phys. Rev.* 136, B864–B871. doi:10.1103/physrev.136.b864

Hu, J., Zhang, Y., Law, M., and Wu, R. (2012). First-principles Studies of the Electronic Properties of Native and Substitutional Anionic Defects in Bulk Iron Pyrite. *Phys. Rev. B* 85, 085203. doi:10.1103/physrevb.85.085203

Hulliger, F., and Mooser, E. (1965b). Semiconductivity in Pyrite, Marcasite and Arsenopyrite Phases. *J. Phys. Chem. Sol.* 26, 429–433. doi:10.1016/0022-3697(65)90173-3

Hulliger, F., and Mooser, E. (1965a). The Bond Description of Semiconductors: Polycompounds. *Prog. Solid State. Chem.* 2, 330–377. doi:10.1016/0079-6786(65)90011-7

Husk, D. E., and Seehra, M. S. (1978). Dielectric Constant of Iron Pyrite (FeS2). *Solid State. Commun.* 27, 1147–1148. doi:10.1016/0038-1098(78)91130-4

Hybertsen, M. S., and Louie, S. G. (1986). Electron Correlation in Semiconductors and Insulators: Band Gaps and Quasiparticle Energies. *Phys. Rev. B* 34, 5390–5413. doi:10.1103/physrevb.34.5390

Jiang, H., and Blaha, P. (2016). GWwith Linearized Augmented Plane Waves Extended by High-Energy Local Orbitals. *Phys. Rev. B* 93, 115203. doi:10.1103/physrevb.93.115203

Jiang, H. (2011). Electronic Band Structure from First-Principles Green's Function Approach: Theory and Implementations. *Front. Chem. China* 6, 253–268. doi:10.1007/s11458-011-0261-6

Jiang, H., Gómez-Abal, R. I., Li, X.-Z., Meisenbichler, C., Ambrosch-Draxl, C., and Scheffler, M. (2013). FHI-gap: A GW Code Based on the All-Electron Augmented Plane Wave Method. *Comp. Phys. Commun.* 184, 348–366. doi:10.1016/j.cpc.2012.09.018

Jiang, H. (2018). Revisiting the GW Approach to d- and f-electron Oxides. *Phys. Rev. B* 97, 245132. doi:10.1103/physrevb.97.245132

Khalid, S., Ahmed, E., Khan, Y., Nawaz, S., Ramzan, M., Khalid, N. R., et al. (2018). "Iron Pyrite (FeS2): Sustainable Photovoltaic materialMicro and Nanomanufacturing Volume II,". Editors M. J. Jackson and W. Ahmed (Cham: Springer, 281–318. doi:10.1007/978-3-319-67132-1_11

Klimes, J., Kaltak, M., and Kresse, G. (2014). Predictive GW Calculations Using Plane Waves and Pseudopotentials. *Phys. Rev. B* 90, 075125.

Kolb, B., and Kolpak, A. M. (2013). Ultrafast Band-gap Oscillations in Iron Pyrite. *Phys. Rev. B* 88, 235208. doi:10.1103/physrevb.88.235208

Koller, D., Blaha, P., and Tran, F. (2013). Hybrid Functionals for Solids with an Optimized Hartree-Fock Mixing Parameter. *J. Phys. Condens. Matter* 25, 435503. doi:10.1088/0953-8984/25/43/435503

Kotani, T., and van Schilfgaarde, M. (2002). All-electron GW Approximation with the Mixed Basis Expansion Based on the Full-Potential LMTO Method. *Solid State. Commun.* 121, 461–465. doi:10.1016/s0038-1098(02)00028-5

Kou, W. W., and Seehra, M. S. (1978). Optical Absorption in Iron Pyrite (FeS_2). *Phys. Rev. B* 18, 7062–7068. doi:10.1103/physrevb.18.7062

Krasovskii, E. E. (1997). Accuracy and Convergence Properties of the Extended Linear Augmented-Plane-Wave Method. *Phys. Rev. B* 56, 12866–12873. doi:10.1103/physrevb.56.12866

Krasovskii, E. E., Yaresko, A. N., and Antonov, V. N. (1994). Theoretical Study of Ultraviolet Photoemission Spectra of noble Metals. *J. Electron Spectrosc. Relat. Phenomena* 68, 157–166. doi:10.1016/0368-2048(94)02113-9

Kresse, G., and Furthmüller, J. (1996). Efficient Iterative Schemes Forab Initiototal-Energy Calculations Using a Plane-Wave Basis Set. *Phys. Rev. B* 54, 11169–11186. doi:10.1103/physrevb.54.11169

Kronik, L., Stein, T., Refaely-Abramson, S., and Baer, R. (2012). Excitation Gaps of Finite-Sized Systems from Optimally Tuned Range-Separated Hybrid Functionals. *J. Chem. Theor. Comput.* 8, 1515–1531. doi:10.1021/ct2009363

Kümmel, S., and Kronik, L. (2008). Orbital-dependent Density Functionals: Theory and Applications. *Rev. Mod. Phys.* 80, 3–60. doi:10.1103/revmodphys.80.3

Laskowski, R., and Blaha, P. (2014). Calculating NMR Chemical Shifts Using the Augmented Plane-Wave Method. *Phys. Rev. B* 89, 014402. doi:10.1103/physrevb.89.014402

Laskowski, R., and Blaha, P. (2012). Calculations of NMR Chemical Shifts with Apw-Based Methods. *Phys. Rev. B* 85, 035132. doi:10.1103/physrevb.85.035132

Lazić, P., Armiento, R., Herbert, F. W., Chakraborty, R., Sun, R., Chan, M. K., et al. (2013). Low Intensity Conduction States in FeS2: Implications for Absorption, Open-Circuit Voltage and Surface Recombination. *J. Phys. Condens Matter* 25, 465801. doi:10.1088/0953-8984/25/46/465801

Lehner, S. W., Newman, N., van Schilfgaarde, M., Bandyopadhyay, S., Savage, K., and Buseck, P. R. (2012). Defect Energy Levels and Electronic Behavior of Ni-, Co-, and As-Doped Synthetic Pyrite (FeS2). *J. Appl. Phys.* 111, 083717. doi:10.1063/1.4706558

Li, B., Huang, L., Zhong, M., Wei, Z., and Li, J. (2015). Electrical and Magnetic Properties of FeS2 and CuFeS2 Nanoplates. *RSC Adv.* 5, 91103–91107. doi:10.1039/c5ra16918f

Li, E. K., Johnson, K. H., Eastman, D. E., and Freeouf, J. L. (1974). Localized and Bandlike Valence-Electron States in FeS2and NiS2. *Phys. Rev. Lett.* 32, 470–472. doi:10.1103/physrevlett.32.470

Li, Y., Chen, J., Chen, Y., Zhao, C., Lee, M.-H., and Lin, T.-H. (2018). DFT+U Study on the Electronic Structures and Optical Properties of Pyrite and Marcasite. *Comput. Mater. Sci.* 150, 346–352. doi:10.1016/j.commatsci.2018.04.009

Limpinsel, M., Farhi, N., Berry, N., Lindemuth, J., Perkins, C. L., Lin, Q., et al. (20141974–1989). An Inversion Layer at the Surface of N-type Iron Pyrite. *Energy Environ. Sci.* 7. doi:10.1039/c3ee43169j

Liu, J., Xu, A., Meng, Y., He, Y., Ren, P., Guo, W.-P., et al. (2019). From Predicting to Correlating the Bonding Properties of Iron Sulfide Phases. *Comput. Mater. Sci.* 164, 99–107. doi:10.1016/j.commatsci.2019.04.001

Liu, P., Franchini, C., Marsman, M., and Kresse, G. (2020). Assessing Model-dielectric-dependent Hybrid Functionals on the Antiferromagnetic Transition-Metal Monoxides MnO, FeO, CoO, and NiO. *J. Phys. Condens. Matter* 32, 015502. doi:10.1088/1361-648x/ab4150

Madsen, G. K. H., Blaha, P., Schwarz, K., Sjöstedt, E., and Nordström, L. (2001). Efficient Linearization of the Augmented Plane-Wave Method. *Phys. Rev. B* 64, 195134. doi:10.1103/physrevb.64.195134

Maier, T. M., Arbuznikov, A. V., and Kaupp, M. (2019). Local Hybrid Functionals: Theory, Implementation, and Performance of an Emerging New Tool in Quantum Chemistry and beyond. *WIREs Comput. Mol. Sci.* 9, e1378. doi:10.1002/wcms.1378

Mamiya, K., Mizokawa, T., Fujimori, A., Takahashi, H., Môri, N., Miyadai, T., et al. (1997). Photoemission Study of Pyrite-type Transition-Metal Chalcogenides MS2−xSex (M^{+}Fe, Co, Ni). *Physica B: Condensed Matter* 237-238, 390–391. doi:10.1016/s0921-4526(97)00243-3

Marques, M. A. L., Vidal, J., Oliveira, M. J. T., Reining, L., and Botti, S. (2011). Density-based Mixing Parameter for Hybrid Functionals. *Phys. Rev. B* 83, 035119. doi:10.1103/physrevb.83.035119

Marsman, M., Paier, J., Stroppa, A., and Kresse, G. (2008). Hybrid Functionals Applied to Extended Systems. *J. Phys. Condens. Matter* 20, 064201. doi:10.1088/0953-8984/20/6/064201

Michalicek, G., Betzinger, M., Friedrich, C., and Blügel, S. (2013). Elimination of the Linearization Error and Improved Basis-Set Convergence within the Flapw Method. *Comp. Phys. Commun.* 184, 2670–2679. doi:10.1016/j.cpc.2013.07.002

Muscat, J., Hung, A., Russo, S., and Yarovsky, I. (2002). First-principles Studies of the Structural and Electronic Properties of Pyrite FeS2. *Phys. Rev. B* 65, 054107. doi:10.1103/physrevb.65.054107

Nabok, D., Gulans, A., and Draxl, C. (2016). Accurate All-Electron G_0W_0 Quasiparticle Energies Employing the Full-Potential Augmented Plane-Wave Method. *Phys. Rev. B* 94, 035118. doi:10.1103/physrevb.94.035118

Nesbitt, H. W., Uhlig, I., Bancroft, G. M., and Szargan, R. (2003). Resonant XPS Study of the Pyrite Valence Band with Implications for Molecular Orbital Contributions. *Am. Mineral.* 88, 1279–1286. doi:10.2138/am-2003-8-910

Ohsawa, A., Yamamoto, H., and Watanabe, H. (1974). X-ray Photoelectron Spectra of Valence Electrons in FeS2, CoS2 and NiS2. *J. Phys. Soc. Jpn.* 37, 568. doi:10.1143/jpsj.37.568

Ollonqvist, T., Perälä, R., and Väyrynen, J. (1997). Unoccupied Electronic States of the FeS2(100) Surface Studied by Inverse Photoemission. *Surf. Sci.* 377-379, 201–205. doi:10.1016/s0039-6028(96)01351-9

Ouarab, N., and Boumaour, M. (2017). First-principles Calculations of Electronic and Optical Properties of Fe 1−x Zn x S 2 and Zn 1−x Mg x O Alloys. *Curr. Appl. Phys.* 17, 1169–1180. doi:10.1016/j.cap.2017.05.008

Paier, J., Marsman, M., Hummer, K., Kresse, G., Gerber, I. C., and Ángyán, J. G. (2006a). Erratum: "Screened Hybrid Density Functionals Applied to Solids" [J. Chem. Phys. 124, 154709 (2006)]. *J. Chem. Phys.* 125, 249901, 2006a . J. Chem. Phys. 124, 154709 (2006). doi:10.1063/1.2403866"

Paier, J., Marsman, M., Hummer, K., Kresse, G., Gerber, I. C., and Ángyán, J. G. (2006b). Screened Hybrid Density Functionals Applied to Solids. *J. Chem. Phys.* 124, 154709. doi:10.1063/1.2187006

Perdew, J. P., Burke, K., and Ernzerhof, M. (1996a). Generalized Gradient Approximation Made Simple. *Phys. Rev. Lett.* 77, 3865–3868. doi:10.1103/physrevlett.77.3865

Perdew, J. P., Ernzerhof, M., and Burke, K. (1996b). Rationale for Mixing Exact Exchange with Density Functional Approximations. *J. Chem. Phys.* 105, 9982–9985. doi:10.1063/1.472933

Perdew, J. P., Parr, R. G., Levy, M., and Balduz, J. L. (1982). Density-functional Theory for Fractional Particle Number: Derivative Discontinuities of the Energy. *Phys. Rev. Lett.* 49, 1691–1694. doi:10.1103/physrevlett.49.1691

Perdew, J. P., and Schmidt, K. (2001). Jacob's Ladder of Density Functional Approximations for the Exchange-Correlation Energy. *AIP Conf. Proc.* 577, 1. doi:10.1063/1.1390175

Perdew, J. P., Yang, W., Burke, K., Yang, Z., Gross, E. K. U., Scheffler, M., et al. (2017). Understanding Band Gaps of Solids in Generalized Kohn-Sham Theory. *Proc. Natl. Acad. Sci. USA* 114, 2801–2806. doi:10.1073/pnas.1621352114

Pickett, W. E., Krakauer, H., and Allen, P. B. (1988). Smooth Fourier Interpolation of Periodic Functions. *Phys. Rev. B* 38, 2721–2726. doi:10.1103/physrevb.38.2721

Rahman, M., Boschloo, G., Hagfeldt, A., and Edvinsson, T. (2020). On the Mechanistic Understanding of Photovoltage Loss in Iron Pyrite Solar Cells. *Adv. Mater.* 32, 1905653. doi:10.1002/adma.201905653

Ren, X., Merz, F., Jiang, H., Yao, Y., Rampp, M., Lederer, H., et al. (2021). All-electron Periodic G_0W_0 Implementation with Numerical Atomic Orbital Basis Functions: Algorithm and Benchmarks. *Phys. Rev. Mater.* 5, 013807. doi:10.1103/physrevmaterials.5.013807

Ren, X., Rinke, P., Blum, V., Wieferink, J., Tkatchenko, A., Sanfilippo, A., et al. (2012). Resolution-of-identity Approach to Hartree-Fock, Hybrid Density Functionals, RPA, MP2 andGWwith Numeric Atom-Centered Orbital Basis Functions. *New J. Phys.* 14, 053020. doi:10.1088/1367-2630/14/5/053020

Rojas, H. N., Godby, R. W., and Needs, R. J. (1995). Space-Time Method forAb InitioCalculations of Self-Energies and Dielectric Response Functions of Solids. *Phys. Rev. Lett.* 74, 1827–1830. doi:10.1103/physrevlett.74.1827

Sánchez, C., Flores, E., Barawi, M., Clamagirand, J. M., Ares, J. R., and Ferrer, I. J. (2016). Marcasite Revisited: Optical Absorption gap at Room Temperature. *Solid State. Commun.* 230, 20–24. doi:10.1016/j.ssc.2016.01.004

Schena, T., Bihlmayer, G., and Blügel, S. (2013). First-Principles Studies of FeS_2 Using Many-Body Perturbation Theory in the G0W0 Approximation. *Phys. Rev. B* 88, 235203. doi:10.1103/physrevb.88.235203

Schlegel, A., and Wachter, P. (1976). Optical Properties, Phonons and Electronic Structure of Iron Pyrite (FeS2). *J. Phys. C: Solid State. Phys.* 9, 3363–3369. doi:10.1088/0022-3719/9/17/027

Seidl, A., Görling, A., Vogl, P., Majewski, J. A., and Levy, M. (1996). Generalized Kohn-Sham Schemes and the Band-gap Problem. *Phys. Rev. B* 53, 3764–3774. doi:10.1103/physrevb.53.3764

Shen, T., Zhang, X.-W., Shang, H., Zhang, M.-Y., Wang, X., Wang, E.-G., et al. (2020). Influence of High-Energy Local Orbitals and Electron-Phonon Interactions on the Band Gaps and Optical Absorption Spectra of Hexagonal boron Nitride. *Phys. Rev. B* 102, 045117. doi:10.1103/physrevb.102.045117

Shimazaki, T., and Asai, Y. (2008). Band Structure Calculations Based on Screened Fock Exchange Method. *Chem. Phys. Lett.* 466, 91–94. doi:10.1016/j.cplett.2008.10.012

Shishkin, M., and Kresse, G. (2007). Self-consistentGWcalculations for Semiconductors and Insulators. *Phys. Rev. B* 75, 235102. doi:10.1103/physrevb.75.235102

Shukla, S., Xing, G., Ge, H., Prabhakar, R. R., Mathew, S., Su, Z., et al. (2016). Origin of Photocarrier Losses in Iron Pyrite (FeS2) Nanocubes. *ACS Nano* 10, 4431–4440. doi:10.1021/acsnano.6b00065

Singh, D. (1991). Ground-state Properties of Lanthanum: Treatment of Extended-Core States. *Phys. Rev. B* 43, 6388–6392. doi:10.1103/physrevb.43.6388

Singh, D. J., and Nordström, L. (2006). *Planewaves, Pseudopotentials and the LAPW Method*. 2nd ed. edn. New York: Springer.

Skone, J. H., Govoni, M., and Galli, G. (2014). Self-consistent Hybrid Functional for Condensed Systems. *Phys. Rev. B* 89, 195112. doi:10.1103/physrevb.89.195112

Spagnoli, D., Refson, K., Wright, K., and Gale, J. D. (2010). Density Functional Theory Study of the Relative Stability of the Iron Disulfide Polymorphs Pyrite and Marcasite. *Phys. Rev. B* 81, 094106. doi:10.1103/physrevb.81.094106

Stankovski, M., Antonius, G., Waroquiers, D., Miglio, A., Dixit, H., Sankaran, K., et al. (2011). G0W0band gap of ZnO: Effects of Plasmon-Pole Models. *Phys. Rev. B* 84, 241201. (R). doi:10.1103/physrevb.84.241201

Sun, R., Chan, M. K. Y., and Ceder, G. (2011). First-principles Electronic Structure and Relative Stability of Pyrite and Marcasite: Implications for Photovoltaic Performance. *Phys. Rev. B* 83, 235311. doi:10.1103/physrevb.83.235311

Tian, A., Xu, Q., Shi, X., Yang, H., Xue, X., You, J., et al. (2015). Pyrite Nanotube Array Films as an Efficient Photocatalyst for Degradation of Methylene Blue and Phenol. *RSC Adv.* 5, 62724–62731. doi:10.1039/c5ra07434g

van der Heide, H., Hemmel, R., van Bruggen, C. F., and Haas, C. (1980). X-ray Photoelectron Spectra of 3d Transition Metal Pyrites. *J. Solid State. Chem.* 33, 17–25. doi:10.1016/0022-4596(80)90543-5

van Setten, M. J., Giantomassi, M., Bousquet, E., Verstraete, M. J., Hamann, D. R., Gonze, X., et al. (2018). The PseudoDojo: Training and Grading a 85 Element Optimized Norm-Conserving Pseudopotential Table. *Comp. Phys. Commun.* 226, 39–54. doi:10.1016/j.cpc.2018.01.012

van Setten, M. J., Giantomassi, M., Gonze, X., Rignanese, G.-M., and Hautier, G. (2017). Automation Methodologies and Large-Scale Validation for GW : Towards High-Throughput GW Calculations. *Phys. Rev. B* 96, 155207. doi:10.1103/physrevb.96.155207

Wadia, C., Alivisatos, A. P., and Kammen, D. M. (2009). Materials Availability Expands the Opportunity for Large-Scale Photovoltaics Deployment. *Environ. Sci. Technol.* 43, 2072–2077. doi:10.1021/es8019534

Walter, J., Zhang, X., Voigt, B., Hool, R., Manno, M., Mork, F., et al. (2017). Surface Conduction in N-type Pyrite FeS2 Single Crystals. *Phys. Rev. Mater.* 1, 065403. doi:10.1103/physrevmaterials.1.065403

Wang, D.-Y., Jiang, Y.-T., Lin, C.-C., Li, S.-S., Wang, Y.-T., Chen, C.-C., et al. (2012). Solution-processable Pyrite FeS2 Nanocrystals for the Fabrication of Heterojunction Photodiodes with Visible to NIR Photodetection. *Adv. Mater.* 24, 3415–3420. doi:10.1002/adma.201200753

Wilson, J. A. (1972). Systematics of the Breakdown of Mott Insulation in Binary Transition Metal Compounds. *Adv. Phys.* 21, 143–198. doi:10.1080/00018737200101278

Wu, L., Dzade, N. Y., Gao, L., Scanlon, D. O., Öztürk, Z., Hollingsworth, N., et al. (2016). Enhanced Photoresponse of FeS2Films: The Role of Marcasite-Pyrite Phase Junctions. *Adv. Mater.* 28, 9602–9607. doi:10.1002/adma.201602222

Zhang, M.-Y., Cui, Z.-H., and Jiang, H. (2018). Relative Stability of FeS_2 Polymorphs with the Random Phase Approximation Approach. *J. Mater. Chem. A.* 6, 6606–6616. doi:10.1039/c8ta00759d

Zhang, M.-Y., and Jiang, H. (2019). Electronic Band Structure of Cuprous and Silver Halides: An All-Electron *GW* Study. *Phys. Rev. B* 100, 205123. doi:10.1103/physrevb.100.205123

Zhang, M. Y., Cui, Z. H., Wang, Y. C., and Jiang, H. (2020). Hybrid Functionals with System-dependent Parameters: Conceptual Foundations and Methodological Developments. *WIREs Comput. Mol. Scimol. Sci.* 10, 1476. doi:10.1002/wcms.1476

Zuñiga-Puelles, E., Cardoso-Gil, R., Bobnar, M., Veremchuk, I., Himcinschi, C., Hennig, C., et al. (2019). Structural Stability and Thermoelectric Performance of High Quality Synthetic and Natural Pyrites (FeS2). *Dalton Trans.* 48, 10703–10713. doi:10.1039/c9dt01902b

Conflict of Interest: The authors declare that the research was conducted in the absence of any commercial or financial relationships that could be construed as a potential conflict of interest.

Publisher's Note: All claims expressed in this article are solely those of the authors and do not necessarily represent those of their affiliated organizations, or those of the publisher, the editors and the reviewers. Any product that may be evaluated in this article, or claim that may be made by its manufacturer, is not guaranteed or endorsed by the publisher.

frontiers in Chemistry

ORIGINAL RESEARCH
published: 08 October 2021
doi: 10.3389/fchem.2021.746735

Photoemission Spectra from the Extended Koopman's Theorem, Revisited

S. Di Sabatino[1,2,3]*, *J. Koskelo*[2,3], *J. Prodhon*[2], *J. A. Berger*[1,3], *M. Caffarel*[1] and *P. Romaniello*[2,3]*

[1]Laboratoire de Chimie et Physique Quantiques, Université de Toulouse, CNRS, UPS, Toulouse, France, [2]Laboratoire de Physique Théorique, Université de Toulouse, CNRS, UPS, Toulouse, France, [3]European Theoretical Spectroscopy Facility (ETSF), Toulouse, France

The Extended Koopman's Theorem (EKT) provides a straightforward way to compute charged excitations from any level of theory. In this work we make the link with the many-body effective energy theory (MEET) that we derived to calculate the spectral function, which is directly related to photoemission spectra. In particular, we show that at its lowest level of approximation the MEET removal and addition energies correspond to the so-called diagonal approximation of the EKT. Thanks to this link, the EKT and the MEET can benefit from mutual insight. In particular, one can readily extend the EKT to calculate the full spectral function, and choose a more optimal basis set for the MEET by solving the EKT secular equation. We illustrate these findings with the examples of the Hubbard dimer and bulk silicon.

Keywords: extended Koopman's theorem, strong correlation, photoemission, one-body Green's function, RDMFT, QMC

OPEN ACCESS

Edited by:
Dorothea Golze,
Aalto University, Finland

Reviewed by:
Thibaud Etienne,
Universite de Montpellier, France
Katarzyna Pernal,
Lodz University of Technology, Poland

***Correspondence:**
S. Di Sabatino
disabatino@irsamc.ups-tlse.fr
P. Romaniello
romaniello@irsamc.ups-tlse.fr

Specialty section:
This article was submitted to Theoretical and Computational Chemistry, a section of the journal Frontiers in Chemistry

Received: *24 July 2021*
Accepted: *15 September 2021*
Published: *08 October 2021*

Citation:
Di Sabatino S, Koskelo J, Prodhon J, Berger J, Caffarel M and Romaniello P (2021) Photoemission Spectra from the Extended Koopman's Theorem, Revisited. Front. Chem. 9:746735. doi: 10.3389/fchem.2021.746735

1 INTRODUCTION

The Extended Koopman's Theorem (EKT) (Morrell et al., 1975; Smith and Day, 1975) has been derived in quantum chemistry and used within various frameworks, from functional theories based on reduced quantities, such as reduced-density matrix functional theory (Gilbert, 1975) (e.g., Pernal and Cioslowski, 2005; Leiva and Piris, 2005; Piris et al., 2012; Piris et al., 2013) and many-body perturbation theory based on Green's functions (Hedin, 1965) (e.g., Dahlen and van Leeuwen, 2005; Stan et al., 2006; Stan et al., 2009), to wavefunction-based methods (e.g., Cioslowski et al., 1997; Kent et al., 1998; Bozkaya, 2013; Zheng, 2016; Bozkaya and Ünal, 2018; Pavlyukh, 2019; Lee et al., 2021). The EKT allows one to calculate energies corresponding to charged excitations. Although it can be formulated both for ionization potentials (IPs) and electron affinities (EAs), it has been widely used only for the former, whereas for the latter applications have been limited to the calculation of the lowest EA as the first IP of the $(N+1)$-electron system (in case of finite systems), with N the number of electrons in the reference system. There exist hence many benchmarks for the IPs. So far, the method has been mainly used for finite systems. The EKT is known to be in principle (i.e., using exact ingredients, namely the one- and two body density matrices, as we shall see) exact for the first ionization potential (Katriel and Davidson, 1980; Sundholm and Olsen, 1993). In the solid state instead there are only a few applications which only focus on the band structure. It would be desirable to have also the spectral function, i.e., the spectrum of electron addition and removal energies weighted by the Dyson amplitudes, which measure the overlap between the eigenstates of the $(N+1)-$electron ($(N-1)-$electron) system and the ground state of the N-electron system

where an electron has been added (removed). The spectral function is related to photoemission spectroscopy, which gives precious information about the electronic structure and excitations in a system, and, moreover, allows one to study metal-insulator transitions, of paramount importance in condensed matter.

A simple way to calculate the spectral function $A(\omega)$ is through the imaginary part of the one-body Green's function $G(\omega)$, as $A(\omega) = \frac{1}{\pi}\mathrm{sgn}(\mu-\omega)\Im G(\omega)$, where μ is the chemical potential. The one-body Green's function is the fundamental quantity of many-body perturbation theory; it can be obtained from the Dyson equation $G = G_0 + G_0\Sigma G$, in which G_0 and G are the noninteracting and interacting Green's functions, respectively, and Σ the so-called self-energy, which contains all the many-body effects of the system. This latter quantity needs to be approximated in practical calculations. Commonly used approximations, such as the well-known GW approximation (Hedin, 1965), cannot capture the Mott physics (Romaniello et al., 2009; Romaniello et al., 2012; Di Sabatino et al., 2015; Di Sabatino et al., 2016; Di Sabatino et al., 2021). Therefore much effort is devoted to develop better approximations to Σ (Springer et al., 1998; Zhukov et al., 2004; Shishkin et al., 2007; Kuneš et al., 2007; Guzzo et al., 2011; Romaniello et al., 2012; Lischner et al., 2013; Stefanucci et al., 2014) or to develop novel ways to determine G (Lani et al., 2012; Berger et al., 2014). In this spirit in these last years we have developed the many-body effective energy theory (MEET) (Di Sabatino et al., 2016), in which the spectral function is expressed in terms of density matrices, or, alternatively, in terms of moments of G, as reported in Ref. (Di Sabatino et al., 2019). This has allowed us to describe the band gap in several paramagnetic transition-metal oxides (Di Sabatino et al., 2016; Di Sabatino et al., 2019; Di Sabatino et al., 2021), such as NiO, which are considered strongly correlated materials and which are described as metals by static mean-field theories, such as DFT, and by GW. This is an important result. However the band gap is hugely overestimated by the MEET within the current low-order approximation in terms of the (approximate) one- and two-body density matrices. Improvements are needed, either by going to higher-order density matrices, which, however, is not guaranteed to converge, or by introducing some sort of screening in the equations. Recently we have obtained promising results for the description of the insulator-to-metal transition of PM FeO under pressure by combining the MEET and the local-density approximation (LDA) (Di Sabatino et al., 2021), and we are currently working on introducing electron-hole screening in the MEET equations. However there is another path which we can explore, and this comes from the relation between the MEET and the EKT. As we will show in the following, within a given basis, the removal and addition energies obtained within the MEET at the lowest-order approximation are equal to the EKT removal and addition energies within the diagonal approximation. In this work we discuss this link and its impact on both theories.

The paper is organized as follows. In ***Theory*** we give the basic equations of the EKT and the MEET and we make the link between them. The Hubbard dimer and bulk silicon are used to illustrate the difference between the EKT and the MEET (removal and addition) energies in ***Mutual Insights and Illustration***. In ***Conclusions and Perspectives*** we draw our conclusions and perspectives.

2 THEORY

In this section we briefly review the MEET and EKT methods, and we make the link between the two. We will consider an N-electron system governed by the following Hamiltonian in second quantization

$$\hat{H} = \sum_{ij} h_{ij}\hat{a}_i^\dagger\hat{a}_j + \frac{1}{2}\sum_{ijkl} V_{ijkl}\hat{a}_i^\dagger\hat{a}_j^\dagger\hat{a}_l\hat{a}_k,$$

where $\hat{a}$ and $\hat{a}^\dagger$ are the annihilation and creation operator, respectively, $h_{ij} = \int d\mathbf{x}\phi_i^*(\mathbf{x})h(\mathbf{r})\phi_j(\mathbf{x})$ are the matrix elements of the one-particle noninteracting Hamiltonian $h(\mathbf{r}) = -\nabla^2/2 + v_{\mathrm{ext}}(\mathbf{r})$, with v_{ext} an external potential, and $V_{ijkl} = \int d\mathbf{x}d\mathbf{x}'\phi_i^*(\mathbf{x})\phi_j^*(\mathbf{x}')v_c(\mathbf{r},\mathbf{r}')\phi_k(\mathbf{x})\phi_l(\mathbf{x}')$ are the matrix elements of the Coulomb interaction v_c. Here $\mathbf{x} = (\mathbf{r}, \alpha)$ combines space and spin variables and $i, j, \ldots$ denote both space and spin labels (they will be made explicit only when necessary).

2.1 Key Equations of the MEET

Within the MEET the time-ordered 1-body Green's function $G(\omega)$ at zero temperature is split into removal (R) and addition (A) parts as $G(\omega) = G^R(\omega) + G^A(\omega)$. In the following we concentrate on the diagonal elements of G, which are related to photoemission spectra. Within the MEET the diagonal matrix elements of $G^{R/A}(\omega)$ are written in terms of an effective energy $\delta_i^{R/A}(\omega)$ as (Di Sabatino et al., 2016):

$$G_{ii}^R(\omega) = \frac{\gamma_{ii}}{\omega - \delta_i^R(\omega) - i\eta}, \tag{1}$$

$$G_{ii}^A(\omega) = \frac{1-\gamma_{ii}}{\omega - \delta_i^A(\omega) + i\eta}, \tag{2}$$

with γ_{ii} the diagonal matrix element of the one-body density matrix in a given basis set. We note that a similar effective energy can be introduced also for the off-diagonal elements of $G^{R/A}$. The spectral function is hence expressed as

$$A_{ii}(\omega) = \gamma_{ii}\delta(\omega - \delta_i^R(\omega)) + (1-\gamma_{ii})\delta(\omega - \delta_i^A(\omega)), \tag{3}$$

where the symbol δ on the right-hand side indicates the Dirac delta function. In our previous works we have chosen the basis set of natural orbitals, i.e., the orbitals which diagonalize the one-body reduced density matrix. In this case $\gamma_{ii} = n_i$, i.e., the natural occupation numbers. This choice has been made based on our results on exactly solvable Hubbard clusters, where the MEET performs very well. (Di Sabatino et al., 2016) However this does not guarantee that it remains the best choice for more realistic systems. In fact this is not the case as we shall see.

The effective energy $\delta_i^{R/A}(\omega)$ can be written as an expansion in terms of reduced density matrices. The expression truncated at

the level of the one- and two-body reduced density matrices (2-RDM) reads (in the basis of natural orbitals).

$$\delta_i^{R,(1)} = h_{ii} + \frac{1}{n_i}\sum_{klm} V_{imkl}\Gamma^{(2)}_{klmi} \tag{4}$$

$$\delta_i^{A,(1)} = h_{ii} + \frac{1}{(1-n_i)}\sum_{k}(V_{ikik} - V_{ikki})n_k - \frac{1}{(1-n_i)}\sum_{klm} V_{imkl}\Gamma^{(2)}_{klmi}, \tag{5}$$

where $\Gamma^{(2)}_{klmi} = \langle\Psi_0^N|\hat{a}_i^\dagger\hat{a}_m^\dagger\hat{a}_l\hat{a}_k|\Psi_0^N\rangle$ are the matrix elements of the two-body reduced density matrix, with Ψ_0^N the ground-state wavefunction of the N-electron system. As discussed in Ref. (Di Sabatino et al., 2016) the various approximations $\delta_i^{R/A,(n)}(\omega)$ are related to the n-th moments

$$\mu_{n,i}^{R/A} = \frac{\sum_k B_{ii}^{k,R/A}(\epsilon_k^{R/A})^n}{\sum_k B_{ii}^{k,R/A}}$$

of the $G_{ii}^{R/A}(\omega)$. Here $\epsilon_k^R = \left(E_0^N - E_k^{N-1}\right)$ and $\epsilon_k^A = \left(E_k^{N+1} - E_0^N\right)$ are removal and addition energies, respectively, and

$$B_{ii}^{k,R} = \langle\Psi_0^N|\hat{c}_i^\dagger|\Psi_k^{N-1}\rangle\langle\Psi_k^{N-1}|\hat{c}_i|\Psi_0^N\rangle$$
$$B_{ii}^{k,A} = \langle\Psi_0^N|\hat{c}_i|\Psi_k^{N+1}\rangle\langle\Psi_k^{N+1}|\hat{c}_i^\dagger|\Psi_0^N\rangle,$$

with E_0^N and Ψ_0^N the ground-state energy and wave function of the N-electron system and $E_k^{N\pm1}$ and $\Psi_k^{N\pm1}$ the kth state energy and wave function of the $(N\pm1)$-electron system. This allows for a more compact expression of $G_{ii}^{R/A}(\omega)$ as a continued fraction of moments

$$G_{ii}^R = \cfrac{n_i}{\omega - \mu_{1,i}^R \cfrac{\omega - \mu_{1,i}^R \cdots}{\mu_{2,i}^R \omega - \mu_{1,i}^R \cdots}}, \tag{6}$$

(and similarly for G_{ii}^A). More details on the continued fraction expression for G can be found in Refs (Di Sabatino et al., 2016; Di Sabatino et al., 2019). At the level of $\delta^{R/A,(1)}$, the Green's function depends only on the first moment, while neglecting all the higher-order frequency-dependent corrections. As shown in Ref. (Di Sabatino et al., 2019) this means that each component $G_{ii}^{R/A}$ has only one pole which is a weighted average of all the poles of $G_{ii}^{R/A}$. If each component of G has a predominant quasiparticle peak, this is a good approximation, provided that the approximation to the first moment is accurate enough. At the level of $\delta^{R/A,(2)}$ the Green's function depends on the first and second moments; since now the corrections are frequency-dependent more poles appear (namely, two removal and two addition poles for each component of G, which are visible if the corresponding weights are nonzero). This approximation tends to reproduce the two most dominant removal/addition peaks for each component of G. Higher-order moments will produce more poles; however, approximations become quickly uncontrolled (Di Sabatino, 2016), which can lead to unphysical results.

2.2 Key Equations of the EKT

Within the EKT one starts from the following approximation for the removal energy ϵ_i^R (Kent et al., 1998)

$$\epsilon_i^R = -\frac{\langle\Psi_0^N|\hat{O}_i^\dagger[\hat{H},\hat{O}_i]|\Psi_0^N\rangle}{\langle\Psi_0^N|\hat{O}_i^\dagger\hat{O}_i|\Psi_0^N\rangle} \tag{7}$$

with Ψ_0^N the ground-state many-body wave function of the N-electron system, and $\hat{O}_i = \sum_k C_{ki}^R\hat{a}_k$, $\hat{O}_i^\dagger = \sum_k C_{ki}^{R\,*}\hat{a}_k^\dagger$, with $\{C_{ki}^R\}$ a set of coefficients to be determined. The stationary condition (with respect to the coefficients C_{ki}^R) for ϵ_i^R leads to the secular equation

$$(\mathbf{V}^R - \epsilon_i^R\mathbf{S}^R)\mathbf{C}_i^R = 0, \tag{8}$$

with $V_{ij}^R = -\langle\Psi_0^N|\hat{a}_j^\dagger[\hat{H},\hat{a}_i]|\Psi_0^N\rangle$ and S^R the one-body density matrix $S_{ij}^R = \gamma_{ij} = \langle\Psi_0^N|\hat{a}_j^\dagger\hat{a}_i|\Psi_0^N\rangle$. If one defines the matrix $\mathbf{\Lambda}^R = \left[\mathbf{S}^R\right]^{-1}\mathbf{V}^R$ in the basis of natural orbitals, with $S_{ij}^R = n_i\delta_{ij}$ and works out the commutator in V_{ij}^R, one arrives at

$$\Lambda_{ij}^R = \frac{1}{n_i}\left[n_i h_{ji} + \sum_{klm} V_{jmkl}\Gamma^{(2)}_{klmi}\right]. \tag{9}$$

The eigenvalues of Λ^R are the removal energies. (Morrell et al., 1975; Pernal and Cioslowski, 2005) By comparing to **Eq. 4** it becomes clear that the diagonal element of Λ^R are the removal energy of the MEET within the low-order approximation. The diagonal element of Λ^R are also referred in literature as the energies of the EKT within the diagonal approximation (DEKT).

Similar equations hold for the addition energies. One can indeed define the addition energy ϵ_i^A as

$$\epsilon_i^A = \frac{\langle\Psi_0^N|[\hat{H},\hat{O}_i]\hat{O}_i^\dagger|\Psi_0^N\rangle}{\langle\Psi_0^N|\hat{O}_i\hat{O}_i^\dagger|\Psi_0^N\rangle} \tag{10}$$

and in a similar way as for ϵ_i^R we arrive at the eigenvalue equation

$$(\mathbf{V}^A - \epsilon_i^A\mathbf{S}^A)\mathbf{C}_i^A = 0, \tag{11}$$

with $V_{ij}^A = \langle\Psi_0^N|\hat{a}_i[\hat{H},\hat{a}_j^\dagger]|\Psi_0^N\rangle$ and S^A related to the one-body density matrix as $S_{ij}^A = 1 - \gamma_{ij}$. Similarly to the removal energy problem, using the basis of natural orbitals, one can work out the commutator in V_{ij}^A and reformulate the problem in terms of the matrix $\mathbf{\Lambda}^A = \left[\mathbf{S}^A\right]^{-1}\mathbf{V}^A$[1], which reads

$$\Lambda_{ij}^A = \frac{1}{(1-n_i)}\times \left[(1-n_i)h_{ji} + \sum_k\left(V_{jkik} - V_{jkki}\right)n_k - \sum_{klm} V_{jmkl}\Gamma^{(2)}_{klmi}\right]. \tag{12}$$

Again, the diagonal elements of Λ^A are the MEET addition energies within the approximation given in **Eq. 5**.[2]

[1]Since in the basis of natural orbitals the S^R (S^A) matrix is a diagonal matrix with the natural occupation numbers n_i ($1\text{-}n_i$) as elements, the invertibility of this matrix is strictly related to the non-existence of so-called pinned states, i.e. states with occupation numbers equal to 1 or 0. This is an important question that has several consequences (e.g., Giesbertz and van Leeuwen, 2013; Baldsiefen et al., 2015). Here we assume that S^R (S^A) is invertible in a restricted space (of natural orbitals) in which the corresponding KS orbitals are occupied (unoccupied). This is a reasonable assumption.

[2]Note that the standard EKT equations in RDMFT (Morrell et al., 1975) present a prefactor $1/\sqrt{n_i n_j}$ ($1/\sqrt{(1-n_i)(1-n_j)}$) instead of $1/n_i$ ($1/(1-n_i)$) in **Eq. 9** (**Eq. 12**); these two choices yield the same eigenvalues for the matrix $\mathbf{\Lambda}^R$ ($\mathbf{\Lambda}^A$).

3 MUTUAL INSIGHTS AND ILLUSTRATION

Now that we have established the link between the EKT and the MEET we will study how these theories can benefit from mutual insight.

3.1 Hubbard Dimer

We use a modified version of the Hubbard dimer in which the on-site Coulomb interaction is different for the two sites. Its Hamiltonian is given by

$$H = -t \sum_{\substack{i,j=1,2 \\ i\neq j}} \sum_{\sigma} \hat{a}^{\dagger}_{i\sigma}\hat{a}_{j\sigma} + U_1\hat{n}_{1\uparrow}\hat{n}_{1\downarrow} + U_2\hat{n}_{2\uparrow}\hat{n}_{2\downarrow}, \tag{13}$$

where i, j run over the sites, $\hat{n}_{i\sigma} = \hat{a}^{\dagger}_{i\sigma}\hat{a}_{i\sigma}$, U_i is the on-site interaction at site i, $-t$ is the hopping kinetic energy (the site energy ϵ_0 has been set to zero). Contrary to the standard dimer with a unique on-site interaction, in the case of two different on-site interactions the $\Lambda^{R/A}$ are not diagonal in the basis of natural orbitals. Therefore, this model allows us to study the effect of the diagonalization on the removal/addition energies in the diagonal approximation. The model can represent the case of a heteronuclear diatomic molecule in a minimal basis set in which the valence orbitals of the two atoms are of different nature, such as HCl or NiO, for example. We note that also using the asymmetric Hubbard dimer with two different site energies the EKT equations are not diagonal in the basis of natural orbitals, however the difference between EKT and DEKT energies is not significant.

3.1.1 Insights Into the EKT

Making the parallel with the MEET, one can readily define the EKT spectral function as.

$$A^R_{ii}(\omega) = \gamma_{ii}\delta(\omega - \epsilon_i^{EKT,R}), \tag{14}$$

$$A^A_{ii}(\omega) = (1-\gamma_{ii})\delta(\omega - \epsilon_i^{EKT,A}), \tag{15}$$

with γ_{ii} and $1-\gamma_{ii}$ the diagonal matrix element of the one-body density matrix in the basis which diagonalizes Λ^R_{ij} and Λ^A_{ij}, respectively (not necessarily the same for Λ^R_{ij} and Λ^A_{ij}). We notice that the factor γ_{ii} should refer to a proper one-body density matrix, i.e., a one-body density matrix which fulfils the ensemble N-representability constraints. In our case this is guaranteed by the total energy minimization (which includes the constraint $0 \leq n_i \leq 1$) in RDMFT. Moreover, as for the MEET removal (addition) energies (in its lowest-order approximation), the removal (addition) EKT energies can be interpreted in terms of the first moment of G^R_{ii} (G^A_{ii}), i.e., as weighted averages of all the poles of G^R_{ii} (G^A_{ii}) within the basis that diagonalizes the Λ^R (Λ^A) matrix. Indeed, inserting a complete set of eigenstates of the $(N-1)$-electron system in **Eq. 7**, the commutator can be rewritten as

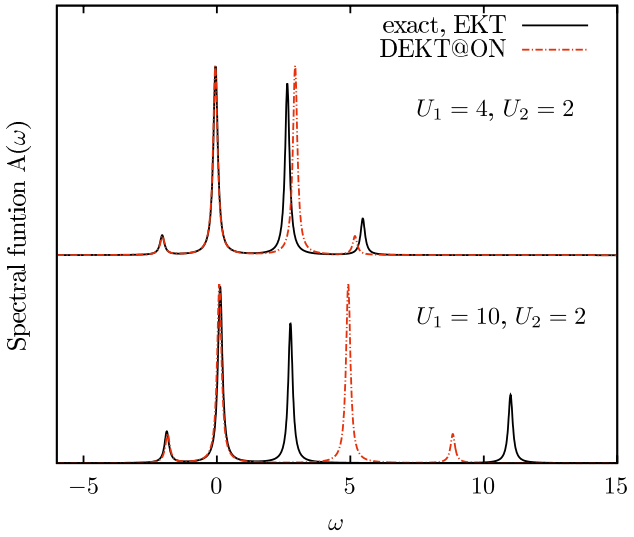

FIGURE 1 | Spectral function of the Hubbard dimer with two different on-site interactions U_1 and U_2 for site 1 and site 2, respectively: exact solution (black curves) *vs.* EKT (black curves, EKT is exact in this case, see text) and DEKT/MEET in the basis of natural orbitals (red curves).

$$\begin{aligned}\epsilon_i^R &= -\sum_k \frac{\langle\Psi_0^N|\hat{O}_i^{\dagger}|\Psi_k^{N-1}\rangle\langle\Psi_k^{N-1}|[\hat{H},\hat{O}_i]|\Psi_0^N\rangle}{\langle\Psi_0^N|\hat{O}_i^{\dagger}\hat{O}_i|\Psi_0^N\rangle} \\ &= -\sum_k \frac{\langle\Psi_0^N|\hat{O}_i^{\dagger}|\Psi_k^{N-1}\rangle\langle\Psi_k^{N-1}|\hat{O}_i|\Psi_0^N\rangle}{\langle\Psi_0^N|\hat{O}_i^{\dagger}\hat{O}_i|\Psi_0^N\rangle}(E_k^{N-1} - E_0^N) \\ &= \frac{\sum_k B_{ii}^{k,R}\epsilon_k^R}{\sum_k B_{ii}^{k,R}},\end{aligned} \tag{16}$$

which is a weighted average of the poles of G^R_{ii}. Inserting a complete set of eigenstates of the $(N+1)$-electron system in **Eq. 10** one can show in a similar way that the $\epsilon_i^A = \sum_k B_{ii}^{k,A}\epsilon_k^A / \sum_k B_{ii}^{k,A}$ within the EKT basis. This means that if there are not satellites in the EKT basis set, then the EKT removal/addition energies are exact, provided that one uses the exact first moment.

We notice that very recently Lee *et al.* (Lee et al., 2021), have also proposed an expression for the spectral function from the EKT.

3.1.2 Insights Into the MEET

Several choices for an optimal basis set for the MEET expressions are now possible. In previous works we considered the basis of natural orbitals as optimal basis set for the MEET based on the following findings (Di Sabatino, 2016): i) the MEET (in this basis of natural orbitals) gives the exact spectral function at all level of approximations for the symmetric Hubbard dimer using exact density matrices; ii) the MEET in its lowest level of approximation in terms of one- and two-body density matrices gives good results for the spectral function of the (symmetric) Hubbard model with

more sites using approximate density matrices. Moreover, for these (symmetric) model systems the $\Lambda^{R/A}$ matrices of the EKT are diagonal in the basis of natural orbitals, therefore there is not another better option. For the asymmetric Hubbard dimer instead, and in general for realistic systems, the basis of natural orbitals does not diagonalize the $\Lambda^{R/A}$ matrices, therefore the set which diagonalizes these matrices can be a better option for the MEET. We notice that this choice of the optimal basis set can be generally applied to other methods which express G as a continued fraction, such as the Lanczos method (Balzer et al., 2011), in order to have more accurate results at a given order of truncation of the series. For example in **Figure 1** we report the spectral function of the Hubbard dimer governed by the Hamiltonian in **Eq. 13** for two different values of $|U_1 - U_2|$. The (D)EKT results are obtained using exact density matrices. The results show that the basis which diagonalizes the $\Lambda^{R/A}$ matrices is a much better choice than the basis of natural orbitals the more the difference $|U_1 - U_2|$ is large. We also observe that the removal part is less affected by the diagonal approximation than the addition part, and we observe this trend also in more complex systems. The diagonal approximation has been addressed in literature also for realistic systems. (Piris et al., 2013; Kent et al., 1998) In particular in bulk silicon QMC results show that the DEKT slightly overestimates the EKT band gaps. Below we will address this system in more details.

3.2 Realistic Systems: The Example of Bulk Si

As an example of realistic systems we use bulk silicon, for which results using the EKT within QMC are reported in Ref. (Kent et al., 1998). The diagonal approximation to the EKT within QMC works very well for the valence states and slightly less well for the conduction states, with a band gap at the Γ point of 4.4 eV *vs.* 3.8 eV from the full EKT compared to 3.4 eV in experiment. (Kent et al., 1998) We note that this discrepency is largely due to the energy of the conduction band at Γ. However, bulk silicon is a relatively weakly correlated system, with hence a predominant quasiparticle-like spectral function for which the EKT is a good approximation. Larger overestimation of the band gap can be expected for strongly correlated systems. This can be understood from the interpretation of the EKT energies as first moments of the one-body Green's function. However, an important point to stress is that even for these systems, which are a challenge for state-of-the-art *ab initio* methods, such as GW, the EKT would open a gap, in accordance with experiment.

As pointed out in Ref. (Kent et al., 1998) the choice of the trial wave function for QMC calculations is of critical importance. Indeed, as a result of the fixed-node approximation, QMC calculations of the matrix elements of the density matrix and operators $\mathbf{V}^{R,A}$ (see EKT **Equations 8**, **11**) are expected to critically depend on the nodal structure of the trial wave function employed. For the weakly correlated bulk silicon the accurate QMC value of 3.8 eV reported above has been obtained by (Kent et al., 1998) using a standard Slater-Jastrow trial wave function whose nodes are those of a single determinant consisting of LDA orbitals. For more strongly correlated systems the wave function acquires a significant multi-determinant character and getting physically meaningful nodes becomes much more difficult. It is thus useful to use the EKT within alternative approaches.

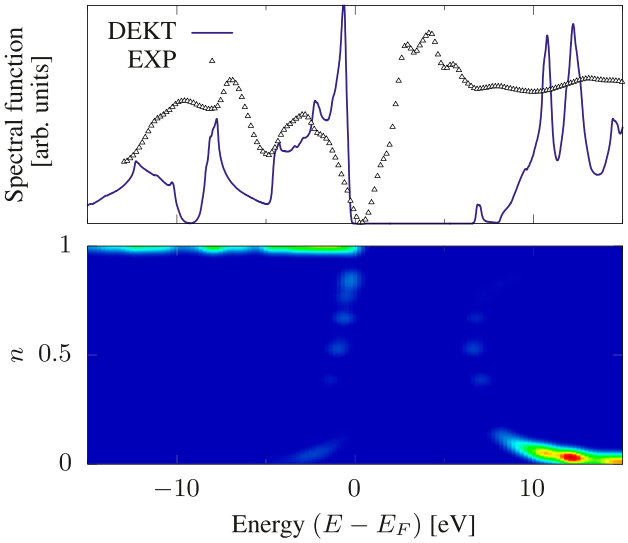

FIGURE 2 | Spectral function of bulk Si within DEKT (violet solid line). The experimental photoemission spectrum (small triangles) is taken from Ref. (Chelikowsky et al., 1989). The color map illustrates the occupation numbers n_i *that play a role into the spectrum for the reported energy range.*

In our previous works (Di Sabatino et al., 2016, 2019, 2021) we used reduced-density matrix functional theory (RDMFT) (Gilbert, 1975) to find approximations to the one- and two-body density matrices which are needed in the MEET equations. More specifically the two-body density matrix in the MEET equations is approximated using the Power functional, which is given by $\Gamma^{(2)}_{ijkl} = n_i n_j \delta_{il}\delta_{jk} - n_i^{\alpha} n_j^{\alpha}\delta_{ik}\delta_{jl}$ ($\alpha = 0.65$). (Sharma et al., 2013) The optimal natural orbitals $\{\phi_i\}$ and occupation numbers $\{n_i\}$ are obtained by minimizing the total energy which is expressed in terms of γ and $\Gamma^{(2)}$, with $\Gamma^{(2)}$ as functional of γ. The Power functional is used also to approximate $\Gamma^{(2)}[\gamma]$ in the energy functional. In this work we use the same protocol for the EKT equations. We implemented the EKT equations in a modified version of the full-potential linearized augmented plane wave (FP-LAPW) code ELK (Elk, 2004), with practical details of the calculations following the scheme described in Ref. (Sharma et al., 2008). For bulk Si we used a lattice constant of 5.43 Å and a Γ-centered 8 × 8 × 8 **k**-point sampling of the Brillouin zone. In **Figure 2** we report the DEKT spectral function of bulk silicon: the direct band gap at Γ is 12.9 eV, while the fundamental band gap is 8.18 eV, which is larger than the experimental one of 1.12 eV (Sze, 1969). We also observe a spurious peak in the band gap due to the fact that the Power functional produces occupation numbers which strongly deviate from 1 and 0 (as one would expect for this weakly correlated system) close to the Fermi energy (see bottom panel of **Figure 2**). This is in contrast with the QMC results. Note that we observe

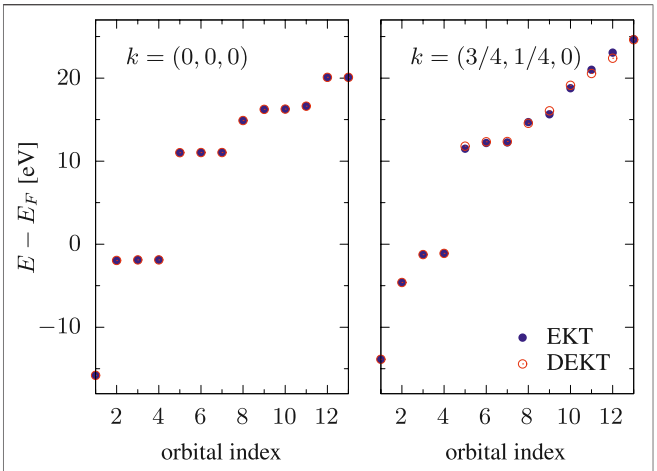

FIGURE 3 | Removal/addition energies of bulk Si: EKT (filled circles) *vs* DEKT (empty circles) for two *k*-points, *k* = (0, 0, 0) and *k* = (3/4, 1/4, 0).

similar deviations from 1 and 0 also for other weakly correlated systems, such as diamond, which points to a problem of the Power functional for the description of occupation numbers of weakly correlated systems. Moreover, the full EKT does not show any improvement over the DEKT, as one can see from **Figure 3**, in which the EKT and DEKT energies are reported: the fundamental band gap is reduced by only 0.06 eV. This is again in contrast with the QMC results in which, although small, there is a significant difference. We attribute this different trend to the use of the Power functional, which contracts the four-point 2-RDM to two points only, and hence probably mitigating the impact of the diagonalization of the $\Lambda^{R/A}$ matrices. These results on bulk Si indicate that, although the EKT/DEKT are expected to overestimate the band gap (even using very accurate density matrices, as for example shown in the case of the Hubbard model (Di Sabatino et al., 2016)), this overestimation can be much amplified by using approximations such as the Power functional. More advanced approximations to $\Gamma^{(2)}$ are hence needed, which give, in particular, more accurate natural occupation numbers. We notice that varying α would change the band gap width. In particular $\alpha = 1$ would give the HF band gap, which still overestimates the experimental one, whereas decreasing α would increase the overestimation of the band gap.

4 CONCLUSIONS AND PERSPECTIVES

We linked our recently derived Many-Body Effective Energy Theory (MEET) for the calculation of photoemission spectra to the Extended Koopman's Theorem (EKT). Within the lowest level of approximation in terms of one- and two-body density matrices, the MEET equations correspond to the so-called diagonal approximation to the EKT (DEKT) equations. This allowed us to readily extend the EKT to the calculation of an approximate spectral function as well as to give an alternative interpretation of the EKT in terms of moments of the one-body Green's function. Using the test case of the Hubbard dimer with two different on-site interactions U_1 and U_2 for site 1 and site 2 we showed the effect of the basis set on the MEET (removal and addition) energies: in particular HOMO-LUMO gap in the basis sets which solve the EKT secular equations (one basis set for the valence part and one for the conduction part) is smaller than the HOMO-LUMO gap obtained using the natural orbital basis set. These results are in line with the EKT results reported in literature for bulk Si using QMC. We have implemented the EKT within reduced-density matrix functional theory (RDMFT), which offers a convenient computationally affordable framework to treat extended systems. However one has to rely on approximate one- and two-body density matrices. We showed that using the currently available approximations the DEKT band gap of Si largely deviates from the DEKT value obtained using QMC (12.9 eV *vs* 4.4 eV at the Γ point) and, moreover, there is no effect of the basis set (EKT *vs* DEKT) on the DEKT energies, contrary to what is observed within QMC, where, although small, there is a significant difference. These results on bulk Si indicate that, although the EKT/DEKT are expected to overestimate the band gap (even using very accurate density matrices), this overestimation can be much amplified by commonly used approximations in RDMFT. This also explains the huge overestimation of the band gap obtained by the MEET within RDMFT in strongly correlated systems such as paramagnetic NiO. We are currently working on improving approximations to correlation in RDMFT by introducing some form of screening (for example the screening due to electron-hole excitations as in GW), which is of particular importance in solids.

DATA AVAILABILITY STATEMENT

The original contributions presented in the study are included in the article/Supplementary Material, further inquiries can be directed to the corresponding authors.

AUTHOR CONTRIBUTIONS

All authors listed have made a substantial, direct, and intellectual contribution to the work and approved it for publication.

FUNDING

This study has been supported through the EUR grant NanoX ANR-17-EURE-0009 in the framework of the "Programme des Investissements d'Avenir" and by ANR (project ANR-18-CE30-0025 and ANR-19-CE30-0011).

REFERENCES

Baldsiefen, T., Cangi, A., and Gross, E. K. U. (2015). Reduced-density-matrix-functional Theory at Finite Temperature: Theoretical Foundations. *Phys. Rev. A.* 92, 052514. doi:10.1103/PhysRevA.92.052514

Balzer, M., Gdaniec, N., and Potthoff, M. (2011). Krylov-space Approach to the Equilibrium and Nonequilibrium Single-Particle Green's Function. *J. Phys. Condens. Matter* 24, 035603. doi:10.1088/0953-8984/24/3/035603

Berger, J. A., Romaniello, P., Tandetzky, F., Mendoza, B. S., Brouder, C., and Reining, L. (2014). Solution to the many-body Problem in One point. *New J. Phys.* 16, 113025. doi:10.1088/1367-2630/16/11/113025

Bozkaya, U. (2013). The Extended Koopmans' Theorem for Orbital-Optimized Methods: Accurate Computation of Ionization Potentials. *J. Chem. Phys.* 139, 154105. doi:10.1063/1.4825041

Bozkaya, U., and Ünal, A. (2018). State-of-the-Art Computations of Vertical Ionization Potentials with the Extended Koopmans' Theorem Integrated with the CCSD(T) Method. *J. Phys. Chem. A.* 122, 4375–4380. doi:10.1021/acs.jpca.8b01851

Chelikowsky, J. R., Wagener, T. J., Weaver, J. H., and Jin, A. (1989). Valence-and Conduction-Band Densities of States for Tetrahedral Semiconductors: Theory and Experiment. *Phys. Rev.* 40, 9644–9651. doi:10.1103/PhysRevB.40.9644

Cioslowski, J., Piskorz, P., and Liu, G. (1997). Ionization Potentials and Electron Affinities from the Extended Koopmans' Theorem Applied to Energy-Derivative Density Matrices: The EKTMPn and EKTQCISD Methods. *J. Chem. Phys.* 107, 6804–6811. doi:10.1063/1.474921

Dahlen, N. E., and van Leeuwen, R. (2005). Self-consistent Solution of the Dyson Equation for Atoms and Molecules within a Conserving Approximation. *J. Chem. Phys.* 122, 164102. doi:10.1063/1.1884965

Di Sabatino, S., Berger, J. A., Reining, L., and Romaniello, P. (2016). Photoemission Spectra from Reduced Density Matrices: The Band gap in Strongly Correlated Systems. *Phys. Rev. B* 94, 155141. doi:10.1103/PhysRevB.94.155141

Di Sabatino, S., Berger, J. A., Reining, L., and Romaniello, P. (2015). Reduced Density-Matrix Functional Theory: Correlation and Spectroscopy. *J. Chem. Phys.* 143, 024108. doi:10.1063/1.4926327

Di Sabatino, S., Berger, J. A., and Romaniello, P. (2019). Many-body Effective Energy Theory: Photoemission at strong Correlation. *J. Chem. Theor. Comput.* 15, 5080–5086. doi:10.1021/acs.jctc.9b00427

Di Sabatino, S., Koskelo, J., Berger, J. A., and Romaniello, P. (2021). Photoemission Spectrum in Paramagnetic Feo under Pressure: Towards an Ab Initio Description. *Phys. Rev. Res.* 3, 013172. doi:10.1103/PhysRevResearch.3.013172

Di Sabatino, S. (2016). *Private Communication.*

Elk (2004). Elk. Available at: http://elk.sourceforge.net.

Giesbertz, K. J. H., and van Leeuwen, R. (2013). Natural Occupation Numbers: When Do They Vanish? *J. Chem. Phys.* 139, 104109. doi:10.1063/1.4820419

Gilbert, T. L. (1975). Hohenberg-kohn Theorem for Nonlocal External Potentials. *Phys. Rev. B* 12, 2111–2120. doi:10.1103/PhysRevB.12.2111

Guzzo, M., Lani, G., Sottile, F., Romaniello, P., Gatti, M., Kas, J. J., et al. (2011). Valence Electron Photoemission Spectrum of Semiconductors:Ab InitioDescription of Multiple Satellites. *Phys. Rev. Lett.* 107, 166401. doi:10.1103/physrevlett.107.166401

Hedin, L. (1965). New Method for Calculating the One-Particle Green's Function with Application to the Electron-Gas Problem. *Phys. Rev.* 139, A796–A823. doi:10.1103/physrev.139.a796

Katriel, J., and Davidson, E. R. (1980). Asymptotic Behavior of Atomic and Molecular Wave Functions. *Proc. Natl. Acad. Sci.* 77, 4403–4406. doi:10.1073/pnas.77.8.4403

Kent, P. R. C., Hood, R. Q., Towler, M. D., Needs, R. J., and Rajagopal, G. (1998). Quantum Monte Carlo Calculations of the One-Body Density Matrix and Excitation Energies of Silicon. *Phys. Rev. B* 57, 15293–15302. doi:10.1103/PhysRevB.57.15293

Kuneš, J., Anisimov, V. I., Skornyakov, S. L., Lukoyanov, A. V., and Vollhardt, D. (2007). Nio: Correlated Band Structure of a Charge-Transfer Insulator. *Phys. Rev. Lett.* 99, 156404. doi:10.1103/PhysRevLett.99.156404

Lani, G., Romaniello, P., and Reining, L. (2012). Approximations for many-body Green's Functions: Insights from the Fundamental Equations. *New J. Phys.* 14, 013056. doi:10.1088/1367-2630/14/1/013056

Lee, J., Malone, F. D., Morales, M. A., and Reichman, D. R. (2021). Spectral Functions from Auxiliary-Field Quantum Monte Carlo without Analytic Continuation: The Extended Koopmans' Theorem Approach. *J. Chem. Theor. Comput.* 17, 3372–3387. PMID: 33983735. doi:10.1021/acs.jctc.1c00100

Leiva, P., and Piris, M. (2005). Assessment of a New Approach for the Two-Electron Cumulant in Natural-Orbital-Functional Theory. *J. Chem. Phys.* 123, 214102. doi:10.1063/1.2135289

Lischner, J., Vigil-Fowler, D., and Louie, S. G. (2013). Physical Origin of Satellites in Photoemission of Doped Graphene: AnAb InitioGWPlus Cumulant Study. *Phys. Rev. Lett.* 110, 146801. doi:10.1103/PhysRevLett.110.146801

Morrell, M. M., Parr, R. G., and Levy, M. (1975). Calculation of Ionization Potentials from Density Matrices and Natural Functions, and the Long-Range Behavior of Natural Orbitals and Electron Density. *J. Chem. Phys.* 62, 549–554. doi:10.1063/1.430509

Pavlyukh, Y. (2019). The Ubiquitous Extended Koopmans' Theorem. *Phys. Status Solidi B* 256, 1800591. doi:10.1002/pssb.201800591

Pernal, K., and Cioslowski, J. (2005). Ionization Potentials from the Extended Koopmans' Theorem Applied to Density Matrix Functional Theory. *Chem. Phys. Lett.* 412, 71–75. doi:10.1016/j.cplett.2005.06.103

Piris, M., Matxain, J. M., Lopez, X., and Ugalde, J. M. (2012). The Extended Koopmans' Theorem: Vertical Ionization Potentials from Natural Orbital Functional Theory. *J. Chem. Phys.* 136, 174116. doi:10.1063/1.4709769

Piris, M., Matxain, J. M., Lopez, X., and Ugalde, J. M. (2013). The One-Electron Picture in the Piris Natural Orbital Functional 5 (Pnof5). *Theor. Chem. Acc.* 132, 1298. doi:10.1007/s00214-012-1298-4

Romaniello, P., Bechstedt, F., and Reining, L. (2012). Beyond theGWapproximation: Combining Correlation Channels. *Phys. Rev. B* 85, 155131. doi:10.1103/physrevb.85.155131

Romaniello, P., Guyot, S., and Reining, L. (2009). The Self-Energy beyond Gw: Local and Nonlocal Vertex Corrections. *J. Chem. Phys.* 131, 154111. doi:10.1063/1.3249965

Sharma, S., Dewhurst, J. K., Lathiotakis, N. N., and Gross, E. K. U. (2008). Reduced Density Matrix Functional for many-electron Systems. *Phys. Rev. B* 78, 201103. doi:10.1103/PhysRevB.78.201103

Sharma, S., Dewhurst, J. K., Shallcross, S., and Gross, E. K. U. (2013). Spectral Density and Metal-Insulator Phase Transition in mott Insulators within Reduced Density Matrix Functional Theory. *Phys. Rev. Lett.* 110, 116403. doi:10.1103/physrevlett.110.116403

Shishkin, M., Marsman, M., and Kresse, G. (2007). Accurate Quasiparticle Spectra from Self-ConsistentGWCalculations with Vertex Corrections. *Phys. Rev. Lett.* 99, 246403. doi:10.1103/PhysRevLett.99.246403

Smith, D. W., and Day, O. W. (1975). Extension of Koopmans' Theorem. I. Derivation. *J. Chem. Phys.* 62, 113–114. doi:10.1063/1.430253

Springer, M., Aryasetiawan, F., and Karlsson, K. (1998). First-PrinciplesT-Matrix Theory with Application to the 6 eV Satellite in Ni. *Phys. Rev. Lett.* 80, 2389–2392. doi:10.1103/PhysRevLett.80.2389

Stan, A., Dahlen, N. E., and Leeuwen, R. v. (2006). Fully Self-Consistent GW Calculations for Atoms and Molecules. *Europhys. Lett.* 76, 298–304. doi:10.1209/epl/i2006-10266-6

Stan, A., Dahlen, N. E., and van Leeuwen, R. (2009). Levels of Self-Consistency in the Gw Approximation. *J. Chem. Phys.* 130, 114105. doi:10.1063/1.3089567

Stefanucci, G., Pavlyukh, Y., Uimonen, A.-M., and van Leeuwen, R. (2014). Diagrammatic Expansion for Positive Spectral Functions beyondGW: Application to Vertex Corrections in the Electron Gas. *Phys. Rev. B* 90, 115134. doi:10.1103/PhysRevB.90.115134

Sundholm, D., and Olsen, J. (1993). The Exactness of the Extended Koopmans' Theorem: A Numerical Study. *J. Chem. Phys.* 98, 3999–4002. doi:10.1063/1.464028

Sze, S. M. (1969). *The Physics of Semiconductor Devices*. New York: Wiley.

Zheng, H. (2016). *First Principles Quantum Monte Carlo Study of Correlated Electronic Systems*. University of Illinois at Urbana-Champaign. Ph.D. thesis.

Zhukov, V. P., Chulkov, E. V., and Echenique, P. M. (2004). Lifetimes of Excited Electrons in Fe and Ni: First-Principles GW and theT-Matrix Theory. *Phys. Rev. Lett.* 93, 096401. doi:10.1103/PhysRevLett.93.096401

Conflict of Interest: The authors declare that the research was conducted in the absence of any commercial or financial relationships that could be construed as a potential conflict of interest.

Publisher's Note: All claims expressed in this article are solely those of the authors and do not necessarily represent those of their affiliated organizations, or those of the publisher, the editors and the reviewers. Any product that may be evaluated in this article, or claim that may be made by its manufacturer, is not guaranteed or endorsed by the publisher.

frontiers in Chemistry

ORIGINAL RESEARCH
published: 29 October 2021
doi: 10.3389/fchem.2021.751054

Scrutinizing GW-Based Methods Using the Hubbard Dimer

S. Di Sabatino[1,2]*, *P.-F. Loos*[1] *and P. Romaniello*[2]

[1]*Laboratoire de Chimie et Physique Quantiques, Université de Toulouse, CNRS, UPS, Toulouse, France,* [2]*Laboratoire de Physique Théorique, Université de Toulouse, CNRS, UPS and ETSF, Toulouse, France*

Using the simple (symmetric) Hubbard dimer, we analyze some important features of the *GW* approximation. We show that the problem of the existence of multiple quasiparticle solutions in the (perturbative) one-shot *GW* method and its partially self-consistent version is solved by full self-consistency. We also analyze the neutral excitation spectrum using the Bethe-Salpeter equation (BSE) formalism within the standard *GW* approximation and find, in particular, that 1) some neutral excitation energies become complex when the electron-electron interaction *U* increases, which can be traced back to the approximate nature of the *GW* quasiparticle energies; 2) the BSE formalism yields accurate correlation energies over a wide range of *U* when the trace (or plasmon) formula is employed; 3) the trace formula is sensitive to the occurrence of complex excitation energies (especially singlet), while the expression obtained from the adiabatic-connection fluctuation-dissipation theorem (ACFDT) is more stable (yet less accurate); 4) the trace formula has the correct behavior for weak (*i.e.*, small *U*) interaction, unlike the ACFDT expression.

Keywords: hubbard dimer, multiple quasiparticle solutions, GW, bethe-salpter equation, trace formula, adiabatic-connection fluctuation-dissipation theorem

OPEN ACCESS

Edited by:
Patrick Rinke,
Aalto University, Finland

Reviewed by:
Gianluca Stefanucci,
University of Rome Tor Vergata, Italy
Maria Hellgren,
Sorbonne Universités, France

***Correspondence:**
S. Di Sabatino
disabatino@irsamc.ups-tlse.fr

Specialty section:
This article was submitted to Theoretical and Computational Chemistry, a section of the journal Frontiers in Chemistry

Received: *31 July 2021*
Accepted: *28 September 2021*
Published: *29 October 2021*

Citation:
Di Sabatino S, Loos P-F and Romaniello P (2021) Scrutinizing GW-Based Methods Using the Hubbard Dimer. Front. Chem. 9:751054. doi: 10.3389/fchem.2021.751054

1 INTRODUCTION

Many-body perturbation theory (MBPT) based on Green's functions is among the standard tools in condensed matter physics for the study of ground- and excited-state properties. (Aryasetiawan and Gunnarsson, 1998; Onida et al., 2002; Martin et al., 2016; Golze et al., 2019). In particular, the *GW* approximation (Hedin, 1965; Golze et al., 2019) has become the method of choice for band-structure and photoemission calculations and, combined with the Bethe-Salpeter equation (BSE@*GW*) formalism, (Salpeter and Bethe, 1951; Strinati, 1988; Albrecht et al., 1998; Rohlfing and Louie, 1998; Benedict et al., 1998; van der Horst et al., 1999a; Blase et al., 2018, 2020), for optical spectra calculations. Thanks to efficient implementations, (Duchemin and Blase, 2019, 2020, 2021; Bruneval et al., 2016; van Setten et al., 2013; Kaplan et al., 2015, 2016; Krause and Klopper, 2017; Caruso et al., 2012, 2013b,a; Caruso, 2013; Wilhelm et al., 2018), this toolkit is acquiring increasing popularity in the traditional quantum chemistry community, (Rohlfing and Louie, 1999; van der Horst et al., 1999b; Puschnig and Ambrosch-Draxl, 2002; Tiago et al., 2003; Boulanger et al., 2014; Jacquemin et al., 2015b; Bruneval et al., 2015; Jacquemin et al., 2015a; Hirose et al., 2015; Jacquemin et al., 2017a,b; Rangel et al., 2017; Krause and Klopper, 2017; Gui et al., 2018; Blase et al., 2018; Liu et al., 2020; Blase et al., 2020; Holzer and Klopper, 2018; Holzer et al., 2018; Loos et al., 2020), partially due to the similarity of the equation structure to that of the standard Hartree-Fock (HF) (Szabo and Ostlund, 1989) or Kohn-Sham (KS) (Hohenberg and Kohn, 1964; Kohn and Sham, 1965) mean-field methods. Several studies of the performance of various flavors of *GW* in atomic and molecular systems are now present in the literature, (Holm

and von Barth, 1998; Stan et al., 2006; Stan et al., 2009; Blase and Attaccalite, 2011; Faber et al., 2011; Bruneval, 2012; Bruneval and Marques, 2013; Bruneval et al., 2015; Karlsson and van Leeuwen, 2016; Bruneval et al., 2016; Bruneval, 2016; Boulanger et al., 2014; Blase et al., 2016; Li et al., 2017; Hung et al., 2016, 2017; van Setten et al., 2015, 2018; Ou and Subotnik, 2016, 2018; Faber, 2014), providing a clearer picture of the *pros* and *cons* of this approach. There are, however, still some open issues, such as 1) how to overcome the problem of multiple quasiparticle solutions, (van Setten et al., 2015; Maggio et al., 2017; Loos et al., 2018; Véril et al., 2018; Duchemin and Blase, 2020; Loos et al., 2020), 2) what is the best way to calculate ground-state total energies, (Casida, 2005; Huix-Rotllant et al., 2011; Caruso et al., 2013b; Casida and Huix-Rotllant, 2016; Colonna et al., 2014; Olsen and Thygesen, 2014; Hellgren et al., 2015; Holzer et al., 2018; Li et al., 2019, 2020; Loos et al., 2020), and 3) what are the limits of the BSE in the simplification commonly used in the so-called Casida equations. (Strinati, 1988; Rohlfing and Louie, 2000; Sottile et al., 2003; Myöhänen et al., 2008; Ma et al., 2009a,b; Romaniello et al., 2009b; Sangalli et al., 2011; Huix-Rotllant et al., 2011; Sakkinen et al., 2012; Zhang et al., 2013; Rebolini and Toulouse, 2016; Olevano et al., 2019; Lettmann and Rohlfing, 2019; Loos and Blase, 2020; Authier and Loos, 2020; Monino and Loos, 2021). In the present work, we address precisely these questions by using a very simple and exactly solvable model, the symmetric Hubbard dimer. Small Hubbard clusters are widely used test systems for the GW approximation (e.g. Verdozzi et al., 1995; Schindlmayr et al., 1998; Pollehn et al., 1998; Puig von Friesen et al., 2010; Romaniello et al., 2009a, 2012). Despite its simplicity, the Hubbard dimer is able to capture lots of the underlying physics observed in more realistic systems, (Romaniello et al., 2009a, 2012; Carrascal et al., 2015, 2018), such as, for example, the nature of the band-gap opening in strongly correlated systems as bulk NiO. (Di Sabatino et al., 2016). Here, we will use it to better understand some features of the *GW* approximation and the BSE@*GW* approach. Of course, care must be taken when extrapolating conclusions to realistic systems.

The paper is organized as follows. **Section 2** provides the key equations employed in MBPT to calculate removal and addition energies (or charged excitations), neutral (or optical) excitation energies, and ground-state correlation energies. In **Sec. 3**, we present and discuss the results that we have obtained for the Hubbard dimer. We finally draw conclusions and perspectives in **Sec. 4**.

2 THEORETICAL FRAMEWORK

In the following we provide the key equations of MBPT (Martin et al., 2016) and, in particular, we discuss how one can calculate ground- and excited-state properties, namely removal and addition energies, spectral function, total energies, and neutral excitation energies. We use atomic units $\hbar = m = e = 1$ and work at zero temperature throughout the paper.

2.1 The *GW* Approximation

Within MBPT a prominent role is played by the one-body Green's function G which has the following spectral representation in the frequency domain:

$$G(\boldsymbol{x}_1, \boldsymbol{x}_2; \omega) = \sum_{\nu} \frac{\psi_\nu(\boldsymbol{x}_1)\psi^*_\nu(\boldsymbol{x}_2)}{\omega - \epsilon_\nu + \mathrm{i}\eta\,\mathrm{sgn}(\epsilon_\nu - \mu)}, \tag{1}$$

where μ is the chemical potential, η is a positive infinitesimal, $\epsilon_\nu = E^{N+1}_\nu - E^N_0$ for $\varepsilon_\nu > \mu$, and $\epsilon_\nu = E^N_0 - E^{N-1}_i$ for $\varepsilon_\nu < \mu$. Here, E^N_ν is the total energy of the νth excited state of the N-electron system ($\nu = 0$ being the ground state). In the case of single-determinant many-body wave functions (such as HF or KS), the so-called Lehmann amplitudes $\psi_\nu(\boldsymbol{x})$ reduce to one-body orbitals and the poles of the Green's function ε_ν to one-body orbital energies.

The one-body Green's function is a powerful quantity that contains a wealth of information about the physical system. In particular, as readily seen from **Eq. 1**, it has poles at the charged excitation energies of the system, which are proper addition/removal energies of the N-electron system. Thus, one can also access the (photoemission) fundamental gap

$$E_\mathrm{g} = I^N - A^N, \tag{2}$$

where $I^N = E^{N-1}_0 - E^N_0$ is the ionization potential and $A^N = E^N_0 - E^{N+1}_0$ is the electron affinity. Moreover, one can straightforwardly obtain the spectral function, which is closely related to photoemission spectra, as

$$A(\boldsymbol{x}_1, \boldsymbol{x}_2; \omega) = \frac{1}{\pi}\mathrm{sgn}(\mu - \omega)\mathrm{Im}G(\boldsymbol{x}_1, \boldsymbol{x}_2; \omega). \tag{3}$$

The ground-state total energy can also be extracted from G using the Galitskii-Migdal (GM) formula (Galitskii and Migdal, 1958)

$$E^\mathrm{GM}_0 = -\frac{\mathrm{i}}{2}\int d\boldsymbol{x}_1 \lim_{2\to 1^+}\left[\mathrm{i}\frac{\partial}{\partial t_1} + h(\boldsymbol{r}_1)\right]G(1,2), \tag{4}$$

where $1 \equiv (\boldsymbol{x}_1, t_1)$ is a space-spin plus time composite variable and $h(\boldsymbol{r}) = -\nabla/2 + v_\mathrm{ext}(\boldsymbol{r})$ is the one-body Hamiltonian, $v_\mathrm{ext}(\boldsymbol{r})$ being the local external potential.

The one-body Green's function can be obtained by solving a Dyson equation of the form $G = G_0 + G_0\Sigma G$, where G_0 is the non-interacting Green's function and the self-energy Σ is an effective potential which contains all the many-body effects of the system under study. In practice, Σ must be approximated and a well-known approximation is the so-called *GW* approximation in which the self-energy reads $\Sigma^{GW} = v_H + \mathrm{i}GW$, where v_H is the classical Hartree potential, and $W = \varepsilon^{-1}v_c$ is the dynamically screened Coulomb interaction, with ε^{-1} the inverse dielectric function and v_c the bare Coulomb interaction. (Hedin, 1965).

The equations stemming from the *GW* approximation should, in principle, be solved self-consistently, since Σ is a functional of G. (Hedin, 1965). Self-consistency, however, is computationally demanding, and one often performs a single *GW* correction (for example using G_0 as starting point one builds W and Σ^{GW} as $\Sigma^{GW} = v_\mathrm{H} + \mathrm{i}G_0W_0$, with $v_\mathrm{H} = -\mathrm{i}v_cG_0$ and $W_0 = [1 + \mathrm{i}v_cG_0G_0]^{-1}v_c$, from

which $G = \{1 - G_0\Sigma^{GW}[G_0]\}^{-1}G_0$). This cost-saving and popular strategy is known as one-shot *GW*. The main drawback of the one-shot *GW* method is its dependence on the starting point (*i.e.*, the orbitals and energies of the HF or KS mean-field eigenstates) originating from its perturbative nature. To overcome this problem, one can introduce some level of self-consistency. Removal/addition energies are thus obtained by solving iteratively the so-called quasiparticle equation

$$\omega = \epsilon_i^{\mathrm{HF}} + \langle \phi_i^{\mathrm{HF}} | \Sigma_{\mathrm{c}}^{GW}(\omega) | \phi_i^{\mathrm{HF}} \rangle. \tag{5}$$

Here, we choose to start from HF spatial orbitals $\phi_i^{\mathrm{HF}}(\boldsymbol{r})$ and energies ϵ_i^{HF}, which are corrected by the (real part of the) correlation contribution of the *GW* self-energy $\Sigma_{\mathrm{c}}^{GW} = \Sigma^{GW} - \Sigma_{\mathrm{HF}}$, where $\Sigma_{\mathrm{HF}} = v_H + \mathrm{i}v_c G$ is the HF (hartree plus exchange) contribution to the self-energy. Σ_c^{GW} is evaluated with G_{HF} at the first iteration, where G_{HF} is the self-consistent solution of $G_{\mathrm{HF}} = G_0 + G_0\Sigma^{\mathrm{HF}}G_{\mathrm{HF}}$. At the nth iteration, Σ_c^{GW} is evaluated as $\Sigma_c^{GW}[G^{n-1}]$, where G^{n-1} has poles at the energies from the $(n-1)$-th iteration of **Eq. 5** and corresponding weights obtained from the Z factors given in **Eq. 6**. As a non-linear equation, **Eq. 5** has potentially many solutions $\epsilon_{i,\nu}^{GW}$. The so-called quasiparticle (QP) solution $\epsilon_{i,\nu=0}^{GW} \equiv \epsilon_i^{\mathrm{QP}}$ has the largest renormalization factor (or spectral intensity)

$$Z_{i,\nu} = \left[1 - \langle \phi_i^{\mathrm{HF}} | \frac{\partial \Sigma_{\mathrm{c}}^{GW}(\omega)}{\partial \omega} | \phi_i^{\mathrm{HF}} \rangle \Big|_{\omega=\epsilon_{i,\nu}^{GW}}\right]^{-1}, \tag{6}$$

while the satellite (sat) peaks $\epsilon_{i,\nu>0}^{GW} \equiv \epsilon_{i,\nu}^{\mathrm{sat}}$ share the remaining of the spectral weight. Moreover, one can show that the following sum rule is fulfilled (von Barth and Holm, 1996)

$$\sum_{\nu} Z_{i,\nu} = 1, \tag{7}$$

where the sum runs over all the solutions of the quasiparticle equation for a given mean-field eigenstate *i*. Throughout this article, *i*, *j*, *k*, and *l* denote general spatial orbitals, *a* and *b* refer to occupied orbitals, *r* and *s* to unoccupied orbitals, while *m* labels single excitations $a \rightarrow r$.

In eigenvalue self-consistent *GW* (commonly abbreviated as ev*GW*), (Hybertsen and Louie, 1986; Shishkin and Kresse, 2007; Blase and Attaccalite, 2011; Faber et al., 2011; Rangel et al., 2016; Gui et al., 2018), one only updates the poles of *G*, while keeping fix the orbitals (or weights). *G* is then used to build Σ^{GW} and *W*. At the *n*th iteration, the removal/addition energies are obtained from the *GW* quasiparticle solutions computed from $G_{n-1}W$ (G_{n-1}) where the satellites are discarded at each iteration. Nonetheless, at the final iteration one can keep the satellite energies to get the full spectral function (**Eq. 3**). In fully self-consistent *GW* (sc*GW*), (Caruso et al., 2012, 2013b,a; Caruso, 2013; Koval et al., 2014), one updates the poles and weights of *G* retaining quasiparticle and satellite energies at each iteration.

It is instructive to mention that, for a conserving approximation, the sum of the intensities corresponding to removal energies equals the number of electrons, *i.e.*, $\sum_{\epsilon_{i,\nu}^{GW} < \mu} Z_{i,\nu} = N$. sc*GW* is an example of conserving approximations, while, in general, the one-shot *GW* does not conserve the number of electrons.

2.2 Bethe-Salpeter Equation

2.2.1 Neutral Excitations

Linear response theory (Oddershede and Jorgensen, 1977; Casida, 1995; Petersilka et al., 1996) in MBPT is described by the Bethe-Salpeter equation. (Strinati, 1988). The standard BSE within the static *GW* approximation (referred to as BSE@*GW* in this work, which means the use of *GW* quasiparticle energies to build the independent-particle excitation energies and of the *GW* self-energy to build the static exchange-correlation kernel) can be recast, assuming a closed-shell reference state, as a non-Hermitian eigenvalue problem known as Casida equations:

$$\begin{pmatrix} \boldsymbol{A}^{\lambda} & \boldsymbol{B}^{\lambda} \\ -\boldsymbol{B}^{\lambda} & -\boldsymbol{A}^{\lambda} \end{pmatrix} \begin{pmatrix} \boldsymbol{X}_m^{\lambda} \\ \boldsymbol{Y}_m^{\lambda} \end{pmatrix} = \Omega_m^{\lambda} \begin{pmatrix} \boldsymbol{X}_m^{\lambda} \\ \boldsymbol{Y}_m^{\lambda} \end{pmatrix}, \tag{8}$$

where Ω_m^{λ} is the *m*th excitation energy with eigenvector $(\boldsymbol{X}_m^{\lambda}\ \boldsymbol{Y}_m^{\lambda})^{\top}$ at interaction strength λ, $^{\top}$ is the matrix transpose, and we have assumed real-valued spatial orbitals. The non-interacting and physical systems correspond to $\lambda = 0$ and 1, respectively. The matrices $\boldsymbol{A}^{\lambda}$ and $\boldsymbol{B}^{\lambda}$ are of size $OV \times OV$, where *O* and *V* are the number of occupied and virtual orbitals, respectively, and $O+V$ is the total number of spatial orbitals. Introducing the so-called Mulliken notation for the bare two-electron integrals

$$(ij|kl) = \iint d\boldsymbol{r}_1 d\boldsymbol{r}_2 \phi_i(\boldsymbol{r}_1)\phi_j(\boldsymbol{r}_1) v_c(\boldsymbol{r}_1 - \boldsymbol{r}_2)\phi_k(\boldsymbol{r}_2)\phi_l(\boldsymbol{r}_2), \tag{9}$$

and the corresponding (static) screened Coulomb potential matrix elements

$$W_{ij,kl}(\omega = 0) = \iint d\boldsymbol{r}_1 d\boldsymbol{r}_2 \phi_i(\boldsymbol{r}_1)\phi_j(\boldsymbol{r}_1) W(\boldsymbol{r}_1, \boldsymbol{r}_2; \omega = 0)\phi_k(\boldsymbol{r}_2)\phi_l(\boldsymbol{r}_2), \tag{10}$$

the BSE matrix elements read (Maggio and Kresse, 2016).

$$A_{ar,bs}^{\lambda,\sigma\sigma'} = \delta_{ab}\delta_{rs}(\epsilon_r^{\mathrm{QP}} - \epsilon_a^{\mathrm{QP}}) + \lambda\left[\alpha_{\sigma\sigma'}(ar|sb) - W_{ab,sr}(\omega = 0)\right], \tag{11a}$$

$$B_{ar,bs}^{\lambda,\sigma\sigma'} = \lambda\left[\alpha_{\sigma\sigma'}(ar|bs) - W_{as,br}(\omega = 0)\right], \tag{11b}$$

where ϵ_i^{QP} are the *GW* quasiparticle energies, and $\alpha_{\uparrow\downarrow} = 2$ and $\alpha_{\uparrow\uparrow} = 0$ for singlet (*i.e.*, spin-conserved) and triplet (*i.e.*, spin-flip) excitations, respectively.

In the absence of instabilities (*i.e.*, when $\boldsymbol{A}^{\lambda} - \boldsymbol{B}^{\lambda}$ is positive-definite), (Dreuw and Head-Gordon, 2005), **Eq. 8** is usually transformed into an Hermitian eigenvalue problem of half the dimension

$$(\boldsymbol{A}^{\lambda} - \boldsymbol{B}^{\lambda})^{1/2}(\boldsymbol{A}^{\lambda} + \boldsymbol{B}^{\lambda})(\boldsymbol{A}^{\lambda} - \boldsymbol{B}^{\lambda})^{1/2}\boldsymbol{V}_m^{\lambda} = (\Omega_m^{\lambda})^2 \boldsymbol{V}_m^{\lambda}, \tag{12}$$

where the excitation amplitudes are

$$(\boldsymbol{X}^{\lambda} + \boldsymbol{Y}^{\lambda})_m = (\Omega_m^{\lambda})^{-1/2}(\boldsymbol{A}^{\lambda} - \boldsymbol{B}^{\lambda})^{+1/2}\boldsymbol{V}_m^{\lambda}, \tag{13a}$$

$$(\boldsymbol{X}^{\lambda} - \boldsymbol{Y}^{\lambda})_m = (\Omega_m^{\lambda})^{+1/2}(\boldsymbol{A}^{\lambda} - \boldsymbol{B}^{\lambda})^{-1/2}\boldsymbol{V}_m^{\lambda}. \tag{13b}$$

Singlet ($\Omega_m^{\uparrow\downarrow} \equiv \Omega_m^{\lambda=1,\uparrow\downarrow}$) and triplet ($\Omega_m^{\uparrow\uparrow} \equiv \Omega_m^{\lambda=1,\uparrow\uparrow}$) excitation energies are obtained by diagonalizing **Eq. 8** at $\lambda = 1$.

2.2.2 Correlation Energies

Our goal here is to compare the BSE correlation energy E_c^{BSE} obtained using two formulas, namely the trace (or plasmon) formula (Rowe, 1968; Ring and Schuck, 1980) and the expression obtained using the adiabatic-connection fluctuation-dissipation theorem (ACFDT) formalism. (Furche and Van Voorhis, 2005; Toulouse et al., 2009, 2010; Hellgren and von Barth, 2010; Angyan et al., 2011; Heßelmann and Görling, 2011; Colonna et al., 2014; Maggio and Kresse, 2016; Holzer et al., 2018; Loos et al., 2020). The two approaches have been recently compared at the random-phase approximation (RPA) level for the case of Be_2, (Li et al., 2020), showing similar improved performances at the RPA@*GW*@PBE level with respect to the RPA@PBE level and an impressive accuracy by introducing BSE (BSE@*GW*@HF) correction in the trace formula. Here we would like to get more insights into the quality of these two approaches.

The ground-state correlation energy within the trace formula is calculated as

$$\begin{aligned} E_c^{\mathrm{Tr@BSE}} &= E_{c,\uparrow\downarrow}^{\mathrm{Tr@BSE}} + E_{c,\uparrow\uparrow}^{\mathrm{Tr@BSE}} \\ &= \frac{1}{2}\left[\sum_m \Omega_m^{\uparrow\downarrow} - \mathrm{Tr}\left(\boldsymbol{A}^{\uparrow\downarrow}\right)\right] + \frac{1}{2}\left[\sum_m \Omega_m^{\uparrow\uparrow} - \mathrm{Tr}\left(\boldsymbol{A}^{\uparrow\uparrow}\right)\right], \end{aligned} \tag{14}$$

where $\boldsymbol{A}^{\sigma\sigma'} \equiv \boldsymbol{A}^{\lambda=1,\sigma\sigma'}$ is defined in **Eq.11a** and Tr denotes the matrix trace. We note that the trace formula is an approximate expression of the correlation energy since it relies on the so-called quasi-boson approximation and on the killing condition on the zeroth-order Slater determinant ground state (Li et al., 2020 for more details). Note that here both sums in **Eq. 14** run over all resonant (hence real- and complex-valued) excitation energies while they are usually restricted to the real-valued resonant BSE excitation energies. Thus, the Tr@BSE correlation energy is potentially a complex-valued function in the presence of singlet and/or triplet instabilities.

The ACFDT formalism, (Furche and Van Voorhis, 2005), instead, provides an in-principle exact expression for the correlation energy within time-dependent density-functional theory (TDDFT). (Runge and Gross, 1984; Petersilka et al., 1996; Ullrich, 2012). In practice, however, one always ends up with an approximate expression, which quality relies on the approximations to the exchange-correlation potential of the KS system and to the kernel of the TDDFT linear response equations. In this work, therefore, we use the ACFDT expression within the BSE formalism and we explore how well it performs and how it compares to the trace **Eq. 14**.

Within the ACFDT framework, only the singlet states do contribute for a closed-shell ground state, and the ground-state BSE correlation energy

$$E_c^{\mathrm{AC@BSE}} = \frac{1}{2}\int_0^1 d\lambda \mathrm{Tr}\left(\boldsymbol{K}^{\uparrow\downarrow}\boldsymbol{P}^{\lambda,\uparrow\downarrow}\right) \tag{15}$$

is obtained via integration along the adiabatic connection path from the non-interacting system at $\lambda = 0$ to the physical system $\lambda = 1$, where

$$\boldsymbol{K} = \begin{pmatrix} \tilde{\boldsymbol{A}}^{\lambda=1} & \boldsymbol{B}^{\lambda=1} \\ \boldsymbol{B}^{\lambda=1} & \tilde{\boldsymbol{A}}^{\lambda=1} \end{pmatrix} \tag{16}$$

is the interaction kernel, (Angyan et al., 2011; Holzer et al., 2018; Loos et al., 2020) $\tilde{A}_{ar,bs}^{\lambda,\sigma\sigma'} = \alpha_{\sigma\sigma'}\lambda(ar|sb)$, and

$$\boldsymbol{P}^{\lambda} = \begin{pmatrix} \boldsymbol{Y}^{\lambda}(\boldsymbol{Y}^{\lambda})^{\top} & \boldsymbol{Y}^{\lambda}(\boldsymbol{X}^{\lambda})^{\top} \\ \boldsymbol{X}^{\lambda}(\boldsymbol{Y}^{\lambda})^{\top} & \boldsymbol{X}^{\lambda}(\boldsymbol{X}^{\lambda})^{\top} \end{pmatrix} - \begin{pmatrix} 0 & 0 \\ 0 & 1 \end{pmatrix} \tag{17}$$

is the correlation part of the two-body density matrix at interaction strength λ. Here again, the AC@BSE correlation energy might become complex-valued in the presence of singlet instabilities.

Note that the trace and ACFDT formulas yield, for any set of eigenstates, the same correlation energy at the RPA level. (Angyan et al., 2011). Moreover, in contrast to density-functional theory where the electron density is fixed along the adiabatic path, (Langreth and Perdew, 1979; Gunnarsson and Lundqvist, 1976; Zhang and Burke, 2004), at the BSE@*GW* level, the density is not maintained as λ varies. Therefore, an additional contribution to **Eq. 15** originating from the variation of the Green's function along the adiabatic connection should, in principle, be added. However, as commonly done within RPA (Toulouse et al., 2009, 2010; Angyan et al., 2011; Colonna et al., 2014) and BSE, (Holzer et al., 2018; Loos et al., 2020), we neglect this additional contribution.

3 RESULTS

As discussed in **Sec. 1**, in this work, we consider the (symmetric) Hubbard dimer as test case, which is governed by the following Hamiltonian

$$\hat{H} = -t\sum_{\sigma=\uparrow,\downarrow}\left(\hat{c}_{1\sigma}^{\dagger}\hat{c}_{2\sigma} + \hat{c}_{2\sigma}^{\dagger}\hat{c}_{1\sigma}\right) + U\left(\hat{n}_{1\uparrow}\hat{n}_{1\downarrow} + \hat{n}_{2\uparrow}\hat{n}_{2\downarrow}\right). \tag{18}$$

Here $\hat{n}_{1\sigma} = \hat{c}_{1\sigma}^{\dagger}\hat{c}_{1\sigma}$ ($\hat{n}_{2\sigma} = \hat{c}_{2\sigma}^{\dagger}\hat{c}_{2\sigma}$) is the spin density operator on site 1 (site 2), $\hat{c}_{1\sigma}^{\dagger}$ and $\hat{c}_{1\sigma}$ ($\hat{c}_{2\sigma}^{\dagger}$ and $\hat{c}_{2\sigma}$) are the creation and annihilation operators for an electron at site 1 (site 2) with spin σ, U is the on-site (spin-independent) interaction, and $-t$ is the hopping kinetic energy. The physics of the Hubbard model arises from the competition between the hopping term, which prefers to delocalize electrons, and the on-site interaction, which favors localization. The ratio U/t is a measure for the relative contribution of both terms and is the intrinsic, dimensionless coupling constant of the Hubbard model, which we use in the following. In this work we consider the dimer at one-half filling.

3.1 Quasiparticle Energies in the *GW* Approximation

We test different flavors of self-consistency in *GW* calculations: one-shot *GW*, ev*GW*, partial self-consistency through the alignment of the chemical potential (psc*GW*), where we shift G_0 or G_{HF} in such a way that the resulting G has the same chemical potential than the shifted G_0 or shifted G_{HF}, (Schindlmayr, 1997), and sc*GW*. In the one-shot formalism, we also test two different starting points: the truly non-interacting Green's function G_0 ($U = 0$) and the HF Green's

function G_{HF}. These two schemes are respectively labeled as G_0W_0 and $G_{\mathrm{HF}}W_{\mathrm{HF}}$ in the following.

The G_0W_0 self-energy (in the site basis) and removal/addition energies are already given in Ref. (Romaniello et al., 2012) for the Hubbard dimer at one-half filling. For completeness we report them in **Supplementary Appendix S1**, together with the renormalization factors, which are discussed in **Sec. 3.1.1**.

Starting from G_{HF}, which reads

$$G_{\mathrm{HF},IJ}(\omega) = \frac{1}{2}\left[\frac{(-1)^{(I-J)}}{\omega - (t+U/2) + \mathrm{i}\eta} + \frac{1}{\omega + (t-U/2) - \mathrm{i}\eta}\right], \quad (19)$$

where I and J run over the sites, the (correlation part of the) $G_{\mathrm{HF}}W_{\mathrm{HF}}$ self-energy is $\Sigma^{GW}_{\mathrm{c},IJ}(\omega) = \Sigma^{GW}_{IJ}(\omega) - \delta_{IJ}U/2$ with

$$\Sigma^{GW}_{\mathrm{c},IJ}(\omega) = \frac{U^2 t}{2h}\left[\frac{1}{\omega - (t+h+U/2) + \mathrm{i}\eta} + \frac{(-1)^{I-J}}{\omega + (t+h-U/2) - \mathrm{i}\eta}\right], \quad (20)$$

where $h = \sqrt{4t^2 + 4Ut}$. Here we used the following expression for the polarizability $P = -iGG$ with elements

$$P_{IJ}(\omega) = \frac{(-1)^{I-J}}{4}\left[\frac{1}{\omega - 2t + \mathrm{i}\eta} - \frac{1}{\omega + 2t - \mathrm{i}\eta}\right] \quad (21)$$

to build the screened interaction $W = v_c + v_c PW$, whose only non-zero matrix elements read

$$W_{II,JJ}(\omega) = U\delta_{IJ} + (-1)^{I-J}\frac{U^2 t}{h}\left[\frac{1}{\omega - h + \mathrm{i}\eta} - \frac{1}{\omega + h - \mathrm{i}\eta}\right] \quad (22)$$

due to the local nature of the electron-electron interaction. The quantities defined in **Eqs 19–22** can then be transformed to the bonding (bn) and antibonding (an) basis (which is used to recast the BSE as **Eq. 8**) thanks to the following expressions:

$$|\mathrm{bn}\rangle = \frac{|1\rangle + |2\rangle}{\sqrt{2}}, |\mathrm{an}\rangle = \frac{|1\rangle - |2\rangle}{\sqrt{2}}. \quad (23)$$

Therefore, the one-shot removal/addition energies read

$$\epsilon_{1,\pm} = +\frac{h}{2} + \frac{U}{2} \pm \frac{\sqrt{(h+2t)^2 + 4tU^2/h}}{2}, \quad (24a)$$

$$\epsilon_{2,\pm} = -\frac{h}{2} + \frac{U}{2} \pm \frac{\sqrt{(h+2t)^2 + 4tU^2/h}}{2}, \quad (24b)$$

with the quasiparticle solutions being $\epsilon^{\mathrm{QP}}_{\mathrm{bn}} = \epsilon_{1,-}$ and $\epsilon^{\mathrm{QP}}_{\mathrm{an}} = \epsilon_{2,+}$, which correspond to the bonding and antibonding energies, respectively. As readily seen in **Eqs 24a**, **24b**, in addition to the quasiparticle, there is a unique satellite per eigenstate given by $\epsilon^{\mathrm{sat}}_{\mathrm{bn}} = \epsilon_{1,+}$ and $\epsilon^{\mathrm{sat}}_{\mathrm{an}} = \epsilon_{2,-}$. Moreover, the closed-form expression of the renormalization factors (**Eq. 6**) reads

$$Z^{\mathrm{QP}}_{\mathrm{bn/an}} = \frac{t\left[h^2 + 2ht + 2U^2 + h\sqrt{(h+2t)^2 + 4tU^2/h}\right]}{h^3 + 4h^2 t + 4ht^2 + 4tU^2 - h^2\sqrt{(h+2t)^2 + 4tU^2/h}} \quad (25)$$

and $Z^{\mathrm{sat}}_{\mathrm{bn/an}} = 1 - Z^{\mathrm{QP}}_{\mathrm{bn/an}}$.

The evGW and scGW calculations were performed numerically using the meromorphic representation of G, following Ref. (Puig von Friesen et al., 2010) with some slight modifications (**Supplementary Appendix S2** for more details). At each iteration, the solution of the Dyson equations for G and W (**Sec. 2.1**) produces extra poles. In order to keep the number of poles under control in scGW, the poles with intensities smaller than a user-defined threshold (set from 10^{-4} to 10^{-6} depending on the ratio U/t) are discarded and the corresponding spectral weight is redistributed among the remaining poles.

In **Figure 1**, we present the spectral function of G (**Eq. 3**) for different values of the ratio U/t (U/t = 1, 5, 10, and 15) and using G_{HF} as starting point. We consider three GW variants: $G_{\mathrm{HF}}W_{\mathrm{HF}}$, ev$GW$, and sc$GW$. For $U/t \lesssim 3$, all the schemes considered here provide a faithful description of the quasiparticle energies. For larger U/t, GW (regardless of the level of self-consistency) tends to underestimate the fundamental gap E_{g} (**Eq. 2**), as shown in the upper left panel of **Figure 2**. $G_{\mathrm{HF}}W_{\mathrm{HF}}$ and evGW give a very similar estimate of E_{g}, whereas the quasiparticle intensity $Z^{\mathrm{QP}}_{\mathrm{bn/an}}$ defined in **Eq. 25** is quite different and overestimated by both methods, at least in the range of U/t considered in **Figure 2** (center left panel).

The main effects of full self-consistency are the reduction of E_{g} (see upper left panel of **Figure 2**), and the creation of extra satellites with decreasing intensity (see upper panel of **Figure 1**). For small U/t, the fundamental gap is similar to the one predicted by other methods while for increasing U/t the agreement worsen and E_{g} is grossly underestimated. The quasiparticle intensity is very similar to the one predicted by $G_{\mathrm{HF}}W_{\mathrm{HF}}$. Concerning the position of the satellites, we observe that the one-shot $G_{\mathrm{HF}}W_{\mathrm{HF}}$ scheme gives the most promising results. Numerical values of quasiparticle and first satellite energies as well as their respective intensities in the spectral functions presented in **Figure 1** are gathered in **Table 1**.

We notice that a similar analysis for H_2 in a minimal basis has been presented in Ref. (Hellgren et al., 2015) with analogous conclusions.

For the sake of completeness, we also report in the bottom left panel of **Figure 2** the total energy calculated using the Galitskii-Migdal formula (**Eq. 4**). Since the Galitskii-Migdal total energy is not stationary with respect to changes in G, one gets meaningful energies only at self-consistency. However, for the Hubbard dimer, we do not observe a significant impact of self-consistency, as one can see from **Figure 1** by comparing the total energy at the $G_{\mathrm{HF}}W_{\mathrm{HF}}$, ev$GW$, and sc$GW$ levels. For each of these schemes which correspond to a different level of self-consistency, the Galitskii-Migdal formula provides accurate total energies only for relatively small U/t ($\lesssim 3$).

If we consider G_{HF} as starting point and we define the chemical potential as $\mu = (\epsilon^{\mathrm{QP}}_{\mathrm{an}} + \epsilon^{\mathrm{QP}}_{\mathrm{bn}})/2$, then the alignment of the chemical potential has no effect on the spectrum, this means that $G_{\mathrm{HF}}W_{\mathrm{HF}}$ and pscGW are equivalent.

3.1.1 G_0: A Bad Starting Point

In the following we will illustrate how the starting point can influence the resulting quasiparticle energies. The Green's

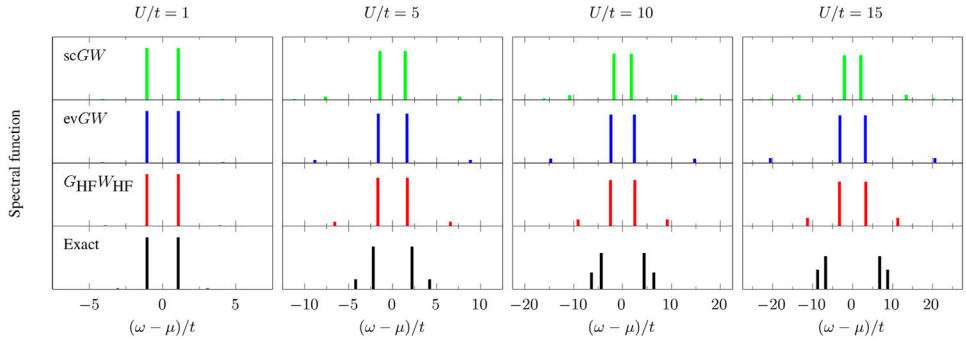

FIGURE 1 | Spectral function of G (**Eq. 3**) as a function of $(\omega-\mu)/t$ (where $\mu = U/2$ is the chemical potential) at various values of the ratio U/t (U/t = 1, 5, 10, and 15) for different levels of theory: exact (black), $G_{HF}W_{HF}$ (red), evGW (blue), and scGW (green). All approximate schemes are obtained using G_{HF} as starting point.

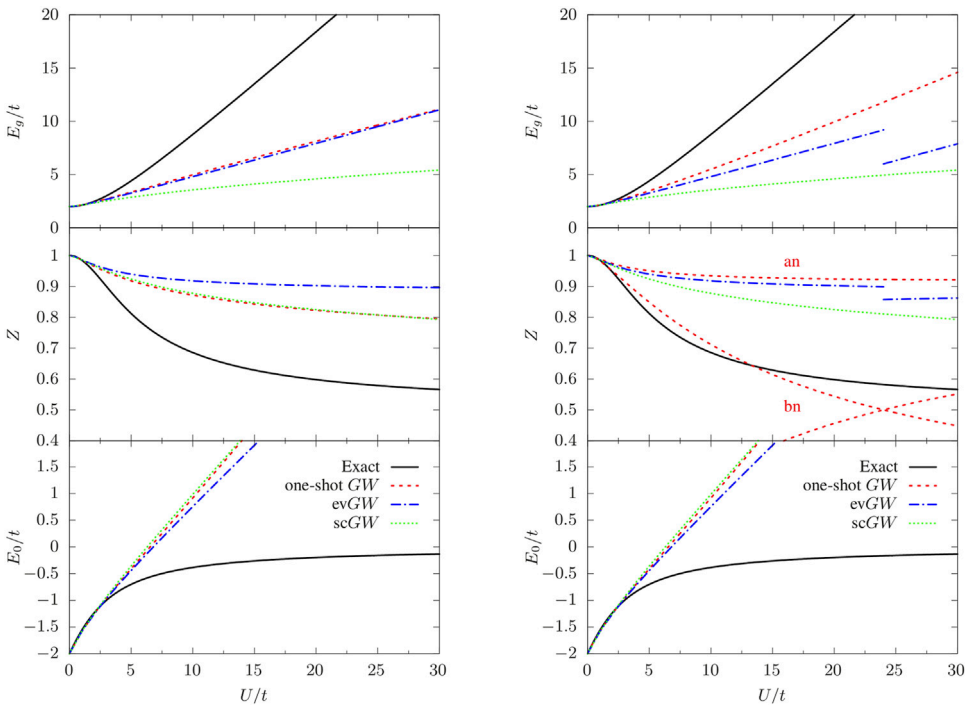

FIGURE 2 | Fundamental gap (E_g), quasiparticle weight factors ($Z^{QP}_{bn/an}$), and ground state energy (E_0) as functions of U/t obtained from one-shot GW (dashed red line), evGW (dashed-dotted blue line), scGW (dotted green line) using G_{HF} **(left)** or G_0 **(right)** as starting point. The black curves are the exact results.

function obtained from the one-shot G_0W_0 does not satisfy particle-hole symmetry, the fundamental gap is underestimated (top right panel of **Figure 2**) yet more accurate than $G_{HF}W_{HF}$ (top left panel of **Figure 2**), the quasiparticle intensity relative to the bonding component is close to the exact result up to $U/t \approx 16$ (center right panel of **Figure 2**), while overestimated for the antibonding components. Moreover, we note that the intensities of the two poles of the bonding component crosses at $U/t = 24$. This means that if we sort the quasiparticle and the satellite according to their intensity at a given U/t, the nature of the two poles is interchanged when one increases U/t, which results in a discontinuity in the QP energy. Meanwhile, the total number of particle is not conserved ($N < 2$). For G_0W_0 we found a small deviation from $N = 2$ for small U/t (e.g. $N = 1.98828$ at $U = 1$), which becomes larger by increasing the interaction (e.g. $N = 1.55485$ for $U/t = 10$). Instead, starting from G_{HF} the particle number is always conserved. We checked that for the self-consistent calculations the total particle number is conserved, as it should.

Considering G_0 as starting point in evGW, we encounter the problem described in Ref. (Véril et al., 2018), namely the discontinuity of various key properties (such as the fundamental gap in the top right panel of **Figure 2**) with respect to the interaction strength U/t. This issue is solved, for

TABLE 1 | Numerical values of quasiparticle energy ϵ_{an}^{QP} and satellite energy ϵ_{an}^{sat} (anti-bonding components) and respective intensities (Z_{an}^{QP} and Z_{an}^{sat}) for the spectral functions presented in **Figure 1**. Energies are relative to the chemical potential $\mu = U/2$. All spectral functions presented in **Figure 1** are symmetric with respect to μ, which means that $\epsilon_{bn}^{QP/sat} = -\epsilon_{an}^{QP/sat}$ and $Z_{bn}^{QP/sat} = Z_{an}^{QP/sat}$.

U/t	ϵ_{an}^{QP}				ϵ_{an}^{sat}				Z_{an}^{QP}				Z_{an}^{sat}			
	Exact	$G_{HF}W_{HF}$	**evGW**	**scGW**	**Exact**	$G_{HF}W_{HF}$	**evGW**	**scGW**	**Exact**	$G_{HF}W_{HF}$	**evGW**	**scGW**	**Exact**	$G_{HF}W_{HF}$	**evGW**	**scGW**
1	1.0615	1.0721	1.0702	1.0651	3.0615	3.9006	4.1175	4.0793	0.9851	0.9855	0.9864	0.9861	0.0149	0.0145	0.0135	0.0132
5	2.2016	1.6739	1.6302	1.4334	4.2016	6.5728	8.8364	7.6389	0.8123	0.9183	0.9398	0.9239	0.1876	0.0817	0.0602	0.0593
10	4.3852	2.4893	2.4001	1.7787	6.3852	9.1225	14.7136	10.8296	0.6857	0.8717	0.9182	0.8777	0.3143	0.1282	0.0818	0.0823
15	6.7621	3.2887	3.1813	2.0542	8.7621	11.2887	20.5769	13.3847	0.6288	0.8430	0.9082	0.8472	0.3712	0.1570	0.0918	0.0934

the Hubbard dimer, by considering a better starting point or using the fully self-consistent scheme sc*GW*. Note, however, that improving the starting point does not always cure the discontinuity problem as this issue stems from the quasiparticle approximation itself. Full self-consistency, instead, avoids systematically discontinuities since no distinction is made between quasiparticle and satellites. Unfortunately, full self-consistency is much more involved from a computational point of view and, moreover, it does not give an overall improvement of the various properties of interest, at least for the Hubbard dimer, for which $G_{HF}W_{HF}$ is to be preferred. For more realistic (molecular) systems, it was shown in Ref. (Berger et al., 2020). that the computationally cheaper self-consistent COHSEX scheme solves the problem of multiple quasiparticle solutions.

3.2 Bethe-Salpeter Equation

For the Hubbard dimer the matrices $\boldsymbol{A}^{\lambda}$ and $\boldsymbol{B}^{\lambda}$ in **Eq. (8)** are just single matrix elements and they simply read, for both spin manifolds,

$$A^{\lambda,\uparrow\downarrow} = \Delta\epsilon^{GW} + \lambda\frac{U}{2},\ B^{\lambda,\uparrow\downarrow} = \lambda\frac{U}{2}\left(\frac{4tU}{h^2}+1\right), \tag{26a}$$

$$A^{\lambda,\uparrow\uparrow} = \Delta\epsilon^{GW} - \lambda\frac{U}{2},\ B^{\lambda,\uparrow\uparrow} = \lambda\frac{U}{2}\left(\frac{4tU}{h^2}-1\right), \tag{26b}$$

while $\tilde{A}^{\lambda,\uparrow\downarrow} = \lambda U$. We employ the screened Coulomb potential given in **Eq. 22** at $\omega = 0$ for the kernel, and the *GW* quasiparticle energies from **Eqs 24a** and **24b** to build the *GW* approximation of the fundamental gap $\Delta\epsilon^{GW} = \epsilon_{an}^{QP} - \epsilon_{bn}^{QP}$. For comparison purposes, we also use the *exact* quasiparticle energies [see Eq. (C3) of Ref. (Romaniello et al., 2012).], which consists in replacing $\Delta\epsilon^{GW}$ by the *exact* fundamental gap $E_g = \sqrt{16t^2+U^2} - 2t$. In such a case, one is able to specifically test how accurate the BSE formalism is at catching the excitonic effect via the introduction of the screened Coulomb potential.

We notice that, within the so-called Tamm-Dancoff approximation (TDA) where one neglects the coupling matrix $\boldsymbol{B}^{\lambda}$ between the resonant and anti-resonant parts of the BSE Hamiltonian (**Eq. 8**), BSE yields RPA with exchange (RPAx) excitation energies for the Hubbard dimer. This is the case also for approximations to the BSE kernel which are beyond *GW*, such as the T-matrix approximation. (Romaniello et al., 2012; Zhang et al., 2017; Li et al., 2021), and it is again related to the local nature of the electron-electron interaction. Hence, to test the effect of approximations on correlation for this model system we must go beyond the TDA.

3.2.1 Neutral Excitations

In **Figure 3**, we report the real part of the singlet and triplet excitation energies obtained from the solution of **Eq. 8** for $\lambda = 1$. For comparison, we report also the exact excitation energies obtained as differences of the excited- and ground-state total energies of the Hubbard dimer obtained by diagonalizing the Hamiltonian (18) in the Slater determinant basis $\{|1\uparrow,1\downarrow\rangle, |1\uparrow,2\downarrow\rangle, |1\downarrow,2\uparrow\rangle, |2\uparrow,2\downarrow\rangle\}$ built from the sites [Ref. (Romaniello et al., 2009a) for the exact total energies]. For the

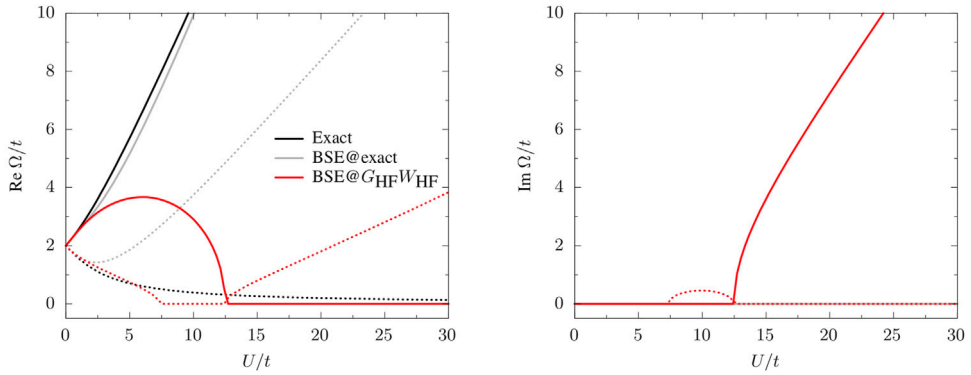

FIGURE 3 | Real and imaginary parts of the singlet (solid) and triplet (dotted) neutral excitations, $\Omega_1^{\uparrow\downarrow}$ and $\Omega_1^{\uparrow\uparrow}$, as functions of U/t: exact (black), BSE with exact quasiparticle energies and W_{HF} (gray), BSE@$G_{HF}W_{HF}$ (red).

singlet manifold, this yields, for the single excitation $\Omega_1^{\uparrow\downarrow}$ and double excitation $\Omega_2^{\uparrow\downarrow}$, the following expressions:

$$\Omega_1^{\uparrow\downarrow} = \frac{1}{2}\left(U + \sqrt{16t^2 + U^2}\right), \Omega_2^{\uparrow\downarrow} = \sqrt{16t^2 + U^2}, \tag{27}$$

while the unique triplet transition energy is

$$\Omega_1^{\uparrow\uparrow} = \frac{1}{2}\left(-U + \sqrt{16t^2 + U^2}\right). \tag{28}$$

Of course, one cannot access the double excitation within the static approximation of BSE, (Strinati, 1988; Romaniello et al., 2009b; Loos and Blase, 2020), so only the lowest singlet and triplet excitations, $\Omega_1^{\uparrow\downarrow}$and $\Omega_1^{\uparrow\uparrow}$, are studied below.

Using one-shot $G_{HF}W_{HF}$ quasiparticle energies (BSE@$G_{HF}W_{HF}$) produces complex excitation energies (see right panel of **Figure 3**). We find the same scenario also with other flavors of *GW* (not reported in the figure), such as sc*GW*. The occurrence of complex poles and singlet/triplet instabilities at the BSE level are well documented (Holzer et al., 2018; Blase et al., 2020; Loos et al., 2020) and is not specific to the Hubbard dimer. For example, one finds complex poles also for H_2 along its dissociation path, (Li and Olevano, 2021), but also for larger diatomic molecules. (Loos et al., 2020). For $U/t > 12.4794$, the singlet energy becomes pure imaginary, the same is observed for the triplet energy for $7.3524 < U/t < 12.4794$. These two points corresponds to discontinuities in the first derivative of the excitation energies with respect to U/t (**Figure 3**). The BSE excitation energies are good approximations to their exact analogs only for $U/t \lesssim 2$ for the singlet and $U/t \lesssim 6$ for the triplet. Using exact quasiparticle energies instead produces real excitation energies, with the singlet energy in very good agreement with the exact result; the triplet energy, instead, largely overestimates the exact value. This seems to suggest that complex poles are caused by the approximate nature of the *GW* quasiparticle energies, although, of course, the quality of the kernel also plays a role. Indeed, setting $W = 0$ but using *GW* QP energies, BSE yields real-valued excitation energies. It would be interesting to further investigate this issue by using the exact kernel together with *GW* QP energies. This is left for future work.

3.2.2 Correlation Energy

For the Hubbard dimer, we have $E^{HF} = -2t + U/2$, and the correlation energy given in **Eq. 15** can be calculated analytically. After a lengthy but simple derivation, one gets

$$E_c^{AC@BSE} = -\frac{U}{2} + \frac{t^2 - 2U^2}{2U(2t+3U)}\left\{\Delta\epsilon^{GW} - \frac{1}{2(t+U)}\sqrt{[-U^2 + 2(t+U)\Delta\epsilon^{GW}][U(2t+3U) + 2(t+U)\Delta\epsilon^{GW}]}\right\} - \frac{t+2U}{2\sqrt{U(2t+3U)}}\left(\frac{3t+4U}{2t+3U} + \frac{t}{U}\right)\Delta\epsilon^{GW} \operatorname{atan}\left\{-\frac{U\sqrt{U(2t+3U)}}{2\Delta\epsilon^{GW}(t+U) + \sqrt{[-U^2 + 2(t+U)\Delta\epsilon^{GW}][U(2t+3U) + 2(t+U)\Delta\epsilon^{GW}]}}\right\}.$$

Results are reported in **Figure 4** and are compared with the exact correlation energy (Romaniello et al., 2009a)

$$E_c = -\frac{\sqrt{16t^2 + U^2}}{2} + 2t. \tag{29}$$

The AC@BSE correlation energy does not possess the correct asymptotic behavior for small U, as Taylor expanding **Eq. 29** for small U, we obtain

$$E_c^{AC@BSE} = -\frac{U^2}{32t} - \frac{5U^3}{96t^2} + \frac{323U^4}{6144t^3} + \mathcal{O}(U^4), \tag{30}$$

while the exact correlation energy behaves as

$$E_c = -\frac{U^2}{16t} + \frac{U^4}{1024t^3} + \mathcal{O}(U^6). \tag{31}$$

Moreover, we found that the radius of convergence of the small-U/t expansion of $E_c^{AC@BSE}$ is very small due to a square-root branch point for $U/t \approx -2/3$.

In the case of the trace formula **Eq. 14**, the singlet and triplet contributions behave as

$$E_{c,\uparrow\downarrow}^{Tr@BSE} = -\frac{U^2}{32t} - \frac{7U^3}{128t^2} + \frac{99U^4}{2048t^3} + \mathcal{O}(U^5), \tag{32a}$$

$$E_{c,\uparrow\uparrow}^{Tr@BSE} = -\frac{U^2}{32t} + \frac{7U^3}{128t^2} - \frac{157U^4}{2048t^3} + \mathcal{O}(U^5), \tag{32b}$$

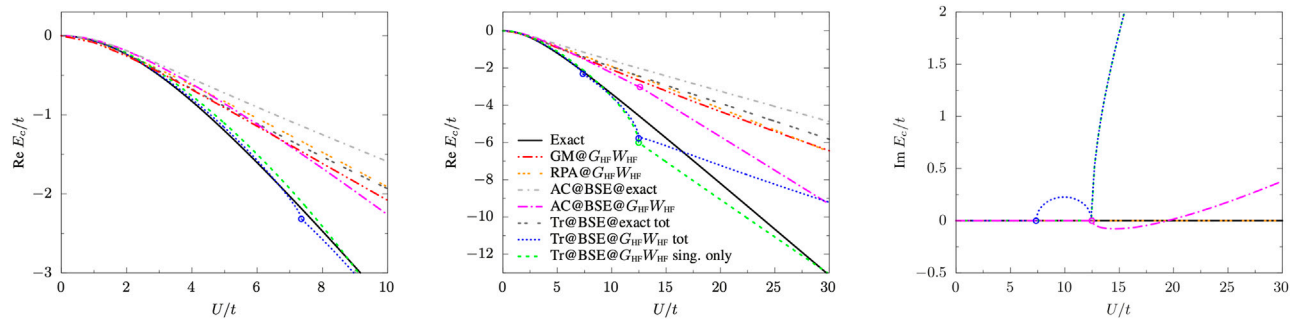

FIGURE 4 | Real and imaginary parts of the BSE@$G_{HF}W_{HF}$ correlation energy as a function of U/t at various levels of theory: total (dotted blue line) and singlet-only (dashed green line) Tr@BSE, AC@BSE (dot-dashed magenta line), RPA (triple-dotted orange line), GM (double-dot-dashed red line), and exact (solid black line). For comparison also the BSE@exact (Tr@BSE, double-dotted dark grey line; AC@BSE, dot-dashed light grey line) correlation energies are shown. Discontinuities in the first derivative of the energy (corresponding to the appearance of complex poles) are indicated by open circles.

which guarantees the correct asymptotic behavior for the total Tr@BSE correlation energy

$$E_c^{\mathrm{Tr@BSE}} = -\frac{U^2}{16t} - \frac{29U^4}{1024t^3} + \mathcal{O}(U^5), \tag{33}$$

and cancels the cubic term (as it should).

The trace formula is strongly affected by the appearance of the imaginary excitation energies: as shown in **Figure 4** where we plot the real and complex components of the BSE@$G_{HF}W_{HF}$ correlation energy as functions of U/t at various levels of theory, irregularities (*i.e.*, discontinuities in the first derivative of the energy) appear at the values of U/t for which the triplet and singlet energies become purely imaginary. The ACFDT expression, instead, is more stable over the range of U/t considered here with only a small cusp on the energy surface at the singlet instability point after which the real part of $E_c^{AC@BSE}$ behaves linearly with respect to U/t. Overall, however, the correlation energy obtained by the trace formula is almost on top of its exact counterpart over a wide range of U/t, with a rather small contribution from the triplet component, *i.e.*, $|E_{c,\uparrow\uparrow}^{\mathrm{Tr@BSE}}| \ll |E_{c,\uparrow\downarrow}^{\mathrm{Tr@BSE}}|$. For comparison purposes, the RPA correlation energy, which is obtained from the trace or ACDFT formula using BSE@$G_{HF}W_{HF}$ with $W = 0$ in the BSE kernel, is also reported in **Figure 4**. Both formulas yield the same correlation energies as expected, and they show no irregularities thanks to the fact that BSE excitation energies are real-valued at the RPA level. Also correlation energies obtained using BSE@exact (also shown in **Figure 4**) do not show irregularities for the same reason. Moreover, they show a visible upshift with respect to the corresponding AC@BSE@$G_{HF}W_{HF}$ and Tr@BSE@$G_{HF}W_{HF}$ results, which worsens the agreement with the exact correlation energy. Finally, we observe that both expressions for the correlation energy (at BSE@*GW* level) produce better results than the Galitskii-Migdal **Eq. 4**, as one can see from **Figure 4**, in particular at large U/t.

4 CONCLUSION

In this work we have used the symmetric Hubbard dimer to better understand some features of the *GW* approximation and of BSE@*GW*. In particular, we have found that the unphysical discontinuities that may occur in quasiparticle energies computed using one-shot or partially self-consistent *GW* schemes disappear using full self-consistency. However, full self-consistency does not give an overall improvement in term of accuracy and, at least for the Hubbard dimer, $G_{HF}W_{HF}$ is to be preferred.

We have also analyzed the performance of the BSE@*GW* approach for neutral excitations and correlation energies. We have found that, at any level of self-consistency, the excitation energies become complex for some critical values of U/t. This seems related to the approximate nature of the *GW* quasiparticle energies, since using exact quasiparticle energies (hence the exact fundamental gap) solves this issue. The BSE excitation energies are good approximations to the exact analogs only for a small range of U/t (or $U/t \lesssim 2$ for the lowest singlet-singlet transition and $U/t \lesssim 6$ for the singlet-triplet transition), while the strong-correlation regime remains a challenge.

The correlation energy obtained from these excitation energies using the trace (or plasmon) formula has been found to be in very good agreement with the exact results over the whole range of U/t for which these energies are real. The occurrence of complex singlet and triplet excitation energies shows up as irregularities in the correlation energy. The ACFDT formula, instead, is less sensitive to this. However, we have found that the AC@BSE correlation energy is less accurate than the one obtained using the trace formula. Both, however, perform better than the standard Galitskii-Migdal formula. Finally, we have studied the small-U expansion of the correlation energy obtained with the trace and ACFDT formulas and we found that the former, contrary to the latter, has the correct behavior when one includes both the singlet and triplet energy contributions. Our findings point out to a possible fundamental problem of the AC@BSE formalism.

Although our study is restricted to the half-filled Hubbard dimer, some of our findings are transferable to realistic (molecular) systems. In particular: 1) a fully self-consistent solution of the *GW* equation cures the problem of multiple QP solutions, avoiding in the process the appearance of discontinuities in key physical quantities such as total or excitation energies, ionization potentials, and electron affinities; 2) a "bad" starting point (G_0 in the case of the Hubbard dimer) may result in the appearence of multiple QP solutions; 3) potential energy surfaces computed with the trace formula and within the ACFDT formalism may exhibit irregularities due to the appearence of complex BSE

excitation energies; 4) for the Hubbard dimer at half-filling, the trace formula has the correct asymptotic behavior (thanks to the inclusion of singlet and triplet excitation energies) for weak interaction, contrary to its ACFDT counterpart. It would be interesting to check if it is also the case in realistic systems.

DATA AVAILABILITY STATEMENT

The original contributions presented in the study are included in the article/**Supplementary Material**, further inquiries can be directed to the corresponding author.

AUTHOR CONTRIBUTIONS

All authors listed have made a substantial, direct, and intellectual contribution to the work and approved it for publication.

FUNDING

This study has been partially supported through the EUR grant NanoX no ANR-17-EURE-0009 in the framework of the "Programme des Investissements d'Avenir" and by the CNRS through the 80|Prime program. PR and SDS also thank the ANR (project ANR-18-CE30-0025) for financial support. PFL also thanks the European Research Council (ERC) under the European Union's Horizon 2020 research and innovation programme (grant agreement no. ~863481) for financial support.

SUPPLEMENTARY MATERIAL

The Supplementary Material for this article can be found online at: https://www.frontiersin.org/articles/10.3389/fchem.2021.751054/full#supplementary-material

REFERENCES

Albrecht, S., Reining, L., Del Sole, R., and Onida, G. (1998). Ab InitioCalculation of Excitonic Effects in the Optical Spectra of Semiconductors. *Phys. Rev. Lett.* 80, 4510–4513. doi:10.1103/PhysRevLett.80.4510

Ángyán, J. G., Liu, R.-F., Toulouse, J., and Jansen, G. (2011). Correlation Energy Expressions from the Adiabatic-Connection Fluctuation-Dissipation Theorem Approach. *J. Chem. Theor. Comput.* 7, 3116–3130. doi:10.1021/ct200501r

Aryasetiawan, F., and Gunnarsson, O. (1998). TheGWmethod. *Rep. Prog. Phys.* 61, 237–312. doi:10.1088/0034-4885/61/3/002

Authier, J., and Loos, P.-F. (2020). Dynamical Kernels for Optical Excitations. *J. Chem. Phys.* 153, 184105. doi:10.1063/5.0028040

Benedict, L. X., Shirley, E. L., and Bohn, R. B. (1998). Optical Absorption of Insulators and the Electron-Hole Interaction: AnAb InitioCalculation. *Phys. Rev. Lett.* 80, 4514–4517. doi:10.1103/PhysRevLett.80.4514

Berger, J. A., Loos, P.-F., and Romaniello, P. (2020). Potential Energy Surfaces without Unphysical Discontinuities: The Coulomb Hole Plus Screened Exchange Approach. *J. Chem. Theor. Comput.* 17, 191–200. doi:10.1021/acs.jctc.0c00896

Blase, X., and Attaccalite, C. (2011). Charge-transfer Excitations in Molecular Donor-Acceptor Complexes within the many-body Bethe-Salpeter Approach. *Appl. Phys. Lett.* 99, 171909. doi:10.1063/1.3655352

Blase, X., Boulanger, P., Bruneval, F., Fernandez-Serra, M., and Duchemin, I. (2016). *GW* and Bethe-Salpeter Study of Small Water Clusters. *J. Chem. Phys.* 144, 034109. doi:10.1063/1.4940139

Blase, X., Duchemin, I., Jacquemin, D., and Loos, P.-F. (2020). The Bethe-Salpeter Equation Formalism: From Physics to Chemistry. *J. Phys. Chem. Lett.* 11, 7371–7382. doi:10.1021/acs.jpclett.0c01875

Blase, X., Duchemin, I., and Jacquemin, D. (2018). The Bethe-Salpeter Equation in Chemistry: Relations with TD-DFT, Applications and Challenges. *Chem. Soc. Rev.* 47, 1022–1043. doi:10.1039/C7CS00049A

Boulanger, P., Jacquemin, D., Duchemin, I., and Blase, X. (2014). Fast and Accurate Electronic Excitations in Cyanines with the many-body Bethe-Salpeter Approach. *J. Chem. Theor. Comput.* 10, 1212–1218. doi:10.1021/ct401101u

Bruneval, F., Hamed, S. M., and Neaton, J. B. (2015). A Systematic Benchmark of the ab initio Bethe-Salpeter Equation Approach for Low-Lying Optical Excitations of Small Organic Molecules. *J. Chem. Phys.* 142, 244101. doi:10.1063/1.4922489

Bruneval, F. (2012). Ionization Energy of Atoms Obtained from *GW* Self-Energy or from Random Phase Approximation Total Energies. *J. Chem. Phys.* 136, 194107. doi:10.1063/1.4718428

Bruneval, F., and Marques, M. A. L. (2013). Benchmarking the Starting Points of the *GW* Approximation for Molecules. *J. Chem. Theor. Comput.* 9, 324–329. doi:10.1021/ct300835h

Bruneval, F. (2016). Optimized Virtual Orbital Subspace for Faster GW Calculations in Localized Basis. *J. Chem. Phys.* 145, 234110. doi:10.1063/1.4972003

Bruneval, F., Rangel, T., Hamed, S. M., Shao, M., Yang, C., and Neaton, J. B. (2016). Molgw 1: Many-body Perturbation Theory Software for Atoms, Molecules, and Clusters. *Computer Phys. Commun.* 208, 149–161. doi:10.1016/j.cpc.2016.06.019

Carrascal, D. J., Ferrer, J., Maitra, N., and Burke, K. (2018). Linear Response Time-dependent Density Functional Theory of the Hubbard Dimer. *Eur. Phys. J. B* 91, 142. doi:10.1140/epjb/e2018-90114-9

Carrascal, D. J., Ferrer, J., Smith, J. C., and Burke, K. (2015). The Hubbard Dimer: A Density Functional Case Study of a many-body Problem. *J. Phys. Condens. Matter* 27, 393001. doi:10.1088/0953-8984/27/39/393001

Caruso, F., Rinke, P., Ren, X., Rubio, A., and Scheffler, M. (2013a). Self-consistentGW: All-Electron Implementation with Localized Basis Functions. *Phys. Rev. B* 88, 075105. doi:10.1103/PhysRevB.88.075105

Caruso, F., Rinke, P., Ren, X., Scheffler, M., and Rubio, A. (2012). Unified Description of Ground and Excited States of Finite Systems: The Self-consistentGWapproach. *Phys. Rev. B* 86, 081102. doi:10.1103/PhysRevB.86.081102

Caruso, F., Rohr, D. R., Hellgren, M., Ren, X., Rinke, P., Rubio, A., et al. (2013b). Bond Breaking and Bond Formation: How Electron Correlation Is Captured in Many-Body Perturbation Theory and Density-Functional Theory. *Phys. Rev. Lett.* 110, 146403. doi:10.1103/PhysRevLett.110.146403

Caruso, F. (2013). "Self-Consistent GW Approach for the Unified Description of Ground and Excited States of Finite Systems,". PhD Thesis (Berlin, Germany: Freie Universität Berlin).

Casida, M. E. (1995). Generalization of the Optimized-Effective-Potential Model to Include Electron Correlation: A Variational Derivation of the Sham-Schlüter Equation for the Exact Exchange-Correlation Potential. *Phys. Rev. A.* 51, 2005–2013. doi:10.1103/PhysRevA.51.2005

Casida, M. E., and Huix-Rotllant, M. (2015). Many-body Perturbation Theory (MBPT) and Time-dependent Density-Functional Theory (TD-DFT): MBPT Insights about what Is Missing in, and Corrections to, the TD-DFT Adiabatic Approximation. *Top. Curr. Chem.* 368, 1–60. doi:10.1007/128_2015_632

Casida, M. E. (2005). Propagator Corrections to Adiabatic Time-dependent Density-Functional Theory Linear Response Theory. *J. Chem. Phys.* 122, 054111. doi:10.1063/1.1836757

Colonna, N., Hellgren, M., and de Gironcoli, S. (2014). Correlation Energy within Exact-Exchange Adiabatic Connection Fluctuation-Dissipation Theory: Systematic Development and Simple Approximations. *Phys. Rev. B* 90, 125150. doi:10.1103/physrevb.90.125150

Di Sabatino, S., Berger, J. A., Reining, L., and Romaniello, P. (2016). Photoemission Spectra from Reduced Density Matrices: The Band gap in Strongly Correlated Systems. *Phys. Rev. B* 94, 155141. doi:10.1103/PhysRevB.94.155141

Dreuw, A., and Head-Gordon, M. (2005). Single-Reference Ab Initio Methods for the Calculation of Excited States of Large Molecules. *Chem. Rev.* 105, 4009–4037. doi:10.1021/cr0505627

Duchemin, I., and Blase, X. (2021). Cubic-Scaling All-Electron GW Calculations with a Separable Density-Fitting Space-Time Approach. *J. Chem. Theor. Comput.* 17, 2383–2393. doi:10.1021/acs.jctc.1c00101

Duchemin, I., and Blase, X. (2020). Robust Analytic-Continuation Approach to many-body GW Calculations. *J. Chem. Theor. Comput.* 16, 1742–1756. doi:10.1021/acs.jctc.9b01235

Duchemin, I., and Blase, X. (2019). Separable Resolution-Of-The-Identity with All-Electron Gaussian Bases: Application to Cubic-Scaling Rpa. *J. Chem. Phys.* 150, 174120. doi:10.1063/1.5090605

Faber, C., Attaccalite, C., Olevano, V., Runge, E., and Blase, X. (2011). First-principlesGWcalculations for DNA and RNA Nucleobases. *Phys. Rev. B* 83, 115123. doi:10.1103/PhysRevB.83.115123

Faber, C. (2014). "Electronic, Excitonic and Polaronic Properties of Organic Systems within the Many-Body GW and Bethe-Salpeter Formalisms: Towards Organic Photovoltaics,". PhD Thesis (Grenoble, France: Université de Grenoble).

Furche, F., and Van Voorhis, T. (2005). Fluctuation-dissipation Theorem Density-Functional Theory. *J. Chem. Phys.* 122, 164106. doi:10.1063/1.1884112

Galitskii, V., and Migdal, A. (1958). Applications of Quantum Field Theory to the many Body Problem. *Sov. Phys. JETP* 7, 96.

Golze, D., Dvorak, M., and Rinke, P. (2019). The Gw Compendium: A Practical Guide to Theoretical Photoemission Spectroscopy. *Front. Chem.* 7, 377. doi:10.3389/fchem.2019.00377

Gui, X., Holzer, C., and Klopper, W. (2018). Accuracy Assessment of GW Starting Points for Calculating Molecular Excitation Energies Using the Bethe-Salpeter Formalism. *J. Chem. Theor. Comput.* 14, 2127–2136. doi:10.1021/acs.jctc.8b00014

Gunnarsson, O., and Lundqvist, B. I. (1976). Exchange and Correlation in Atoms, Molecules, and Solids by the Spin-Density-Functional Formalism. *Phys. Rev. B* 13, 4274–4298. doi:10.1103/PhysRevB.13.4274

Hedin, L. (1965). New Method for Calculating the One-Particle Green's Function with Application to the Electron-Gas Problem. *Phys. Rev.* 139, A796–A823. doi:10.1103/physrev.139.a796

Hellgren, M., Caruso, F., Rohr, D. R., Ren, X., Rubio, A., Scheffler, M., et al. (2015). Static Correlation and Electron Localization in Molecular Dimers from the Self-Consistent RPA andGWapproximation. *Phys. Rev. B* 91, 165110. doi:10.1103/physrevb.91.165110

Hellgren, M., and von Barth, U. (2010). Correlation Energy Functional and Potential from Time-dependent Exact-Exchange Theory. *J. Chem. Phys.* 132, 044101. doi:10.1063/1.3290947

Heßelmann, A., and Görling, A. (2011). Correct Description of the Bond Dissociation Limit without Breaking Spin Symmetry by a Random-Phase-Approximation Correlation Functional. *Phys. Rev. Lett.* 106, 093001. doi:10.1103/PhysRevLett.106.093001

Hirose, D., Noguchi, Y., and Sugino, O. (2015). All-electronGW+Bethe-Salpeter Calculations on Small Molecules. *Phys. Rev. B* 91, 205111. doi:10.1103/physrevb.91.205111

Hohenberg, P., and Kohn, W. (1964). Inhomogeneous Electron Gas. *Phys. Rev.* 136, B864–B871. doi:10.1103/PhysRev.136.B864

Holm, B., and von Barth, U. (1998). Fully Self-consistentGWself-Energy of the Electron Gas. *Phys. Rev. B* 57, 2108–2117. doi:10.1103/PhysRevB.57.2108

Holzer, C., Gui, X., Harding, M. E., Kresse, G., Helgaker, T., and Klopper, W. (2018). Bethe-Salpeter Correlation Energies of Atoms and Molecules. *J. Chem. Phys.* 149, 144106. doi:10.1063/1.5047030

Holzer, C., and Klopper, W. (2018). Communication: A Hybrid Bethe-salpeter/time-dependent Density-Functional-Theory Approach for Excitation Energies. *J. Chem. Phys.* 149, 101101. doi:10.1063/1.5051028

Huix-Rotllant, M., Ipatov, A., Rubio, A., and Casida, M. E. (2011). Assessment of Dressed Time-dependent Density-Functional Theory for the Low-Lying Valence States of 28 Organic Chromophores. *Chem. Phys.* 391, 120–129. doi:10.1016/j.chemphys.2011.03.019

Hung, L., Bruneval, F., Baishya, K., and Öğüt, S. (2017). Benchmarking the GW Approximation and Bethe-Salpeter Equation for Groups IB and IIB Atoms and Monoxides. *J. Chem. Theor. Comput.* 13, 2135–2146. doi:10.1021/acs.jctc.7b00123

Hung, L., da Jornada, F. H., Souto-Casares, J., Chelikowsky, J. R., Louie, S. G., and Öğüt, S. (2016). Excitation Spectra of Aromatic Molecules within a Real-spaceGW-BSE Formalism: Role of Self-Consistency and Vertex Corrections. *Phys. Rev. B* 94, 085125. doi:10.1103/PhysRevB.94.085125

Hybertsen, M. S., and Louie, S. G. (1986). Electron Correlation in Semiconductors and Insulators: Band Gaps and Quasiparticle Energies. *Phys. Rev. B* 34, 5390–5413. doi:10.1103/PhysRevB.34.5390

Jacquemin, D., Duchemin, I., and Blase, X. (2015a). 0-0 Energies Using Hybrid Schemes: Benchmarks of TD-DFT, CIS(D), ADC(2), CC2, and BSE/GW Formalisms for 80 Real-Life Compounds. *J. Chem. Theor. Comput.* 11, 5340–5359. doi:10.1021/acs.jctc.5b00619

Jacquemin, D., Duchemin, I., and Blase, X. (2015b). Benchmarking the Bethe-Salpeter Formalism on a Standard Organic Molecular Set. *J. Chem. Theor. Comput.* 11, 3290–3304. doi:10.1021/acs.jctc.5b00304

Jacquemin, D., Duchemin, I., and Blase, X. (2017a). Is the Bethe-Salpeter Formalism Accurate for Excitation Energies? Comparisons with TD-DFT, CASPT2, and EOM-CCSD. *J. Phys. Chem. Lett.* 8, 1524–1529. doi:10.1021/acs.jpclett.7b00381

Jacquemin, D., Duchemin, I., Blondel, A., and Blase, X. (2017b). Benchmark of Bethe-Salpeter for Triplet Excited-States. *J. Chem. Theor. Comput.* 13, 767–783. doi:10.1021/acs.jctc.6b01169

Kaplan, F., Harding, M. E., Seiler, C., Weigend, F., Evers, F., and van Setten, M. J. (2016). Quasi-Particle Self-Consistent *GW* for Molecules. *J. Chem. Theor. Comput.* 12, 2528–2541. doi:10.1021/acs.jctc.5b01238

Kaplan, F., Weigend, F., Evers, F., and van Setten, M. J. (2015). Off-Diagonal Self-Energy Terms and Partially Self-Consistency in *GW* Calculations for Single Molecules: Efficient Implementation and Quantitative Effects on Ionization Potentials. *J. Chem. Theor. Comput.* 11, 5152–5160. doi:10.1021/acs.jctc.5b00394

Karlsson, D., and van Leeuwen, R. (2016). Partial Self-Consistency and Analyticity in many-body Perturbation Theory: Particle Number Conservation and a Generalized Sum Rule. *Phys. Rev. B* 94, 125124. doi:10.1103/PhysRevB.94.125124

Kohn, W., and Sham, L. J. (1965). Self-consistent Equations Including Exchange and Correlation Effects. *Phys. Rev.* 140, A1133–A1138. doi:10.1103/PhysRev.140.A1133

Koval, P., Foerster, D., and Sánchez-Portal, D. (2014). Fully Self-consistentGWand Quasiparticle Self-consistentGWfor Molecules. *Phys. Rev. B* 89, 155417. doi:10.1103/PhysRevB.89.155417

Krause, K., and Klopper, W. (2017). Implementation of the Bethe–Salpeter Equation in the TURBOMOLE Program. *J. Comput. Chem.* 38, 383–388. doi:10.1002/jcc.24688

Langreth, D. C., and Perdew, J. P. (1979). The Gradient Approximation to the Exchange-Correlation Energy Functional: A Generalization that Works. *Solid State. Commun.* 31, 567–571. doi:10.1016/0038-1098(79)90254-0

Lettmann, T., and Rohlfing, M. (2019). Electronic Excitations of Polythiophene within many-body Perturbation Theory with and without the Tamm-Dancoff Approximation. *J. Chem. Theor. Comput.* 15, 4547–4554. doi:10.1021/acs.jctc.9b00223

Li, J., Chen, Z., and Yang, W. (2021). Renormalized Singles Green's Function in the T-Matrix Approximation for Accurate Quasiparticle Energy Calculation. *J. Phys. Chem. Lett.* 12, 6203–6210. doi:10.1021/acs.jpclett.1c01723

Li, J., Drummond, N. D., Schuck, P., and Olevano, V. (2019). Comparing many-body Approaches against the Helium Atom Exact Solution. *Scipost Phys.* 6, 040. doi:10.21468/SciPostPhys.6.4.040

Li, J., Duchemin, I., Blase, X., and Olevano, V. (2020). Ground-state Correlation Energy of Beryllium Dimer by the Bethe-Salpeter Equation. *Scipost Phys.* 8, 20. doi:10.21468/SciPostPhys.8.2.020

Li, J., Holzmann, M., Duchemin, I., Blase, X., and Olevano, V. (2017). Helium Atom Excitations by the GW and Bethe-Salpeter Many-Body Formalism. *Phys. Rev. Lett.* 118, 163001. doi:10.1103/PhysRevLett.118.163001

Li, J., and Olevano, V. (2021). Hydrogen-molecule Spectrum by the many-body *Gw* Approximation and the Bethe-Salpeter Equation. *Phys. Rev. A.* 103, 012809. doi:10.1103/PhysRevA.103.012809

Liu, C., Kloppenburg, J., Yao, Y., Ren, X., Appel, H., Kanai, Y., et al. (2020). All-electron ab initio Bethe-Salpeter Equation Approach to Neutral Excitations in Molecules with Numeric Atom-Centered Orbitals. *J. Chem. Phys.* 152, 044105. doi:10.1063/1.5123290

Loos, P.-F., and Blase, X. (2020). Dynamical Correction to the Bethe-Salpeter Equation beyond the Plasmon-Pole Approximation. *J. Chem. Phys.* 153, 114120. doi:10.1063/5.0023168

Loos, P.-F., Romaniello, P., and Berger, J. A. (2018). Green Functions and Self-Consistency: Insights from the Spherium Model. *J. Chem. Theor. Comput.* 14, 3071–3082. doi:10.1021/acs.jctc.8b00260

Loos, P.-F., Scemama, A., Duchemin, I., Jacquemin, D., and Blase, X. (2020). Pros and Cons of the Bethe-Salpeter Formalism for Ground-State Energies. *J. Phys. Chem. Lett.* 11, 3536–3545. doi:10.1021/acs.jpclett.0c00460

Ma, Y., Rohlfing, M., and Molteni, C. (2009a). Excited States of Biological Chromophores Studied Using many-body Perturbation Theory: Effects of Resonant-Antiresonant Coupling and Dynamical Screening. *Phys. Rev. B* 80, 241405. doi:10.1103/PhysRevB.80.241405

Ma, Y., Rohlfing, M., and Molteni, C. (2009b). Modeling the Excited States of Biological Chromophores within Many-Body Green's Function Theory. *J. Chem. Theor. Comput.* 6, 257–265. doi:10.1021/ct900528h

Maggio, E., and Kresse, G. (2016). Correlation Energy for the Homogeneous Electron Gas: Exact Bethe-Salpeter Solution and an Approximate Evaluation. *Phys. Rev. B* 93, 235113. doi:10.1103/PhysRevB.93.235113

Maggio, E., Liu, P., van Setten, M. J., and Kresse, G. (2017). GW100: A Plane Wave Perspective for Small Molecules. *J. Chem. Theor. Comput.* 13, 635–648. doi:10.1021/acs.jctc.6b01150

Martin, R. M., Reining, L., and Ceperley, D. (2016). *Interacting Electrons: Theory and Computational Approaches*. New York, NY: Cambridge University Press.

Monino, E., and Loos, P.-F. (2021). Spin-Conserved and Spin-Flip Optical Excitations from the Bethe-Salpeter Equation Formalism. *J. Chem. Theor. Comput.* 17, 2852–2867. doi:10.1021/acs.jctc.1c00074

Myöhänen, P., Stan, A., Stefanucci, G., and van Leeuwen, R. (2008). A many-body Approach to Quantum Transport Dynamics: Initial Correlations and Memory Effects. *Europhys. Lett.* 84, 67001. doi:10.1209/0295-5075/84/67001

Oddershede, J., and Jo/rgensen, P. (1977). An Order Analysis of the Particle-Hole Propagator. *J. Chem. Phys.* 66, 1541–1556. doi:10.1063/1.434118

Olevano, V., Toulouse, J., and Schuck, P. (2019). A Formally Exact One-Frequency-Only Bethe-salpeter-like Equation. Similarities and Differences between Gw+bse and Self-Consistent Rpa. *J. Chem. Phys.* 150, 084112. doi:10.1063/1.5080330

Olsen, T., and Thygesen, K. S. (2014). Static Correlation beyond the Random Phase Approximation: Dissociating H2 with the Bethe-Salpeter Equation and Time-dependent Gw. *J. Chem. Phys.* 140, 164116. doi:10.1063/1.4871875

Onida, G., Reining, L., and Rubio, A. (2002). Electronic Excitations: Density-Functional versus many-body green's Function Approaches. *Rev. Mod. Phys.* 74, 601–659. doi:10.1103/RevModPhys.74.601

Ou, Q., and Subotnik, J. E. (2016). Comparison between *GW* and Wave-Function-Based Approaches: Calculating the Ionization Potential and Electron Affinity for 1D Hubbard Chains. *J. Phys. Chem. A.* 120, 4514–4525. doi:10.1021/acs.jpca.6b03294

Ou, Q., and Subotnik, J. E. (2018). Comparison between the Bethe–Salpeter Equation and Configuration Interaction Approaches for Solving a Quantum Chemistry Problem: Calculating the Excitation Energy for Finite 1D Hubbard Chains. *J. Chem. Theor. Comput.* 14, 527–542. doi:10.1021/acs.jctc.7b00246

Petersilka, M., Gossmann, U. J., and Gross, E. K. U. (1996). Excitation Energies from Time-dependent Density-Functional Theory. *Phys. Rev. Lett.* 76, 1212. doi:10.1103/PhysRevLett.76.1212

Pollehn, T. J., Schindlmayr, A., and Godby, R. W. (1998). Assessment of theGWapproximation Using hubbard Chains. *J. Phys. Condensed Matter* 10, 1273–1283. doi:10.1088/0953-8984/10/6/011

Puig von Friesen, M., Verdozzi, C., and Almbladh, C.-O. (2010). Kadanoff-baym Dynamics of hubbard Clusters: Performance of many-body Schemes, Correlation-Induced Damping and Multiple Steady and Quasi-Steady States. *Phys. Rev. B* 82, 155108. doi:10.1103/PhysRevB.82.155108

Puschnig, P., and Ambrosch-Draxl, C. (2002). Suppression of Electron-Hole Correlations in 3d Polymer Materials. *Phys. Rev. Lett.* 89, 056405. doi:10.1103/PhysRevLett.89.056405

Rangel, T., Hamed, S. M., Bruneval, F., and Neaton, J. B. (2017). An Assessment of Low-Lying Excitation Energies and Triplet Instabilities of Organic Molecules with an *ab initio* Bethe-Salpeter Equation Approach and the Tamm-Dancoff Approximation. *J. Chem. Phys.* 146, 194108. doi:10.1063/1.4983126

Rangel, T., Hamed, S. M., Bruneval, F., and Neaton, J. B. (2016). Evaluating the Gw Approximation with Ccsd(t) for Charged Excitations across the Oligoacenes. *J. Chem. Theor. Comput.* 12, 2834–2842. doi:10.1021/acs.jctc.6b00163

Rebolini, E., and Toulouse, J. (2016). Range-separated Time-dependent Density-Functional Theory with a Frequency-dependent Second-Order Bethe-Salpeter Correlation Kernel. *J. Chem. Phys.* 144, 094107. doi:10.1063/1.4943003

Ring, P., and Schuck, P. (1980). *The Nuclear Many-Body Problem*. New York: Springer-Verlag.

Rohlfing, M., and Louie, S. G. (2000). Electron-hole Excitations and Optical Spectra from First Principles. *Phys. Rev. B* 62, 4927–4944. doi:10.1103/PhysRevB.62.4927

Rohlfing, M., and Louie, S. G. (1998). Electron-hole Excitations in Semiconductors and Insulators. *Phys. Rev. Lett.* 81, 2312–2315. doi:10.1103/PhysRevLett.81.2312

Rohlfing, M., and Louie, S. G. (1999). Optical Excitations in Conjugated Polymers. *Phys. Rev. Lett.* 82, 1959–1962. doi:10.1103/PhysRevLett.82.1959

Romaniello, P., Bechstedt, F., and Reining, L. (2012). Beyond the G W Approximation: Combining Correlation Channels. *Phys. Rev. B* 85, 155131. doi:10.1103/PhysRevB.85.155131

Romaniello, P., Guyot, S., and Reining, L. (2009a). The Self-Energy beyond GW: Local and Nonlocal Vertex Corrections. *J. Chem. Phys.* 131, 154111. doi:10.1063/1.3249965

Romaniello, P., Sangalli, D., Berger, J. A., Sottile, F., Molinari, L. G., Reining, L., et al. (2009b). Double Excitations in Finite Systems. *J. Chem. Phys.* 130, 044108. doi:10.1063/1.3065669

Rowe, D. J. (1968). Methods for Calculating Ground-State Correlations of Vibrational Nuclei. *Phys. Rev.* 175, 1283. doi:10.1103/PhysRev.175.1283

Runge, E., and Gross, E. K. U. (1984). Density-functional Theory for Time-dependent Systems. *Phys. Rev. Lett.* 52, 997–1000. doi:10.1103/PhysRevLett.52.997

Sakkinen, N., Manninen, M., and van Leeuwen, R. (2012). The Kadanoff-Baym Approach to Double Excitations in Finite Systems. *New J. Phys.* 14, 013032. doi:10.1088/1367-2630/14/1/013032

Salpeter, E. E., and Bethe, H. A. (1951). A Relativistic Equation for Bound-State Problems. *Phys. Rev.* 84, 1232. doi:10.1103/PhysRev.84.1232

Sangalli, D., Romaniello, P., Onida, G., and Marini, A. (2011). Double Excitations in Correlated Systems: A many–body Approach. *J. Chem. Phys.* 134, 034115. doi:10.1063/1.3518705

Schindlmayr, A., Pollehn, T. J., and Godby, R. W. (1998). Spectra and Total Energies from Self-Consistent many-body Perturbation Theory. *Phys. Rev. B* 58, 12684–12690. doi:10.1103/PhysRevB.58.12684

Schindlmayr, A. (1997). Violation of Particle Number Conservation in the GW Approximation. *Phys. Rev. B* 56, 3528–3531. doi:10.1103/PhysRevB.56.3528

Shishkin, M., and Kresse, G. (2007). Self-consistent G W Calculations for Semiconductors and Insulators. *Phys. Rev. B* 75, 235102. doi:10.1103/PhysRevB.75.235102

Sottile, F., Olevano, V., and Reining, L. (2003). Parameter-free Calculation of Response Functions in Time-dependent Density-Functional Theory. *Phys. Rev. Lett.* 91, 056402. doi:10.1103/PhysRevLett.91.056402

Stan, A., Dahlen, N. E., and van Leeuwen, R. (2006). Fully Self-Consistent *GW* Calculations for Atoms and Molecules. *Europhys. Lett. EPL* 76, 298–304. doi:10.1209/epl/i2006-10266-6

Stan, A., Dahlen, N. E., and van Leeuwen, R. (2009). Levels of Self-Consistency in the Gw Approximation. *J. Chem. Phys.* 130, 114105. doi:10.1063/1.3089567

Strinati, G. (1988). Application of the Green's Functions Method to the Study of the Optical Properties of Semiconductors. *Riv. Nuovo Cimento* 11, 1–86. doi:10.1007/BF02725962

Szabo, A., and Ostlund, N. S. (1989). *Modern Quantum Chemistry*. New York: McGraw-Hill.

Tiago, M. L., Northrup, J. E., and Louie, S. G. (2003). Ab Initio calculation of the Electronic and Optical Properties of Solid Pentacene. *Phys. Rev. B* 67, 115212. doi:10.1103/PhysRevB.67.115212

Toulouse, J., Gerber, I. C., Jansen, G., Savin, A., and Angyan, J. G. (2009). Adiabatic-connection Fluctuation-Dissipation Density-Functional Theory Based on Range Separation. *Phys. Rev. Lett.* 102, 096404. doi:10.1103/PhysRevLett.102.096404

Toulouse, J., Zhu, W., Angyan, J. G., and Savin, A. (2010). Range-separated Density-Functional Theory with the Random-phase Approximation:

Detailed Formalism and Illustrative Applications. *Phys. Rev. A.* 82, 032502. doi:10.1103/PhysRevA.82.032502

Ullrich, C. (2012). *Time-Dependent Density-Functional Theory: Concepts and Applications. Oxford Graduate Texts*. New York: Oxford University Press.

van der Horst, J.-W., Bobbert, P. A., Michels, M. A. J., Brocks, G., and Kelly, P. J. (1999a). Ab Initio calculation of the Electronic and Optical Excitations in Polythiophene: Effects of Intra- and Interchain Screening. *Phys. Rev. Lett.* 83, 4413–4416. doi:10.1103/PhysRevLett.83.4413

van der Horst, J.-W., Bobbert, P. A., Michels, M. A. J., Brocks, G., and Kelly, P. J. (1999b). Ab Initio calculation of the Electronic and Optical Excitations in Polythiophene: Effects of Intra- and Interchain Screening. *Phys. Rev. Lett.* 83, 4413–4416. doi:10.1103/PhysRevLett.83.4413

van Setten, M. J., Caruso, F., Sharifzadeh, S., Ren, X., Scheffler, M., Liu, F., et al. (2015). *GW* 100: Benchmarking $G_0 W_0$ for Molecular Systems. *J. Chem. Theor. Comput.* 11, 5665–5687. doi:10.1021/acs.jctc.5b00453

van Setten, M. J., Costa, R., Viñes, F., and Illas, F. (2018). Assessing *GW* Approaches for Predicting Core Level Binding Energies. *J. Chem. Theor. Comput.* 14, 877–883. doi:10.1021/acs.jctc.7b01192

van Setten, M. J., Weigend, F., and Evers, F. (2013). The *GW* -Method for Quantum Chemistry Applications: Theory and Implementation. *J. Chem. Theor. Comput.* 9, 232–246. doi:10.1021/ct300648t

Verdozzi, C., Godby, R. W., and Holloway, S. (1995). Evaluation of *GW* Approximations for the Self-Energy of a hubbard Cluster. *Phys. Rev. Lett.* 74, 2327–2330. doi:10.1103/PhysRevLett.74.2327

Véril, M., Romaniello, P., Berger, J. A., and Loos, P. F. (2018). Unphysical Discontinuities in Gw Methods. *J. Chem. Theor. Comput.* 14, 5220. doi:10.1021/acs.jctc.8b00745

von Barth, U., and Holm, B. (1996). Self-consistent GW 0 Results for the Electron Gas: Fixed Screened Potential W 0 within the Random-phase Approximation. *Phys. Rev. B* 54, 8411. doi:10.1103/PhysRevB.54.8411

Wilhelm, J., Golze, D., Talirz, L., Hutter, J., and Pignedoli, C. A. (2018). Toward Gw Calculations on Thousands of Atoms. *J. Phy. Chem. Lett.* 9, 306–312. doi:10.1021/acs.jpclett.7b02740

Zhang, D., Steinmann, S. N., and Yang, W. (2013). Dynamical Second-Order Bethe-Salpeter Equation Kernel: A Method for Electronic Excitation beyond the Adiabatic Approximation. *J. Chem. Phys.* 139, 154109. doi:10.1063/1.4824907

Zhang, D., Su, N. Q., and Yang, W. (2017). Accurate Quasiparticle Spectra from the T-Matrix Self-Energy and the Particle–Particle Random Phase Approximation. *J. Phys. Chem. Lett.* 8, 3223–3227. doi:10.1021/acs.jpclett.7b01275

Zhang, F., and Burke, K. (2004). Adiabatic Connection for Near Degenerate Excited States. *Phys. Rev. A.* 69, 052510. doi:10.1103/PhysRevA.69.052510

Conflict of Interest: The authors declare that the research was conducted in the absence of any commercial or financial relationships that could be construed as a potential conflict of interest.

Publisher's Note: All claims expressed in this article are solely those of the authors and do not necessarily represent those of their affiliated organizations or those of the publisher, the editors, and the reviewers. Any product that may be evaluated in this article or claim that may be made by its manufacturer is not guaranteed or endorsed by the publisher.

frontiers in Chemistry

ORIGINAL RESEARCH
published: 25 November 2021
doi: 10.3389/fchem.2021.746162

The GW/BSE Method in Magnetic Fields

Christof Holzer[1], *Ansgar Pausch*[2] *and Wim Klopper*[2,3]*

[1]Institute of Theoretical Solid State Physics, Karlsruhe Institute of Technology (KIT), Karlsruhe, Germany, [2]Institute of Physical Chemistry, Karlsruhe Institute of Technology (KIT), Karlsruhe, Germany, [3]Institute of Nanotechnology, Karlsruhe Institute of Technology (KIT), Eggenstein-Leopoldshafen, Germany

The *GW* approximation and the Bethe–Salpeter equation have been implemented into the TURBOMOLE program package for computations of molecular systems in a strong, finite magnetic field. Complex-valued London orbitals are used as basis functions to ensure gauge-invariant computational results. The implementation has been benchmarked against triplet excitation energies of 36 small to medium-sized molecules against reference values obtained at the approximate coupled-cluster level (CC2 approximation). Finally, a spectacular change of colour from orange to green of the tetracene molecule is induced by applying magnetic fields between 0 and 9,000 T perpendicular to the molecular plane.

Keywords: GW, Bethe-Salpeter, excitation energy, magnetic field, density functional theory

OPEN ACCESS

Edited by:
Linn Leppert,
University of Twente, Netherlands

Reviewed by:
Xinguo Ren,
Institute of Physics (CAS), China
Antonios Alvertis,
Lawrence Berkeley National Laboratory, United States

***Correspondence:**
Wim Klopper
klopper@kit.edu

Specialty section:
This article was submitted to Theoretical and Computational Chemistry, a section of the journal Frontiers in Chemistry

Received: *23 July 2021*
Accepted: *19 October 2021*
Published: *25 November 2021*

Citation:
Holzer C, Pausch A and Klopper W (2021) The GW/BSE Method in Magnetic Fields. Front. Chem. 9:746162. doi: 10.3389/fchem.2021.746162

1 INTRODUCTION

The description of excited states of molecules in strong magnetic fields poses a major challenge for quantum chemical methods. (Delos et al., 1983; Turbiner and López Vieyra, 2004; Hampe and Stopkowicz, 2017; Stopkowicz, 2018; Hampe and Stopkowicz, 2019; Wibowo et al., 2021). On the one hand, it is well known that introducing magnetic fields also introduces a gauge-dependence when standard, real-valued Gaussian-type basis functions are used. As a solution, as proposed by London, a complex phase factor countering the gauge-dependence of the magnetic field, can be used. (London, 1937; Helgaker and Jørgensen, 1991; Ruud et al., 1993; Tellgren et al., 2008). This in turn leads to complex-valued basis functions, which significantly increase the cost of subsequent calculations. On the other hand, many "work-horse" methods used to describe excited states as linear-response (LR) time-dependent density functional theory (TD-DFT) cannot be straightforwardly adapted to include arbitrary magnetic fields due to instabilities occurring in the respective non-collinear exchange-correlation (XC) kernel. The instabilities in the XC kernel are related to the same instabilities that also plague other non-collinear TD-DFT kernels in, for example, relativistic two-component TD-DFT. (Gao et al., 2005; Egidi et al., 2017; Komorovsky et al., 2019). While solutions to these problems have been proposed, they inevitably lead to XC kernels that do not exhibit full rotational invariance. (Egidi et al., 2017; Komorovsky et al., 2019). Contrary to TD-DFT, coupled-cluster methods are not plagued by any instabilities, but suffer from their steep cost, which increases exponentially with their accuracy. Furthermore, the complex gauge-independent London atomic orbitals lead to another steep increase in the computational complexity, effectively preventing calculations on systems with more than a few electrons. (Hampe and Stopkowicz, 2017; Hampe et al., 2020). Even though the computational limitations are severe, the investigation of molecular properties in strong external magnetic fields has become an increasingly popular topic within the field of quantum chemistry in recent years. Several field-dependent properties including non-linear effects on the electronic structure of small molecules, (Tellgren et al., 2008; Tellgren et al., 2009; Lange et al., 2012;

Stopkowicz et al., 2015), molecular geometries, (Tellgren et al., 2012; Irons et al., 2021), spin-phase transitions (Sun et al., 2019a) and excited state properties (Sun et al., 2019b; Sen et al., 2019; Stetina et al., 2019; Wibowo et al., 2021) have been explored using quantum-chemical methods at different levels of theory.

Since the largest magnetic field currently created on Earth exhibits a field strength of about 100 T, (Sims et al., 2008), there is hardly any need to treat strong magnetic fields in more than a perturbative manner from an experimental point of view. Still, scientific curiosity has for a long time been a strong motor to investigate also situations which are (currently) not directly accessible. Given the lack of experimental data, highly accurate quantum-chemical methods are desirable in order to explore molecular properties in the field regime of >100 tesla.

With the *GW*/Bethe–Salpeter equation (BSE) method, a suitable way of calculating properties from Kohn-Sham (KS) reference states has emerged within the last few years. (Bruneval et al., 2015; Jacquemin et al., 2015; Leng et al., 2016; Holzer and Klopper, 2017; Krause and Klopper, 2017; Gui et al., 2018; Blase et al., 2020; Kehry et al., 2020). It has seen great success, exhibiting a more favourable behaviour than TD-DFT on many occasions. While both TD-DFT and the *GW*/BSE method start from the same Kohn-Sham reference, *GW*/BSE fully accounts for charge-transfer and Rydberg excitations due to its correct asymptotic long-range behaviour. (Sagmeister and Ambrosch-Draxl, 2009; Blase and Attaccalite, 2011; Blase et al., 2011; Blase et al., 2018). Furthermore, the description of core excitations is significantly improved within the *GW*/BSE method. (Olovsson et al., 2009; Vinson et al., 2011; Kehry et al., 2020). The accuracy of the *GW*/BSE method is an improvement over TD-DFT. Therefore, adapting the *GW*/BSE method to be applicable to arbitrary molecules in arbitrary magnetic fields is worthwhile. It allows for an investigation of the effects of strong magnetic fields in sizable molecular systems while still retaining a certain robustness with respect to accuracy.

Within this paper we therefore aim at describing a fully consistent formulation and implementation of the *GW*/BSE method for the description of optical spectra of sizable molecules within strong magnetic fields. In the following chapters, the general formulas for the G_0W_0 and the eigenvalue self-consistent *GW* (ev*GW*) methods as well as the BSE in strong magnetic fields are outlined. The resulting implementation is able to describe excited states of molecules of significant size. As such strong external magnetic fields are not accessible in experimental setups, a set of benchmark values obtained from truncated coupled cluster theory is provided for 36 small to medium-sized molecules. Finally, we demonstrate the capabilities of the *GW*/BSE equation in strong magnetic fields by predicting the colour change of tetracene in a strong uniform magnetic field.

2 THEORY

2.1 GW Approach in Magnetic Fields Using London Atomic Orbitals

GW quasiparticle (QP) energies form the basis for calculating excitation energies from the Bethe–Salpeter equation. The principal theory to obtain *GW* QP energies in a magnetic field has been outlined in Ref. (Holzer et al., 2019). for atoms and complex-valued spinors. For molecules, to retain full gauge-invariance, instead of real Gaussian-type atomic orbitals, complex London-type atomic orbitals (LAOs) have to be used. These are obtained as a direct product of a Gaussian-type orbital $\phi_\mu(\mathbf{r})$ and a complex phase factor:

$$\xi_\mu(\mathbf{r}) = \phi_\mu(\mathbf{r}) e^{-\mathrm{i}\,\mathbf{k}_\mu\cdot\mathbf{r}} \tag{1a}$$

$$\mathbf{k}_\mu = \frac{1}{2}\mathbf{B}\times\left(\mathbf{R}_\mu - \mathbf{O}\right) \tag{1b}$$

The complex phase factor is used in order to cancel the dependency of all observable properties on the gauge origin $\mathbf{O}$ which naturally arises from the choice of a Coulomb gauge ($\nabla\cdot\mathbf{A} = 0$) for a magnetic vector potential ($\nabla\times\mathbf{A} = \mathbf{B}$). In a two-component (2c) framework, complex spinors can be constructed as a linear combination of LAOs:

$$|p\rangle = \varphi_p(\mathbf{x}) = \sum_\mu \left\{ C^\alpha_{\mu p}\xi_\mu(\mathbf{r})\alpha(\sigma) + C^\beta_{\mu p}\xi_\mu(\mathbf{r})\beta(\sigma)\right\}. \tag{2}$$

Non-collinear spin densities are well represented in this 2c spinor framework. Therefore, uniform and non-uniform magnetic fields can be included in this way. (Sen et al., 2019). More generally, within the notation used in this paper, any arbitrary non-collinear spin density can be employed. Furthermore, the complex phase-factor including LAOs are strictly needed to ensure gauge-independence for *GW* quasiparticle energy evaluations of multi-atomic systems, as well as for consecutive calculations of excitation energies using the Bethe–Salpeter equation. As the magnetic field is represented by a one-electron operator within 2c Kohn–Sham equations, the according information is fully absorbed into the complex spinors expanded in LAOs. Therefore, all quantities occurring in the BSE in a magnetic field must generally be assumed to be complex, unless further symmetries can be exploited.

To obtain the working formulas for G_0W_0 and ev*GW*, we closely follow Refs. (Holzer et al., 2019). and (Hedin, 1991) and define the charge-fluctuation potential as

$$V_m(\mathbf{x}) = \int_{-\infty}^{\infty} \frac{1}{|\mathbf{r}-\mathbf{r}'|}\rho_m(\mathbf{x}')\,\mathrm{d}\mathbf{x}', \tag{3}$$

where m denotes an excited state, and where the space-spin-coordinate $\mathbf{x} \equiv (\mathbf{r}, \sigma)$ includes both space and spin coordinates. The charge fluctuation can be expressed using molecular spinors as

$$\rho_m(\mathbf{x}) = \sum_{ia}\left[\varphi^*_a(\mathbf{x})\varphi_i(\mathbf{x})X^m_{ia} + \varphi^*_i(\mathbf{x})\varphi_a(\mathbf{x})Y^m_{ia}\right], \tag{4}$$

where X^m_{ia} (Y^m_{ia}) refers to the elements "ia" of the mth column of the matrix $\mathbf{X}$ ($\mathbf{Y}$) obtained from solving the direct random-phase approximation equation (dRPA) as defined by **Equations 4–7** of Ref. (Holzer et al., 2019). Here and in the following, we use the indices i, j, k, … for occupied molecular spinors, a, b, c, … for unoccupied (virtual) molecular spinors, and p, q, r, … for arbitrary molecular spinors, expanded in a basis set of LAOs. It is worthwhile to note that complex molecular spinors can be obtained from

London atomic orbitals as well as from real Gaussian orbitals, and after the transformation from an atomic to a molecular picture, the working equations are the same for the two basis sets. However, only molecular spinors from LAOs incorporate the information needed for proper gauge-invariant calculations.

In the *GW* approximation, the correlation self-energy is obtained from the expression

$$\begin{aligned}\Sigma_c(\mathbf{x},\mathbf{x}';\omega) &= -\frac{1}{2\pi \mathrm{i}}\int_{-\infty}^{\infty} e^{\mathrm{i}\omega' 0^+} W_c(\mathbf{x},\mathbf{x}';\omega') \\ &\quad \times G(\mathbf{x},\mathbf{x}';\omega+\omega')\mathrm{d}\omega',\end{aligned} \tag{5}$$

where G is the one-electron Green's function

$$G(\mathbf{x},\mathbf{x}';\omega) = \sum_p \frac{\varphi_p(\mathbf{x})\varphi_p^*(\mathbf{x}')}{\omega-\varepsilon_p+\mathrm{i}\delta\mathrm{sgn}\left(\varepsilon_p-\mu\right)}. \tag{6}$$

As usual, to avoid instabilities and to make **Eq. 6** integratable, a small positive number δ is added to the denominator. ε_p is the eigenvalue of the pth spinor that solves the Kohn-Sham equation for the underlying density functional approximation. The Fermi-level chemical potential μ is chosen to lie between the energy levels of the lowest unoccupied and highest occupied spinors, and W_c is the correlation contribution to the linearly screened potential,

$$W_c(\mathbf{x},\mathbf{x}';\omega) = \sum_{m\neq 0}\left[\frac{V_m(\mathbf{x})V_m^*(\mathbf{x}')}{\omega-\omega_m+\mathrm{i}\delta} - \frac{V_m^*(\mathbf{x})V_m(\mathbf{x}')}{\omega+\omega_m-\mathrm{i}\delta}\right]. \tag{7}$$

Evaluating the integral on the right-hand side of **Eq. 5** yields

$$\begin{aligned}\Sigma_c(\mathbf{x},\mathbf{x}';\omega) &= \sum_k \sum_{m\neq 0} \frac{V_m(\mathbf{x})V_m^*(\mathbf{x}')\varphi_k(\mathbf{x})\varphi_k^*(\mathbf{x}')}{\omega+\omega_m-\varepsilon_k-\mathrm{i}\eta} \\ &\quad + \sum_c \sum_{m\neq 0} \frac{V_m^*(\mathbf{x})V_m(\mathbf{x}')\varphi_c(\mathbf{x})\varphi_c^*(\mathbf{x}')}{\omega-\omega_m-\varepsilon_c+\mathrm{i}\eta},\end{aligned} \tag{8}$$

where $\eta = 2\delta$. We thus obtain the following working equation for the real-valued correlation contribution to the quasiparticle energy:

$$\begin{aligned}\langle p|\Sigma_c\left(\varepsilon_p\right)|p\rangle &= \sum_k \sum_{m\neq 0} |(pk|\rho_m)|^2 D^+_{p,k,m} \\ &\quad + \sum_c \sum_{m\neq 0} |(cp|\rho_m)|^2 D^-_{p,c,m},\end{aligned} \tag{9}$$

with

$$D^{\pm}_{p,q,m} = \frac{\varepsilon_p-\varepsilon_q\pm\omega_m}{\left(\varepsilon_p-\varepsilon_q\pm\omega_m\right)^2+\eta^2}. \tag{10}$$

The two-electron integrals $(pq|\rho_m)$ are computed as

$$(pq|\rho_m) = \sum_{ia}\left[(pq|ai)X^m_{ia} + (pq|ia)Y^m_{ia}\right]. \tag{11}$$

The exchange self-energy is

$$\langle p|\Sigma_x|p\rangle = -\sum_k (pk|kp), \tag{12}$$

and the G_0W_0 quasiparticle energies are computed as (van Setten et al., 2012; Krause et al., 2015; Holzer et al., 2019)

$$\varepsilon_p^{G_0W_0} = \varepsilon_p^{(0)} + Z_p\langle p|\Sigma_c\left(\varepsilon_p^{(0)}\right) + \Sigma_x - V_{\mathrm{xc}}|p\rangle, \tag{13}$$

with

$$Z_p = \left\{1 - \langle p|\left(\partial\Sigma_c(\varepsilon)/\partial\varepsilon\right)_{\varepsilon=\varepsilon_p^{(0)}}|p\rangle\right\}^{-1}, \tag{14}$$

where Σ_{X} is the exchange self-energy and V_{xc} is the exchange-correlation potential of the underlying density functional theory. To obtain eigenvalue self-consistent quasiparticle energies (i.e., ev*GW* quasiparticle energies), **Eq. 13** is evaluated repeatedly with $Z = 1$ until the obtained eigenvalues are converged.

$$\varepsilon_p^{(n+1)} = \varepsilon_p^{(0)} + \langle p|\Sigma_c\left(\varepsilon_p^{(n)}\right) + \Sigma_x - V_{\mathrm{xc}}|p\rangle. \tag{15}$$

It was found that DIIS (direct inversion in the iterative subspace) (Pulay, 1980) procedures can speed up this process considerably. Usually less than ten consecutive evaluations of **Eq. 15** are then needed to obtain converged ev*GW* quasiparticle energies.

Finally, we note that also the analytic continuation (AC) and contour deformation (CD) *GW* variants described in Ref. (Holzer and Klopper, 2019) can be adapted to LAOs in the same manner. However, unlike the previous formulas derived for the analytic *GW* variant in an magnetic field, our current AC-*GW* and CD-*GW* variants are approximate in the sense that they ignore the lack of time-reversal (Kramers) symmetry. While we expect our AC-*GW* and CD-*GW* variants to be well behaved in a system with a vanishing spin expectation value ($\langle S^2\rangle \approx 0$), more research on these methods has to be performed in cases of non-vanishing $\langle S^2\rangle$.

2.2 The Bethe–Salpeter Equation in a Magnetic Field

Starting from the gauge-invariant quasiparticle energies described in the previous section, the gauge-invariant excitation energies can be obtained from the Bethe–Salpeter equation also making use of LAOs. The BSE can be expressed in terms of complex spinors as

$$\begin{pmatrix}\mathbf{A} & \mathbf{B}\\ \mathbf{B}^* & \mathbf{A}^*\end{pmatrix}\begin{pmatrix}\mathbf{X}^m\\ \mathbf{Y}^m\end{pmatrix} = \omega_m\begin{pmatrix}\mathbf{1} & \mathbf{0}\\ \mathbf{0} & -\mathbf{1}\end{pmatrix}\begin{pmatrix}\mathbf{X}^m\\ \mathbf{Y}^m\end{pmatrix}. \tag{16}$$

The orbital rotation matrices **A** and **B** are defined as

$$A_{ia,jb} = (\varepsilon_i-\varepsilon_a)\delta_{ij}\delta_{ab} + \nu_{ai,bj} - W_{ji,ba}, \tag{17a}$$

$$B_{ia,jb} = \nu_{ai,jb} - W_{bi,ja}, \tag{17b}$$

where ε_i is the quasiparticle energy of the ith Kohn–Sham eigenstate from a preceding *GW* computation, $\nu_{ia,bj}$ is a Coulomb integral over complex spinors,

$$\nu_{ia,bj} = \left(\varphi_a\varphi_i|\varphi_b\varphi_j\right) = \iint \varphi_a^*(\mathbf{x})\varphi_i(\mathbf{x})\frac{1}{|\mathbf{r}-\mathbf{r}'|}\varphi_b^*(\mathbf{x}')\varphi_j(\mathbf{x}')\,\mathrm{d}\mathbf{x}\mathrm{d}\mathbf{x}', \tag{18}$$

and $W_{pq,rs}$ is the static screened potential from the BSE. Properties such as for example oscillator strengths, excited state dipole moments, or nuclear forces can be obtained in a straightforward manner from the solutions of the eigenvalue problem of the BSE, again expressed in a basis of LAOs. Using complex LAO-based

spinors, the static (*i.e.*, $\omega = 0$) screened potential W, which is given in its real-space expression in **Eq. 7**, takes the form

$$W_{pq,rs} = \sum_{tu} \left(\epsilon^{-1}\right)_{pq,tu} v_{tu,rs} \tag{19a}$$

$$\epsilon_{pq,tu} = \delta_{pt}\delta_{qu} - \sum_{tu} v_{pq,tu} \left(\chi_0\right)_{tu,tu}, \tag{19b}$$

where ϵ is the dielectric function. The non-interacting response-function χ_0 is diagonal and real if the quasiparticle energies are real, even if complex LAO-based spinors are used:

$$\left(\chi_0\right)_{tu,tu} = \sum_{kc} \frac{\delta_{tk}\delta_{uc} + \delta_{tc}\delta_{uk}}{\varepsilon_k - \varepsilon_c}. \tag{20}$$

From the response function, and using the resolution-of-the-identity (RI) approximation

$$v_{pq,rs} = \sum_{P} \left(R^P_{pq}\right)^* R^P_{rs}, \tag{21}$$

the screened potential $W_{pq,rs}$ can be evaluated as (Krause and Klopper, 2017)

$$W_{pq,rs} = \sum_{PQ} \left(R^P_{pq}\right)^* \left[\delta_{PQ} - 2\Re \sum_{ck} R^P_{ck} \left(\chi_0\right)_{ck,ck} \left(R^Q_{ck}\right)^*\right]^{-1} R^Q_{rs}. \tag{22}$$

For the 3-index intermediate R^P_{pq}

$$R^P_{pq} = \sum_{Q} \left(\mathbf{V}^{-1/2}\right)_{PQ} \left(\phi_Q | \varphi_p \varphi_q\right), \tag{23a}$$

$$V_{PQ} = \left(\phi_P | \phi_Q\right) = \iint \phi_P(\mathbf{r}) \frac{1}{|\mathbf{r} - \mathbf{r}'|} \phi_Q(\mathbf{r}')\, \mathbf{d}\mathbf{r}\mathbf{d}\mathbf{r}', \tag{23b}$$

$$\left(\phi_Q | \varphi_p \varphi_q\right) = \iint \phi_Q(\mathbf{r}) \frac{1}{|\mathbf{r} - \mathbf{r}'|} \varphi^*_p(\mathbf{x}') \varphi_q(\mathbf{x}')\, \mathbf{d}\mathbf{r}\mathbf{d}\mathbf{x}', \tag{23c}$$

the auxiliary functions ϕ_P are chosen to be real as ordinary Gaussian-type atomic orbitals without losing gauge invariance of the results obtained from computations in a magnetic field. This considerably simplifies the inner part of **Eq. 22**, representing the response function in the auxiliary subspace,

$$\chi_{PQ} = \delta_{PQ} - 2\Re \sum_{ck} R^P_{ck} \left(\chi_0\right)_{ck,ck} \left(R^Q_{ck}\right)^*, \tag{24}$$

which is symmetric and real for the special case of the static BSE even in a (uniform or nonuniform) magnetic field. Finally, the efficient evaluation of the 3-index integrals $(\phi_Q|\varphi_p\varphi_q)$ has been described in Ref. (Pausch and Klopper, 2020). Therefore, the evaluation of the BSE in magnetic fields can proceed in a straightforward manner, making it an invaluable tool to assess excited stats of molecules in magnetic fields at roughly the same cost as required for linear-response Hartree–Fock computations, with the advantage of being significantly more accurate.

3 COMPUTATIONAL DETAILS

All implementation work in this work have been carried out in the framework of the TURBOMOLE (Ahlrichs et al., 1989; Furche et al., 2014; Balasubramani et al., 2020) program package. Consequently, all calculations have also been done using TURBOMOLE.

To assess the correctness of the implementation and theory of the *GW*/BSE method in magnetic fields, the first excited triplet states of 36 small molecules have been evaluated using ev*GW*/BSE in a magnetic field of 1,000 T in z-direction with respect to the coordinates supplied in the Supporting Information (SI). The molecules used in this evaluation are acetaldehyde, acetylene, CCl_2, CClF, CF_2, cyanoacetylene, cyanoformaldehyde, cyanogen, diacetylene, difluorodiazirine, formaldehyde, formic acid, formyl chloride, formyl fluoride, glyoxal, H_2C_3, HCN, HCP, HNO, HPO, HPO, HPS, HSiF, isocyanogen, nitrosamine, nitrosylcyanide, phosgene, propynal, pyrazine, selenoformaldehyde, $SiCl_2$, silylidene, tetrazine, thioformaldehye, thioformylchloride, thionylcarbonylfluoride, and thiophosgene. The set of molecules is taken from Ref. (Suellen et al., 2019). Starting from the geometries provided in Ref. (Suellen et al., 2019), the geometries have been re-optimized using RI-MP2 (resolution-of-identity Møller–Plesset perturbation theory to second order) in the corresponding magnetic field of 1,000 T in z-direction using numerical gradients. At the RI-MP2-optimized geometries, the three first excited states have been evaluated using ev*GW*/BSE and PBE0, (Perdew et al., 1997; Adamo and Barone, 1999), LC-ωPBE, (Vydrov and Scuseria, 2006), BHLYP (also known as BH&HLYP), (Becke, 1993), and CAM-B3LYP (Yanai et al., 2004) as underlying functionals. In all calculations the energy and norm of the difference density matrix were converged to 10^{-8} hartree and 10^{-7}, respectively. The def2-TZVP basis set (Weigend and Ahlrichs, 2005) was used throughout, in conjunction with the resolution-of-identity (RI) approximation for the Hartree and exchange terms with the corresponding auxiliary fitting basis sets for the Kohn–Sham ground-state (Weigend, 2006; Weigend, 2008) as well as the appropriate auxiliary fitting basis sets for the RI-MP2 and GW/BSE calculations. (Hättig, 2005).

For further comparison, the corresponding excited state energies have also been determined using the approximate coupled-cluster RI-CC2 method, (Hättig and Weigend, 2000), which has been adapted to calculations in finite magnetic fields in the course of the present work. It is closely related to the equation-of-motion coupled-cluster singles-and-doubles (EOM-CCSD) method in magnetic fields that has been described by Hampe and Stopkowicz, (Hampe and Stopkowicz, 2017), and to the two-component RI-CC2 implementation of Krause and Klopper. (Krause and Klopper, 2015). Compared to EOM-CCSD, RI-CC2 is computationally significantly less involved. This allows for the assessment of the larger molecules in the test set in the applied magnetic field.

For tetracene, we performed calculations on the ev*GW* (10)/BSE@DFT level using the contour deformation (CD) technique. (Holzer and Klopper, 2019). CD-ev*GW* (10) denotes that only the highest 10 occupied and lowest 10 unoccupied spinor energies have been corrected using CD-ev*GW*, while the remaining spinor energies are shifted ("scissoring") accordingly. Testing the self-energy obtained from the CD-*GW* variant reveals that indeed for the systems and magnetic field strengths investigated in this paper, CD-*GW* exhibits errors of the order of 1 meV or less, making it perfectly feasible for (not too strong) magnetic fields.

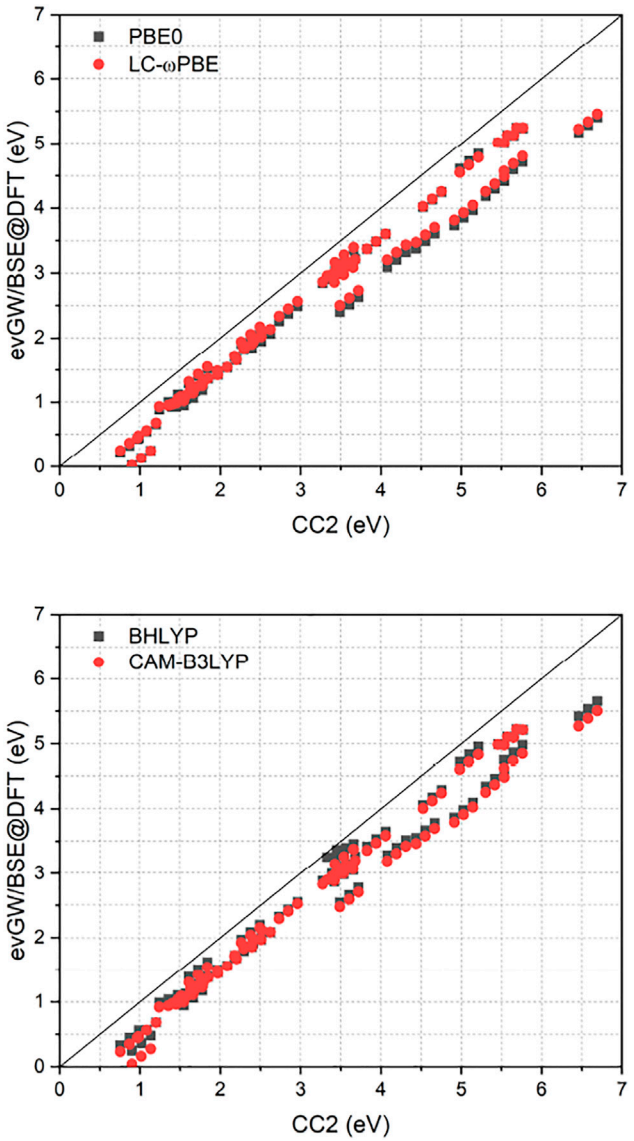

FIGURE 1 | Comparison of excitation energies from the RI-CC2 and ev*GW*/BSE@DFT methods. ev*GW*/BSE calculations have been performed using either PBE0, LC-ωPBE, BHLYP or CAM-B3LYP spinors. All calculations used the def2-TZVP basis set. All values in eV.

As reference density functionals for the ev*GW*(10)/BSE@DFT calculations, we used PBE0, B3LYP, BHLYP and CAM-B3LYP. Also the tetracene calculations were carried out in the def2-TZVP basis.

4 RESULTS AND DISCUSSION

4.1 Test Set of Small Molecules

For the 36 molecules tested, in a field of 1,000 T, all ground states retain their closed-shell character, yielding no spin polarization. Therefore, the spacing in-between the three triplet states ($T_{-1,0,1}$), which are non-degenerate in the magnetic field, are solely determined by the Zeeman effect. The $T_{-1,1}$ components of the triplet are found exactly at $E_{T_0} \pm B$. At a field of B = 1,000 tesla, this translates into ≈ ± 0.116 eV above and below the T_0 state. The center-of-mass of the triplet, being located exactly at the zero-component of the triplet, is however shifted when compared to the degenerate triplet state in the field-free case.

Figure 1 compares the RI-CC2 and ev*GW*/BSE excitation energies of the full set. It exhibits a near-linear shift between the two methods, with the difference getting more pronounced for excited states with higher energy. Furthermore, RI-CC2 consistently yields blue-shifted excitation energies when compared to ev*GW*/BSE. This is in accordance with the finding

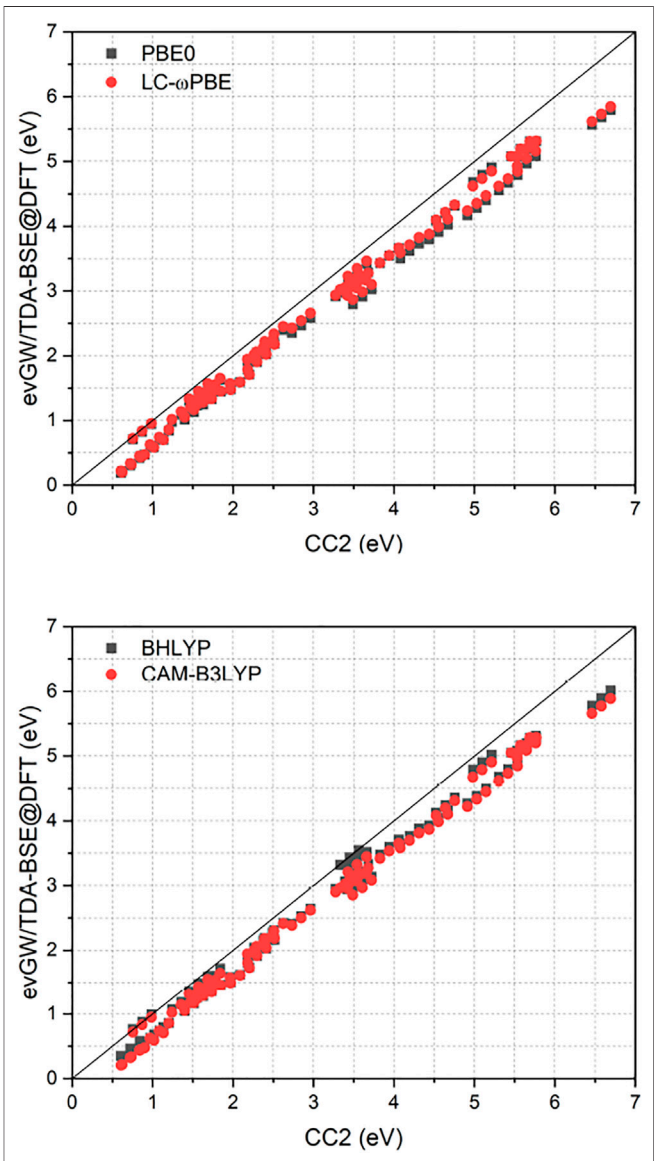

FIGURE 2 | Comparison of excitation energies from the RI-CC2 and ev*GW*/TDA-BSE@DFT methods. ev*GW*/BSE calculations have been performed using either PBE0 or LC-ωPBE spinors. All calculations used the def2-TZVP basis set. All values in eV.

TABLE 1 | Mean average error (MAE), mean signed error (MSE), standard deviation (SD), and maximum error (MAX) of ev*GW*/BSE@DFT ("BSE") and ev*GW*/TDA-BSE@DFT ("TDA") excitation energies with respect to CC2 excitation energies. All values in eV.

DFT	PBE0		LC-ωPBE		BHLYP		CAM-B3LYP	
Method	BSE	TDA	BSE	TDA	BSE	TDA	BSE	TDA
MAE	0.61	0.41	0.58	0.38	0.53	0.34	0.59	0.39
MSE	–0.61	–0.41	–0.58	–0.38	–0.53	–0.34	–0.59	–0.39
SD	0.28	0.18	0.25	0.17	0.23	0.16	0.25	0.16
MAX	1.29	0.90	1.24	0.85	1.05	0.68	1.19	0.81

of Suellen *et al.*, who also found CC2 to yield too high excitation energies on average for this test set, though in the field-free case. In contrast, ev*GW*/BSE was found to yield too low excitation energies on average, especially for triplet excited states. (Gui et al., 2018). Too low triplet excited states are well known phenomenon for the *GW*/BSE method. (Rangel et al., 2017; Jacquemin et al., 2017; Holzer and Klopper, 2018). While Jacquemin *et al.* proposed to use the Tamm-Dancoff approximation (TDA) to improve this, (Jacquemin et al., 2017), two of us proposed adding the correlation kernel of the underlying density functional approximation to improve triplet excitations, yielding the correlation-kernel augmented BSE (cBSE) approach. (Holzer and Klopper, 2018). While a linear-response time-dependent DFT implementation in magnetic fields would be needed to apply the cBSE method, using the TDA is straightforwardly obtained by setting $\mathbf{B} = \mathbf{0}$ in **Eq. 16**. For the tested molecules, these findings can be partly confirmed, with the TDA leading to a significantly blue shift of especially the lower lying excited states, improving the agreement between ev*GW*/TDA-BSE and RI-CC2 (**Figure 2**). The improvement of the *GW*/BSE method when using the TDA is generally also observed in field-free cases. (Rangel et al., 2017).

A closer inspection of **Figure 1** reveals that for the ev*GW*/BSE method, two distinct groups, one with smaller deviations from RI-CC2 and one with larger deviations, are found. The "high-error" group is composed of the molecules nitrosamine (1.02 eV), HCP (3.61 eV), diacetylene (4.20 eV), cyanoacetylene (4.55 eV), cyanogen (5.03 eV), isocyanogen (5.42 eV), acetylene (5.65 eV), and HCN (6.58 eV). The values in parenthesis are the T_0 excitation energies of the corresponding RI-CC2 references. Except for the low-energy excited state of nitrosamine, all these molecules feature triple bonds in their respective ground states. Furthermore we find instabilities for the molecules HNO (0.74 eV) and nitrosylcyanide (0.72 eV) with rather low lying triplet excited states. This is further hinting at triple bonds and nitrosyl groups being described with sub-par quality within the ev*GW*/BSE methods. For the remaining molecules significantly smaller errors are found.

Employing the TDA removes the instabilities encountered in the ev*GW*/BSE calculations for the molecules HNO and nitrosylcyanide, in both cases yielding excitation energies that are lower by ≈ 0.4eV when compared to their RI-CC2 counterparts as shown in **Table 1**.

As displayed also in **Figure 1** and **Figure 2**, **Table 1** reveals that BHLYP, which incorporates a relatively large amount of Hartree–Fock exchange, performs best for the investigated molecules. The range-separated hybrids LC-ωPBE and CAM-B3LYP yield comparable results, and generally perform better than PBE0 but worse than BHLYP. This is in line with observations for field-free cases, indicating that (at least for moderate field strength) conclusions drawn from field-free benchmarks are still applicable. (Holzer et al., 2021).

As shown in **Figure 2**, the class of molecules with triple bonds or nitrosyl groups exhibits a significantly reduced error within the TDA for all investigated functionals. Triplet excitation energies from the latter class of molecules are now in line with all other molecules. We therefore expect the TDA to be especially valuable for molecules with triple bonds or nitrosyl groups. Still, regarding the TDA, there are some caveats left. While some of the improvements can indeed be related to error compensation, where the blue-shift of the TDA counteracts the general red-shift of the ev*GW*/BSE method with respect to CC2 excitation energies, this can not fully explain the strong reduction of the error regarding the class of molecules with triple bonds or nitrosyl groups, which indicates that also the correlation from the BSE is sometimes insufficient to describe triplet excitations sufficiently well. Given the overall increase in accuracy from the TDA, it may be advisable to even use it by default in magnetic fields until the cBSE method becomes available. (Holzer and Klopper, 2018). However, it shall be noted that the usage of CC2 as reference method is not the best possible but a pragmatic choice for this test set. While its accuracy is comparable or even slightly better than that of EOM-CCSD, (Suellen et al., 2019), more refined methods as CC3 or EOM-CCSDT would be needed to obtain true reference values with errors significantly below 0.1 eV. Given the immense computational cost of the latter two methods, only results for a single diatomic molecule, namely CH^+, have been reported for EOM-CCSDT so far in a finite magnetic field. (Hampe et al., 2020). RI-CC2 as computational efficient method is therefore a suitable compromise, providing robust values. However, as shown in Ref. (Suellen et al., 2019), CC2 has a tendency to deliver too high excitation energies when compared to experimental and CC3 excitation energies. In contrast, ev*GW*/BSE tends to underestimate excitation energies as shown in Ref. (Gui et al., 2018), especially for triplet excited states. This has to be taken into account when comparing the CC2 and ev*GW*/BSE methods. Concerning the reference state, ev*GW* is able to even out the differences between the underlying functionals completely. The difference between excitation energies obtained from either ev*GW*/BSE@PBE0 or ev*GW*/BSE@LC-ωPBE is statistically insignificant. The presented results suggest that the performance of the ev*GW*/BSE method in magnetic fields is similar to its performance in field-free situations, yielding good to excellent excitation energies, at a considerably reduced effort when compared to coupled-cluster methods.

4.2 Optical Properties of Tetracene in a Magnetic Field

As established in the last section, the ev*GW*/BSE method quite accurately predicts molecular excitation energies in the presence of an external magnetic field. Our implementation

TABLE 2 | Wavelengths of p-, α- and β-excitations in nm as calculated at the CD-ev*GW*/BSE@DFT level employing different reference functionals. In order to highlight the dependence on the geometry, all calculations were performed both on the geometry as optimized using the reference functional as well as on the geometry as optimized using the range-separated hybrid (RSH) functional CAM-B3LYP. Experimental values are also given.

Geometry	Geometry optimization			CAM-B3LYP (RSH) geometry				
Functional	PBE0	B3LYP	BHLYP	RSH	PBE0	B3LYP	BHLYP	Exp. Guidez and Aikens, (2013); Sony and Shukla, (2007); Klevens and Platt, (1949); Biermann and Schmidt, (1980); Bree and Lyons, (1960)
p-Excitation	614	505	465	470	484	487	468	455–477
α-Excitation	370	369	349	354	359	360	351	373–393
β-Excitation	270	269	260	265	264	264	261	272–275

into the TURBOMOLE package thus appears to be an efficient yet reliable method of predicting excited state properties of sizable molecules in strong magnetic fields. As a consequence, real-world properties such as the absorption and emission spectra, and therefore also the colour, of a substance can now be obtained by simulating the vertical excitations and related oscillator strengths of a molecule under such extreme conditions. In this section, the effects of a strong external magnetic field on the excited states of tetracene are studied in detail, exemplifying the effects such extreme environments can have on chemical substances.

The optical spectrum of tetracene in the absence of an external magnetic field is mainly composed of three bands. The p-band (peak at 455–477 nm) corresponds to the HOMO → LUMO transition (B_{2u} symmetry). The α- and β-bands correspond to the HOMO → LUMO+1 and HOMO −1 → LUMO transitions (both B_{3u} symmetry), respectively, and show peaks at 373–393 nm (α-band) as well as 272–275 nm (β-band). While the two bands in the visible (p) and near-UV (α) region of the spectrum exhibit relatively small oscillator strengths, the β excitation is associated with an oscillator strength several orders of magnitude larger than that of the two other transitions. (Guidez and Aikens, 2013; Sony and Shukla, 2007; Klevens and Platt, 1949; Biermann and Schmidt, 1980; Bree and Lyons, 1960).

In order to investigate the optical properties of tetracene for the field-free case, we first optimized the geometry at the PBE0, B3LYP, BHLYP and CAM-B3LYP levels, respectively. Using these structures, subsequent CD-ev*GW*/BSE@DFT calculations were carried out. The resulting wavelengths for the excitations are presented in **Table 2**. The different reference functionals provide similar values for the α- and β-excitations, slightly overestimating the energies of both excitations. The energies of the p-excitation, however, vastly differ with respect to the reference functional, ranging from 465 nm at the CD-ev*GW*/BSE@BHLYP level to 614 nm at the CD-ev*GW*/BSE@PBE0 level. Further investigations reveal that this is almost exclusively an effect of the geometry and not the method itself as using the CAM-B3LYP reference geometry yields wavelengths between 468 and 487 nm for the p-excitation in all cases. This is to be expected as the impact of the reference functional is usually not very large for ev*GW*/BSE calculations. (Holzer et al., 2021).

In order to gain a better insight into the electronic processes behind the optical spectrum, the transition densities are examined for the p-, α- and β-excitations. In accordance with the literature, (Lim et al., 2004; Guidez and Aikens, 2013), it is found that while the p-band corresponds to a transition polarized along the short axis of the molecule, the α- and β-excitations can be described by transitions polarized along the long axis of the

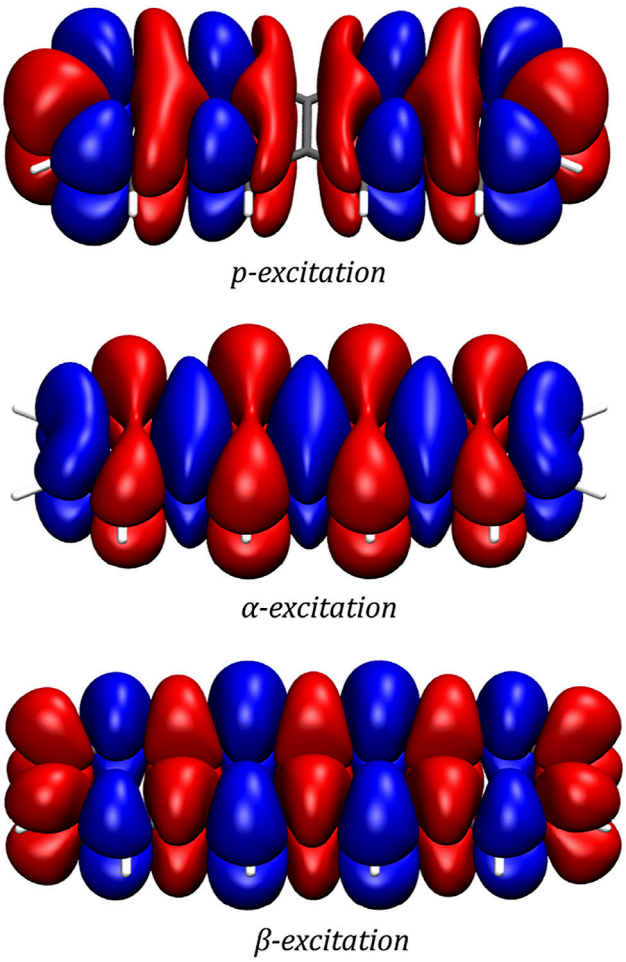

FIGURE 3 | Transition densities of the p-, α- and β-excitations as generated by a two-component CD-ev*GW*/BSE@CAM-B3LYP calculation. The plots were generated with VMD using an isovalue of 0.0001 a_0^{-3} for the p-excitation and 0.0002 a_0^{-3} for the α- and β-excitations. The colour blue indicates a loss while red indicates a gain of electron density.

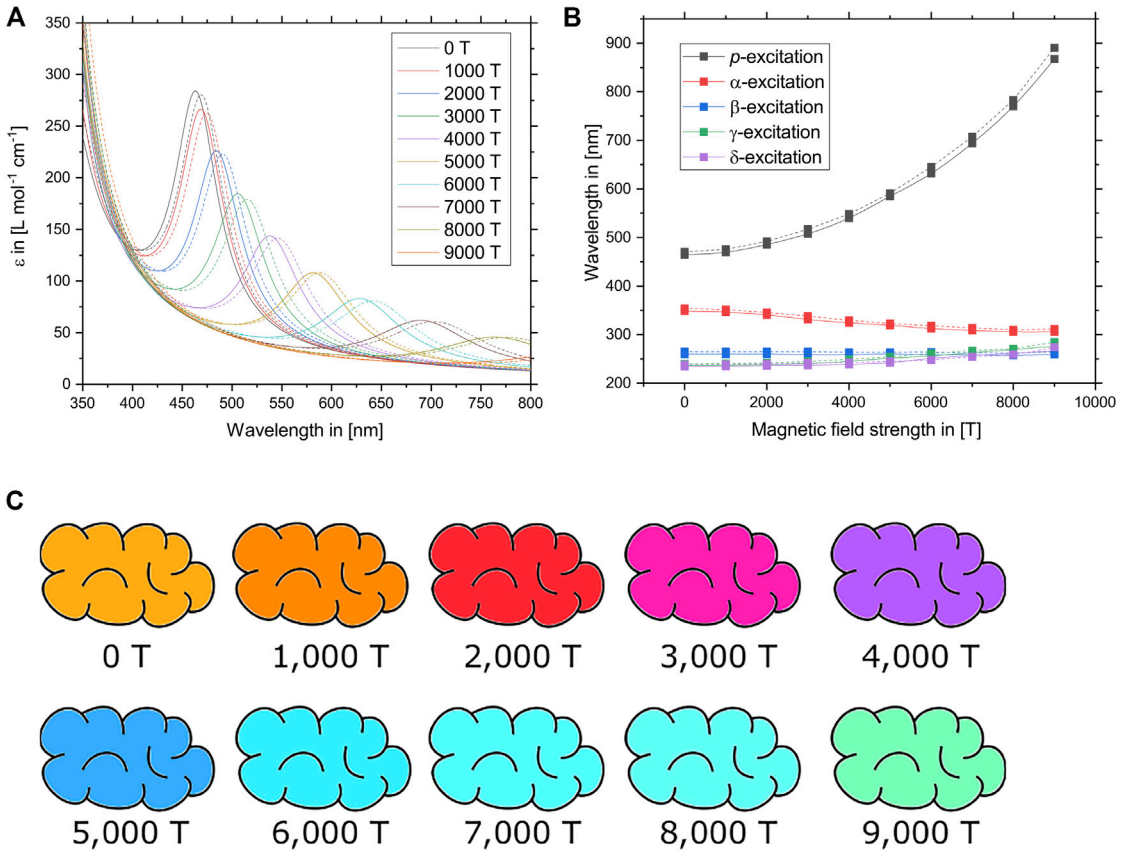

FIGURE 4 | (A) UV/Vis spectra of tetracene as predicted at different magnetic field strengths between 0 T and 9,000 T. Solid lines denote calculations using the CD-ev*GW* (10)/BSE@BHLYP method while dashed lines denote CD-ev*GW* (10)/BSE@CAM-B3LYP calculations. **(B)** Wavelengths of the relevant lowest vertical excitations of tetracene at different magnetic field strengths between 0 T and 9,000 T. The *p*-excitation, which is predominantly responsible for the colour of tetracene, is most affected by the external field. Solid lines denote calculations using the CD-ev*GW* (10)/BSE@BHLYP method while dashed lines denote CD-ev*GW* (10)/BSE@CAM-B3LYP calculations. **(C)** Colour of tetracene as predicted at the CD-ev*GW* (10)/BSE@CAM-B3LYP level of theory at different magnetic field strengths between 0 T and 9,000 T. To obtain the depicted colours, the vertical excitations of the optical spectrum were broadened by 0.15 eV and converted into a RGB colour code while the intensity was scaled relative to the zero-field by integrating over the visible region of the spectrum.

molecule. The transition densities of the three excitations are depicted in **Figure 3**.

Having gained a general overview of the electronic excitations that mainly constitute the optical spectrum of tetracene, it is now possible to extend these findings in order to understand the effect a strong external magnetic field may have on such a system. Furthermore, it is now possible to use these findings in order to predict the colour shift of the tetracene molecule under the influence of such a strong magnetic field.

This investigation contains three steps: Firstly, it is necessary to generate the optical spectrum of tetracene in the absence of a magnetic field. This was done using the CD-ev*GW* (10)/BSE@DFT methods employing BHLYP and CAM-B3LYP as reference functionals as they most accurately describe the electronic excitations in the zero-field compared to the experimental values. The peaks are broadened using a damped sum-over-states formalism which translates to a Lorentzian line shape with full width at half maximum of 0.15 eV for all excitations. (Norman et al., 2004; Barron, 2004; Fernandez-Corbaton et al., 2020). From this information, the RGB colour code of the substance can be computed. By calculating the integrals over the entire visible part of the spectrum and arbitrarily setting it to 1 for the zero-field case, the relative intensities of the colour may also be calculated.

Secondly, the immediate influence of an external magnetic field has to be assessed. Applying the external field perpendicular to the molecular plane lowers the symmetry of the system. The point group of tetracene in such an external field is C_{2h} instead of D_{2h}. The excitations of the *p*-, *α*- and *β*-bands are all of B_u symmetry. A further investigation reveals that the subsequent two excitations (here denoted as *γ* and *δ*) are also of B_u symmetry.

Thirdly, by slowly raising the magnetic field strength in steps of 1,000 T and generating the optical spectrum at each field strength as previously described, it is possible to track how the excitations are influenced by the external magnetic field. The resulting UV/Vis spectra and the energies of the five lowest excitations are plotted in **Figures 4A,B**. While the excitation energies of the *α*–*δ*-excitations are only slightly shifted between 0 T and 9,000 T, the *p*-band is strongly red-shifted. At the same time, the oscillator strength of the *p*-excitation decreases with an increasing field strength. The resulting

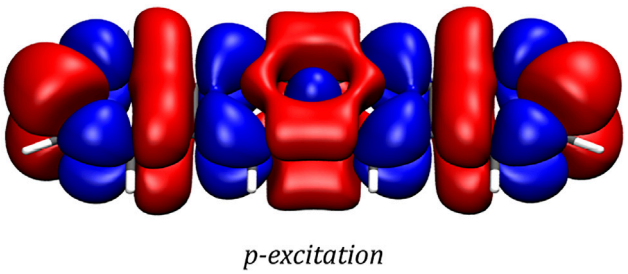

FIGURE 5 | Transition density of the *p*-excitation at a magnetic field strength of 8,000 T as generated by a two-component CD-ev*GW*/BSE@CAM-B3LYP calculation. The plot was generated with VMD using an isovalue of 0.0001 a_0^{-3}. The colour blue indicates a loss while red indicates a gain of electron density.

UV/Vis spectrum is mostly dominated by both the location and intensity of the *p*-band while only a small section of the violet and blue part of the spectrum between 400 and 500 nm is caused by the other excitations. Only the five lowest excitations (*p*, *α*–*δ*) are depicted in **Figure 4B**, but the UV/Vis spectrum was generated by the 75 lowest excitations. However, none of the other excitations contribute significantly to the visible part of the spectrum.

The resulting predicted colours of tetracene at various magnetic field strengths are shown in **Figure 4C**. As the *p*-band is red-shifted, the main absorption band moves from the blue part of the spectrum towards the red. The orange-red colour of tetracene therefore shifts towards the colour blue. Finally, between 5,000 T and 9,000 T, the contribution of the *p*-band does not contribute significantly to the spectrum anymore. Since the *α*–*δ*-bands are still active and relatively unchanged in their location, part of the blue light is still absorbed, resulting in a turquoise to green colour which becomes less and less intense as the magnetic field strength is increased.

It is worth noting that while the peak positions of the *α*–*δ*-excitations exhibit only a minor dependence on the applied field, their respective oscillator strengths change significantly as the *β*-excitation becomes less important. Subsequently, the *γ*- and *δ*-excitations become dominant at different magnetic field strengths. Furthermore, certain additional transitions slowly start to arise as they are no longer symmetry forbidden due to a lowering of the point group symmetry in the magnetic field. At a magnetic field strength of approximately 6,000 T, specifically, the *γ*- and *δ*-excitations are very close energetically to the usually predominant *β*-excitation, leading to resonance phenomena such as a splitting into multiplets.

Finally, the strong influence of the external field on the excitation energy of the *p*-band can best be understood by examining the changes to the electronic structure of tetracene. In the magnetic field, the energy of the HOMO increases and the energy of the LUMO decreases. Thus, the HOMO-LUMO gap decreases significantly. As the *p*-excitation corresponds to the HOMO → LUMO transition, the resulting excitation energy is subsequently lowered.

The transition density of the *p*-excitation at a magnetic field strength of 8,000 T is depicted in **Figure 5**. It exhibits the effects the magnetic field has on this most important transition, showing a slightly more delocalized nature of this transition in the magnetic field compared to the zero-field case. In order to ensure gauge-origin invariance, the transition density plot was generated employing London atomic orbitals.

5. CONCLUSION

In this paper, we have presented a gauge-invariant formulation of the *GW*/BSE method for excited states in strong magnetic fields. The resulting implementation was benchmarked against reference values obtained from approximate coupled-cluster (CC2) theory. The obtained results indicate that the *GW*/BSE method provides a similar accuracy in strong magnetic fields as in the field-free case. The known issue of an underestimation of the excitation energy of triplet excited states is also present in magnetic fields. Like in the field-free case, it is shown that the Tamm-Dancoff approximation is able to remove a significant amount of this underestimation, improving the overall accuracy when compared to coupled-cluster values. The remaining error is nearly linear, making it easy to be accounted for.

Furthermore, using the tetracene molecule as showcase example, it was demonstrated that the *GW*/BSE method is able to tackle systems far beyond the possibilities of any prior ansatz that has been used to describe excited states in strong magnetic fields. For the tetracene molecule, we analyzed the shift of the main absorption peaks in magnetic fields ranging from 0 to 9,000 T. It was found that some excited state energies are more affected than others, leading to prominent changes in the spectrum. Ultimately, the colour of tetracene was estimated from the calculated spectra in the assessed magnetic fields. Starting from the bright orange colour of tetracene, we predict the compound to exhibit a blue colour at 5,000, which is converted towards a green colour at 9,000 T. While the dependence of the excited states on the external magnetic field are interesting on their own, the example of tetracene also outlines the fascinating world that even moderately strong magnetic fields could open for the broad field of photochemistry.

To summarize, the *GW*/BSE method has proven once more that it has become a formidable member of the toolbox of quantum chemistry.

DATA AVAILABILITY STATEMENT

The original contributions presented in the study are included in the article/**Supplementary Material**, further inquiries can be directed to the corresponding author.

AUTHOR CONTRIBUTIONS

CH, AP, and WK have formulated the theory and derived the equations. CH and AP have implemented the formalism in a basis set of London atomic orbitals. CH has performed the calculations on the test set of 36 molecules and AP has performed the calculations on tetracene. CH, AP and WK have written parts of the manuscript.

ACKNOWLEDGMENTS

CH gratefully acknowledges the Volkswagen Stiftung for financial support. AP gratefully acknowledges financial support by Fonds der chemischen Industrie and Studienstiftung des deutschen Volkes.

SUPPLEMENTARY MATERIAL

The Supplementary Material for this article can be found online at: https://www.frontiersin.org/articles/10.3389/fchem.2021.746162/full#supplementary-material

REFERENCES

Adamo, C., and Barone, V. (1999). Toward Reliable Density Functional Methods Without Adjustable Parameters: The PBE0 Model. *J. Chem. Phys.* 110, 6158–6170. doi:10.1063/1.478522

Ahlrichs, R., Bär, M., Häser, M., Horn, H., and Kölmel, C. (1989). Electronic Structure Calculations on Workstation Computers: The Program System Turbomole. *Chem. Phys. Lett.* 162, 165–169. doi:10.1016/0009-2614(89)85118-8

Balasubramani, S. G., Chen, G. P., Coriani, S., Diedenhofen, M., Frank, M. S., Franzke, Y. J., et al. (2020). TURBOMOLE: Modular Program Suite for Ab Initio Quantum-Chemical and Condensed-Matter Simulations. *J. Chem. Phys.* 152, 184107. doi:10.1063/5.0004635

Barron, L. D. (2004). *Molecular Light Scattering and Optical Activity* (2nd Edition). Cambridge, UK: Cambridge University Press.

Becke, A. D. (1993). A New Mixing of Hartree-Fock and Local Density-Functional Theories. *J. Chem. Phys.* 98, 1372–1377. doi:10.1063/1.464304

Biermann, D., and Schmidt, W. (1980). Diels-Alder Reactivity of Polycyclic Aromatic Hydrocarbons. 1. Acenes and Benzologs. *J. Am. Chem. Soc.* 102, 3163–3173. doi:10.1021/ja00529a046

Blase, X., and Attaccalite, C. (2011). Charge-transfer Excitations in Molecular Donor-Acceptor Complexes Within the Many-Body Bethe-Salpeter Approach. *Appl. Phys. Lett.* 99, 171909. doi:10.1063/1.3655352

Blase, X., Attaccalite, C., and Olevano, V. (2011). First-PrinciplesGWcalculations for Fullerenes, Porphyrins, Phtalocyanine, and Other Molecules of Interest for Organic Photovoltaic Applications. *Phys. Rev. B.* 83, 115103. doi:10.1103/physrevb.83.115103

Blase, X., Duchemin, I., Jacquemin, D., and Loos, P.-F. (2020). The Bethe-Salpeter Equation Formalism: From Physics to Chemistry. *J. Phys. Chem. Lett.* 11, 7371–7382. doi:10.1021/acs.jpclett.0c01875

Blase, X., Duchemin, I., and Jacquemin, D. (2018). The Bethe-Salpeter Equation in Chemistry: Relations With TD-DFT, Applications and Challenges. *Chem. Soc. Rev.* 47, 1022–1043. doi:10.1039/c7cs00049a

Bree, A., and Lyons, L. E. (1960). 1002 The Intensity of Ultraviolet-Light Absorption by Monocrystals. Part IV. Absorption by Naphthacene of Plane-Polarized Light. *J. Chem. Soc.* 1960, 5206–5212. doi:10.1039/JR9600005206

Bruneval, F., Hamed, S. M., and Neaton, J. B. (2015). A Systematic Benchmark of the Ab Initio Bethe-Salpeter Equation Approach for Low-Lying Optical Excitations of Small Organic Molecules. *J. Chem. Phys.* 142, 244101. doi:10.1063/1.4922489

Delos, J. B., Knudson, S. K., and Noid, D. W. (1983). Highly Excited States of a Hydrogen Atom in a Strong Magnetic Field. *Phys. Rev. A.* 28, 7–21. doi:10.1103/physreva.28.7

Egidi, F., Sun, S., Goings, J. J., Scalmani, G., Frisch, M. J., and Li, X. (2017). Two-Component Noncollinear Time-Dependent Spin Density Functional Theory for Excited State Calculations. *J. Chem. Theor. Comput.* 13, 2591–2603. doi:10.1021/acs.jctc.7b00104

Fernandez-Corbaton, I., Beutel, D., Rockstuhl, C., Pausch, A., and Klopper, W. (2020). Computation of Electromagnetic Properties of Molecular Ensembles. *ChemPhysChem.* 21, 878–887. doi:10.1002/cphc.202000072

Furche, F., Ahlrichs, R., Hättig, C., Klopper, W., Sierka, M., and Weigend, F. (2014). Turbomole. *Wires Comput. Mol. Sci.* 4, 91–100. doi:10.1002/wcms.1162

Gao, J., Zou, W., Liu, W., Xiao, Y., Peng, D., Song, B., et al. (2005). Time-Dependent Four-Component Relativistic Density-Functional Theory for Excitation Energies. II. The Exchange-Correlation Kernel. *J. Chem. Phys.* 123, 054102. doi:10.1063/1.1940609

Gui, X., Holzer, C., and Klopper, W. (2018). Accuracy Assessment of GW Starting Points for Calculating Molecular Excitation Energies Using the Bethe-Salpeter Formalism. *J. Chem. Theor. Comput.* 14, 2127–2136. doi:10.1021/acs.jctc.8b00014

Guidez, E. B., and Aikens, C. M. (2013). Origin and TDDFT Benchmarking of the Plasmon Resonance in Acenes. *J. Phys. Chem. C.* 117, 21466–21475. doi:10.1021/jp4059033

Hampe, F., Gross, N., and Stopkowicz, S. (2020). Full Triples Contribution in Coupled-Cluster and Equation-Of-Motion Coupled-Cluster Methods for Atoms and Molecules in strong Magnetic fields. *Phys. Chem. Chem. Phys.* 22, 23522–23529. doi:10.1039/d0cp04169f

Hampe, F., and Stopkowicz, S. (2017). Equation-of-Motion Coupled-Cluster Methods for Atoms and Molecules in Strong Magnetic Fields. *J. Chem. Phys.* 146, 154105. doi:10.1063/1.4979624

Hampe, F., and Stopkowicz, S. (2019). Transition-Dipole Moments for Electronic Excitations in Strong Magnetic Fields Using Equation-Of-Motion and Linear Response Coupled-Cluster Theory. *J. Chem. Theor. Comput.* 15, 4036–4043. doi:10.1021/acs.jctc.9b00242

Hättig, C. (2005). Optimization of Auxiliary Basis Sets for RI-MP2 and RI-CC2 Calculations: Core-Valence and Quintuple-ζ Basis Sets for H to Ar and QZVPP Basis Sets for Li to Kr. *Phys. Chem. Chem. Phys.* 7, 59–66. doi:10.1039/b415208e

Hättig, C., and Weigend, F. (2000). CC2 Excitation Energy Calculations on Large Molecules Using the Resolution of the Identity Approximation. *J. Chem. Phys.* 113, 5154–5161. doi:10.1063/1.1290013

Hedin, L. (1991). Properties of Electron Self-Energies and Their Role in Electron Spectroscopies. *Nucl. Instr. Methods Phys. Res. Section A: Acc. Spectrometers, Detectors Associated Equipment.* 308, 169–177. doi:10.1016/0168-9002(91)90619-2

Helgaker, T., and Jørgensen, P. (1991). An Electronic Hamiltonian for Origin Independent Calculations of Magnetic Properties. *J. Chem. Phys.* 95, 2595–2601. doi:10.1063/1.460912

Holzer, C., Franzke, Y. J., and Kehry, M. (2021). Assessing the Accuracy of Local Hybrid Density Functional Approximations for Molecular Response Properties. *J. Chem. Theor. Comput.* 17, 2928–2947. doi:10.1021/acs.jctc.1c00203

Holzer, C., and Klopper, W. (2017). Communication: Symmetry-Adapted Perturbation Theory With Intermolecular Induction and Dispersion Energies From the Bethe-Salpeter Equation. *J. Chem. Phys.* 147, 181101. doi:10.1063/1.5007929

Holzer, C., and Klopper, W. (2018). Communication: A Hybrid Bethe-Salpeter/Time-dependent Density-Functional-Theory Approach for Excitation Energies. *J. Chem. Phys.* 149, 101101. doi:10.1063/1.5051028

Holzer, C., and Klopper, W. (2019). Ionized, Electron-Attached, and Excited States of Molecular Systems With Spin-Orbit Coupling: Two-Component GW and Bethe-Salpeter Implementations. *J. Chem. Phys.* 150, 204116. doi:10.1063/1.5094244

Holzer, C., Teale, A. M., Hampe, F., Stopkowicz, S., Helgaker, T., and Klopper, W. (2019). GW Quasiparticle Energies of Atoms in Strong Magnetic Fields. *J. Chem. Phys.* 150, 214112. doi:10.1063/1.5093396

Irons, T. J. P., David, G., and Teale, A. M. (2021). Optimizing Molecular Geometries in Strong Magnetic Fields. *J. Chem. Theor. Comput.* 17, 2166–2185. doi:10.1021/acs.jctc.0c01297

Jacquemin, D., Duchemin, I., and Blase, X. (2015). Benchmarking the Bethe-Salpeter Formalism on a Standard Organic Molecular Set. *J. Chem. Theor. Comput.* 11, 3290–3304. doi:10.1021/acs.jctc.5b00304

Jacquemin, D., Duchemin, I., Blondel, A., and Blase, X. (2017). Benchmark of Bethe-Salpeter for Triplet Excited-States. *J. Chem. Theor. Comput.* 13, 767–783. doi:10.1021/acs.jctc.6b01169

Kehry, M., Franzke, Y. J., Holzer, C., and Klopper, W. (2020). Quasirelativistic Two-Component Core Excitations and Polarisabilities From a Damped-Response Formulation of the Bethe-Salpeter Equation. *Mol. Phys.* 118, e1755064. doi:10.1080/00268976.2020.1755064

Klevens, H. B., and Platt, J. R. (1949). Spectral Resemblances of Cata-Condensed Hydrocarbons. *J. Chem. Phys.* 17, 470–481. doi:10.1063/1.1747291

Komorovsky, S., Cherry, P. J., and Repisky, M. (2019). Four-Component Relativistic Time-Dependent Density-Functional Theory Using a Stable

Noncollinear DFT Ansatz Applicable to Both Closed- and Open-Shell Systems. *J. Chem. Phys.* 151, 184111. doi:10.1063/1.5121713

Krause, K., Harding, M. E., and Klopper, W. (2015). Coupled-Cluster Reference Values for the GW27 and GW100 Test Sets for the Assessment of GW Methods. *Mol. Phys.* 113, 1952–1960. doi:10.1080/00268976.2015.1025113

Krause, K., and Klopper, W. (2015). Description of Spin-Orbit Coupling in Excited States With Two-Component Methods Based on Approximate Coupled-Cluster Theory. *J. Chem. Phys.* 142, 104109. doi:10.1063/1.4908536

Krause, K., and Klopper, W. (2017). Implementation of the Bethe–Salpeter Equation in the TURBOMOLE Program. *J. Comput. Chem.* 38, 383–388. doi:10.1002/jcc.24688

Lange, K. K., Tellgren, E. I., Hoffmann, M. R., and Helgaker, T. (2012). A Paramagnetic Bonding Mechanism for Diatomics in Strong Magnetic Fields. *Science.* 337, 327–331. doi:10.1126/science.1219703

Leng, X., Jin, F., Wei, M., and Ma, Y. (2016). GW Method and Bethe-Salpeter Equation for Calculating Electronic Excitations. *Wires Comput. Mol. Sci.* 6, 532–550. doi:10.1002/wcms.1265

Lim, S.-H., Bjorklund, T. G., Spano, F. C., and Bardeen, C. J. (2004). Exciton Delocalization and Superradiance in Tetracene Thin Films and Nanoaggregates. *Phys. Rev. Lett.* 92, 107402. doi:10.1103/physrevlett.92.107402

London, F. (1937). Théorie Quantique du Diamagnétisme des Combinaisons Aromatiques. *Comptes rendus.* 205, 28–30.

Norman, P., Ruud, K., and Helgaker, T. (2004). Density-Functional Theory Calculations of Optical Rotatory Dispersion in the Nonresonant and Resonant Frequency Regions. *J. Chem. Phys.* 120, 5027–5035. doi:10.1063/1.1647515

Olovsson, W., Tanaka, I., Puschnig, P., and Ambrosch-Draxl, C. (2009). Near-Edge Structures From First Principles All-Electron Bethe-Salpeter Equation Calculations. *J. Phys. Condens. Matter.* 21, 104205. doi:10.1088/0953-8984/21/10/104205

Pausch, A., and Klopper, W. (2020). Efficient Evaluation of Three-Centre Two-Electron Integrals Over London Orbitals. *Mol. Phys.* 118, e1736675. doi:10.1080/00268976.2020.1736675

Perdew, J. P., Burke, K., and Ernzerhof, M. (1997). Generalized Gradient Approximation Made Simple. *Phys. Rev. Lett.* 77, 1396–3868. doi:10.1103/physrevlett.77.3865

Pulay, P. (1980). Convergence Acceleration of Iterative Sequences. The Case of SCF Iteration. *Chem. Phys. Lett.* 73, 393–398. doi:10.1016/0009-2614(80)80396-4

Rangel, T., Hamed, S. M., Bruneval, F., and Neaton, J. B. (2017). An Assessment of Low-Lying Excitation Energies and Triplet Instabilities of Organic Molecules With an Ab Initio Bethe-Salpeter Equation Approach and the Tamm-Dancoff Approximation. *J. Chem. Phys.* 146, 194108. doi:10.1063/1.4983126

Ruud, K., Helgaker, T., Bak, K. L., Jo/rgensen, P., and Jensen, H. J. r. A. (1993). Hartree-Fock Limit Magnetizabilities From London Orbitals. *J. Chem. Phys.* 99, 3847–3859. doi:10.1063/1.466131

Sagmeister, S., and Ambrosch-Draxl, C. (2009). Time-Dependent Density Functional Theory Versus Bethe-Salpeter Equation: an All-Electron Study. *Phys. Chem. Chem. Phys.* 11, 4451–4457. doi:10.1039/b903676h

Sen, S., Lange, K. K., and Tellgren, E. I. (2019). Excited States of Molecules in Strong Uniform and Nonuniform Magnetic Fields. *J. Chem. Theor. Comput.* 15, 3974–3990. doi:10.1021/acs.jctc.9b00103

Sims, J. R., Rickel, D. G., Swenson, C. A., Schillig, J. B., Ellis, G. W., and Ammerman, C. N. (2008). Assembly, Commissioning and Operation of the NHMFL 100 Tesla Multi-Pulse Magnet System. *IEEE Trans. Appl. Supercond.* 18, 587–591. doi:10.1109/tasc.2008.922541

Sony, P., and Shukla, A. (2007). Large-scale Correlated Calculations of Linear Optical Absorption and Low-Lying Excited Statesof Polyacenes: Pariser-Parr-Pople Hamiltonian. *Phys. Rev. B.* 75, 155208. doi:10.1103/physrevb.75.155208

Stetina, T. F., Sun, S., Williams-Young, D. B., and Li, X. (2019). Modeling Magneto-Photoabsorption Using Time-Dependent Complex Generalized Hartree-Fock. *ChemPhotoChem.* 3, 739–746. doi:10.1002/cptc.201900161

Stopkowicz, S., Gauss, J., Lange, K. K., Tellgren, E. I., and Helgaker, T. (2015). Coupled-Cluster Theory for Atoms and Molecules in strong Magnetic Fields. *J. Chem. Phys.* 143, 074110. doi:10.1063/1.4928056

Stopkowicz, S. (2018). Perspective: Coupled Cluster Theory for Atoms and Molecules in strong Magnetic Fields. *Int. J. Quan. Chem.* 118, e25391. doi:10.1002/qua.25391

Suellen, C., Freitas, R. G., Loos, P.-F., and Jacquemin, D. (2019). Cross-Comparisons Between Experiment, TD-DFT, CC, and ADC for Transition Energies. *J. Chem. Theor. Comput.* 15, 4581–4590. doi:10.1021/acs.jctc.9b00446

Sun, S., Williams-Young, D. B., Stetina, T. F., and Li, X. (2019a). Generalized Hartree-Fock With Nonperturbative Treatment of Strong Magnetic Fields: Application to Molecular Spin Phase Transitions. *J. Chem. Theor. Comput.* 15, 348–356. doi:10.1021/acs.jctc.8b01140

Sun, S., Williams-Young, D., and Li, X. (2019b). An Ab Initio Linear Response Method for Computing Magnetic Circular Dichroism Spectra With Nonperturbative Treatment of Magnetic Field. *J. Chem. Theor. Comput.* 15, 3162–3169. doi:10.1021/acs.jctc.9b00095

Tellgren, E. I., Helgaker, T., and Soncini, A. (2009). Non-Perturbative Magnetic Phenomena in Closed-Shell Paramagnetic Molecules. *Phys. Chem. Chem. Phys.* 11, 5489–5498. doi:10.1039/b822262b

Tellgren, E. I., Reine, S. S., and Helgaker, T. (2012). Analytical GIAO and Hybrid-Basis Integral Derivatives: Application to Geometry Optimization of Molecules in Strong Magnetic fields. *Phys. Chem. Chem. Phys.* 14, 9492–9499. doi:10.1039/c2cp40965h

Tellgren, E. I., Soncini, A., and Helgaker, T. (2008). Nonperturbative Ab Initio Calculations in strong Magnetic Fields Using London Orbitals. *J. Chem. Phys.* 129, 154114. doi:10.1063/1.2996525

Turbiner, A. V., and López Vieyra, J. C. (2004). $\\mathrm{H}_{2}^{+}$Ion in a strong Magnetic Field: Lowest Excited States. *Phys. Rev. A.* 69, 053413. doi:10.1103/physreva.69.053413

van Setten, M. J., Weigend, F., and Evers, F. (2012). The GW-Method for Quantum Chemistry Applications: Theory and Implementation. *J. Chem. Theor. Comput.* 9, 232–246. doi:10.1021/ct300648t

Vinson, J., Rehr, J. J., Kas, J. J., and Shirley, E. L. (2011). Bethe-Salpeter Equation Calculations of Core Excitation Spectra. *Phys. Rev. B.* 83, 115106. doi:10.1103/physrevb.83.115106

Vydrov, O. A., and Scuseria, G. E. (2006). Assessment of a Long-Range Corrected Hybrid Functional. *J. Chem. Phys.* 125, 234109. doi:10.1063/1.2409292

Weigend, F. (2006). Accurate Coulomb-Fitting Basis Sets for H to Rn. *Phys. Chem. Chem. Phys.* 8, 1057–1065. doi:10.1039/b515623h

Weigend, F., and Ahlrichs, R. (2005). Balanced Basis Sets of Split Valence, Triple Zeta Valence and Quadruple Zeta Valence Quality for H to Rn: Design and Assessment of Accuracy. *Phys. Chem. Chem. Phys.* 7, 3297–3305. doi:10.1039/b508541a

Weigend, F. (2008). Hartree-Fock Exchange Fitting Basis Sets for H to Rn. *J. Comput. Chem.* 29, 167–175. doi:10.1002/jcc.20702

Wibowo, M., Irons, T. J. P., and Teale, A. M. (2021). Modeling Ultrafast Electron Dynamics in Strong Magnetic Fields Using Real-Time Time-Dependent Electronic Structure Methods. *J. Chem. Theor. Comput.* 17, 2137–2165. doi:10.1021/acs.jctc.0c01269

Yanai, T., Tew, D. P., and Handy, N. C. (2004). A New Hybrid Exchange-Correlation Functional Using the Coulomb-Attenuating Method (CAM-B3lyp). *Chem. Phys. Lett.* 393, 51–57. doi:10.1016/j.cplett.2004.06.011

Conflict of Interest: The authors declare that the research was conducted in the absence of any commercial or financial relationships that could be construed as a potential conflict of interest.

Publisher's Note: All claims expressed in this article are solely those of the authors and do not necessarily represent those of their affiliated organizations, or those of the publisher, the editors, and the reviewers. Any product that may be evaluated in this article, or claim that may be made by its manufacturer, is not guaranteed or endorsed by the publisher.

frontiers in Chemistry

ORIGINAL RESEARCH
published: 21 December 2021
doi: 10.3389/fchem.2021.749779

The GW Miracle in Many-Body Perturbation Theory for the Ionization Potential of Molecules

Fabien Bruneval[*1], *Nike Dattani*[2] *and Michiel J. van Setten*[3]

[1]CEA, Service de Recherches de Métallurgie Physique, Direction des Energies, Université Paris-Saclay, Paris, France, [2]HPQC Labs, Waterloo, ON, Canada, [3]IMEC, Leuven, Belgium

We use the GW100 benchmark set to systematically judge the quality of several perturbation theories against high-level quantum chemistry methods. First of all, we revisit the reference CCSD(T) ionization potentials for this popular benchmark set and establish a revised set of CCSD(T) results. Then, for all of these 100 molecules, we calculate the HOMO energy within second and third-order perturbation theory (PT2 and PT3), and, *GW* as post-Hartree-Fock methods. We found *GW* to be the most accurate of these three approximations for the ionization potential, by far. Going beyond *GW* by adding more diagrams is a tedious and dangerous activity: We tried to complement *GW* with second-order exchange (SOX), with second-order screened exchange (SOSEX), with interacting electron-hole pairs (W_{TDHF}), and with a *GW* density-matrix (γ^{GW}). Only the γ^{GW} result has a positive impact. Finally using an improved hybrid functional for the non-interacting Green's function, considering it as a cheap way to approximate self-consistency, the accuracy of the simplest *GW* approximation improves even more. We conclude that *GW* is a miracle: Its subtle balance makes *GW* both accurate and fast.

Keywords: electronic structure ab initio calculations, many-body ab initio structure, ionization potential (IP), density-functional theory (DFT), Green's function (GF), feynman diagram expansion, coupled-cluster method, high-precision benchmarks

OPEN ACCESS

Edited by:
Dorothea Golze,
Aalto University, Finland

Reviewed by:
Christof Holzer,
Karlsruhe Institute of Technology (KIT), Germany
Xiaopeng Wang,
Shandong University, China

***Correspondence:**
Fabien Bruneval
fabien.bruneval@cea.fr

Specialty section:
This article was submitted to Theoretical and Computational Chemistry, a section of the journal Frontiers in Chemistry

Received: *29 July 2021*
Accepted: *14 September 2021*
Published: *21 December 2021*

Citation:
Bruneval F, Dattani N and van Setten MJ (2021) The GW Miracle in Many-Body Perturbation Theory for the Ionization Potential of Molecules. Front. Chem. 9:749779. doi: 10.3389/fchem.2021.749779

1 INTRODUCTION

Many-body perturbation theory (MBPT) (Fetter and Walecka, 1971) is currently actively used to predict the excitation energies of molecules (Shirley and Martin, 1993; Grossman et al., 2001; Rostgaard et al., 2010; Blase et al., 2011; Bruneval, 2012; Körzdörfer and Marom, 2012; Ren et al., 2012; Sharifzadeh et al., 2012; Bruneval and Marques, 2013; van Setten et al., 2013; Koval et al., 2014; Govoni and Galli, 2015; van Setten et al., 2015; Blase et al., 2016; Knight et al., 2016; Kuwahara et al., 2016; Heßelmann, 2017; Maggio et al., 2017; Golze et al., 2018; Lange and Berkelbach, 2018; Wilhelm et al., 2018; Golze et al., 2019; Lewis and Berkelbach, 2019; Blase et al., 2020). The boost in the application of MBPT to molecules is being driven by the advent of physicists' methods, most noticeably the *GW* approximation (Hedin, 1965) for electron attachment and detachment energies and the Bethe-Salpeter equation (Onida et al., 1995) for neutral excitations. The present *Research Topic* acknowledges this new situation and this contribution will specifically focus on electron detachment energies.

The arrival of the physicists' methods that had been limited in their application to extended systems should not hide the fact that MBPT had been already present in chemistry for several decades, however with different approximations (Szabó and Ostlund, 1996). Indeed in the 70s,

Cederbaum and coworkers explored the performance of MBPT for electron attachment and detachment energies (Cederbaum et al., 1973; Cederbaum and Niessen, 1974; Cederbaum, 1975; von Niessen et al., 1977; Cederbaum and Domcke, 1977; Cederbaum et al., 1978). Their approximations were based on a strict order-by-order expansion with respect to the electron-electron Coulomb interaction v. Here we name the second-order perturbation theory, PT2, and the third-order perturbation theory, PT3. Going beyond the third-order has seldom been attempted (Ortiz, 1988) for computational reasons.

The physical approximations took another path when it was realized that PT2 was producing divergent energies for the homogeneous electron gas (Mahan, 2000). It was then proposed to consider the *screened* Coulomb interaction W (Hedin, 1965) instead of the bare Coulomb interaction v as the perturbation. It turned out that the first-order correction, namely the GW approximation (Onida et al., 2002), was very effective for extended systems (Hanke and Sham, 1975; Godby et al., 1986; Hybertsen and Louie, 1986).

Now that the GW approximation has permeated chemistry, we think it is time to compare the performance in both accuracy and speed of the different approximations on a fair, unbiased basis. Fortunately, one of us has recently introduced a wide benchmark, named GW100 (van Setten et al., 2015), which consists of the ionization potentials (IP) of 100 atoms and small to medium-sized molecules. Close to twenty different codes have by now used this set to evaluate their results, and in general, when all convergence parameters are considered, the results agree well. Reference IP energies were calculated by Krause et al. (2015) via differences in the total energies calculated for the neutral and positively-charged species with the CCSD(T) approximation.

The GW100 benchmark is hence to be the boxing ring in which we want to scrutinize the quality of the different MBPT approximations (PT2, PT3, GW, and beyond GW). With GW we denote here the one-shot GW appoximation that does not include self-consistency; in the literature it is sometimes denoted as G_0W_0. However, before doing so, we will revisit the CCSD(T) reference IPs. We observed that the set from Krause et al. (2015) is not sufficiently precise for this level of benchmarking: for instance the SO_2 IP was more than 1 eV off the trend. We present here a complete recalculation of the CCSD(T) reference IPs for the GW100 benchmark.

With this updated benchmark, we explain the success of the GW approximation for the IP of molecules: The GW approximation is both accurate and fast. Going beyond GW often worsens the result.

The article is organized as follows: In *MBPT: v-based or W-based expansions*, we recapitulate the different MBPT approximations and explain them with Goldstone-Feynman diagrams. In *CCSD(T) ionization potentials for GW100*, we set up new CCSD(T) reference values of the IPs for the GW100 benchmark set. *Benchmarking the MBPT Strategies* compares the performance of the different approximations based on a standard Hartree-Fock starting point. *MBPT From an Improved Mean-Field Starting Point* shows an attempt to approach MBPT self-consistency with tuned hybrid functionals. Finally the conclusions are drawn in *Conclusion*. Hartree atomic units are used throughout this work. The numerical values are made available as Supplemental Material, under the wide-spread machine- and human-readable JSON file format.

2 MBPT: *V*-BASED OR *W*-BASED EXPANSIONS

2.1 Green's Function and Self-Energy in MBPT

In MBPT, the central quantity is the one-electron Green's function. The Green's function describes the time-propagation of an additional particle in the electronic system: an extra electron for propagation forward in time, or a hole for propagation backward in time. The Green's function contains a great deal of information. For instance its diagonal is the electronic density, and, most interesting for us, its poles are the ionization energies (Fetter and Walecka, 1971).

Once an approximate Green's function G_0 is known, the exact Green's function G can be obtained thanks to the Dyson equation:

$$G(\omega) = G_0(\omega) + G_0(\omega)\Delta\Sigma(\omega)G(\omega), \tag{1}$$

where the spatial indices, later defined as p and q, have been dropped for simplicity.

The operator $\Delta\Sigma$ stands for the self-energy difference. It performs the humongous task of connecting G_0 to G. If the Hartree-Fock approximation (HF) is used for G_0, then $\Delta\Sigma$ coincides with the missing correlation part of the self-energy Σ_c.

When a mean-field approximation is selected for G_0, it can be expressed analytically:

$$G_{0\,pq}(\omega) = \delta_{pq}\frac{2}{\omega - \epsilon_p \pm i\eta}, \tag{2}$$

where the factor of 2 accounts for spin, p and q are molecular orbital (MO) indices, ϵ_p and $\pm\,\mathrm{i}\eta$ is a vanishing imaginary number that ensures the correct analytic behavior of G_0. G_0 is diagonal in the corresponding MO basis.

In practice, we make the further approximation that the self-energy difference is also diagonal in the MO basis:

$$\Delta\Sigma_{pq}(\omega) = \delta_{pq}\Delta\Sigma_{pp}(\omega). \tag{3}$$

This approximation is believed to be very good and is common practice in this field (Golze et al., 2019).

Recasting the Dyson **Eq. 1** into

$$\left[G_0^{-1}(\omega) - \Delta\Sigma(\omega)\right]G(\omega) = I, \tag{4}$$

where I is the identity operator, it becomes clear that the diagonal approximation of $\Delta\Sigma$ will induce a diagonal approximation to G, since G and therefore also G_0^{-1} are diagonal in the corresponding molecular basis.

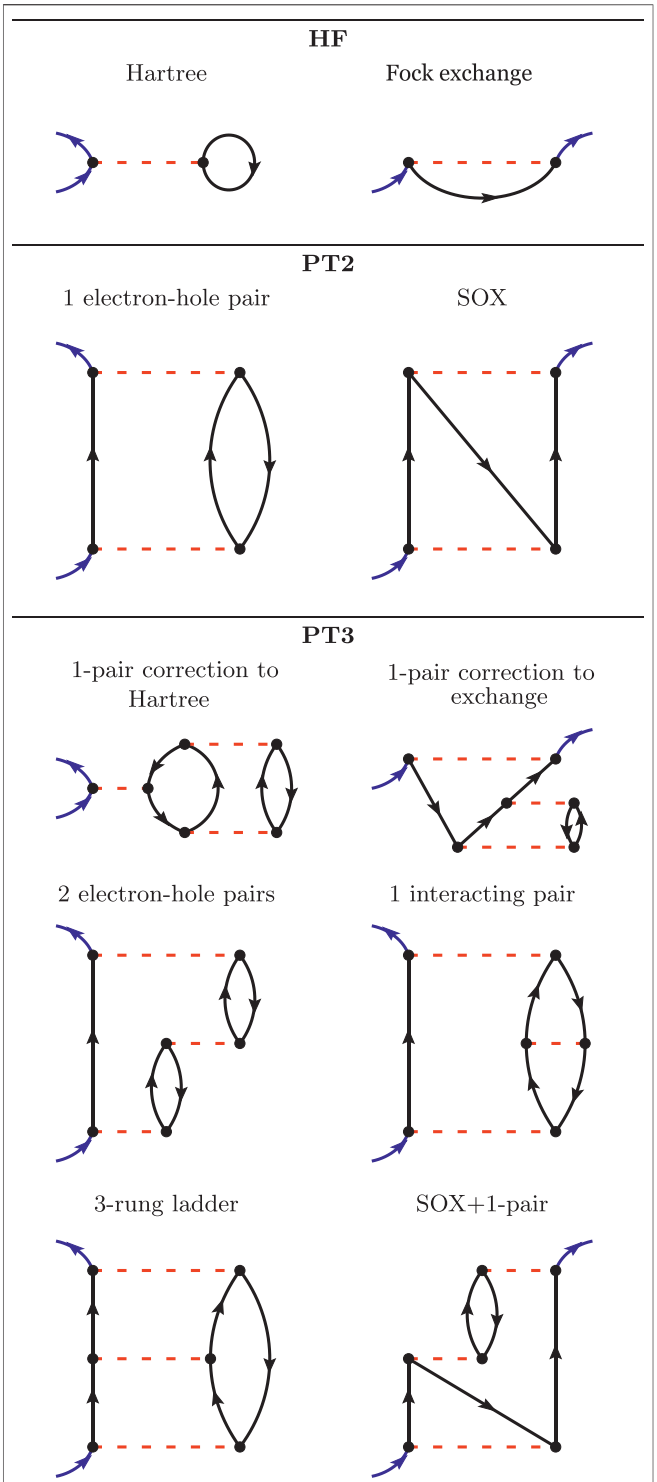

FIGURE 1 | All the Goldstone-Feynman diagrams in HF **(upper panel)**, PT2 **(central panel)** and an illustrative subset of the Goldstone-Feynman diagrams in PT3 **(lower panel)**.

Furthermore, the poles of G correspond to the zeroes of the term in between the brackets in **Eq. 4**:

$$\omega - \epsilon_p = \Delta\Sigma_{pp}(\omega). \tag{5}$$

This equation is named the quasiparticle equation and the highest zero for the p index that corresponds to occupied states is $\epsilon_{\mathrm{HOMO}} = -\mathrm{IP}$. The HOMO energies reported in this work are obtained with this procedure, which is often referred to as the "graphical solution" of the quasiparticle equation (Golze et al., 2019).

We can calculate the spectral weight Z associated with a pole of G with

$$Z_p(\omega) = \left(1 - \frac{\partial \Delta\Sigma_{pp}}{\partial \omega}\right)^{-1}. \tag{6}$$

Being a weight, this quantity should range from 0 to 1 and hence $\frac{\partial \Delta\Sigma_{pp}}{\partial \omega}$ should be negative.

Note that the mean-field orbitals indexed by p might not be ordered properly. That is why in practice one needs to consider not only the mean-field HOMO, but also a few states below. This pathological behavior is known to occur for N_2 for instance (von Niessen et al., 1977).

The challenge in MBPT is then to derive approximate expressions for $\Delta\Sigma$ that are both accurate and computationally tractable. Henceforth, we use the Goldstone-Feynman diagram representation to describe the different working approximations. The analytic expressions can be found in the cited references.

2.2 HF, PT2, PT3

In this Section, we follow the traditional approach in quantum chemistry for the so-called post-Hartree-Fock calculations (Szabó and Ostlund, 1996; Helgaker et al., 2000).

Let us start gradually and begin with the formulation of the HF approximation in terms of Goldstone-Feynman diagrams. In the upper panel of **Figure 1**, we have presented the two Goldstone-Feynman diagrams of HF: the Hartree and the Fock exchange terms. The blue arrows indicate the entry and the exit points. The black arrow is a Green's function and the red dashed line is the bare Coulomb interaction v. As v is assumed to be instantaneous, we represent it horizontally (so that the vertical axis would be the time axis).

The Hartree diagram (upper left-hand diagram in **Figure 1**) translates into the following integral:

$$v_H(\mathbf{r}) = \int d\mathbf{r}' \frac{\rho(\mathbf{r}')}{|\mathbf{r} - \mathbf{r}'|}, \tag{7}$$

Where $\rho(\mathbf{r}) = G(\mathbf{r}t, \mathbf{r}t^+)$ is the electronic density. From the Hartree Goldstone-Feynman diagram, we can immediately see that the Hartree potential is local in space and in time, since the entry and exit points are identical. The exchange diagram (upper right-hand diagram in **Figure 1**) is non-local in space, but local in time, since its entry and exit points share the same y coordinate.

In regular MBPT, one considers the electron-electron interaction v as the meaningful order parameter that will allow us to derive more and more complex approximations.

The second-order perturbation theory, PT2, considers all the possible Goldstone-Feynman diagrams having two Coulomb interactions. There are only two of those diagrams and they

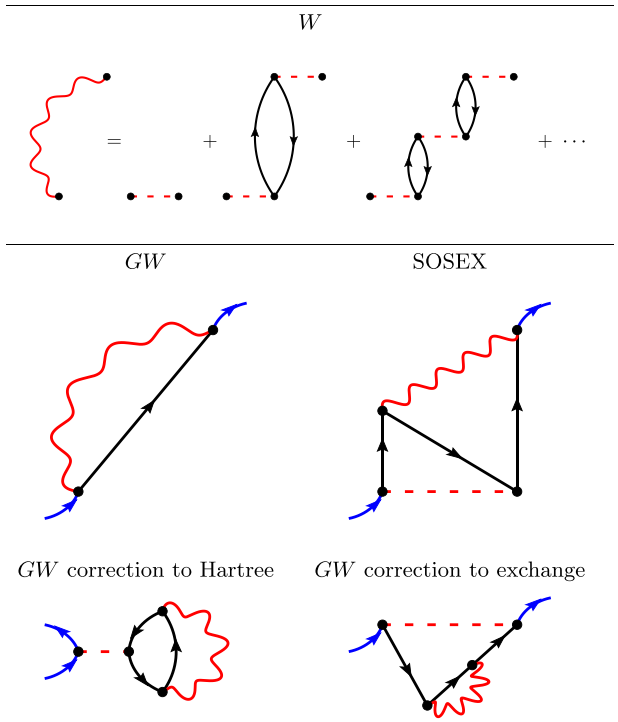

FIGURE 2 | The first Goldstone-Feynman diagrams in the RPA screened Coulomb interaction *W* **(upper panel)**, the *GW* diagrams **(middle left-hand panel)**, the SOSEX diagram **(middle right-hand panel)**, and the two γ^{GW} diagrams **(lower panel)**.

are drawn in the middle panel of **Figure 1**. The first one accounts for the propagation of an electron (or a hole) interacting with an electron-hole pair. The second one is the so-called second-order exchange (SOX). These two diagrams are still rather simple and can be found in chemistry textbooks (Szabó and Ostlund, 1996).

However, the next level, namely PT3, brings in many new terms. PT3 considers all the possible Goldstone-Feynman diagrams with three Coulomb interactions, which results in the analytic terms reported in the Appendix of Ref. (Cederbaum and Domcke, 1977). The formulas extend over three printed pages and will not be reproduced here. We will instead draw a few instructive Goldstone-Feynman diagrams in the lower panel of **Figure 1**. PT3 contains some static diagrams (the A-diagrams in Cederbaum's notation), such as the two first diagrams drawn in the PT3 panel. They can be interpreted as corrections to the Hartree and Fock terms due to a correction to the density and the density-matrix. Besides these, some dynamical diagrams are displayed with two electron-hole pairs, or one interacting electron-hole pair, or a ladder diagram, etc.

The PT3 approximation had been implemented and tested by Cederbaum and coworkers (Cederbaum et al., 1973; Cederbaum and Niessen, 1974; Cederbaum, 1975; Cederbaum and Domcke, 1977; Cederbaum et al., 1978), but never applied to a systematic benchmark, to the best of our knowledge. Those authors noticed that PT3 was not fully satisfactory and proposed the rescaling of some of the terms to form a better estimate of the IP. This empirical rescaling, known as outer valence Green's function (OVGF) or as electron propagator theory (EPT), is *not* applied here, as our focus is the MBPT itself.

Considering the huge number of terms in PT3, it is not surprising that PT4 has only rarely been used (Ortiz, 1988).

2.3 *W*, *GW*, SOSEX

In condensed-matter physics, it has been realized that the one-ring diagram in PT2 (See **Figure 1**) was producing an infinite value when evaluated for a gapless system (Mahan, 2000). A renormalized interaction was then introduced then to mitigate this problem (Baym and Kadanoff, 1961; Hedin, 1965).

The upper panel of **Figure 2** represents the screened Coulomb interaction *W* within the random-phase approximation. *W* is represented with wiggly lines that are not necessarily horizontal in the diagrams, because *W* is not instantaneous as *v* is. *W* is an infinite series of subsequent non-interacting electron-hole pairs.

There exists only one first-order diagram in *W*: the so-called *GW* approximation to the self-energy, represented in the middle left-hand panel of **Figure 2**. As *W* contains an infinite number of diagrams, the *GW* approximation cannot be rationalized with the *v*-based MBPT recapitulated in the previous section. Notice the similarity between the exchange diagram in HF (**Figure 1**) and the *GW* diagram: The Coulomb interaction has just been replaced by a non-horizontal *W* wiggly line.

This single *GW* diagram has been proven to yield very good results for the homogeneous electron gas (Hedin, 1965; Lundqvist, 1967), and for real periodic solids (Hanke and Sham, 1975; Strinati et al., 1982; Hybertsen and Louie, 1985; Godby et al., 1986). More recently, it has been realized that the same good performance is reached for molecules (Shirley and Martin, 1993; Grossman et al., 2001; Rostgaard et al., 2010; Blase et al., 2011; Bruneval, 2012; Körzdörfer and Marom, 2012; Ren et al., 2012; Sharifzadeh et al., 2012; Bruneval and Marques, 2013; van Setten et al., 2013; Koval et al., 2014; Govoni and Galli, 2015; van Setten et al., 2015; Blase et al., 2016; Knight et al., 2016; Kuwahara et al., 2016; Maggio et al., 2017; Golze et al., 2018; Lange and Berkelbach, 2018; Wilhelm et al., 2018; Golze et al., 2019; Lewis and Berkelbach, 2019; Blase et al., 2020).

Of course, the single *GW* diagram is just the first of an infinite expansion in *W*. However, the next diagrams become very complex, very quickly. They are often named "vertex corrections" in the literature. Vertex corrections appear in two different locations in Hedin's equations (Hedin, 1965) (or equivalently in the diagrams): in *W* beyond RPA and in the self-energy itself.

Adding more diagrams in *W* would incorporate the electron-hole interaction that is present in PT3 but not in *GW*. Lewis and Berkelbach have worked on this point and showed a small effect (Lewis and Berkelbach, 2019). We will test improving *GW* along that line by using a *W* interaction calculated within time-dependent Hartree-Fock (TDHF), labeled W_{TDHF}.

Adding more diagrams in the self-energy would incorporate the SOX diagram and more. For instance, we represent in

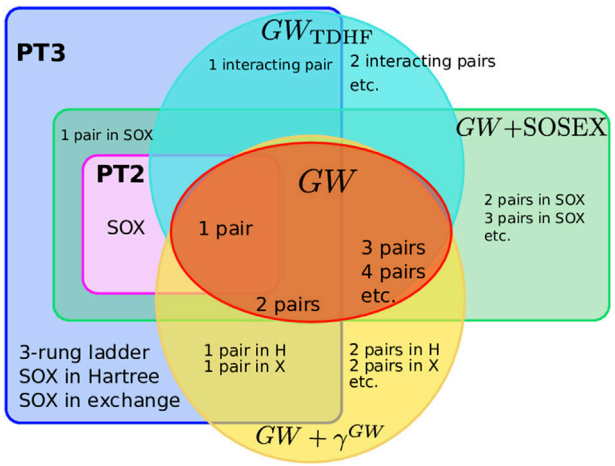

FIGURE 3 | Sets of Goldstone-Feynman diagrams considered here: PT2, PT3, *GW*, GW_{TDHF}, *GW* + SOSEX, $GW+\gamma^{GW}$. Some diagrams are explicitly named to give examples.

Figure 2 the so-called second-order screened exchange (SOSEX) of Ren and coworkers (Ren et al., 2015). It is an extension to SOX that considers a screened interaction W together with an unscreened interaction v. The complete second-order diagrams with two W wiggly lines has been very recently considered in Ref. (Wang et al., 2021). The authors conclude that it does not bring large contributions and we will use the simpler SOSEX diagram here.

It should be added that there exist additional low-order diagrams when the Green's function is not calculated self-consistently. Indeed, the two diagrams in the lower panel of **Figure 2** are first-order diagrams in W that give corrections to the Hartree potential and the Fock exchange. Similar diagrams show up in PT3, however with one electron-hole pair only. These two diagrams do not appear in Hedin's equations, because Hedin's derivation is obtained considering the self-consistent G. One of us has recently studied these diagrams and highlighted a sizable effect on the IP (Bruneval, 2019a), on the electronic densities (Bruneval, 2019b), and on the total energies (Bruneval et al., 2021). We shall name these diagrams γ^{GW} in this work, as they only affect the one-electron reduced-density-matrix.

To summarize the many approximations we have presented above, **Figure 3** sketches the different diagram sets used in this study. We see that PT3 contains PT2 and that *GW* has an overlap with PT2, but misses the SOX diagram. Some diagrams of *GW* are not present in PT2, nor in PT3: the n-pair diagrams with $n > 2$. *GW* + SOSEX entirely contains PT2, but obviously misses many diagrams of PT3. GW_{TDDFT} captures the 1-interacting-pair diagram of PT3 and adds the further interacting pairs. $GW + \gamma^{GW}$ has the 1-pair inclusion in Hartree and Fock exchange. For instance, the ladder diagram is present in PT3 only.

At this stage, there is no way to judge which approximation is best. Ideally in a perturbation theory, the more diagrams, the better. However, in MBPT, the perturbation is by no means "small" and, in our opinion, only practical calculations on trusted benchmarks are able to draw conclusions. This will be the topic of the next Sections.

3 CCSD(T) IONIZATION POTENTIALS FOR GW100

3.1 GW100

In this work we use the set of molecules defined in the GW100 set as our boxing ring. This set came into existence first in a comparison between only three codes (van Setten et al., 2015). In the meantime the developers of many other codes have used the set to test and benchmark their implementations, both for *GW* and other computational approaches aiming at the calculation of ionization energies and electron affinities (Caruso et al., 2016; Vlček et al., 2017a; Maggio et al., 2017; Wilhelm and Hutter, 2017; Govoni and Galli, 2018; Rodrigues Pela et al., 2018; Colonna et al., 2019; Gao and Chelikowsky, 2019; Brémond et al., 2020; Förster and Visscher, 2020; Gao and Chelikowsky, 2020; Bintrim and Berkelbach, 2021; Duchemin and Blase, 2021; Förster and Visscher, 2021; Wilhelm et al., 2021). At present over a hundred data sets have appeared for the GW100 set.

The GW100 set uses established geometries and keeps them fixed for each set of calculations. In the work on the GW100 set using plane-wave basis sets in the PAW formalism using the VASP code (Maggio et al., 2017), it was noticed that for two molecules, phenol and vinyl bromide, the structure used originally was not correct. From this point the two new structures have been added to the set in order to enable comparison between sets containing only one or both versions. In this work, we use the updated geometries, so that the total number of data points is 100.

For a completely correct comparison of the molecules in the GW100 set, between codes employing different basis sets, an extrapolation to the complete basis set limits is paramount (van Setten et al., 2015; Maggio et al., 2017; Govoni and Galli, 2018). However, the use of more complete basis sets that are necessary for an extrapolation is limited by the numerical scaling of the reference CCSD(T) calculations. Fortunately, for comparisons of different methods "beyond" one-shot *GW* in codes that are based on Gaussian orbitals, this is not strictly necessary, as long as the *same* basis set is used consistently. The def2-TZVPP basis set (Weigend and Ahlrichs, 2005) has historically been used for these comparisons (Krause et al., 2015; Caruso et al., 2016). We will hence use this basis set in this work as well. In this work, we refrain from interpreting small differences below 0.1 eV that could be affected by the basis set incompleteness, so that our qualitative conclusions would be equally valid for larger basis sets.

In their work providing CCSD(T) reference values for the GW100 molecules, Krause *et al.* also used the def2-TZVPP basis set (Krause et al., 2015). Close inspection of these results however shows that in some cases large deviations with the experimental values exist and larger than one would hope for CCSD(T). Moreover, in a number of these cases the discrepancy is larger than the one between *GW* and experiment. In the present comparison we need especially accurate reference energies and since also three molecular systems of the GW100 set are missing in the data by Krause *et al.*, we start by revisiting the CCSD(T) reference set.

TABLE 1 | Energies for SO_2^+ calculated with a default initial UHF guess in CFOUR (Matthews et al., 2020), and with the lowest-energy UHF solution. As in Ref. (Krause et al., 2015), no spatial symmetry was enforced at any time, and the number of frozen (uncorrelated) electrons was the same as for the calculations in Ref. (Krause et al., 2015).

Type of reference	SCF	CCSD(T)
UHF (default)	−546.861 914	−547.532 246
UHF (lowest)	−546.881 967	−547.488 601

3.2 Update of the CCSD(T) Reference IP

The CCSD(T) benchmark values for the ionization potentials, which have been used by all GW100 studies up to now, were done by the authors of Ref. (Krause et al., 2015). using an unrestricted Hartree-Fock (UHF) reference and no spatial symmetry constraints. In all cases, stability analysis was done at the UHF level to ensure that the UHF solution was indeed the lowest in energy, within their convergence tolerance.

While using the lowest energy UHF solution determined via such a stability analysis, can be a very *convenient* choice, it may not lead to the most accurate CCSD(T) energy. For example, in the case of SO_2^+, the UHF solution with the lowest energy at Hartree-Fock level, actually can lead to a higher energy at the frozen-core CCSD(T) level than a UHF solution with a higher energy at the Hartree-Fock level (see **Table 1**). While it is true that in general, a lower CCSD(T) energy does not necessarily mean a better one, the lowest energy in **Table 1** is the closest one to our FCI (full configuration interaction, a numerically exact energy within the chosen basis set) estimates (Dattani, 2021), so the lowest CCSD(T) energy is actually the more accurate one *in this case*. Indeed, SO_2^+ was one of the worst cases in the benchmark study of Ref. (Krause et al., 2015), in terms of the disagreement between CCSD(T) and experiment for the ionization energy, and it was a case where the *GW* calculation matched the experimental ionization energy better than the "benchmark" CCSD(T) calculations did.

In this work we have re-calculated the frozen-core CCSD(T) energies for the entire GW100 set, however we chose to use GAUSSIAN 16 (Frisch et al., 2016) (with default settings) instead of CFOUR, and the default in GAUSSIAN is an RHF (restricted Hartree-Fock) reference for all singlet species (in this paper, all neutral species), and a UHF reference for all species with a higher multiplicity (in this paper, all of the cations). This led to 46 IP values being updated with respect to Ref. (Krause et al., 2015), including the case of OCSe, for which Krause *et al.* accidentally used sulfur instead of selenium in their calculation. The most noticeable updates are SO_2, MgO, cytosine, and uracil with changes larger than 0.4 eV.

Our revised IPs improve very much the consistency of CCSD(T) with the related method named equation-of-motion coupled-cluster (EOM-IP-CCSD). Indeed, Lange and Berkelbach (Lange and Berkelbach, 2018) have evaluated the IPs for the complete GW100 set within this approximation and found a somewhat good agreement with Krause *et al.* with an MAE of 0.09 eV. However, this correct MAE is hiding a few terrible outliers, such as SO_2, MgO, cytosine, and uracil.

Now, comparing our updated CCSD(T) to Lange's EOM-IP-CCSD yields not only an improved MAE of 0.06 eV, but also fixes all the mentioned outliers. The deviations between the updated CCSD(T) and EOM-IP-CCSD never exceed 0.30 eV.

As our updated CCSD(T) set very much improves the consistency across the methods and the comparison to experiment when experimental data are available, we have confidence that our updated values are a genuine improvement. We remind the Reader that all the numerical values are reported in the Supplemental Material.

4 BENCHMARKING THE MBPT STRATEGIES

A noticeable source of misunderstanding between the different MBPT flavors is the starting mean-field approximation used for the non-interacting Green's function G_0 in **Eq. 2**. Chemists using PT2 and PT3 typically use HF. This has several advantages: the strict order-by-order expansion is enforced and no first-order terms exist by virtue of the Brillouin theorem (Szabó and Ostlund, 1996). However, an HF G_0 is maybe not the optimal Green's function.

The physicists, quite the opposite, constantly play with the starting mean-field in order to improve the final quasiparticle energy. This strategy, sometimes named "best *G*, best *W*", is very effective for periodic systems (Hybertsen and Louie, 1986; Aulbur et al., 1999). Indeed the HF approximation is typically not accurate for solids: the band gaps are overestimated by a lot (Silvi and Dovesi, 1988). Contrarily, *GW* based on a local density approximation (LDA) or on a semi-local approximation yields very decent results (van Schilfgaarde et al., 2006). For molecules, hybrid functionals (Bruneval and Marques, 2013) with a significant amount of Hartree-Fock exchange like BHLYP (Becke, 1993) or CAM-B3LYP (Yanai et al., 2004) are known to often produce good results.

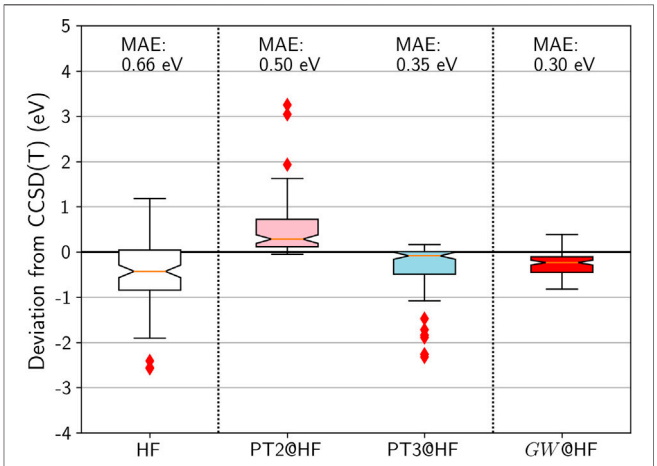

FIGURE 4 | Box plots for GW100 HOMO energy errors for HF, PT2, PT3, and *GW* from an HF G_0. CCSD(T) total energy differences are considered as the reference. Mean absolute errors (MAE) are also printed.

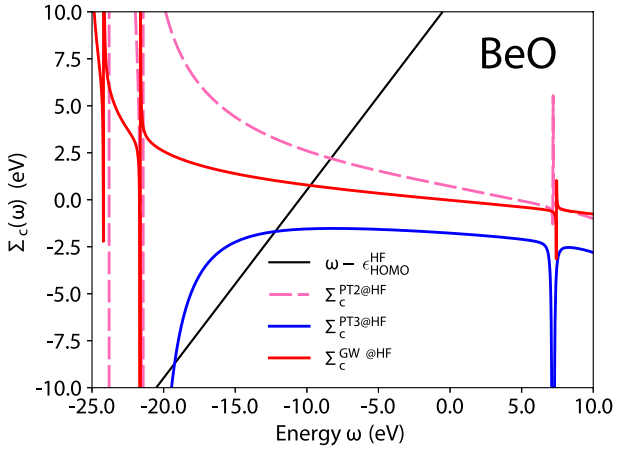

FIGURE 5 | BeO quasiparticle equation graphical solution of **Eq. 5** for the different self-energy approximations. HF is used for G_0.

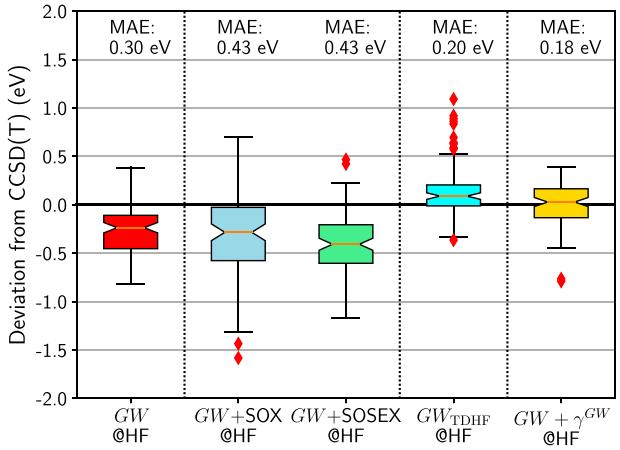

FIGURE 6 | Box plots for GW100 HOMO energy errors for *GW* and beyond starting from an HF G_0. CCSD(T) total energy differences are considered as the reference. Mean absolute errors (MAE) are also printed.

As the discussion about the mean-field starting point can blur the conclusions, we only use an HF starting point in this Section. Discussion about an improved starting point and its connection to self-consistency is postponed to the next Section.

Henceforth, all the self-energy calculations are performed with the code MOLGW (Bruneval et al., 2016). It implements MBPT self-energies on a Gaussian-type orbital basis. It also takes advantage of the approximation of the resolution-of-the-identity (RI) (Weigend et al., 2002; Blase et al., 2011; Ren et al., 2012) with the automatic generation of the auxiliary basis set as described in Ref. (Yang et al., 2007). This technical approximation has been proven to be very accurate (Blase et al., 2016). We systematically evaluate the MBPT self-energy for the four highest occupied molecular orbitals in order to cure the possible incorrect ordering of the states in the starting mean-field approximation.

We will use box plots like in **Figure 4** to summarize the error distribution of the HOMO energies with respect to CCSD(T). These plots, also known as whisker plots, report in a graphical way several relevant statistical characteristics: the median with the orange horizontal line, the first quartile with the lower box limit (25% of the distribution is below), and the last quartile with the upper box limit (75% of the distribution is below). The whiskers extend to 1.5 times the first to last quartile distance on each side. They are used to determine the so-called outliers, which are shown with the red diamonds. In addition to these box plots, we also provide the mean absolute error:

$$\mathrm{MAE}^X = \frac{1}{100}\sum_{i=1}^{100}\left|\epsilon^X_{\mathrm{HOMO},i} - \epsilon^{\mathrm{CCSD(T)}}_{\mathrm{HOMO},i}\right|, \tag{8}$$

Where i runs over the 100 molecules in GW100.

4.1 Standard MBPT Methods: PT2, PT3, *GW*

Figure 4 shows that HF HOMO energies are too deep compared to CCSD(T), with a large spread. PT2 improves very little compared to HF: While the median is closer to zero, the mean-absolute error (MAE) remains almost as large. PT3 is a significant improvement: The median is closer to zero and the spread is reasonable. However there exists a dozen outliers with an error over 1 eV, among which the molecules containing fluorine are over-represented.

Turning to the *GW* approximation, the situation improves significantly. Not only is the MAE reduced to 0.3 eV, but also the spread is decreased. Furthermore, not a single outlier is identified in the whisker plot! It is striking to see how the computationally simpler *GW* outperforms PT3, even though PT3 contains many diagrams that *GW* does not have.

To understand some of the problems with PT3, let us analyze here in greater details the case of beryllium oxide. BeO is one of the worst failures of PT3, with a 2.26 eV deviation from CCSD(T). In **Figure 5** we represent the correlation part of the self-energy expectation value (the right-hand side of **Eq. 5**) and the line $\omega - \epsilon^{\mathrm{HF}}_{\mathrm{HOMO}}$. The intersection between these two curves defines the quasiparticle energy.

In **Figure 5**, we observe a pathological behavior of PT3: its derivative $\partial\Sigma_c/\partial\omega$ is sometimes positive, which is not allowed for the exact self-energy. Remember that Z introduced in **Eq. 6** is a spectral weight. A positive slope yields a nonphysical spectral weight that exceeds 1. The PT3 analytic expression contains double poles, such as the C1, D1, C6, D6 terms in the Appendix of Ref. (Cederbaum and Domcke, 1977). These terms can induce this pathological behavior. PT2 and *GW* only contain single poles as shown for *GW* in Eq. 47 of Ref. (Bruneval et al., 2016) and have the correct analytic behavior by construction.

As a conclusion, based on the GW100 IP benchmark set, *GW* is clearly the winner by knock-out on the boxing ring: It shows the best MAE, the narrower distribution of errors, and no outlier. It has, by construction, the correct analytic behavior. Furthermore, the structure of the *GW* self-energy that contains only electron-hole pairs is perfectly suited for the RI approximation. An N^4 scaling is then achieved with the contour deformation integration technique (Mejia-Rodriguez et al., 2021) and numerical methods

with better scaling have also been proposed (Foerster et al., 2011; Vlček et al., 2017b; Wilhelm et al., 2018; Duchemin and Blase, 2021). In comparison, PT2 also has N^4 scaling due to the infamous "atomic orbital to molecular orbital integral transform" step and PT3 has N^5 scaling due to the quintuple MO summations (Cederbaum and Domcke, 1977).

4.2 Beyond *GW*

Now a legitimate question would be whether one could improve the *GW* approximation by adding some of the diagrams shown in **Figure 3**.

The simplest addition to *GW* would be to add the SOX diagram of **Figure 1**. This idea has already been tested by Marom *et. al.* (Marom et al., 2012) and was not successful according to them. In **Figure 6**, we confirm their conclusion: the results are better than PT2, but worse than *GW* alone.

Intuitively, it seems that the effect of the SOX diagram is too strong. That is why the *GW* + SOSEX proposal is appealing. The SOSEX diagram would temper the bare SOX. And this is precisely what it does: the spread of *GW* + SOSEX is narrower than that of *GW* + SOX. However, the results in **Figure 6** show that the median and the MAE are still far from zero and that *GW* alone is still better.

Now let us test the possibility to incorporate the interacting electron-hole pairs, by using the TDHF screened Coulomb interaction W_{TDHF}. This contribution gives a significant push upwards, so that the median is close to zero. Unfortunately, many outliers appear, mostly the ionic dimers of GW100, such as LiH, LiF, BeO, MgO, FH, KH. Please note that boron nitride, BN, had to be excluded from the benchmark here. Indeed the TDHF calculation failed because of a negative excitation energy. In other words, the HF self-consistent solution reached by MOLGW is not the lowest HF energy. A stability search could solve the problem (Seeger and Pople, 1977), but this implementation is not currently available in MOLGW.

Finally, we evaluate the effect of the first-order correction to the Hartree and Fock exchange terms, as depicted in **Figure 2**. In agreement with previous work on a smaller benchmark (Bruneval, 2019a), we observe a significant improvement over the *GW* approximation. The MAE becomes very good and the distribution is well centered around zero. The only worrying point is the existence of two outliers: TiF4 and MgO. While the TiF4 HOMO was already much too negative in *GW*@HF (−0.62 eV compared to CCSD(T)), MgO is more intriguing. It was very good with *GW* (−0.08 eV compared to CCSD(T)) and deteriorates very much with $GW + \gamma^{GW}$. BeO, which is chemically similar to MgO, is quite different in terms of its deviation, with a deviation of only 0.01 eV for $GW + \gamma^{GW}$ with respect to CCSD(T).

Of course, we did not explore all the possible combinations of diagrams beyond *GW*. However, we can state that with *GW* being already very good, it is a difficult task to improve over it. Adding diagrams may destroy the subtle balance, which makes *GW* so successful. Among all the additions we considered, only $GW + \gamma^{GW}$ can be considered as a systematic improvement.

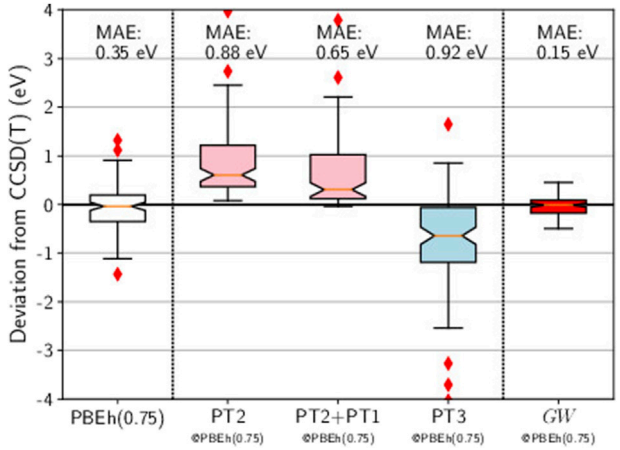

FIGURE 7 | Box plots for GW100 HOMO energy errors for HF, PT2, PT2+PT1, PT3, and *GW*, starting from a PBEh(0.75) G_0. CCSD(T) total energy differences are considered as the reference. Mean absolute errors (MAE) are also printed.

5 MBPT FROM AN IMPROVED MEAN-FIELD STARTING POINT

It is attractive to calculate Green's functions self-consistently for several theoretical reasons. First, this is a systematic way to include more diagrams (Fetter and Walecka, 1971). The Green's function lines in **Figures 1**, **2** would already include an infinite series of interactions. Second, Baym and Kadanoff (Baym and Kadanoff, 1961) showed that self-consistency enforces the fulfillment of several conservation laws, including the number of electrons itself.

However for practical reasons, self-consistent calculations are rarely carried out and one rather uses a one-shot approximation on top of a mean-field calculation. In the previous Section, we only used an HF mean-field for comparison reasons.

Now with the idea of approximating the self-consistent Green's function, we can consider using an improved non-interacting Green's function G_0. For molecules, it has been identified (Bruneval, 2016; Rangel et al., 2016; Bruneval, 2019a) that hybrid functionals with boosted Hartree-Fock exchange have the best HOMO compared to CCSD(T). Then one can reasonably hope these hybrid functionals would also be good approximations to the self-consistent *G*.

Here we use PBEh(0.75), a global hybrid functional which mixes the PBE exchange energy and the Hartree-Fock exchange energy in a 1:3 ratio (25% PBE, 75% Hartree-Fock). In the box plot reported in **Figure 7**, we show that the HOMO energies obtained with PBEh(0.75) are quite close to the CCSD(T) references: The distribution is nearly perfectly centered around zero and the MAE is reasonably low (0.35 eV).

At this point, there is a cross-road between chemistry and physics methods again. When performing a perturbation theory based on a mean-field different from HF, the Brillouin theorem breaks down (Szabó and Ostlund, 1996) and first-order terms, named PT1, appear (Ren et al., 2011). Should we include those

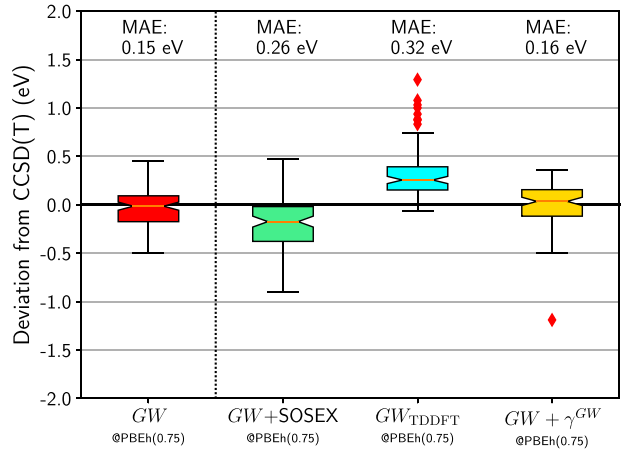

FIGURE 8 | Box plots for GW100 HOMO energy errors for *GW*, *GW* + SOSEX, GW_{TDDFT}, and $GW + \gamma^{GW}$ starting from a PBEh(0.75) G_0. CCSD(T) total energy differences are considered as the reference. Mean absolute errors (MAE) are also printed.

terms? In a strict order by order expansion, the answer would be affirmative. We have tested this inclusion in the case of PT2 based on PBEh(0.75), as reported in **Figure 7**. Looking at the two box plots for PT2 and PT2+PT1, we conclude that the effect of the PT1 term is not significant.

Then we consider that the PBEh(0.75) Green's function G_0 is an approximation to the self-consistent *G*. As a consequence, no first-order terms appear in PT2 and some Goldstone-Feynman diagrams should be removed from the original PT3. The static diagrams ("A" diagrams in Cederbaum's notation) are corrections to the Hartree and Fock exchange terms (See **Figure 1**). If PBEh(0.75) gives the correct Green's function, it would also give the correct density and density-matrix, and then it would yield the correct Hartree and Fock exchange contributions.

Hence, **Figure 7** reports the box plot of PT3 without the static diagrams. The outcome is very bad, which means that providing PT3 with a better starting point actually worsens the final result. This statement clearly advocates against PT3.

Now turning to *GW*@PBEh(0.75) in **Figure 7**, we obtain the best result of this study: The errors are evenly distributed around zero, no outliers are spotted, and the MAE is very low (0.15 eV). The accuracy is even better than that reached by the genuine self-consistent *GW* calculations of Caruso and coworkers (Caruso et al., 2016). It is often stated that self-consistent *GW* has quasiparticle peaks that are too weak (Holm and von Barth, 1998). We conjecture that this might be a reason why mean-field Green's functions are superior in the end.

Finally, we make an attempt at combining a better non-interacting Green's function with the additional diagrams we tested in Section IVB. In **Figure 8** we report the box plots for the HOMO errors with respect to CCSD(T) for *GW* + SOSEX, GW_{TDDFT}, and $GW + \gamma^{GW}$ based on the PBEh(0.75) Green's function. The *GW* + SOSEX somewhat improves compared to *GW* + SOSEX@HF. But it is still deteriorating the results compared to the simpler *GW* approximation. Next, we test GW_{TDDFT} where *W* was obtained from time-dependent DFT using the same functional as for G_0. Again the results are disappointing.

Last, we consider $GW + \gamma^{GW}$. If G_0 was the self-consistent *GW* Green's function, the γ^{GW} diagrams would vanish. Remember that the γ^{GW} diagrams are not present in Hedin's equations, which are obtained for a self-consistent *G*. **Figure 8** shows that it is indeed the case: $GW + \gamma^{GW}$ is very similar to *GW*. Besides MgO, which behaves badly again, the similarity between the error distribution of *GW* and $GW + \gamma^{GW}$ is compelling.

6 CONCLUSION

In this study, we have conducted a comprehensive benchmark of the MBPT performance for the calculation of the IP of molecules. Our boxing ring was the GW100 set introduced by one of us (van Setten et al., 2015) a few years ago. Our reference was the CCSD(T) total energy difference, often coined as the "gold standard" in quantum chemistry. But before the competition could even start, we realized the CCSD(T) reference energies needed a thorough update. Indeed CCSD(T) energies strongly depend on the prior HF step, especially for the cations. We updated almost half of the reference IPs with respect to the existing list in Ref. (Krause et al., 2015).

Based on the same HF starting point, we evaluated the 100 HOMO energies of GW100 for PT2, PT3, *GW*, and several methods beyond *GW*. Among the classical approximations, *GW* is clearly the winner. Then our attempts to improve over *GW* by adding more diagrams have been unsuccessful, besides the $GW + \gamma^{GW}$ diagrams that add corrections to the Hartree and Fock exchange expectation values.

Then starting from an improved mean-field (here we chose PBEh(0.75)), deteriorates the classical approximations, PT2 and PT3. Contrarily, GW improves with a more realistic starting mean-field. Our champion is then *GW*@PBEh(0.75) with a claimed MAE of 0.15 eV.

Of course, other accurate diagrammatic techniques exist, such as the algebraic diagrammatic construction (ADC) (Schirmer et al., 1983) or equation-of-motion coupled-cluster (EOM-CC) (Lange and Berkelbach, 2018). However they do not box in the same weight class. The miracle of *GW* is the fact that its in a featherweight class: *GW*, when combined with the resolution-of-the-identify, has an attractive N^4 scaling. *GW* now routinely runs on molecular systems with several hundreds of atoms (Vlček et al., 2017b; Wilhelm et al., 2018; Bruneval et al., 2020; Duchemin and Blase, 2021).

DATA AVAILABILITY STATEMENT

The original contributions presented in the study are included in the article/**Supplementary Material**, further inquiries can be directed to the corresponding author.

AUTHOR CONTRIBUTIONS

FB, ND, and MvS planned the research. FB, and ND conducted the calculations. FB, ND, and MvS wrote the manuscript.

FUNDING

This work was performed using HPC resources from GENCI-CCRT-TGCC (Grants No. 2021-096018), and from SHARCNET/Compute Canada.

ACKNOWLEDGMENTS

We thank X. Ren and Y. Wang for sharing with us their *GW* + SOSEX raw data. We are grateful to M. Harding for insightful discussions about the CCSD(T) calculations in (Krause et al. 2015).

SUPPLEMENTARY MATERIAL

The Supplementary Material for this article can be found online at: https://www.frontiersin.org/articles/10.3389/fchem.2021.749779/full#supplementary-material

REFERENCES

Aulbur, W. G., Jönsson, L., and Wilkins, J. W. (1999). Quasiparticle Calculations in Solids. *Solid State. Phys.* 54, 1.

Bruneval, F. (2021). Available at: www.molgw.org (Accessed September 1, 2021).

Baym, G., and Kadanoff, L. P. (1961). Conservation Laws and Correlation Functions. *Phys. Rev.* 124, 287–299. doi:10.1103/PhysRev.124.287

Becke, A. D. (1993). A New Mixing of Hartree-Fock and Local Density-functional Theories. *J. Chem. Phys.* 98, 1372–1377. doi:10.1063/1.464304

Bintrim, S. J., and Berkelbach, T. C. (2021). Full-frequency GW without Frequency. *J. Chem. Phys.* 154, 041101. doi:10.1063/5.0035141

Blase, X., Attaccalite, C., and Olevano, V. (2011). First-principles GW calculations for Fullerenes, Porphyrins, Phtalocyanine, and Other Molecules of Interest for Organic Photovoltaic Applications. *Phys. Rev. B* 83, 115103. doi:10.1103/physrevb.83.115103

Blase, X., Boulanger, P., Bruneval, F., Fernandez-Serra, M., and Duchemin, I. (2016). *GW* and Bethe-Salpeter Study of Small Water Clusters. *J. Chem. Phys.* 144, 034109. doi:10.1063/1.4940139

Blase, X., Duchemin, I., Jacquemin, D., and Loos, P.-F. (2020). The Bethe-Salpeter Equation Formalism: From Physics to Chemistry. *J. Phys. Chem. Lett.* 11, 7371–7382. pMID: 32787315. doi:10.1021/acs.jpclett.0c01875

Brémond, É., Pérez-Jiménez, Á. J., Sancho-García, J. C., and Adamo, C. (2020). Range-separated Hybrid and Double-Hybrid Density Functionals: A Quest for the Determination of the Range-Separation Parameter. *J. Chem. Phys.* 152, 244124. doi:10.1063/5.0010976

Bruneval, F. (2019). Improved Density Matrices for Accurate Molecular Ionization Potentials. *Phys. Rev. B* 99, 041118. doi:10.1103/physrevb.99.041118

Bruneval, F. (2019). Assessment of the Linearized GW Density Matrix for Molecules. *J. Chem. Theor. Comput.* 15, 4069–4078. doi:10.1021/acs.jctc.9b00333

Bruneval, F. (2012). Ionization Energy of Atoms Obtained from *GW* Self-Energy or from Random Phase Approximation Total Energies. *J. Chem. Phys.* 136, 194107. doi:10.1063/1.4718428

Bruneval, F., Maliyov, I., Lapointe, C., and Marinica, M.-C. (2020). Extrapolating Unconverged GW Energies up to the Complete Basis Set Limit with Linear Regression. *J. Chem. Theor. Comput.* 16, 4399–4407. pMID: 32491851. doi:10.1021/acs.jctc.0c00433

Bruneval, F., and Marques, M. A. L. (2013). Benchmarking the Starting Points of the GW Approximation for Molecules. *J. Chem. Theor. Comput.* 9, 324–329. doi:10.1021/ct300835h

Bruneval, F. (2016). Optimized Virtual Orbital Subspace for Faster GW Calculations in Localized Basis. *J. Chem. Phys.* 145, 234110. doi:10.1063/1.4972003

Bruneval, F., Rangel, T., Hamed, S. M., Shao, M., Yang, C., and Neaton, J. B. (2016). MOLGW 1: Many-body Perturbation Theory Software for Atoms, Molecules, and Clusters. *Comp. Phys. Commun.* 208, 149–161. doi:10.1016/j.cpc.2016.06.019

Bruneval, F., Rodriguez-Mayorga, M., Rinke, P., and Dvorak, M. (2021). Improved One-Shot Total Energies from the Linearized GW Density Matrix. *J. Chem. Theor. Comput.* 17, 2126–2136. pMID: 33705127. doi:10.1021/acs.jctc.0c01264

Caruso, F., Dauth, M., van Setten, M. J., Rinke, P., and Rinke, P. (2016). Benchmark of GW Approaches for the GW100 Test Set. *J. Chem. Theor. Comput.* 12, 5076–5087. doi:10.1021/acs.jctc.6b00774

Cederbaum, L. S., Domcke, W., Schirmer, J., von Niessen, W., Diercksen, G. H. F., and Kraemer, W. P. (1978). Correlation Effects in the Ionization of Hydrocarbons. *J. Chem. Phys.* 69, 1591–1603. doi:10.1063/1.436733

Cederbaum, L. S., and Domcke, W. (1977). *Theoretical Aspects of Ionization Potentials and Photoelectron Spectroscopy: A Green's Function Approach*. New York: Wiley-Interscience, 205.

Cederbaum, L. S., Hohlneicher, G., and von Niessen, W. (1973). On the Breakdown of the Koopmans' Theorem for Nitrogen. *Chem. Phys. Lett.* 18, 503–508. doi:10.1016/0009-2614(73)80451-8

Cederbaum, L. S., and von Niessen, W. (1974). A New Approach to Calculation of Electron Affinities. *Phys. Lett. A* 47, 199–200. doi:10.1016/0375-9601(74)90006-1

Cederbaum, L. S. (1975). One-body Green's Function for Atoms and Molecules: Theory and Application. *J. Phys. B: Mol. Phys.* 8, 290–303. doi:10.1088/0022-3700/8/2/018

Colonna, N., Nguyen, N. L., Ferretti, A., and Marzari, N. (2019). Koopmans-compliant Functionals and Potentials and Their Application to the GW100 Test Set. *J. Chem. Theor. Comput.* 15, 1905–1914. doi:10.1021/acs.jctc.8b00976

Dattani, N. (2021). *HPQC-LABS/AI_ENERGIES*. Zenodo. doi:10.5281/zenodo.5529103

Duchemin, I., and Blase, X. (2021). Cubic-Scaling All-Electron GW Calculations with a Separable Density-Fitting Space-Time Approach. *J. Chem. Theor. Comput.* 17, 2383–2393. pMID: 33797245. doi:10.1021/acs.jctc.1c00101

Fetter, A. L., and Walecka, J. D. (1971). *Quantum Theory of Many-Particle Systems*. New York: MacGraw-Hill.

Foerster, D., Koval, P., and Sánchez-Portal, D. (2011). An $O(N^3)$ Implementation of Hedin's GW Approximation for Molecules. *J. Chem. Phys.* 135, 074105. doi:10.1063/1.3624731

Förster, A., and Visscher, L. (2021). GW100: A Slater-Type Orbital Perspective. *J. Chem. Theor. Comput.* 17, 5080–5097. doi:10.1021/acs.jctc.1c00308

Förster, A., and Visscher, L. (2020). Low-order Scaling G0W0 by Pair Atomic Density Fitting. *J. Chem. Theor. Comput.* 16, 7381–7399. doi:10.1021/acs.jctc.0c00693

Frisch, M. J., Trucks, G. W., Schlegel, H. B., Scuseria, G. E., Robb, M. A., Cheeseman, J. R., et al. (2016). *Gaussian16 Revision C.01*. Wallingford CT: Gaussian Inc.

Gao, W., and Chelikowsky, J. R. (2020). Accelerating Time-dependent Density Functional Theory and GW Calculations for Molecules and Nanoclusters with Symmetry Adapted Interpolative Separable Density Fitting. *J. Chem. Theor. Comput.* 16, 2216–2223. doi:10.1021/acs.jctc.9b01025

Gao, W., and Chelikowsky, J. R. (2019). Real-Space Based Benchmark of G0W0 Calculations on GW100: Effects of Semicore Orbitals and Orbital Reordering. *J. Chem. Theor. Comput.* 15, 5299–5307. doi:10.1021/acs.jctc.9b00520

Godby, R. W., Schlüter, M., and Sham, L. J. (1986). Accurate Exchange-Correlation Potential for Silicon and its Discontinuity on Addition of an Electron. *Phys. Rev. Lett.* 56, 2415–2418. doi:10.1103/physrevlett.56.2415

Golze, D., Dvorak, M., and Rinke, P. (2019). The GW Compendium: A Practical Guide to Theoretical Photoemission Spectroscopy. *Front. Chem.* 7, 377. doi:10.3389/fchem.2019.00377

Golze, D., Wilhelm, J., van Setten, M. J., Rinke, P., and Rinke, Patrick. (2018). Core-level Binding Energies from GW: An Efficient Full-Frequency Approach within a Localized Basis. *J. Chem. Theor. Comput.* 14, 4856–4869. pMID: 30092140. doi:10.1021/acs.jctc.8b00458

Govoni, M., and Galli, G. (2018). GW100: Comparison of Methods and Accuracy of Results Obtained with the WEST Code. *J. Chem. Theor. Comput.* 14, 1895–1909. doi:10.1021/acs.jctc.7b00952

Govoni, M., and Galli, G. (2015). Large Scale GW Calculations. *J. Chem. Theor. Comput.* 11, 2680–2696. pMID: 26575564. doi:10.1021/ct500958p

Grossman, J. C., Rohlfing, M., Mitas, L., Louie, S. G., and Cohen, M. L. (2001). High Accuracy many-body Calculational Approaches for Excitations in Molecules. *Phys. Rev. Lett.* 86, 472–475. doi:10.1103/physrevlett.86.472

Hanke, W., and Sham, L. J. (1975). Local-field and Excitonic Effects in the Optical Spectrum of a Covalent Crystal. *Phys. Rev. B* 12, 4501–4511. doi:10.1103/physrevb.12.4501

Hedin, L. (1965). New Method for Calculating the One-Particle Green's Function with Application to the Electron-Gas Problem. *Phys. Rev.* 139, A796–A823. doi:10.1103/physrev.139.a796

Helgaker, T., Jørgensen, P., and Olsen, J. (2000). *Molecular Electronic Structure Theory*. Chichester: John Wiley & Sons.

Heßelmann, A. (2017). Ionization Energies and Electron Affinities from a Random-Phase-Approximation many-body Green's-function Method Including Exchange Interactions. *Phys. Rev. A.* 95, 062513. doi:10.1103/physreva.95.062513

Holm, B., and von Barth, U. (1998). Fully Self-Consistent GW Self-Energy of the Electron Gas. *Phys. Rev. B* 57, 2108–2117. doi:10.1103/physrevb.57.2108

Hybertsen, M. S., and Louie, S. G. (1986). Electron Correlation in Semiconductors and Insulators: Band Gaps and Quasiparticle Energies. *Phys. Rev. B* 34, 5390–5413. doi:10.1103/physrevb.34.5390

Hybertsen, M. S., and Louie, S. G. (1985). First-principles Theory of Quasiparticles: Calculation of Band Gaps in Semiconductors and Insulators. *Phys. Rev. Lett.* 55, 1418–1421. doi:10.1103/physrevlett.55.1418

Knight, J. W., Wang, X., Gallandi, L., Dolgounitcheva, O., Ren, X., Ortiz, J. V., et al. (2016). Accurate Ionization Potentials and Electron Affinities of Acceptor Molecules III: A Benchmark of GW Methods. *J. Chem. Theor. Comput.* 12, 615–626. doi:10.1021/acs.jctc.5b00871

Körzdörfer, T., and Marom, N. (2012). Strategy for Finding a Reliable Starting point for G_0W_0 Demonstrated for Molecules. *Phys. Rev. B* 86, 041110. doi:10.1103/physrevb.86.041110

Koval, P., Foerster, D., and Sánchez-Portal, D. (2014). Fully Self-Consistent GW and Quasiparticle Self-Consistent GW for Molecules. *Phys. Rev. B* 89, 155417. doi:10.1103/physrevb.89.155417

Krause, K., Harding, M. E., and Klopper, W. (2015). Coupled-Cluster Reference Values for the GW27 and GW100 Test Sets for the Assessment of GW Methods. *Mol. Phys.* 113, 1952–1960. doi:10.1080/00268976.2015.1025113

Kuwahara, R., Noguchi, Y., and Ohno, K. (2016). GWΓ+Bethe-Salpeter Equation Approach for Photoabsorption Spectra: Importance of Self-Consistent GWΓ calculations in Small Atomic Systems. *Phys. Rev. B* 94, 121116. doi:10.1103/physrevb.94.121116

Lange, M. F., and Berkelbach, T. C. (2018). On the Relation between Equation-Of-Motion Coupled-Cluster Theory and the GW Approximation. *J. Chem. Theor. Comput.* 14, 4224–4236. doi:10.1021/acs.jctc.8b00455

Lewis, A. M., and Berkelbach, T. C. (2019). Vertex Corrections to the Polarizability Do Not Improve the GW Approximation for the Ionization Potential of Molecules. *J. Chem. Theor. Comput.* 15, 2925–2932. pMID: 30933508. doi:10.1021/acs.jctc.8b00995

Lundqvist, B. I. (1967). Single-particle Spectrum of the Degenerate Electron Gas. *Phys. Kondens Materie* 6, 193–205. doi:10.1007/bf02422716

Maggio, E., Liu, P., van Setten, M. J., Kresse, G., and Kresse, Georg. (2017). GW100: A Plane Wave Perspective for Small Molecules. *J. Chem. Theor. Comput.* 13, 635–648. doi:10.1021/acs.jctc.6b01150

Mahan, G. D. (2000). *Many-particle Physics*. 3rd ed. Kluwer Academic/Plenum Publishers.

Marom, N., Caruso, F., Ren, X., Hofmann, O. T., Körzdörfer, T., Chelikowsky, J. R., et al. (2012). Benchmark of GW Methods for Azabenzenes. *Phys. Rev. B* 86, 245127. doi:10.1103/physrevb.86.245127

Matthews, D. A., Cheng, L., Harding, M. E., Lipparini, F., Stopkowicz, S., Jagau, T.-C., et al. (2020). Coupled-Cluster Techniques for Computational Chemistry: The CFOUR Program Package. *J. Chem. Phys.* 152, 214108. doi:10.1063/5.0004837

Mejia-Rodriguez, D., Alexander, K., Aprà, E., and Govind, N. (2021). *Scalable Molecular GW Calculations: Valence and Core Spectra*. arXiv:2107.10423 [physics.chem-ph].

Onida, G., Reining, L., Godby, R. W., Del Sole, R., and Andreoni, W. (1995). *Ab initio* Calculations of the Quasiparticle and Absorption Spectra of Clusters: The Sodium Tetramer. *Phys. Rev. Lett.* 75, 818–821. doi:10.1103/physrevlett.75.818

Onida, G., Reining, L., and Rubio, A. (2002). Electronic Excitations: Density-Functional Versus Many-Body Green's-Function Approaches. *Rev. Mod. Phys.* 74, 601–659. doi:10.1103/revmodphys.74.601

Ortiz, J. V. (1988). Electron Binding Energies of Anionic Alkali Metal Atoms from Partial Fourth Order Electron Propagator Theory Calculations. *J. Chem. Phys.* 89, 6348–6352. doi:10.1063/1.455401

Rangel, T., Hamed, S. M., Bruneval, F., and Neaton, J. B. (2016). Evaluating the GW Approximation with CCSD(T) for Charged Excitations across the Oligoacenes. *J. Chem. Theor. Comput.* 12, 2834–2842. pMID: 27123935. doi:10.1021/acs.jctc.6b00163

Ren, X., Marom, N., Caruso, F., Scheffler, M., and Rinke, P. (2015). Beyond the *GW* Approximation: A Second-Order Screened Exchange Correction. *Phys. Rev. B* 92, 081104. doi:10.1103/physrevb.92.081104

Ren, X., Rinke, P., Blum, V., Wieferink, J., Tkatchenko, A., Sanfilippo, A., et al. (2012). Resolution-of-identity Approach to Hartree-Fock, Hybrid Density Functionals, RPA, MP2 and GW with Numeric Atom-Centered Orbital Basis Functions. *New J. Phys.* 14, 053020. doi:10.1088/1367-2630/14/5/053020

Ren, X., Tkatchenko, A., Rinke, P., and Scheffler, M. (2011). Beyond the Random-phase Approximation for the Electron Correlation Energy: The Importance of Single Excitations. *Phys. Rev. Lett.* 106, 153003. doi:10.1103/physrevlett.106.153003

Rodrigues Pela, R., Gulans, A., and Draxl, C. (2018). The LDA-1/2 Method Applied to Atoms and Molecules. *J. Chem. Theor. Comput.* 14, 4678–4686. doi:10.1021/acs.jctc.8b00518

Rostgaard, C., Jacobsen, K. W., and Thygesen, K. S. (2010). Fully Self-Consistent GW Calculations for Molecules. *Phys. Rev. B* 81, 085103. doi:10.1103/physrevb.81.085103

Schirmer, J., Cederbaum, L. S., and Walter, O. (1983). New Approach to the One-Particle Green's Function for Finite Fermi Systems. *Phys. Rev. A.* 28, 1237–1259. doi:10.1103/physreva.28.1237

Seeger, R., and Pople, J. A. (1977). Self-Consistent Molecular Orbital Methods. XVIII. Constraints and Stability in Hartree-Fock Theory. *J. Chem. Phys.* 66, 3045–3050. doi:10.1063/1.434318

Sharifzadeh, S., Tamblyn, I., Doak, P., Darancet, P. T., and Neaton, J. B. (2012). Quantitative Molecular Orbital Energies within a G0W0 Approximation. *Eur. Phys. J. B* 85, 323. doi:10.1140/epjb/e2012-30206-0

Shirley, E. L., and Martin, R. M. (1993). GW Quasiparticle Calculations in Atoms. *Phys. Rev. B* 47, 15404–15412. doi:10.1103/physrevb.47.15404

Silvi, B., and Dovesi, R. (1988). Periodic Hartree-Fock Calculations Involving Core Pseudopotentials. *J. Mol. Struct. THEOCHEM* 170, 19–26. doi:10.1016/0166-1280(88)80044-7

Strinati, G., Mattausch, H. J., and Hanke, W. (1982). Dynamical Aspects of Correlation Corrections in a Covalent Crystal. *Phys. Rev. B* 25, 2867–2888. doi:10.1103/physrevb.25.2867

Szabó, A., and Ostlund, N. S. (1996). *Modern Quantum Chemistry: Introduction to Advanced Electronic Structure Theory*. Mineola (N.Y.): Dover Publications.

van Schilfgaarde, M., Kotani, T., and Faleev, S. (2006). Quasiparticle Self-Consistent *GW* Theory. *Phys. Rev. Lett.* 96, 226402. doi:10.1103/PhysRevLett.96.226402

van Setten, M. J., Caruso, F., Sharifzadeh, S., Ren, X., Scheffler, M., Liu, F., et al. (2015). GW100: Benchmarking G0W0 for Molecular Systems. *J. Chem. Theor. Comput.* 11, 5665–5687. pMID: 26642984. doi:10.1021/acs.jctc.5b00453

van Setten, M. J., Weigend, F., and Evers, F. (2013). The GW-Method for Quantum Chemistry Applications: Theory and Implementation. *J. Chem. Theor. Comput.* 9, 232–246. pMID: 26589026. doi:10.1021/ct300648t

Vlček, V., Rabani, E., Neuhauser, D., and Baer, R. (2017). Stochastic GW Calculations for Molecules. *J. Chem. Theor. Comput* 13, 4997–5003. doi:10.1021/acs.jctc.7b00770

Vlček, V., Rabani, E., Neuhauser, D., and Baer, R. (2017). Stochastic GW Calculations for Molecules. *J. Chem. Theor. Comput.* 13, 4997–5003. pMID: 28876912. doi:10.1021/acs.jctc.7b00770

von Niessen, W., Diercksen, G. H. F., and Cederbaum, L. S. (1977). On the Accuracy of Ionization Potentials Calculated by Green's Functions. *J. Chem. Phys.* 67, 4124–4131. doi:10.1063/1.435389

Wang, Y., Rinke, P., and Ren, X. (2021). Assessing the $G_0W_0\Gamma_0^{(1)}$ Approach: Beyond G_0W_0 with Hedin's Full Second-Order Self-Energy Contribution. *J. Chem. Theor. Comput.* 17, 5140–5154. pMID: 34319724. doi:10.1021/acs.jctc.1c00488

Weigend, F., and Ahlrichs, R. (2005). Balanced Basis Sets of Split Valence, Triple Zeta Valence and Quadruple Zeta Valence Quality for H to Rn: Design and Assessment of Accuracy. *Phys. Chem. Chem. Phys.* 7, 3297–3305. doi:10.1039/b508541a

Weigend, F., Köhn, A., and Hättig, C. (2002). Efficient Use of the Correlation Consistent Basis Sets in Resolution of the Identity MP2 Calculations. *J. Chem. Phys.* 116, 3175–3183. doi:10.1063/1.1445115

Wilhelm, J., Golze, D., Talirz, L., Hutter, J., and Pignedoli, C. A. (2018). Toward GW Calculations on Thousands of Atoms. *J. Phys. Chem. Lett.* 9, 306–312. doi:10.1021/acs.jpclett.7b02740

Wilhelm, J., and Hutter, J. (2017). Periodic GW Calculations in the Gaussian and Plane-Waves Scheme. *Phys. Rev. B* 95. doi:10.1103/physrevb.95.235123

Wilhelm, J., Seewald, P., and Golze, D. (2021). Low-scaling GW with Benchmark Accuracy and Application to Phosphorene Nanosheets. *J. Chem. Theor. Comput.* 17, 1662–1677. doi:10.1021/acs.jctc.0c01282

Yanai, T., Tew, D. P., and Handy, N. C. (2004). A New Hybrid Exchange-Correlation Functional Using the Coulomb-Attenuating Method (CAM-B3lyp). *Chem. Phys. Lett.* 393, 51–57. doi:10.1016/j.cplett.2004.06.011

Yang, R., Rendell, A. P., and Frisch, M. J. (2007). Automatically Generated Coulomb Fitting Basis Sets: Design and Accuracy for Systems Containing H to Kr. *J. Chem. Phys.* 127, 074102. doi:10.1063/1.2752807

Conflict of Interest: The authors declare that the research was conducted in the absence of any commercial or financial relationships that could be construed as a potential conflict of interest.

frontiers in Chemistry

ORIGINAL RESEARCH
published: 20 January 2022
doi: 10.3389/fchem.2021.763946

Double k-Grid Method for Solving the Bethe-Salpeter Equation *via* Lanczos Approaches

Ignacio M. Alliati[1], *Davide Sangalli*[2†] *and Myrta Grüning*[1*†]

[1]School of Mathematics and Physics, Queen's University Belfast, Northern Ireland, United Kingdom, [2]Division of Ultrafast Processes in Materials (FLASHit), Istituto di Struttura della Materia—Consiglio Nazionale delle Ricerche (CNR-ISM), Rome, Italy

Convergence with respect to the size of the **k**-points sampling grid of the Brillouin zone is the main bottleneck in the calculation of optical spectra of periodic crystals *via* the Bethe-Salpeter equation (BSE). We tackle this challenge by proposing a double grid approach to **k**-sampling compatible with the effective Lanczos-based Haydock iterative solution. Our method relies on a coarse **k**-grid that drives the computational cost, while a dense **k**-grid is responsible for capturing excitonic effects, albeit in an approximated way. Importantly, the fine **k**-grid requires minimal extra computation due to the simplicity of our approach, which also makes the latter straightforward to implement. We performed tests on bulk Si, bulk GaAs and monolayer MoS_2, all of which produced spectra in good agreement with data reported elsewhere. This framework has the potential of enabling the calculation of optical spectra in semiconducting systems where the efficiency of the Haydock scheme alone is not enough to achieve a computationally tractable solution of the BSE, e.g., large-scale systems with very stringent **k**-sampling requirements for achieving convergence.

Keywords: theoretical spectroscopy, optical properties, Bethe-Salpeter equation (BSE), excitonic effects, semiconductors

OPEN ACCESS

Edited by:
Marc Dvorak,
Aalto University, Finland

Reviewed by:
Andre Schleife,
University of Illinois at Urbana-Champaign, United States
Christian Vorwerk,
University of Chicago, United States

****Correspondence:***
Myrta Grüning
M.gruening@qub.ac.uk

†Also at European Theoretical Spectroscopy Facility (ETSF)

Specialty section:
This article was submitted to Theoretical and Computational Chemistry, a section of the journal Frontiers in Chemistry

Received: *24 August 2021*
Accepted: *09 December 2021*
Published: *20 January 2022*

Citation:
Alliati IM, Sangalli D and Grüning M (2022) Double ***k****-Grid Method for Solving the Bethe-Salpeter Equation via Lanczos Approaches. Front. Chem. 9:763946. doi: 10.3389/fchem.2021.763946*

1 INTRODUCTION

Many-body perturbation theory (MBPT) offers the right framework for treating neutral excitations *via* Green's function methods (Onida et al., 2002; Marini et al., 2009; Martin et al., 2016; Reining, 2018; Golze et al., 2019). This requires solving the Bethe-Salpeter equation (BSE) (Salpeter and Bethe, 1951; Hedin, 1965; Hedin and Lundqvist, 1971), which relies on a two-particle propagator to account for the presence of electron-hole pairs (i.e., excitons). The description of excitonic effects is crucial to compute optical spectra in extended systems, particularly in semi-conductors and insulators, for which methods based on the Random Phase Approximation (RPA) or time-dependent (TD-) density functional theory (DFT) with (semi-)local exchange-correlation functionals tend not to agree with experimental results (Onida et al., 2002; Martin et al., 2016). Calculations within the BSE framework are generally much more cumbersome and computationally demanding than DFT ones, and it is rather easy to reach the limits of what can be practically computed. Hence, the need for convergence studies is a key aspect of every MBPT calculation to alleviate the computational burden as much as possible while, at the same time, trying to ensure an accurate description of the system at hand. In general, electronic structure calculations in periodic systems treated with plane waves require convergence with respect to the size of this basis set as well as the sampling of the Brillouin zone (BZ). In particular, MBPT methods also require the inclusion of unoccupied states in the form of an, in principle, infinite summation that needs to be truncated to the minimum value that nonetheless

captures the physics at play. Furthermore, the solution of the BSE requires far denser **k**-sampling than DFT calculations to achieve an accurate description of excitons. This is because the excitonic wave-functions are usually quite spread out, with a periodicity well beyond the unit cell, and in order to expand them in a basis of transitions {*vc***k**} (electron-hole space), very dense **k**-grids are required. Moreover, BSE methods do not exploit symmetry so they are solved in the full BZ. The cubic scaling of the number of **k**-points in bulk systems from one grid to the next makes matters even worse (the quadratic scaling in 2D systems is more manageable). Such **k**-grid requirements may still be feasible for small systems, with few atoms per unit cell and few valence electrons per atom. However, medium to large size unit cells of atoms with many valence electrons (e.g., transition metals) become prohibitively costly as the number of **k**-points increases, and the solution of the BSE in a very dense grid (e.g., $60 \times 60 \times 60$) is simply out of reach. For all these reasons, the issue of **k**-point convergence is critical for the solution of the BSE and represents the bottleneck in its computational implementation. Therefore, the introduction of alternative numerical methods and approximations that can effectively deal with **k**-point convergence in the BSE is of utmost importance.

Albeit with the limitations described above, there are currently several approaches to solve the BSE. These are, in order of decreasing computational cost, inversion, full diagonalisation and Lanczos approaches, and will be described below. A first distinction would be based on whether the equation is solved in its Dyson-like form or re-cast as a two-particle Hamiltonian in transition space. The first approach requires the inversion of the BSE kernel matrix which, depending on the size of the matrix, can become impracticable. In such cases one would turn to the Hamiltonian formulation of the problem [see, for example, Onida et al. (2002)]. In the latter, the two-particle Hamiltonian is diagonalised to obtain the eigen-values (excitonic energies) and eigen-vectors (excitonic wave-functions). If the BSE matrix of a given system is still too big for full diagonalisation, one can resort to Lanczos (1950) approaches which are usually a cost-effective option for sparse matrices (Cini, 2007). These algorithms have been widely used for the calculation of response functions, both at the TD-DFT (Rocca et al., 2008; Ge et al., 2014) and BSE (Rocca et al., 2012) levels. In the latter, Lanczos approaches eliminate the need for inverting the BSE kernel or fully diagonalising the two-particle Hamiltonian. Rather, the latter is re-expressed as a tri-diagonal matrix based on recursive relations, which leads to an iterative solution of the problem that is computationally cheaper than full diagonalisation. Unfortunately, while previously described solvers produce the full set of both excitonic energies and wavefunctions of the system at hand, Lanczos schemes lead to a partial solution of the problem. For instance, Haydock's implementation (Haydock, 1980) of the Lanczos approach provides only the full set of the eigen-values of the two-particle Hamiltonian (i.e., one obtains the full spectrum but not the excitonic wave-functions). Despite the numerical advantages of Lanczos solvers, a given system could still be too big for computing optical spectra. As the diagonalisation itself ceases to be a problem with Lanczos schemes, the bottleneck now shifts to the previous step of computing and storing the BSE kernel, which can render the calculation impracticable depending on the size of the electron-hole (*e-h*) basis. Nothing too extreme would be required to reach this condition, e.g., a magnetic system with around 100 electrons per unit cell, slow convergence with respect to bands and a $6 \times 6 \times 6$ **k**-grid would certainly be beyond reach. At this point, there is little alternative for solving the BSE and computing optical spectra, which is the challenge we intend to tackle in this manuscript.

The work presented here concentrates on improving the convergence of optical response spectra calculations within the BSE with respect to the number of **k**-points. This issue has been the target of many research efforts over the years. Rohlfing et al. introduced a scheme to interpolate the BSE matrix in the BZ (Rohlfing and Louie, 1998). Their strategy is based on a double grid approach by which the kernel matrix elements are properly calculated on a coarse **k**-grid and approximated on a fine **k**-grid. As a function of **q**, the **k**-point difference between two transitions in *e-h* space, the BSE kernel is sharply peaked at the origin and a regular interpolation in the BZ would fail. However, expressing these matrix elements as $a\mathbf{q}^{-2} + b\mathbf{q}^{-1} + c$ results in the coefficients varying slowly in the BZ. These coefficients are then interpolated by virtue of knowing them exactly in the coarse **k**-grid. Their approximation also considers the varying phases of the single-particle states in the BZ, which requires knowledge of the wavefunctions in the fine **k**-grid. This crucial point becomes a drawback when one is limited by memory and disk storage rather than computation, which is increasingly the case nowadays. More recently, Fuchs et al. proposed the use of hybrid **k**-meshes in the form of a coarse **k**-grid for the whole BZ and a denser **k**-grid around the Γ-point only (Fuchs et al., 2008). Even though the kernel matrix elements are properly calculated on both grids, this method allows to refine **k**-sampling only where is needed, resulting in fewer **k**-points in total. The downside of using non-uniform grids becomes apparent in the calculation of the electron-hole attraction term of the BSE kernel, as knowledge of the screening at **q**-points not included in the hybrid grid itself will be needed. This complication requires additional computation (or at least an interpolation) if one intends to use the RPA screening, as is the case in this work. Kammerlander et al. applied double grid techniques to solving the BSE by inversion (Kammerlander et al., 2012). In the latter, the BSE is solved on the coarse **k**-grid while the fine **k**-grid is used compute the independent particle part of the two-particle response function. This technique, which also benefits from Wannier interpolation of the Kohn-Sham (KS) orbitals, has proven successful in accurately reproducing the spectra of several materials. However, as it ultimately relies on matrix inversion, its application is limited to *small* systems, i.e., systems which could be computed by the inversion solver in the coarse grid, albeit underconverged. Finally, an interesting generalisation of the method in Rohlfing and Louie (1998) has been proposed by Gillet et al. (2016), where the interpolation of the BSE kernel matrix element at a given fine-grid **k**-point considers eight coarse-grid **k**-points around it. Importantly, this method is compatible with Haydock's solution scheme to the BSE.

Moreover, substantial savings in memory requirements and disk storage are achieved by interpolating kernel matrix elements on the fly. Nevertheless, this method still requires knowledge of the KS orbitals in the fine grid. Depending on the number of bands and density of the fine grid, this can entail prohibitive memory requirements.

In this work, we also propose a double grid approach, including a coarse **k**-grid where the BSE kernel is properly calculated and a fine, denser **k**-grid where the corresponding matrix elements are approximated. At variance with Kammerlander et al. (2012), we propose an approximation that is compatible with the computationally cheapest solution to the BSE, namely Lanczos-based iterative solvers. Crucially, this allows us to target materials for which optical spectra cannot be currently computed, i.e., relatively big systems that can only be solved by Lanczos approaches and in **k**-grids that fall short of a converged solution. Another distinctive feature of the method presented here is its simplicity. It is far easier to implement than previous attempts (Rohlfing and Louie, 1998; Fuchs et al., 2008). Importantly, the introduction of the fine **k**-grid requires minimal extra computation and memory with respect to the coarse **k**-grid. In particular, knowledge of the wavefunctions in the fine **k**-grid is not needed, nor is the calculation of the RPA screening in any extra **k**-point. Therefore, the computational cost remains roughly at the level of the coarse **k**-grid, while an approximate description of broad excitons is achieved by virtue of adding a fine **k**-grid. The remainder of the manuscript is structured as follows. **Section 2** describes the proposed double grid approach in detail while **Section 3** reports the results obtained for a variety of semiconductors. **Section 4** presents the gains in computational cost that our implementation achieves. It also outlines a comparative assessment of particular choices made within the method and discusses the limitations of the approach.

2 METHODS

2.1 Haydock Solution of the BSE

Optical absorption spectra are represented by the imaginary part of the macroscopic dielectric function $\mathfrak{Im}[\epsilon_{\mathrm{M}}]$, which is obtained by taking the long wavelength limit of an expression involving the microscopic dielectric function $\epsilon(\mathbf{q}, \omega)$—where $\mathbf{q}$ represents the transferred momenta while ω is the frequency. For neutral excitations, $\epsilon(\mathbf{q}, \omega)$ is defined in terms of the polarisation or density-density response function χ, which is in turn calculated within the RPA, i.e., as a Dyson-like equation being the non-interacting polarisation χ^0 a product of non-interacting one-particle Green's functions that describe the propagation of one electron or one hole. However, optical spectra of extended systems require the inclusion of excitonic effects, which will ultimately lead us to a two-particle Green's function that describes the dynamics of an electron-hole pair ($v\mathbf{c}\mathbf{k}$) (we only consider vertical transitions at point $\mathbf{k}$ in the BZ between an occupied band v and an empty band c). This is achieved by defining the macroscopic dielectric function via an interacting polarisation $\bar{\chi}$, i.e., $\epsilon_{\mathrm{M}}(\mathbf{q}, \omega) \equiv 1 - v(\mathbf{q})\bar{\chi}_{\mathbf{G}=0,\mathbf{G}'=0}(\mathbf{q}, \omega)$. This interacting polarisation is obtained in terms of an electron-hole (e-h) Green's function $\bar{L}$ as in **Eq. 1**,

$$\lim_{\mathbf{q}\to 0}\bar{\chi}_{\mathbf{G}=0,\mathbf{G}'=0}(\mathbf{q},\omega) = -i\sum_{nm\mathbf{k}}\sum_{n'm'\mathbf{k}'}\lim_{\mathbf{q}\to 0}\left[\rho^{*}_{nm\mathbf{k}}(\mathbf{q},\mathbf{G}=0)\rho_{n'm'\mathbf{k}'}(\mathbf{q},\mathbf{G}'=0)\right]\bar{L}_{\substack{nm\mathbf{k}\\ n'm'\mathbf{k}'}}(\omega). \tag{1}$$

In **Eq. 1**, $\rho_{nm\mathbf{k}}(\mathbf{q},\mathbf{G}) = \langle n\mathbf{k}|e^{i(\mathbf{q}+\mathbf{G})\cdot\mathbf{r}}|m\mathbf{k}-\mathbf{q}\rangle$ are the oscillator strengths. For simplicity, unpolarised electrons are assumed in the discussion, however we stress that the method is not limited to non-magnetic systems. The Bethe-Salpeter equation is then the Dyson-like equation for $\bar{L}$,

$$\bar{L}_{\substack{nm\mathbf{k}\\ n'm'\mathbf{k}'}}(\omega) = L^{0}_{nm\mathbf{k}}(\omega)\left[\delta_{nn'}\delta_{mm'}\delta_{\mathbf{k}\mathbf{k}'} + i\sum_{vc\mathbf{k}_1}\Xi_{\substack{nm\mathbf{k}\\ vc\mathbf{k}_1}}\bar{L}_{\substack{vc\mathbf{k}_1\\ n'm'\mathbf{k}'}}(\omega)\right], \tag{2}$$

where the matrix Ξ is the so called BSE kernel,

$$\Xi_{\substack{nm\mathbf{k}\\ vc\mathbf{k}_1}} = W_{\substack{nm\mathbf{k}\\ vc\mathbf{k}_1}} - 2\bar{V}_{\substack{nm\mathbf{k}\\ vc\mathbf{k}_1}}, \tag{3}$$

$$W_{\substack{nm\mathbf{k}\\ vc\mathbf{k}_1}} = \frac{1}{\Omega N_q}\sum_{\mathbf{G},\mathbf{G}'}\rho_{nv\mathbf{k}}(\mathbf{q}=\mathbf{k}-\mathbf{k}_1,\mathbf{G})\rho^{*}_{mc\mathbf{k}_1}(\mathbf{q}=\mathbf{k}-\mathbf{k}_1,\mathbf{G}')\,\epsilon^{-1}_{\mathbf{G},\mathbf{G}'}v(\mathbf{q}+\mathbf{G}'), \tag{4}$$

$$\bar{V}_{\substack{nm\mathbf{k}\\ vc\mathbf{k}_1}} = \frac{1}{\Omega N_q}\sum_{\mathbf{G}\neq\mathbf{0}}\rho_{nm\mathbf{k}}(\mathbf{q}=0,\mathbf{G})\rho^{*}_{vc\mathbf{k}_1}(\mathbf{q}=0,\mathbf{G})v(\mathbf{G}). \tag{5}$$

The BSE kernel is written as shown in **Eq. 3** and its two contributions, namely the e-h attraction W and the e-h exchange $\bar{V}$, can be calculated as in **Eqs. 4**, **5**. The solution of this Dyson-like equation would require to invert the BSE kernel, which can be prohibitively costly as explained in **Section 1**. Hence, the problem is re-cast in terms of a two-particle Hamiltonian in e-h space,

$$H^{2p}_{\substack{nm\mathbf{k}\\ n'm'\mathbf{k}'}} = E_{nm\mathbf{k}}\,\delta_{nn'}\delta_{mm'}\delta_{\mathbf{k}\mathbf{k}'} + \left(f_{n\mathbf{k}} - f_{m\mathbf{k}}\right)\Xi_{\substack{nm\mathbf{k}\\ n'm'\mathbf{k}'}}, \tag{6}$$

where $E_{nm\mathbf{k}}$ is the energy of the vertical transition from band n to band m at point $\mathbf{k}$ according to either the KS or quasi-particle (QP) energies.

Diagonalising this matrix would provide the excitonic eigen-values and eigen-vectors required to compute optical spectra, however in this work, we focus on Lanczos-based methods. In particular, Haydock's algorithm (Haydock, 1980; Benedict et al., 1998; Benedict and Shirley, 1999) consists on an iterative method based on a set of recursive relations, namely,

$$a_n = \langle V_n|H^{2p}|V_n\rangle, \tag{7}$$

$$b_{n+1} = \|(H^{2p} - a_n)|V_n\rangle - b_n|V_{n-1}\rangle\|, \tag{8}$$

$$|V_{n+1}\rangle = \frac{1}{b_{n+1}}\left[(H^{2p} - a_n)|V_n\rangle - b_n|V_{n-1}\rangle\right], \tag{9}$$

with n being the iteration index. This set of equations corresponds to Hermitian Hamiltonians [the pseudo-Hermitian case has a slightly more complicated form (Grüning et al., 2011)]. **Eqs. 7–9** allow for the calculation of the factors a and b, and the so called Haydock vector for the next iteration $|V_{n+1}\rangle$. The initial Haydock vector is calculated as $|V_0\rangle = \frac{|P\rangle}{\|P\|}$ being $|P\rangle$ the vector defined as

$$|P\rangle = \sum_{vc\mathbf{k}} \lim_{\mathbf{q}\to 0} \frac{1}{|\mathbf{q}|} \rho^*_{vc\mathbf{k}}(\mathbf{q}, \mathbf{G}=0)|vc\mathbf{k}\rangle. \tag{10}$$

On each iteration n, the optical spectrum is calculated according to,

$$\epsilon_M^{(n)}(\omega) = 1 - \|P\|^2 \frac{1}{(\omega - a_1) - \cfrac{b_2^2}{(\omega - a_2) - \cfrac{b_3^2}{\ddots}}}, \tag{11}$$

until the difference between spectra of successive iterations is below an acceptable threshold.

2.2 Double Grid Approach

First, we consider a coarse **k**-grid where no approximations are applied, i.e., the BSE kernel is computed for all vertical transitions involving **k**-points in this grid, which requires knowledge of the KS orbitals and energies (potentially corrected to QP energies) at each of these **k**-points. The solution of the BSE in this grid would typically be computationally manageable but produce underconverged optical spectra. Thus, a much denser fine **k**-grid will be added to the system. We will denote **k**-points belonging to the fine grid with the letter $\boldsymbol{\kappa}$, while those in the coarse grid will be labelled **K**. Moreover, $\boldsymbol{\kappa}$-points will be grouped in domains centred around the **K**-points in such way that **Dom** ($\mathbf{K_I}$) will be composed by the $\boldsymbol{\kappa}$-points that are closer to $\mathbf{K_I}$ than to any other **K**-point. The number of **k**-points in this fine grid would ordinarily be too large for the BSE to be solved in full, and hence, approximations will be introduced for the fine grid. The two-particle Hamiltonian in **Eq. 6** can be thought of as a shift (the diagonal matrix containing the energies of each transition) plus a rotation (the BSE kernel). The approximation proposed implies that the diagonal matrix is calculated in the fine grid, for which knowledge of the KS energies of each band at every $\boldsymbol{\kappa}$-point in the fine grid is required. The BSE kernel, however, will not be calculated in full but rather, every matrix element involving at least one transition in the fine grid will be approximated according to some rules for kernel extension. This allows the method to dispense with the KS orbitals in the fine grid, which has a great impact on memory requirements.

The way in which the BSE kernel is extended from the coarse to the fine grid has been carefully considered as it has significant impact on the results. The best agreement with experimental spectra was achieved with an approach we refer to as diagonal kernel extension (DKE). Let us consider one **k**-point in the coarse grid, $\mathbf{K_I}$. There will be a group of $\boldsymbol{\kappa}$-points in the fine grid that map to it, namely those in the domain **Dom** ($\mathbf{K_I}$). We will label those with a second numerical sub-index as $\kappa_{\mathbf{I}_1}, \kappa_{\mathbf{I}_2}, \kappa_{\mathbf{I}_3}, \ldots, \kappa_{\mathbf{I}_i}, \ldots$. Given that the fine grid contains the coarse grid, we have that $\kappa_{\mathbf{I}_1} = \mathbf{K_I}$, while $\kappa_{\mathbf{I}_i}$ with $i \neq 1$ are other fine grid points close to $\mathbf{K_I}$. Having established the nomenclature in this way, then DKE would imply the definition

$$\Xi_{\substack{nm\kappa_{\mathbf{I}_i} \\ n'm'\kappa_{\mathbf{I}'_{i'}}}} \equiv \Xi_{\substack{nm\mathbf{K_I} \\ n'm'\mathbf{K}_{\mathbf{I}'}}} \delta_{ii'}, \tag{12}$$

where the R.H.S is known and calculated exactly while the L.H.S is the unknown matrix element we are trying to approximate (see **Supplementary Material** for a visual representation of **Eq. 12**). Thus, **Eq. 12** is only exact for the **k**-point that belongs both the coarse and the fine grids ($i = i' = 1$), and approximated otherwise. Even though the BSE kernel is not, in general, a diagonally-dominant matrix, it is true that the diagonal matrix elements usually have values orders of magnitude higher than those of immediately close off-diagonal elements. The DKE approach preserves this character when extending the kernel from the coarse grid to the fine grid. Essentially, each matrix element of the coarse grid BSE kernel expands into a block in the fine grid matrix. The DKE method ensures that each block is strictly diagonal, which is very relevant when expanding one of the diagonal matrix elements of the coarse grid matrix. In **Section 4.2**, the DKE is compared with a possible alternative kernel extension.

Finally, let us discuss how this double grid method fits within the Haydock algorithm. It is apparent from **Eqs. 7–9** that this scheme relies mainly on the matrix vector multiplication $H^{2p}|V_n\rangle$, so we will focus on how this is adapted to account for the fine grid. The two-particle Hamiltonian has already been described above, i.e., the BSE kernel is approximated by DKE (**Eq. 12**) and the diagonal part needs no approximation as the KS (or QP) energies are known in the fine grid. All there is left is then to define how the Haydock vectors $|V_n\rangle$ are extended to the fine grid and initialised. The initial Haydock vector $|V_0\rangle$ is calculated in the coarse grid according to **Eq. 10**. Each component is associated to one transition $vc\mathbf{k}$ and thus, when moving from the coarse to the fine grid, the number of components will increase according to the ratio between the number of $\boldsymbol{\kappa}$-points and **K**-points. From **Eq. 10**, it is clear that the KS orbitals at the $\boldsymbol{\kappa}$-points would be required to properly initialise the Haydock vector in the fine grid. As these orbitals are not available in our method, those components will be initialised as being equal to the corresponding transition in the coarse grid. In other words,

$$|P\rangle_{\mathrm{FG}} = \sum_{vc\mathbf{K_I}} \lim_{\mathbf{q}\to 0} \frac{1}{|\mathbf{q}|} \rho^*_{vc\mathbf{K_I}}(\mathbf{q}, \mathbf{G}=0) \sum_{\substack{\kappa_{\mathbf{I}_i} \in \\ \mathbf{Dom}(\mathbf{K_I})}} |vc\kappa_{\mathbf{I}_i}\rangle, \tag{13}$$

where FG denotes the fine grid. It is apparent that $|P\rangle_{\mathrm{FG}}$ has many more components than $|P\rangle$, due to each coarse grid transition (at $\mathbf{K_I}$) being replicated into many transitions at all the $\boldsymbol{\kappa}$-points in the domain of $\mathbf{K_I}$. The recursive relations in **Eqs. 7–9** would formally require the multiplication of the fine grid (full) BSE kernel times Haydock vectors of the size of $|P\rangle_{\mathrm{FG}}$. In our implementation, we calculate the matrix-vector multiplication without storing the BSE kernel on the fine grid. Let us divide a given Haydock vector $|V\rangle$ in *fragments* according to the $\boldsymbol{\kappa}$-point of each transition. Formally, this would mean projecting $|V\rangle$ over the different transitions (i.e, the abstract vectors $|vc\boldsymbol{\kappa}_{\mathbf{I}_i}\rangle$ that form the new/extended basis of *e-h* space) and then grouping components by their $\boldsymbol{\kappa}$-point as *fragments*. These fragments are convenient for the matrix vector multiplication. In fact, this operation can be expressed as

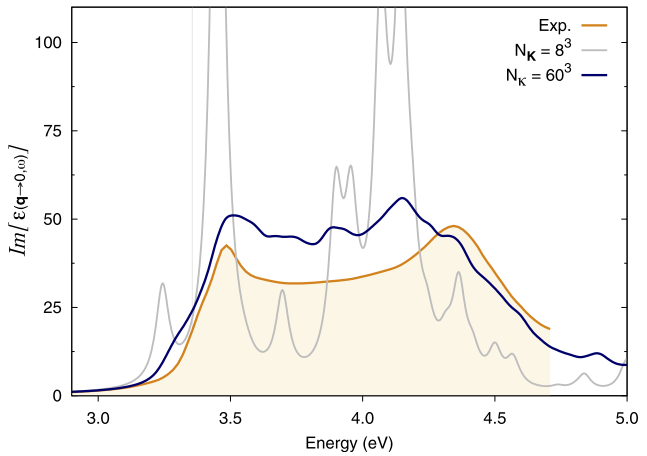

FIGURE 1 | Optical absorption spectra of bulk Si. BSE spectra calculated using the double-grid approach described in this work are assessed against the experimental spectrum at 10 K from Jellison and Modine (1983). Spectra are calculated on an 8 × 8 × 8 coarse **k**-grid and a denser fine **k**-grid, indicated by N_{κ}. $N_{\mathbf{K}} = 8^3$ corresponds to a standard calculation on an 8 × 8 × 8 **k**-grid while $N_{\kappa} = 60^3$ corresponds to a double-grid calculation with a 60 × 60 × 60 fine grid. We consider all *e*–*h* pairs from the top four valence bands to the four bottom conduction bands. All **k**-grids are Gamma-centred.

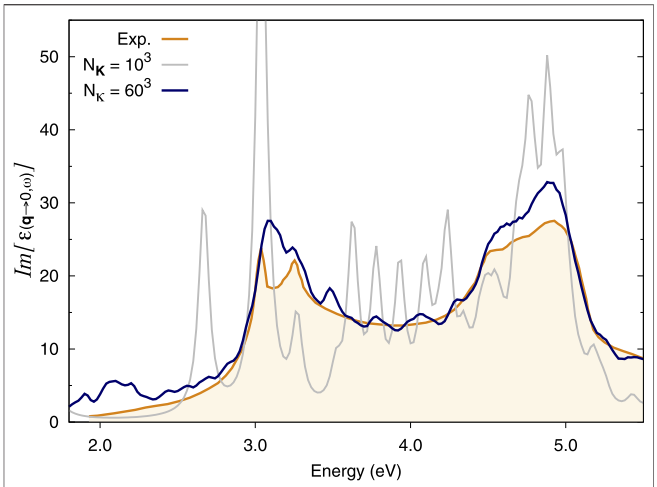

FIGURE 2 | Optical absorption spectra of bulk GaAs. BSE spectra calculated using the double-grid approach described in this work are assessed against the experimental spectrum at 22 K from Lautenschlager et al. (1987). Spectra are calculated on a 10 × 10 × 10 coarse **k**-grid and a denser fine **k**-grid, indicated by N_{κ}. $N_{\mathbf{K}} = 10^3$ corresponds to a standard calculation on a 10 × 10 × 10 **k**-grid while $N_{\kappa} = 60^3$ corresponds to a double-grid calculation with a 60 × 60 × 60 fine grid. We consider all *e*–*h* pairs from the top four valence bands to the four bottom conduction bands. All **k**-grids are Gamma-centred.

$$r_{nm\kappa_{\mathbf{I}_i}} = \sum_{n'm'\kappa_{\mathbf{I}'_{i'}}} \Xi_{\substack{nm\kappa_{\mathbf{I}_i} \\ n'm'\kappa_{\mathbf{I}'_{i'}}}} c_{n'm'\kappa_{\mathbf{I}'_{i'}}}, \tag{14}$$

where $c_{vc\kappa_{\mathbf{I}_i}} = \langle vc\kappa_{\mathbf{I}_i}|V\rangle$ are the components of the vector to be multiplied and r are, analogously, the coefficients of the resulting vector. Applying the DKE to the BSE matrix (**Eq. 12**), we obtain

$$r_{nm\kappa_{\mathbf{I}_i}} = \sum_{n'm'\mathbf{K}_{\mathbf{I}'}} \sum_{\substack{i' \in \\ \mathbf{Dom}\left(\mathbf{K}_{\mathbf{I}'}\right)}} \Xi_{\substack{nm\mathbf{K}_{\mathbf{I}} \\ n'm'\mathbf{K}_{\mathbf{I}'}}} \delta_{i,i'}\, c_{n'm'\kappa_{\mathbf{I}'_{i'}}} = \sum_{n'm'\mathbf{K}_{\mathbf{I}'}} \Xi_{\substack{nm\mathbf{K}_{\mathbf{I}} \\ n'm'\mathbf{K}_{\mathbf{I}'}}} c_{n'm'\kappa_{\mathbf{I}'_i}}, \tag{15}$$

where matrix elements in the R.H.S are those of the coarse-grid BSE kernel and the resulting summation runs over the **K**-points in the coarse grid only. Computationally, this means adding a loop over the $\boldsymbol{\kappa}$-points in the domain of each **K**.

3 RESULTS

The double grid method proposed here to calculate optical spectra via the BSE has been implemented in the Haydock solver of the Yambo code (Marini et al., 2009; Sangalli et al., 2019) and tested on a variety of semiconductors. In this section, we present the resulting optical spectra of each material. We note that the spectra produced by this approach represented a sharp improvement with respect to the coarse grid solution, while requiring only a marginal increase in computational cost. Although Gamma-centred **k**-grids were used throughout this study, our method can also be used with shifted grids (see an example in **Supplementary Material**).

3.1 Si Bulk

It is notoriously difficult to converge the optical spectrum of bulk Si with respect to **k**-points since a very dense **k**-sampling is required to properly describe its excitons. The starting point for our Si calculations is a severely under-converged 8 × 8 × 8 **k**-point grid. The spectrum produced by this coarse grid alone shows numerous spurious peaks (**Figure 1**), which reveals a high degree of artificial localisation of the excitons imposed by the 8 × 8 × 8 **k**-grid. We then took the latter as the coarse grid for the double grid method and added a fine grid of $\boldsymbol{\kappa}$-points to it. **Supplementary Figure S1** shows that a fine (double) grid of 24 × 24 × 24 $\boldsymbol{\kappa}$-points on top of this coarse grid immediately suppresses this artificial localisation. Denser double grids improve upon this result (**Supplementary Figure S2**). Ultimately, the spectrum obtained with a 60 × 60 × 60 fine $\boldsymbol{\kappa}$-grid on top of an 8 × 8 × 8 coarse **K**-grid is in close agreement with experiments (**Figure 1**). The comparison here is done with experimental data at 10 K available in the literature for Si bulk (Jellison and Modine, 1983).

3.2 GaAs Bulk

As in the case of Si, GaAs also requires very dense **k**-sampling for its optical response to be converged. The coarse grid in this case is an under-converged 10 × 10 × 10 Gamma-centred **k**-point grid. Indeed, the spectrum produced by this coarse grid alone also presents various spurious peaks, revealing a high degree of artificial localisation of its excitons (**Figure 2**). **Supplementary Figure S3** shows that adding a fine (double) $\boldsymbol{\kappa}$-grid of 20 × 20 × 20 does not solve the problem fully. However, the spectra with 40 × 40 × 40 or 60 × 60 × 60 $\boldsymbol{\kappa}$-grids match the experimental data relatively well (**Supplementary Figure S4** and **Figure 2**,

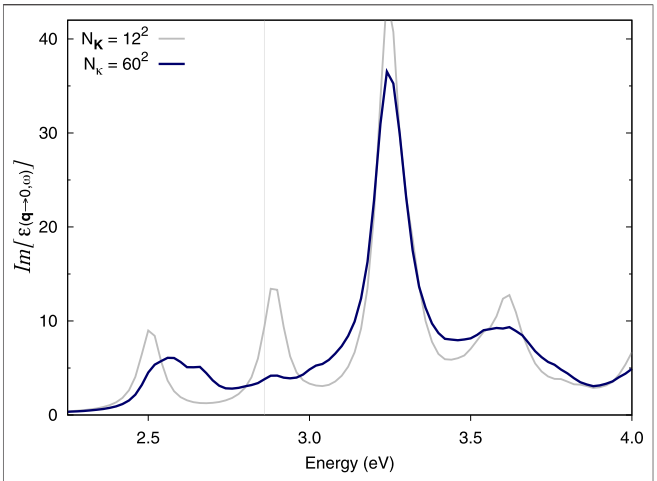

FIGURE 3 | Optical absorption spectra of monolayer MoS_2. BSE spectra calculated using the double-grid approach described in this work. Spectra are calculated on a 12 × 12 × 1 coarse **k**-grid and a denser fine **k**-grid, indicated by N_{κ}. $N_{\mathbf{K}} = 12^2$ corresponds to a standard calculation on a 12 × 12 × 1 **k**-grid while $N_{\kappa} = 60^2$ corresponds to a double-grid calculation with a 60 × 60 × 1 fine grid. We consider all *e*–*h* pairs from the top three valence bands to the five bottom conduction bands. All **k**-grids are Gamma-centred.

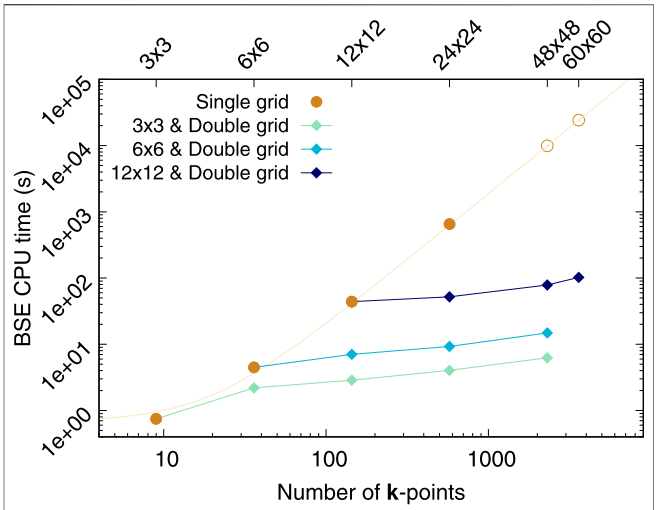

FIGURE 4 | CPU time in seconds required to calculate and store the BSE kernel, and solve it *via* Haydock's iterative scheme as a function of the number of **k**-points. Brown circles represent *full* BSE calculations. The data for 48 × 48 × 1 and 60 × 60 × 1 **k**-grids have been estimated via a quadratic fitting. The diamonds denote double-grid BSE calculations. Lines connect double-grid calculations using the same coarse-grid. All calculations were carried out in one processor for comparability purposes. The data plotted here corresponds to monolayer MoS_2. We consider all *e*–*h* pairs from the top three valence bands to the five bottom conduction bands.

respectively). In particular, the latter grid appears to capture the splitting of the first exciton present in the experimental data, although a denser coarse grid would be required as a better starting point to fully reproduce this feature. Indeed, this result still seems to suffer from slight artificial localisation, e.g., at 3.5 eV. The comparison is drawn to available experimental data for GaAs at 22 K (Lautenschlager et al., 1987).

3.3 MoS_2 Monolayer

The convergence of the absorption spectrum of monolayer MoS_2 with the **k**-grid within BSE has been discussed in the appendix of Molina-Sánchez et al. (2013). The latter study reports a converged spectrum using a very dense **k**-point grid and clarifies that when spin-orbit coupling is not considered, the first excitonic peak should not show any splitting. In fact, other works which used an under-converged **k**-grid, mistakenly showed a splitting of the first excitonic peak in collinear spin-polarised calculations with no spin-orbit coupling accounted for.

Here, we aim to reproduce the spectra in Molina-Sánchez et al. (2013) *via* the double-grid method (i.e., at a fraction of the computational cost). Our results follow a similar trend to the spectrum thereby reported. In the work of Molina-Sanchez et al., spectra with 12 × 12 × 1 or 18 × 18 × 1 (single grids) show splitting of the first peak while (single) **k**-grids of 24 × 24 × 1 or 30 × 30 × 1 solve the issue. Our result with a 12 × 12 × 1 single grid is equivalent to that of Molina-Sánchez et al. (2013) (except for a rigid shift in energy), i.e., it shows undue splitting (**Figure 3**). Adding a double grid of 24 × 24 × 1 $\boldsymbol{\kappa}$-points also results in undue splitting while 48 × 48 × 1 appears to eliminate it (**Supplementary Figures S5, S6**, respectively). A double grid of 60 × 60 × 1 further improves upon this result (**Figure 3**). Importantly, the quality of the double grid spectrum with a double grid of 60 × 60 × 1 $\boldsymbol{\kappa}$-points is not far from what was achieved in Molina-Sánchez et al. (2013) with a 30 × 30 × 1 single grid. The double grid approach correctly captures the physics at play despite representing roughly the computational cost of a 12 × 12 × 1 regular BSE Haydock calculation (see **Section 4**).

4 DISCUSSION

4.1 Computational Cost

As described above, Lanczos approaches to the BSE eliminate the need to invert the BSE kernel or fully diagonalise the two-particle Hamiltonian, which would become the bottleneck of the calculation whenever required. Instead, Lanczos solvers replace these highly demanding tasks by very efficient and computationally inexpensive iterative schemes. This numerical advantage means that the solution step itself does not drive the computational cost any longer, but rather, computing and storing the BSE matrix now becomes the bottleneck of the calculation. The method proposed in this work addresses this issue directly. First, the KS orbitals in the fine grid need not be available, i.e., not stored nor loaded into memory. Moreover, the kernel matrix elements in the fine grid, and consequently, the corresponding oscillator strengths, need not be calculated. As a result, the size of the BSE kernel matrix will effectively be that of the coarse grid. For instance, if we consider a coarse grid of 10 × 10 × 10 and a fine grid of 60 × 60 × 60 then there would be 1000 **K**-points and 216 000 $\boldsymbol{\kappa}$-points. The full BSE kernel would have $(200 \times N_c \times N_b)^2$ more matrix elements than the approximated one. Depending on the number of bands

required for convergence, the steps of computing and storing that many matrix elements may draw the line between what is feasible and what is not, not only in terms of processing power, but also due to memory and disk-storage limitations.

Let us consider monolayer MoS_2 to address how the computational cost compares between our double grid approach with a given fine $\boldsymbol{\kappa}$-grid and the regular (*full*) BSE calculation using that same fine grid as the only (single) **k**-grid. **Figure 4** shows the combined time required to calculate the BSE kernel and solve the eigen-problem via Haydock's scheme as a function of **k**-points used in the calculations. For comparability purposes, all the calculations shown in **Figure 4** have been carried out with just one processor. For the *full* solution of the problem (brown circles) the number of **k**-points has quadratic scaling from one **k**-grid to another (as it does for any 2D material) and the CPU time scales quadratically with the total number of **k**-points. This latter dependence stems from the size of the *e-h* basis set and the number of matrix elements of the BSE kernel, i.e., $(N_{\mathbf{k}} \times N_c \times N_b)^2$. The computational cost of the double grid approach proposed in this work (green-blue diamonds connected by lines) increases only slightly with the size of the fine-grid, when the same coarse grid is used. Since the BSE kernel is calculated only in the coarse-grid, this increase is due to the Haydock solver, which now has to process larger Haydock vectors. Nonetheless, it is apparent that the increased CPU time due to Haydock is minor and far more manageable than the scaling of the *full* BSE problem. Overall, fine grid has little impact on the CPU time required by the method we propose. In fact, **Figure 4** clearly shows that the computational cost of the double grid method is roughly driven by the coarse grid.

4.2 Kernel Extension to Fine Grid

The kernel extension is the key approximation used in the double-grid approach. The DKE in **Section 2** was selected for its simplicity and low computational cost. There are other possible kernel extensions. In particular, we also considered a kernel extension with similar characteristics, that we refer to as full kernel extension (FKE). First, let us define the FKE approach formally: FKE implies that each matrix element of the coarse grid BSE kernel is expanded into an all-ones block times the original matrix element, which leads to

$$\Xi_{\substack{nm\kappa_{\mathbf{I}_i} \\ n'm'\kappa_{\mathbf{I}_{i'}}}} \equiv \Xi_{\substack{nm\mathbf{K_I} \\ n'm'\mathbf{K_{I'}}}} \quad \forall\, i, i' \tag{16}$$

(see **Supplementary Material** for a visual representation of **Eq. 16**). As a result, the way in which the fine-grid matrix vector multiplication is carried out also differs from DKE. In FKE, this operation is performed as

$$r_{nm\kappa_{\mathbf{I}_i}} = \sum_{n'm'\mathbf{K_{I'}}} \Xi_{\substack{nm\mathbf{K_I} \\ n'm'\mathbf{K_{I'}}}} \sum_{\substack{i' \in \\ \mathbf{Dom}\left(\mathbf{K_{I'}}\right)}} c_{n'm'\kappa_{\mathbf{I}_{i'}}}. \tag{17}$$

Eqs. 16, **17** of FKE are analogous to **Eqs. 12**, **15** of DKE, respectively.

In terms of the spectra produced by either kernel extensions, the comparison consistently favours DKE over FKE in all the materials tested in this work. The difference may be less noticeable in systems with weaker excitonic effects. A comparison for the materials in **Section 3** is shown in **Figure 5**. In the case of Silicon (**Figure 5A**), it is apparent that DKE is better than FKE at suppressing the artificial localisation found around 3.6 eV. For GaAs (**Figure 5B**), DKE also shows an improvement with respect to FKE when dealing with the artificial localisation at around 3.1 eV. Finally, monolayer MoS_2 (**Figure 5C**) also follows the trend found in this work, i.e., DKE is consistently better than FKE. In this case in particular, the difference between both approaches is very stark. In fact, the FKE approach shows little to no improvement with respect to the $12 \times 12 \times 1$ single **k**-grid as far as the first exciton is concerned (cf. **Figure 3**).

In order to explain the better performance of DKE over FKE, we will discuss the properties of the BSE kernel and the two-particle Hamiltonian matrices, which are related by **Eq. 6**. In general, the kernel matrix elements $\Xi_{\substack{nm\mathbf{k} \\ n'm'\mathbf{k}'}}$ are sharply peaked at $\mathbf{q} = 0$ (Rohlfing and Louie, 1998; Rohlfing and Louie, 2000), i.e., for $\mathbf{k} = \mathbf{k}'$. This does not mean that every matrix element with $\mathbf{q} = 0$ will have a higher value than the remaining matrix elements. In fact, that is only true for the diagonal elements $\Xi_{\substack{nm\mathbf{k} \\ n'm'\mathbf{k}'}}$, while the $\mathbf{q} = 0$ elements coupling different sets of bands ($\Xi_{\substack{nm\mathbf{k} \\ n'm'\mathbf{k}'}}$) are closer in value to all other $\mathbf{q} \neq 0$ matrix elements. This is again exemplified with monolayer MoS_2 in **Figure 6**. The latter shows the module of every matrix element between a given transition ($v = 13$, $c = 14$ and $\mathbf{k}_1 = (-0.166, -0.166, 0)$) and every other transition in the *e-h* space, i.e., one row of the BSE kernel matrix. This data is plotted as a function of the magnitude $\|\mathbf{q}\|/\|\mathbf{q}\|_{max}\ sgn\,(q_x)$, where $\mathbf{q} = \mathbf{k} - \mathbf{k}_1$. **Figure 6A** shows the BSE kernel as obtained with a single grid of $6 \times 6 \times 1$ **k**-points, where we can see that the diagonal matrix element (the selected transition with itself) is an order of magnitude higher than all other matrix elements (many of which also have $\mathbf{q} = 0$). The fine grid of $12 \times 12 \times 1$ **k**-points better captures the build-up to the peak of the graph as it has many more **k**-points around the selected one (**Figure 6B**). Unfortunately, the double grid approach proposed here cannot capture this feature because it is meant not to imply any extra computation or storage of matrix elements at fine grid $\boldsymbol{\kappa}$-points. However, the reader should bear in mind that while this feature is missing in our approximated BSE kernel, the benefits of this double grid approach reside in exactly knowing the transition energies at the fine grid $\boldsymbol{\kappa}$-points (see **Supplementary Material** for detailed discussion). At this point, what we expect from the approximated kernel is not to introduce unphysical matrix elements, and in this regard DKE performs much better than FKE. **Figure 6C** shows how the BSE kernel matrix elements approximated by DKE still represent a function of **q** that is sharply peaked at the origin. Conversely, the FKE approach

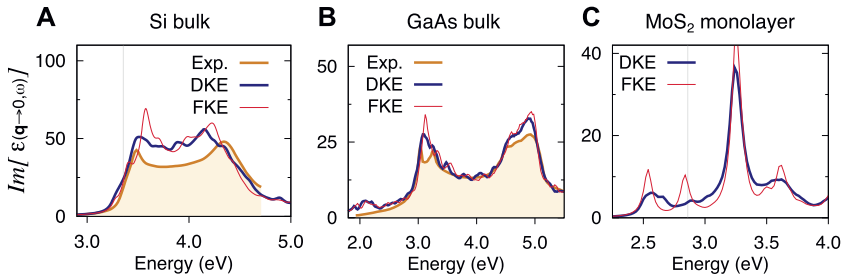

FIGURE 5 | Optical absorption spectra of bulk Si **(A)**, GaAs **(B)** and MoS_2 monolayer **(C)**. Comparison of spectra obtained by diagonal kernel extension (DKE) and full kernel extension (FKE). For Si and GaAs the coarse **k**-grid was 8 × 8 × 8 and 10 × 10 × 10 respectively and the fine **k**-grid, 60 × 60 × 60. For the MoS_2 monolayer, the coarse **k**-grid was 12 × 12 × 1 and the fine **k**-grid, 60 × 60 × 1.

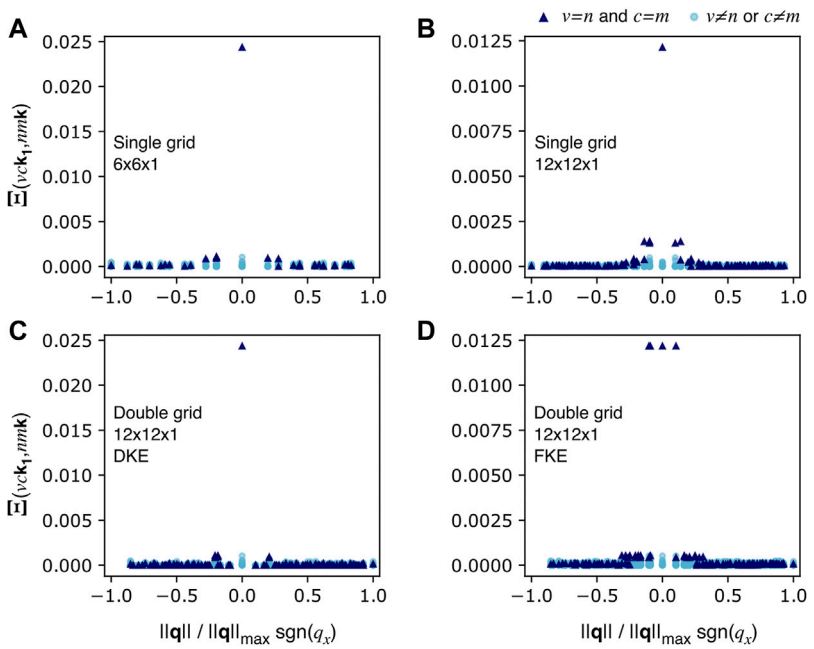

FIGURE 6 | Module of the BSE Kernel matrix element between one transition ($vc\mathbf{k}_1$) and every other transition in the *e-h* space ($nm\mathbf{k}$). The data plotted here corresponds to MoS_2 considering all *e-h* pairs from the top three valence bands to the five bottom conduction bands. **(A)** shows the matrix elements considering only a single grid of 6 × 6 × 1 **k**-points. The DKE and FKE (**(C,D)**, respectively) matrix elements are obtained from a 6 × 6 × 1 coarse **K**-grid and a 12 × 12 × 1 double $\boldsymbol{\kappa}$-grid. The fine grid data **(B)** is simply what DKE and FKE try to approximate, i.e., the kernel matrix elements obtained with one single grid of 12 × 12 × 1 **k**-points.

means that many matrix elements in **Dom** ($\mathbf{k}_1$), and consequently at $\mathbf{q} \neq \mathbf{0}$, will take the value of the peak. We know that such behaviour as a function of **q** would not arise should more **k**-points be included (**Figure 6B**). Hence, we believe DKE constitutes a better approximation of the BSE kernel than FKE. Further arguments in favour of the DKE over the FKE are presented in **Supplementary Material**.

4.3 Limitations of the Approach

The double-grid approach presented in Sec. IIB is based on two approximations: the DKE (**Eq. 12**) and the approximation of the starting Haydock vector (**Eq. 13**). The DKE has been extensively analysed in Sec. IVB. From the analysis, it emerges that the predominance of the matrix elements with $\mathbf{q} \approx 0$ is crucial to the success of the approximation. This is consistent with the spatial de-localisation of the exciton over many unit cells. Conversely, when the exciton is localised on few unit cells—as it is the case for instance in wide-gap insulators—the approximation may break down because of the significant contribution to the BSE kernel of matrix elements with $\mathbf{q} \neq 0$. We verified this is the case, for example, for bulk hexagonal boron nitride (h-BN). The breakdown of the approach for these cases is, however, not critical. In fact, excitons that are localised on few unit cells can be described accurately with a modest **k**-point sampling and the double-grid is not needed.

The approximation for the starting Haydock vector (**Eq. 13**) implies the assumption that (within the length gauge and dipole

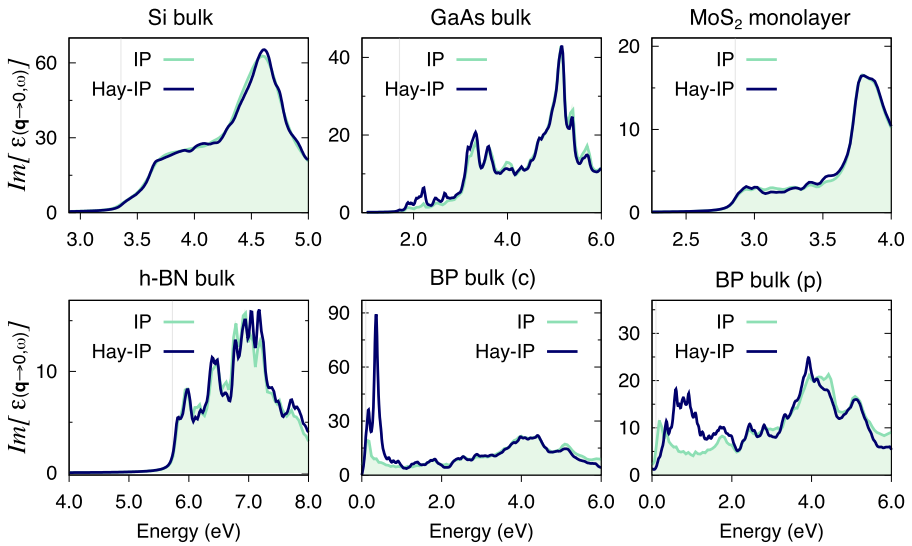

FIGURE 7 | Optical absorption spectra at the IP level calculated with the double grid method (labelled Haydock-IP) and *via* a full calculation on a fine grid (labelled IP), for all materials considered in this study. In all cases, the fine grid in the double-grid Haydock-IP calculation is of the same dimensions as the fine grid used in full for the IP calculation. The coarse grids and double/fine grids used for each material are listed below. Si: 8 × 8 × 8 and 60 × 60 × 60, GaAs: 10 × 10 × 10 and 40 × 40 × 40, MoS_2: 12 × 12 × 1 and 60 × 60 × 1, h-BN: 12 × 12 × 4 and 24 × 24 × 8, BP(c): 14 × 10 × 4 and 42 × 30 × 12, BP(p): 5 × 5 × 6 and 30 × 30 × 36. All **k**-grids are Gamma-centred.

approximation) the dipole matrix elements in the fine grid can be approximated by those in the coarse grid, namely,

$$\langle n\kappa_{\mathbf{I}_i}|\ \hat{\mathbf{r}}\ |m\kappa_{\mathbf{I}_i}\rangle \approx \langle n\mathbf{K}_\mathbf{I}|\ \hat{\mathbf{r}}\ |m\mathbf{K}_\mathbf{I}\rangle, \tag{18}$$

for $\kappa_{\mathbf{I}_i} \in \mathbf{Dom}(\mathbf{K}_\mathbf{I})$, where $\hat{\mathbf{r}}$ is the position operator. This assumption can be verified at the level of the independent particle approximation (IPA) by comparing the IPA spectrum obtained with the double-grid approach (which we call Haydock-IP) with the IPA spectrum calculated on the fine grid. In fact, in the independent particle case, **Eq. 18** is the only approximation introduced by the double grid. For the systems considered in **Section 3**, we verified that indeed the IPA spectra obtained within the double-grid approach agree well with the IPA calculated on the corresponding fine grid (**Figure 7**). It is also interesting to note that this particular approximation is valid for h-BN, which singles out the BSE kernel ($\mathbf{q} \approx 0$) approximation as the only factor hindering the application of the double-grid method to this material. In particular, GaAs shows a minor discrepancy in the IPA spectra around 2.1 eV (**Figure 7**), a region of the spectrum where **k**-point convergence is markedly difficult. This is due to the steep dispersion of the conduction band of GaAs around the Gamma point, where the optical gap occurs [see, for example, (Lautenschlager et al., 1987)]. As a result, the approximation of the oscillator strengths around Gamma by the corresponding matrix element at Gamma (**Eq. 18**) is a rather poor one, which translates into an unphysical feature around 2.1 eV in the BSE spectrum as well (**Figure 2**).

There are also instances in which the approximation in **Eq. 18** breaks down substantially. As an example, **Figure 7** shows this breakdown for the optical absorption of bulk black-phosphorous (BP) along the armchair direction (Tran et al., 2014). The IPA spectrum obtained within the double-grid approach has strong peaks around 0.3 eV which are not present in the reference calculation. The appearance of this artefact can be understood considering that the dipole matrix elements (**Eq. 18**) are calculated as $\frac{\langle n\mathbf{K}_I|\ \hat{\mathbf{v}}\ |m\mathbf{K}_I\rangle}{E_{nm\kappa_I}}$, where $\hat{\mathbf{v}}$ is the velocity operator. BP has a minimum KS band-gap of about 0.2 eV (0.1 eV at the DFT level) and thus the corresponding dipole matrix element is large. Within the double-grid approach, all fine-grid **k**-points in the domain of the **k**-point corresponding to the minimum KS band-gap use the same value which largely overestimates the actual dipole matrix element. Notably, carrying out the calculations in the primitive rather than in the conventional unit cell (**Figure 7**), improves the agreement with the reference IPA fine-grid spectrum, suggesting that in this case the coarse grid does a better job at sampling the Brillouin zone around the **k**-point corresponding to the minimum KS band-gap. Nevertheless, this Haydock-IP spectrum still presents artificial features between 0.5 and 1.0 eV, preventing the application of the double-grid method presented in this work to BP.

Further to note is that using **Eq. 18** the extension from the coarse to the full grid is done for the position dipoles, i.e. within the length gauge. This implies that, to ensure gauge invariance (Sangalli et al., 2017), $\langle n\kappa_{\mathbf{I}_i}|\ \hat{\mathbf{v}}\ |m\kappa_{\mathbf{I}_i}\rangle = \langle n\mathbf{K}_\mathbf{I}|\ \hat{\mathbf{v}}\ |m\mathbf{K}_\mathbf{I}\rangle (E_{nm\kappa_{\mathbf{I}_i}}/E_{nm\mathbf{K}_\mathbf{I}})$. An alternative choice could be instead to assume $\langle n\kappa_{\mathbf{I}_i}|\ \hat{\mathbf{v}}\ |m\kappa_{\mathbf{I}_i}\rangle = \langle n\mathbf{K}_I|\ \hat{\mathbf{v}}\ |m\mathbf{K}_I\rangle$, i.e. to perform the extension of the velocity matrix elements and accordingly obtain $\langle n\kappa_{\mathbf{I}_i}|\ \hat{\mathbf{r}}\ |m\kappa_{\mathbf{I}_i}\rangle = \langle n\mathbf{K}_I|\ \hat{\mathbf{r}}\ |m\mathbf{K}_I\rangle (E_{nm\mathbf{K}_I}/E_{nm\kappa_{\mathbf{I}_i}})$. Preliminary results show that such choice may in fact lead to better results for BP.

4.4 Workflow Implementation

Based on this discussion, we can propose a workflow to assess whether a given material satisfies these approximations and could thus be described well by the double-grid method presented here. Firstly, a *full* fine grid IP calculation must be converged with respect to **k**-points. Alternatively one could choose the densest **k**-grid that can be treated at the IP level, where limitations usually reside on memory. Let us take an example where this first step of the procedure returns a $60 \times 60 \times 60$ **k**-grid. The next stage would be to find an appropriate coarse **k**-grid, i.e., one that satisfies the approximation in **Eq. 18**. This would entail running several double-grid calculations at the IPA level (Haydock-IP) with varying coarse grid and with a fine grid of $60 \times 60 \times 60$. By matching the Haydock-IP spectrum to the *full* $60 \times 60 \times 60$ fine-grid IP spectrum, a sound coarse grid can be chosen by means of a fairly inexpensive procedure (e.g., $8 \times 8 \times 8$). The next step in the workflow would necessarily involve BSE calculations as the approximation on the BSE kernel cannot be tested at the IPA level. With the chosen coarse grid, successive double-grid BSE calculations with varying fine grids should be carried out in order to converge the dimensions of the latter. It is worth mentioning that all these calculations have roughly the same computational cost and requirements, at the level of the coarse-grid $8 \times 8 \times 8$ BSE calculation. It should be highlighted that convergence of the fine-grid in the double-grid method does not guarantee the validity of the DKE approximation. At this point, one should turn to available data, either experimental or theoretical, in order to assess the validity of the results on physical grounds.

5 CONCLUSION

In this work, we presented a double grid approach to the problem of **k**-point sampling in the solution of the BSE equation for the calculation of optical spectra of semiconductors. This responds to the fact that very dense **k**-point grids are required for BSE calculations to be fully converged due to the large periodicity of excitonic wavefunctions, usually reaching several supercells. This sampling requirement is the bottleneck in BSE calculations and, for a wide variety of solids, this imposes a computational burden that renders the calculation prohibitively costly. We tackled this challenge by applying a double grid approach to the computationally cheapest among the BSE solvers, i.e., the Lanczos-based Haydock scheme, thus maximising the size and range of materials for which this method could be useful. Our double grid approach is based on combining a coarse **k**-grid where both KS eigen-values and eigen-vectors are known with a fine **k**-grid where only KS energies are required, which eases memory and disk storage requirements. With this strategy, the coarse **k**-grid drives the computational cost while the **k**-fine grid tries to capture the physics of spread out excitons in an approximated way without requiring significant extra computation.

This scheme was implemented in the Yambo code (see **Supplementary Material** for availability) and tested for bulk Si, bulk GaAs and monolayer MoS_2, all of which are known to require very dense **k**-point grids to achieve convergence. The results are satisfactory in all cases, reproducing data reported elsewhere with a relatively low computational cost close to that of the coarse grid alone. There is a slight increase in the CPU time required by the Haydock step, however this scales very favourably with increasingly dense **k**-meshes, at variance with regular non-double grid approaches. Different ways to extend the BSE kernel calculated in the coarse grid to the fine grid are discussed and compared, determining that the so-called diagonal kernel extension is the preferred method.

The approximations introduced with the double-grid approach have been discussed, together with the limits they impose to its validity. On the one hand, the diagonal kernel extension limits the applicability of this approach to systems with excitons delocalised over many unit cells. On the other hand, the latter are precisely the main target of the double-grid approach, given that spatially localised excitons are usually well described by a relatively coarse **k**-grids. Further, we discussed how the validity of the approximation on the dipole matrix elements can be verified and controlled with inexpensive calculations at the level of the independent particle approximation.

In light of the promising results achieved by the double grid approach presented in this work, considering its simplicity and taking into account its compatibility with the very efficient Lanczos based BSE solution schemes (i.e., Haydock), we hope our work will facilitate the calculation of optical spectra in semiconductors that could not be computationally afforded to date.

DATA AVAILABILITY STATEMENT

Input and output files of the calculations presented in this study can be found in a GitHub repository (https://github.com/aim137/double_grid_data_repository.git). The double-grid method developed in this work for calculating optical absorption spectra via the Haydock solution scheme of the BSE will be available in the next release of the Yambo code (Yambo 5.1).

AUTHOR CONTRIBUTIONS

IA contributed to the development of the approach and implemented it into Yambo. IA also carried out the calculations, analysed their results and wrote most of the manuscript. DS put forward the idea of the approach—that was then improved together with IA and MG—assisted with the implementation of the approach and contributed to the analysis of the results. MG contributed to the development of the approach and assisted with its implementation. MG also contributed to the analysis of the results and wrote a part of the manuscript.

FUNDING

MG is grateful for support from the Engineering and Physical Sciences Research Council, under grant EP/V029908/1. DS acknowledges support from Italian Ministry of Education, University and Research (MIUR) through the Research Project of National Relevance (PRIN) BIOX under Grant No. 20173B72NB; from the European Union project MaX (Materials design at the eXascale) H2020-EINFRA-2015-1 (Grant Agreement 824 143) and from the Nanoscience Foundries and Fine Analysis-Europe H2020-INFRAIA-2014-2015 (Grant Agreement No. 654 360).

REFERENCES

Benedict, L. X., and Shirley, E. L. (1999). Ab Initiocalculation Ofε2(ω)including the Electron-Hole Interaction: Application to GaN andCaF2. *Phys. Rev. B* 59, 5441–5451. doi:10.1103/physrevb.59.5441

Benedict, L. X., Shirley, E. L., and Bohn, R. B. (1998). Optical Absorption of Insulators and the Electron-Hole Interaction: AnAb InitioCalculation. *Phys. Rev. Lett.* 80, 4514–4517. doi:10.1103/physrevlett.80.4514

Cini, M. (2007). *Topics and Methods in Condensed Matter Theory*. Springer-Verlag.

Fuchs, F., Rödl, C., Schleife, A., and Bechstedt, F. (2008). Efficient O (N2) Approach to Solve the Bethe-Salpeter Equation for Excitonic Bound States. *Phys. Rev. B - Condensed Matter Mater. Phys.* 78, 1–13. doi:10.1103/physrevb.78.085103

Ge, X., Binnie, S. J., Rocca, D., Gebauer, R., and Baroni, S. (2014). turboTDDFT 2.0-Hybrid Functionals and New Algorithms within Time-dependent Density-Functional Perturbation Theory. *Comp. Phys. Commun.* 185, 2080–2089. doi:10.1016/j.cpc.2014.03.005.1402.0486

Gillet, Y., Giantomassi, M., and Gonze, X. (2016). Efficient On-The-Fly Interpolation Technique for Bethe-Salpeter Calculations of Optical Spectra. *Comp. Phys. Commun.* 203, 83–93. doi:10.1016/j.cpc.2016.02.008.1602.01863

Golze, D., Dvorak, M., and Rinke, P. (2019). The GW Compendium: A Practical Guide to Theoretical Photoemission Spectroscopy. *Front. Chem.* 7, 377. doi:10.3389/fchem.2019.00377

Grüning, M., Marini, A., and Gonze, X. (2011). Implementation and Testing of Lanczos-Based Algorithms for Random-phase Approximation Eigenproblems. *Comput. Mater. Sci.* 50, 2148–2156. doi:10.1016/j.commatsci.2011.02.021

Haydock, R. (1980). The Recursive Solution of the Schrödinger Equation. *Comp. Phys. Commun.* 20, 11–16. doi:10.1016/0010-4655(80)90101-0

Hedin, L., and Lundqvist, B. I. (1971). Explicit Local Exchange-Correlation Potentials. *J. Phys. C: Solid State. Phys.* 4, 2064–2083. doi:10.1088/0022-3719/4/14/022

Hedin, L. (1965). New Method for Calculating the One-Particle Green's Function with Application to the Electron-Gas Problem. *Phys. Rev.* 139, A796–A823. doi:10.1103/physrev.139.a796

Jellison, G. E., and Modine, F. A. (1983). Optical Functions of Silicon between 1.7 and 4.7 Ev at Elevated Temperatures. *Phys. Rev. B* 27, 7466–7472. doi:10.1103/physrevb.27.7466

Kammerlander, D., Botti, S., Marques, M. A., Marini, A., and Attaccalite, C. (2012). Speeding up the Solution of the Bethe-Salpeter Equation by a Double-Grid Method and Wannier Interpolation. *Phys. Rev. B - Condensed Matter Mater. Phys.* 86, 1209–1509. 1–5. doi:10.1103/physrevb.86.125203

Lanczos, C. (1950). An Iteration Method for the Solution of the Eigenvalue Problem of Linear Differential and Integral Operators. *J. Res. Natl. Bur. Stan.* 45, 255–282. doi:10.6028/jres.045.026

Lautenschlager, P., Garriga, M., Logothetidis, S., and Cardona, M. (1987). Interband Critical Points of GaAs and Their Temperature Dependence. *Phys. Rev. B* 35, 9174–9189. doi:10.1103/physrevb.35.9174

Marini, A., Hogan, C., Grüning, M., and Varsano, D. (2009). Yambo: An Ab Initio Tool for Excited State Calculations. *Comp. Phys. Commun.* 180, 1392–1403. doi:10.1016/j.cpc.2009.02.003

Martin, R., Reining, L., and Ceperley, D. (2016). *Interacting Electrons*. Cambridge University Press.

Molina-Sánchez, A., Sangalli, D., Hummer, K., Marini, A., and Wirtz, L. (2013). Effect of Spin-Orbit Interaction on the Optical Spectra of Single-Layer, Double-Layer, and Bulk MoS2. *Phys. Rev. B - Condensed Matter Mater. Phys.* 88, 1–6. doi:10.1103/physrevb.88.045412

Onida, G., Reining, L., and Rubio, A. (2002). Electronic Excitations: Density-Functional versus many-body Green's-function Approaches. *Rev. Mod. Phys.* 74, 601–659. doi:10.1103/revmodphys.74.601

Reining, L. (2018). The GW Approximation: Content, Successes and Limitations. *Wiley Interdiscip. Rev. Comput. Mol. Sci.* 8. doi:10.1002/wcms.1344

Rocca, D., Gebauer, R., Saad, Y., and Baroni, S. (2008). Turbo Charging Time-dependent Density-Functional Theory with Lanczos Chains. *J. Chem. Phys.* 128, 154105. doi:10.1063/1.2899649

Rocca, D., Ping, Y., Gebauer, R., and Galli, G. (2012). Solution of the Bethe-Salpeter Equation without Empty Electronic States: Application to the Absorption Spectra of Bulk Systems. *Phys. Rev. B - Condensed Matter Mater. Phys.* 85, 1–10. doi:10.1103/physrevb.85.045116

Rohlfing, M., and Louie, S. G. (1998). Electron-hole Excitations in Semiconductors and Insulators. *Phys. Rev. Lett.* 81, 2312–2315. doi:10.1103/physrevlett.81.2312

Rohlfing, M., and Louie, S. G. (2000). Electron-hole Excitations and Optical Spectra from First Principles. *Phys. Rev. B* 62, 1–18. doi:10.1103/physrevb.62.4927

Salpeter, E. E., and Bethe, H. A. (1951). A Relativistic Equation for Bound-State Problems. *Phys. Rev.* 84, 1232–1242. doi:10.1103/physrev.84.1232

Sangalli, D., Berger, J. A., Attaccalite, C., Grüning, M., and Romaniello, P. (2017). Optical Properties of Periodic Systems within the Current-Current Response Framework: Pitfalls and Remedies. *Phys. Rev. B* 95, 155203. doi:10.1103/physrevb.95.155203

Sangalli, D., Ferretti, A., Miranda, H., Attaccalite, C., Marri, I., Cannuccia, E., et al. (2019). Many-body Perturbation Theory Calculations Using the Yambo Code. *J. Phys. Condens Matter* 31, 325902, 2019 . 03837. doi:10.1088/1361-648X/ab15d0

Tran, V., Soklaski, R., Liang, Y., and Yang, L. (2014). Layer-controlled Band gap and Anisotropic Excitons in Few-Layer Black Phosphorus. *Phys. Rev. B - Condensed Matter Mater. Phys.* 89, 1–6. doi:10.1103/physrevb.89.235319

ACKNOWLEDGMENTS

The authors acknowledge useful discussions with Daniele Varsano, Matteo Zanfrognini and Claudio Attaccalite.

SUPPLEMENTARY MATERIAL

The Supplementary Material for this article can be found online at: https://www.frontiersin.org/articles/10.3389/fchem.2021.763946/full#supplementary-material

Conflict of Interest: The authors declare that the research was conducted in the absence of any commercial or financial relationships that could be construed as a potential conflict of interest.

Publisher's Note: All claims expressed in this article are solely those of the authors and do not necessarily represent those of their affiliated organizations, or those of the publisher, the editors and the reviewers. Any product that may be evaluated in this article, or claim that may be made by its manufacturer, is not guaranteed or endorsed by the publisher.

Advantages of publishing in Frontiers

OPEN ACCESS
Articles are free to read for greatest visibility and readership

FAST PUBLICATION
Around 90 days from submission to decision

HIGH QUALITY PEER-REVIEW
Rigorous, collaborative, and constructive peer-review

TRANSPARENT PEER-REVIEW
Editors and reviewers acknowledged by name on published articles

Frontiers
Avenue du Tribunal-Fédéral 34
1005 Lausanne | Switzerland

Visit us: www.frontiersin.org
Contact us: frontiersin.org/about/contact

REPRODUCIBILITY OF RESEARCH
Support open data and methods to enhance research reproducibility

DIGITAL PUBLISHING
Articles designed for optimal readership across devices

FOLLOW US
@frontiersin

IMPACT METRICS
Advanced article metrics track visibility across digital media

EXTENSIVE PROMOTION
Marketing and promotion of impactful research

LOOP RESEARCH NETWORK
Our network increases your article's readership